
THESES, SIS/LIBRARY
R.G. MENZIES BUILDING NO.2
Australian National University
Canberra ACT 0200 Australia

Telephone: +61 2 6125 4631
Facsimile: +61 2 6125 4063
Email: library.theses@anu.edu.au

USE OF THESES

**This copy is supplied for purposes
of private study and research only.
Passages from the thesis may not be
copied or closely paraphrased without the
written consent of the author.**

**THE ARDLETHAN TIN
FIELD, NEW SOUTH WALES:
BRECCIA PIPES AND MINERALIZATION**

SHUANG K. REN

A thesis submitted for the degree of
Doctor of Philosophy
of the Australian National University

July, 1989

DECLARATION

Except where otherwise indicated this thesis is my own work.

Shuang K. REN

Ren Shuang kui

July, 1989

ABSTRACT

The Ardlethan Tin Field is located near the western edge of the Lachlan Fold Belt in New South Wales, Australia. The oldest rocks in the Ardlethan Tin Field are metasedimentary rocks of Ordovician age. They were intruded during late Silurian-early Devonian times by the Mine Granite and the Ardlethan Granite dated at 417 ± 2.5 and 410 ± 2.5 Ma respectively. The latter is strongly fractionated and has three daughter phases: the Garnet-Bearing Quartz Feldspar Porphyry (GQFP), the microgranite and the Mine Porphyry. The GQFP represents a marginal phase, the microgranite a moderately fractionated phase and the Mine Porphyry a late stage strongly fractionated phase.

Four breccia pipes, the Mine Granite, Carpathia-Blackreef, Stackpool-Godfrey and the White Crystal Breccia Pipes were formed sequentially in three brecciation events. They are hosted by the Mine Granite. Each brecciation event was followed by hydrothermal alteration, and cassiterite and sulphide mineralization.

Fluid exsolution during crystallization of the most fractionated phase of the Ardlethan Granite was responsible for the brecciation. Structural data suggest that three major intersecting joints controlled the distribution of the breccia pipes.

The distribution of fragments of the microgranite, Mine Porphyry, sediment and mafic dykes in the breccia pipes indicates a complex evolutionary history during their formation. The materials in the Mine Granite, Carpathia-Blackreef and the Stackpool-Godfrey Breccia Pipes have moved upward significantly. The White Crystal Breccia Pipe is the only one which has collapsed.

The mineralization in the breccia pipes was strongly controlled by permeability. The Mine Granite Breccia Pipe has an impermeable central zone of rock flour-supported breccia and a marginal zone of fragment-supported breccia. Mineralization of economic grades only occurs in the marginal zone. A similar situation occurs in the upper levels of the Carpathia-Blackreef and Stackpool-Godfrey Breccia Pipes. The White Crystal Breccia Pipe contains no rock flour-supported breccia so that mineralization occurs mainly in the central zone.

Cassiterite and sulphide mineralization in the breccia pipes is associated with hydrothermal biotite, sericite, tourmaline, quartz, topaz

and chlorite. A common paragenetic sequence observed in all the breccia pipes is early cassiterite deposition with sericite, tourmaline and milky quartz, followed by sulphide deposition with clear quartz, toothy quartz, fluorite and cookeite vug infill and chlorite alteration. An independent event of cosalite mineralization, associated with native bismuth and bismuthinite, occurs in fractures and veins postdating the cassiterite and sulphide mineralization in the Blackreef-Godfrey area.

The compositions of biotite, tourmaline, muscovite and chlorite in the Ardlethan Granite are enriched in FeO and depleted in MgO compared to biotite, tourmaline, muscovite and chlorite in fresh Mine Granite. Those in the alteration zones formed during rock-fluid reactions are generally of intermediate compositions.

Fluid inclusion microthermometric data indicate that cassiterite and milky quartz deposition in the Ardlethan Tin Field occurred at temperatures between 360 and 310°C; sulphide and clear quartz between 270 and 220°C; and toothy quartz, fluorite and cookeite between 200 and 150°C. Coexistence of CO₂-rich and H₂O-rich fluid inclusions allowed a minimum pressure estimate of about 450 bars during mineralization.

Temperatures calculated from the compositions of the hydrothermal biotite, muscovite and chlorite suggest that biotite alteration occurred between 420 and 360°C, sericite alteration between 330 and 290°C and chlorite alteration mainly between 290 and 105°C. These results are in good agreement with the fluid inclusion microthermometry and the paragenesis.

The oxygen isotope compositions of milky quartz, clear quartz and toothy quartz are mostly between 11.5 and 13.5 per mil regardless of the wide temperature range of their formation. This suggests a complex evolution in the fluid during mineralization probably due to continued rock-fluid equilibria. The sulphur isotope compositions of the sulphides formed during the main stage mineralization are very close to 0 per mil and the carbon isotope values mostly 4.3±1.0 per mil. They either support or permit a interpretation that the fluid responsible for the cassiterite and sulphide mineralization was derived from the Ardlethan Granite and continuously equilibrated with the Mine Granite. The sulphur isotope compositions of the sulphides in association with the cosalite mineralization are >10.0 per mil and indicate that the cosalite mineralization was an independent event.

Thermodynamic study of mineral-fluid equilibria suggests that there were continual changes in temperature, pH and redox conditions as the fluid flowed upwards in the breccia pipes. These changes caused

various styles of hydrothermal alteration and cassiterite and sulphide depositions.

The brecciation and breccia pipe-hosted cassiterite and sulphide mineralization may be interpreted in terms of a dynamic process involving magma fractionation in the Ardlethan Granite, episodic brecciation, fluid flow, rock-fluid reactions, fluid boiling, alteration and mineral deposition. The process started with the fractionation in the Ardlethan Granite. Accumulated volatiles build up an over-pressure which caused brecciation and formation of the Mine Granite Breccia Pipe. At this stage the Ardlethan Granite was only partially crystallized and the brecciation was followed by the intrusion of a differentiated magma, represented by the Mine Porphyry, which moved the materials in the Mine Granite Breccia Pipe upwards. The continual crystallization in the Ardlethan Granite kept a steady supply of fluid which was channelled into the most permeable marginal zones of the breccia pipe. As the fluid flowed upwards, it cooled, reacted with minerals in the brecciated rocks and boiled. The resultant physico-chemical gradients along the fluid paths caused biotite alteration; cassiterite and milky quartz deposition with sericite and tourmaline alteration; sulphide and clear quartz deposition; toothy quartz, fluorite and cookeite deposition and chlorite alteration sequentially in zones from depth to surface. Mineral deposition gradually reduced the permeability of the Mine Granite Breccia Pipe and the fluid flux, caused a slow retreat of the vertical zonations. When the Mine Granite was completely sealed by mineral deposition, fluid accumulation started again at depth and resulted in the brecciation of the Carpathia-Blackreef and the Stackpool-Godfrey Breccia Pipes. Similar processes occurred. The White Crystal Breccia Pipe represents the third brecciation event in the Ardlethan Tin Field. Its collapse reflects the depletion of volatiles and completion of crystallization of the Ardlethan Granite.

ACKNOWLEDGEMENT

I acknowledge Dr J. L. Walshe for his tremendous help and perseverance in supervising this project. The manuscript was reviewed by Dr J. L. Walshe, Dr N. C. Higgins and W. D. Platts. Dr N. C. Higgins, Dr R. A. Eggleton and Dr P. Eadington are also thanked for providing supervision. Prof. K. S. W. Campbell and Dr R. A. Eggleton kindly assisted in obtaining an ANU Ph.D. scholarship. I thank Dr D. Ellis, Dr W. Cameron, Dr C. Johnson, Dr S. Eldridge, Dr S. Lonker and Dr C. Perkins for their advice.

Aberfoyle Pty Ltd is greatly acknowledged for their permission to undertake this project and for financial assistance. I particularly wish to thank Mr W. Lannen, R. Paterson, the late I. Keyes, D. Barrell, M. Flemming, A. McDougall and R. Smith. I also want to acknowledge Geopeko Pty Ltd and its staffs for their cooperation.

I thank R. Paterson for his kind permission to use his whole rock geochemistry data, geological maps and sections. Dr S. S. Sun is thanked for providing some unpublished isotope data and many instructive discussions. Mr C. Foudoulus helped in photographic and X-ray works. Stable isotope analyses were done through Dr R. Both at Adelaide University, Dr S. S. Sun at the Bureau of Mineral Resources and Dr A. Andrew at CSIRO. Mr N. Ware supervised the electron microprobe work. All the petrographic thin sections and fluid inclusion thin sections were made by R. Popovich and H. Zapasnik. B. Harrold assisted with computer programming.

I also wish to thank Prof. Tu Guangzhi, Director of the Institute of Geochemistry, Academia Sinica, for his kind recommendation and encouragement for me to study overseas. Profs. Wang Kui-Ren and Sun Li-Guang, University of Sciences and Technology of China, are also acknowledged for their assistance during my study.

Many discussions with my Ph.D. colleagues S. Halley, P. S. Heithersay, M. Liu, F. Luan, W. Platts, W. Sawka, P. S. Smith, Q. Wang and W. Zang were extremely helpful.

Finally I thank my wife Weiping for her consistent support and patience throughout this project, particularly after we had our first child Samuel.

Table of Contents

Declaration	II
Abstract	III
Acknowledgement	VI
Table of Contents	VII
List of Figures	XI
List of Plates	XIII
Chapter 1 Introduction	1
1.1 Location and Climate	1
1.2 Regional Geology and Mineralization	1
1.3 The Ardlethan Tin Field	2
1.4 Mining History	2
1.5 Previous Work	3
1.6 The Current Study	4
Chapter 2 Geology and Petrology	12
2.1 The Sediments	12
2.2 The Mine Granite	13
2.3 The Ardlethan Granite	13
2.4 The GQFP	15
2.5 The Pyroclastic Volcanics	15
2.6 The Microgranite Dykes	16
2.7 The Mine Porphyry	16
2.8 The Mafic Dykes	17
2.9 Summary	17
Chapter 3 Geochemistry of the Granitoids	20
3.1 Samples	20
3.2 Types of the Granitoids	20
3.3 Harker Diagrams	23
3.4 Discussion	24
3.5 Potentials of Tin Enrichment	32
3.6 Summary	33
Chapter 4 Breccia Pipes and Their Foemation	34
4.1 Descriptions	34
4.1.1 The Mine Granite Breccia Pipe	34
4.1.2 The Carpathia-Blackreef and the Stackpool-Godfrey Breccia Pipes	39
4.1.3 The White Crystal Breccia Pipe	45
4.2 Correlation Between Igneous and Brecciation Events	46
4.3 Sources of the Sediment Fragments	47
4.4 Structural Control Over Brecciation	49
4.5 The Process of Brecciation	50
4.6 Summary of the Magmatic and Brecciation events	53

Chapter 5	Mineralization, Hydrothermal Alteration and Paragenesis	76
5.1	The Ardwest Group of Deposits	76
5.1.1	General Descriptions	76
5.1.2	Hydrothermal Alteration	79
5.1.3	Cassiterite and Sulphide Mineralization	85
5.1.4	Toothy Quartz, Fluorite and Cookeite	87
5.1.5	Paragenesis of the Ardwest Group of Deposits	87
5.2	The Carpathis Group of Deposits	89
5.2.1	General Descriptions	89
5.2.2	Hydrothermal Alteration	91
5.2.3	Cassiterite and Sulphide Mineralization	95
5.2.4	Toothy Quartz, Fluorite and Cookeite	97
5.2.5	Cosalite Mineralization in the Blackreef Deposit	98
5.2.6	Paragenesis of the Carpathia Group of Deposits	99
5.3	The White Crystal Deposit	100
5.3.1	General Description	100
5.3.2	Hydrothermal Alteration	101
5.3.3	Cassiterite and Sulphide Mineralization	101
5.3.4	Toothy Quartz, Fluorite and Cookeite	102
5.3.5	Paragenesis of the White Crystal Deposit	102
5.4	Overall Paragenesis of the Ardlethan Tin Field	102
5.5	Geometry of Ore Bodies	103
5.6	Correlation Between Styles of Brecciation and Mineralization	104
5.7	Summary and Conclusions	104
Chapter 6	Mineral Chemistry	107
6.1	Feldspars	107
6.2	Biotite	107
6.3	Muscovite	111
6.4	Chlorite	113
6.5	Tourmaline	115
6.6	Siderite	116
6.7	Cookeite	117
6.8	Cosalite	117
6.9	Summary	119
Chapter 7	Fluid Inclusion Studies	120
7.1	Samples and Microthermometry	120
7.2	Types of Fluid Inclusions	121
7.2.1	Type A Fluid Inclusions	121
7.2.2	Type B Fluid Inclusions	122
7.2.3	Type C Fluid Inclusions	122
7.2.4	Type D Fluid Inclusions	122
7.2.5	Type E Fluid Inclusions	132
7.3	Salinities of Fluid Inclusions	132
7.4	Type A, B, and C Fluid Inclusions	134

7.5	Temperatures of Mineralization	135
7.5.1	The Blackreef Deposit	135
7.5.2	The White Crystal Deposit	137
7.5.3	The Ardwest Group of Deposits	138
7.6	Pressure of Mineralization	138
7.7	Oxidation Conditions	139
7.8	Summary and Conclusions	141
Chapter 8	Stable Isotope Studies	142
8.1	Carbon Isotopes	142
8.2	Sulphur Isotopes	143
8.3	Oxygen Isotopes	145
8.3.1	Whole Rock Samples	145
8.3.2	Quartz Samples	146
8.3.3	Other Minerals	150
8.3.4	Oxygen Isotope Compositions of the Hydrothermal Fluids	151
8.4	Origin of the Hydrothermal Fluids	152
8.4.1	A Mixing Model	152
8.4.2	A Dynamic Evolution Model	153
8.5	Conclusions	157
Chapter 9	Conditions of Mineral Deposition	158
9.1	Temperature	158
9.2	Pressure	160
9.3	Redox Conditions	160
9.4	pH Conditions	162
9.5	Cassiterite Deposition	163
9.6	Summary and Discussion	164
Chapter 10	Summary and Conclusions	167
Appendix 1	Mineral Chemistry and Whole Rock Chemistry Data	172
A1-1	Mineral Chemistry Data	172
A1-2	Whole Rock Chemistry Data	193
Appendix 2	Sample Catalog	198
Appendix 3	Tin Enrichment During Granite Differentiation and Implications	214
A3-1	Introduction	214
A3-2	Dynamics of Tin Enrichment during Granite Differentiation	216
A3-2.1	Differentiation	216
A3-2.2	Differentiation of Tin	220
A3-3	Kinetic Factors	225
A3-4	Conclusions	227
Appendix 4	A Geothermometer and A Geobarometer Based On A Eight-Component Biotite Solid Solution Model	228
A4-1	Introduction	228
A4-2	Choice of End Members	230

A4-3 Standard States and Activity-Composition Relationship	232
A4-4 Calculation of Ferric Iron and Water Contents and Temperature of Formation	233
A4-5 Calculating log f_{O_2} and Cation/Proton Activity Ratios	235
A4-6 Source of Thermodynamic Data and Estimations	236
A4-7 Summary	241
Appendix 5 Solubility of Cassiterite in Saline Fluid	242
A5-1 Introduction	242
A5-2 Sn^{2+} , Sn^{4+} , and Sn-OH Complexes	244
A5-3 Sn-Cl Complexes	246
A5-4 Sn-F Complexes	247
A5-5 Solubility of Cassiterite	250
References	254

List of Figures

Fig. 1-1 Structural geology map of New South Wales	8
Fig. 1-2 Tin granites of southeastern Australia	9
Fig. 1-3 Mineralization of the Girilambone-Wagga Anticlinorial zone	10
Fig. 1-4 Projected locations of tin deposits of the Ardlethan Tin Field	11
Fig. 2-1 Bed rock geology of the Ardlethan Tin Mine Area	18
Fig. 2-2 Timing relations of the igneous events in the Ardlethan area	19
Fig. 3-1A. Harker Diagram TiO ₂ vs SiO ₂	25
Fig. 3-1B. Harker Diagram FeO vs SiO ₂	25
Fig. 3-2A. Harker Diagram MgO vs SiO ₂	26
Fig. 3-2B. Harker Diagram V vs SiO ₂	26
Fig. 3-3A. Harker Diagram Rb vs SiO ₂	27
Fig. 3-3B. Harker Diagram U vs SiO ₂	27
Fig. 3-4A. Harker Diagram Sn vs SiO ₂	28
Fig. 3-4B. Harker Diagram Y vs SiO ₂	28
Fig. 3-5A. Harker Diagram P ₂ O ₅ vs SiO ₂	29
Fig. 3-5B. Harker Diagram Pb vs SiO ₂	29
Fig. 3-6A. Harker Diagram Rb vs Ba	30
Fig. 3-6B. Harker Diagram Rb vs Sr	30
Fig. 3-7A. Harker Diagram U vs Ba	31
Fig. 3-7B. Harker Diagram Th vs Ba	31
Fig. 4-1 The major Breccia Pipes in the Ardlethan Tin Field and reference of cross sections.	55
Fig. 4-2 Cross section 12N.	56
Fig. 4-3 Cross section 8N.	57
Fig. 4-4 Cross section 3N.	58
Fig. 4-5 Cross section 2N.	59
Fig. 4-6 Cross section 0 N.	60
Fig. 4-7 Cross section 4S.	61
Fig. 4-8 Cross section 24S.	62
Fig. 4-9 Geological plan at RL 250 m.	63
Fig. 4-10 Geological plan at RL 200 m.	64
Fig. 4-11 Geological plan at RL 150 m.	65
Fig. 4-12 Geological plan at RL 100 m.	66
Fig. 4-13 Geological plan at RL 50 m.	67
Fig. 4-14 Geological plan at RL 0 m.	68
Fig. 4-15 Geological plan at RL -100 m.	69
Fig. 4-16 The styles of Brecciation and Mineralization in the Mine Granite Breccia Pipe	70
Fig. 4-17 Schematic 3-d diagram of the Breccia Pipes.	71
Fig. 4-18 Schematic diagram showing the irregular contact of the Carpathia-Blackreef Breccia Pipe	72
Fig. 4-19 Three major linears in the Ardlethan Tin Field	73
Fig. 4-20 Stereo plot (equal area) of the measured linears	74
Fig. 4-21 The evolution of Breccia Pipe formation	75
Fig. 5-1 Zonation of alteration.	106
Fig. 6-1 Octahedral Mg vs Octahedral Ti plot of biotites	109
Fig. 6-2 Octahedral Al vs Mg/Mg+Fe of biotites	109
Fig. 6-3 Plot of octahedral Fe vs tetrahedral Si of muscovites	112
Fig. 6-4 Plot of Mg/Mg+Fe vs tetrahedral Si of chlorites	114
Fig. 6-5 Mg/Mg+Fe vs Si(t) plot of tourmalines	115

Fig. 7-1 Types of fluid inclusions in the Ardlethan Tin Field.	121
Fig. 7-2 Salinities vs filling temperatures of type E fluid inclusions	133
Fig. 7-3 Salinities vs filling temperatures of fluid inclusions in the Ardlethan Granite	134
Fig. 7-4 Homogenization temperatures of fluid inclusions in the Blackreef deposit	136
Fig. 7-5 Homogenization temperatures of fluid inclusions in the White Crystal deposit.	138
Fig. 7-6 Plot of homogenization temperatures vs estimated X_{CO_2} of type D fluid inclusions of the White Crystal deposit.	140
Fig. 8-1: Frequency plot of sulphur isotope values	145
Fig. 8-2: Plot of $\delta^{18}O$ values of quartz and fluids against temperatures of depositions of the Blackreef deposit.	149
Fig. 8-3: Plot of $\delta^{18}O$ values of quartz and fluids against temperatures of deposition of the White Crystal deposit.	149
Fig.8-4 Schematic diagram illustrating the dynamic process of rock-fluid isotopic exchange.	153
Fig. 9-1. Temperatures and $\log f_{O_2}$ calculated from secondary biotite compositions.	159
Fig. 9-2 Frequency plot of temperatures calculated from biotite, muscovite and chlorite geothermometers.	159
Fig. 9-3 T- $\log f_{O_2}$ cooling path of the fluid estimated by biotite geothermometry.	161
Fig. 9-4. Calculated cassiterite solubility with declining temperatures	164
Fig. 9-5. Illustrative diagram showing the process of mineralization in the Mine Granite Breccia Pipe.	166
Fig. A2-1 Drill hole paths and their major ore-grade intersections	205
Fig. A3-1 An diagram showing the principles of differentiation.	218
Fig. A4-1 Plot of $\log K_{12}$ vs $10000/T$ of the Salton Sea geothermal biotite.	237
Fig. A4-2 Plot of ΔG_r for Mg-Tschermak's substitution vs ESO.	240
Fig. A4-3 Plot of ΔH_r for Mg-Tschermak's substitution vs ESO.	240
Fig. A5-1 T- $\log f_{O_2}$ space bounded by hematite/magnetite buffer and H ₂ O/H ₂ buffer.	244
Fig. A5-2A Concentrations of Sn-Cl complexes at 275°C.	248
Fig. A5-2B Concentrations of Sn-Cl complexes at 300°C.	248
Fig. A5-2C Concentrations of Sn-Cl complexes at 325°C.	249
Fig. A5-2D Concentrations of Sn-Cl complexes at 350°C.	249
Fig. A5-3A Calculated cassiterite solubility at 350°C.	252
Fig. A5-3B Calculated cassiterite solubility at 325°C.	252
Fig. A5-3C Calculated cassiterite solubility at 300°C.	253
Fig. A5-3D Calculated cassiterite solubility at 275°C.	253

List of Plates

Plate 4-1: Rock flour supported breccia.	35
Plate 4-2: Rock flour rich breccia in contact with the Mine Porphyry	36
Plate 4-3: Strongly chlorite altered rock flour-rich breccia.	37
Plate 4-4: Secondary biotite alteration in rock flour zone.	38
Plate 4-5: Angular Mine porphyry fragment supported breccia.	39
Plate 4-6: Breccia enriched in sediment fragments.	40
Plate 4-7: A rock flour pocket in the Mine Porphyry.	41
Plate 4-8: Mineralized breccia of mainly angular Mine Granite fragments.	43
Plate 4-9: Laminar mass flow patterns in rock flour zone.	44
Plate 4-10: Large vugs in the White Crystal Breccia Pipe.	46
Plate 5-1: Altered Mine Granite.	83
Plate 5-2: Coarse cassiterite crystals in association with milky quartz in the Wildcherry deposit	86
Plate 5-3: Relicts of tourmaline in massive chlorite bands	93
Plate 5-4: Relicts of tourmaline and cassiterite in massive chlorite bands	93
Plate 5-5: Two types of chlorite in massive chlorite bands	94
Plate 5-6: Alteration zonation around a large Mine Granite fragment	95
Plate 5-7: Coarse cassiterite and tourmaline intergrowth	96
Plate 5-8: Sulphides filling open spaces	97
Plate 5-9: Cassiterite and interstitial sulphides	98
Plate 5-10: Cosalite in fractures in arsenopyrite	99

Chapter 1

INTRODUCTION

A close correlation between precious and base metal mineralization and breccia pipes has been recognized in a diverse range of deposit types including particularly porphyry and epithermal style deposits. In addition to their great economic value, breccia pipe-hosted deposits are of intrinsic interest to those studying the conditions and processes of brecciation, hydrothermal alteration, and ore genesis. The recent focus of mineral exploration on precious metal has renewed interest in the study of such styles of mineralization (Sillitoe, 1985).

This thesis documents the results of the study of the breccia pipes and cassiterite and sulphide mineralization in the Ardlethan Tin Field, New South Wales, Australia.

1.1 Location and Climate

Ardlethan is a small town with a population of about 700 in central New South Wales. It is located about 570 km west-southwest of Sydney and approximately midway between the two regional towns of Griffith and Temora. The climate is classified as temperate with a mean temperature of 76°F in summer, 45°F in winter, and an average annual rainfall of about 483 mm (Stone, 1969). The Ardlethan Tin Mine, a hard-rock mining operation, is located about 5.5 km northwest of the Ardlethan township, near the abandoned town of Yithan. The mean altitude of the Mine area is about 300 m above sea level.

1.2 Regional Geology and Mineralization

The Ardlethan Tin Field occurs in the Girilambone-Wagga Anticlinorial Zone (Fig. 1-1) at the western extremity of the Lachlan Fold Belt (Scheibner, 1975; Markham, 1980). The Lachlan Fold Belt is an area of metamorphosed and deformed volcanic, plutonic and sedimentary rocks of Palaeozoic age (Packham, 1960; Scheibner, 1975). The Girilambone-Wagga Anticlinorial Zone is composed of Ordovician

sedimentary rocks intruded by granitoids (Markham, 1980). Cassiterite mineralization occurs in association with some of the granitoids and forms the Wagga Tin Belt (Fig. 1-2). However, mineralization of gold, silver, zinc, lead, copper and fluorite (Fig. 1-3) also occurs in the belt (Markham, 1980; Markham and Basden, 1974).

1.3 The Ardlethan Tin Field

The Ardlethan Tin Field includes a number of disseminated cassiterite and sulphide deposits hosted in breccia pipes, joints or joint intersections. Two main granitic intrusions, the Mine Granite and the Ardlethan Granite, and a number of granitic dykes of late Silurian-early Devonian age intrude a sequence of metamorphosed sedimentary rocks of Ordovician age. Hydrothermal activity related to these intrusive events produced brecciation and mineralization (Paterson, 1976; Clarke, 1979; Clarke *et al.*, 1984). Disseminated cassiterite mineralization is associated with wolframite, rutile, arsenopyrite, pyrite, chalcopyrite, sphalerite, galena, fluorite and siderite. Extensive hydrothermal alteration resulted in alteration minerals including biotite, sericite, tourmaline, quartz, topaz and chlorite. Cassiterite was the only mineral extracted by bulk mining methods.

The main deposits in the Ardlethan Tin Field are hosted by four breccia pipes. The Mine Granite Breccia Pipe hosted the Wildcherry, Ardwest, Wildcherry South, Perseverance and the Keogh West deposits. The Carpathia-Blackreef hosted the Carpathia and the Blackreef deposits. The Stackpool deposit was and the Godfrey deposits is hosted by the Stackpool-Godfrey Breccia Pipe. The White Crystal deposit was hosted by the White Crystal Breccia Pipe. These breccia pipes occur in an area of about 1.5 km² (Fig. 1-4). This study is mainly concentrated on these deposits hosted by breccia pipes.

A number of small zones of cassiterite mineralization occur along the eastern margin of the Ardlethan Granite. Details of these small mines are given in Table 1-1.

1.4 Mining History

Cassiterite was first discovered in the Ardlethan Tin Field near the old Carpathia deposit and the White Crystal deposit (Fig. 1-4) by Mr J. J. Keogh in 1912 (Godfrey, 1915). He found a layer of coarse-grained residual cassiterite on top of the old Carpathia Hill while prospecting for gold. Widespread interest was shown following the discovery. Over a hundred mining leases were established in a rush which formed the so-

called "Ardlethan Tin Boom". It was soon realized that the Ardlethan Tin Field consisted of a number of ore bodies of "tin rich veins" and "massive lodes of much lower grades". Mining of the high-grade ore, containing between 2 and 46% Sn in cassiterite-sulphide-tourmaline pipes and veins, proceeded profitably till 1956. During this period about 10,000 tonnes of tin concentrate were produced, which included a small amount from alluvial workings.

Aberfoyle Pty Ltd commenced exploration in the area in 1961 for large-tonnage low-grade tin resources and soon found the White Crystal and Wildcherry deposits. Production by hard-rock operations using open-cut mining method started in 1964, initially from the Wildcherry deposit and then from the Stackpool and White Crystal deposits (Fig. 1-4). Underground decline and stope methods were used in mining the Carpathia deposit. The Ardwest and Wildcherry South deposits were found in the 1970's and were also mined by open-cut method. The high-grade Blackreef deposit, which lay between 200 and 300 m below surface, was found and mined in early 1980's. The remaining ore bodies in the Ardlethan Tin Field are the Keogh West, Godfrey and Godfrey South deposits. Altogether these deposits contain about 10-13 million tonnes of ore with varying grades averaging between 0.48 and 0.56% Sn approximately. There are also several alluvial deposits with about 22 million tonnes of ore averaging 0.32 wt% Sn around the Ardlethan Tin Mine area. Aberfoyle Pty Ltd closed the Ardlethan Tin Mine in 1986 when the world tin market collapsed.

1.5 Previous Work

Geological studies investigating the mineralization control in the Ardlethan Tin Field started soon after the original discovery. Godfrey (1915) reported his inspection to the area and concluded that the Ardlethan Tin Field consisted of rich cassiterite-sulphide-tourmaline veins and pipes and low-grade lodes. Raggatt (1938) described the geological control over the high-grade cassiterite mineralization in the Carpathia deposit and found that it correlated with tourmaline-rich greisenic pipes. A regional geological study was done by Stone (1969). The geochemistry of the granitoids was studied by Netzel (1970). Taylor (1972) recognized the existence of breccia pipes and emphasized the importance of the relationship between the brecciation and mineralization. Paterson (1976) summarized the geology, brecciation and mineralization of the Ardlethan Tin Field and described the differences between the Mine Granite and the Ardlethan Granite. Clarke (1979) and Clarke *et al.* (1984) classified several styles of brecciation and their study concluded that the hydrothermal alteration and mineralization were all post-brecciation events. They also proposed that the brecciation, hydrothermal alteration

and mineralization were products of magmatic fluid from the Ardlethan Granite. Scott (1980) proposed a model which was very similar to that proposed for porphyry copper systems for the genesis of the Ardlethan Tin Field. Rb-Sr dating by Richards *et al.* (1982) suggested ages of 417 million years for the Mine Granite and 410 million years for the Ardlethan Granite, which are in agreement with the conclusions from the geological relations. Fluid inclusion study (Eadington and Paterson, 1984; Eadington, 1985b) suggested volatile pressures of 1.5 kb and 0.5 kb before and after the brecciation in the White Crystal Breccia Pipe and a range of salinities which were interpreted as the results of mixing of saline magmatic water and diluted meteoric water. Eadington (1985b) very briefly described the alteration, microfractures and brecciation of the Ardlethan Tin Field.

1.6 The Present Study

The exposures of various rock types in and around the Ardlethan Tin Field together with the extensive collection of diamond drillcores provided an excellent opportunity to study the relations between various styles of brecciation, mineralization and alteration. This study includes a review of the geology (Chapter 2), geochemistry of the granitoids (Chapter 3), the breccia pipes and brecciation (Chapter 4), hydrothermal alteration and mineralization (Chapter 5), mineral chemistry (Chapter 6), fluid inclusions (Chapter 7), stable isotopes (Chapter 8), conditions of mineralization (Chapter 9), and summary and conclusions (Chapter 10). The abilities of granitoids to enrich tin into late-stage fractionates are discussed in Appendix 3. Appendix 4 presents a eight-component biotite solid solution model which can be used to calculate temperatures and redox conditions of formation of hydrothermal biotite from microprobe analyses. Solubility of cassiterite in saline fluids is discussed in Appendix 5.

**Table 1-1: Tin Mines Operated During
1912-1963 in the Ardlethan Tin Field**

1. The Little Bygoo group of Mines

Mining methods	Shafts; Shallow Pits
Periods of mining	1913-1915, 1936-1946
Total production	94.6 metric tons
Mineralization	Cassiterite+Arsenopyrite
Styles of alteration	Greisen, quartz, tourmaline, topaz, chlorite, kaolinite
Structures	Joints, Joint Intersections
Mines	Dumbrells Bygoo Mine, Murphys Mine, Corners Lease, Schulzs Mine, Smiths Little Bygoo Mine

2. The Big Bygoo group of Mines

Mining methods	Shafts; Drives; Crosscuts, Open Cut; Shallow Pits
Periods of mining	1913-1918?
Total production	1197 metric tons
Mineralization	Cassiterite+Bismuth +Bismuthinite+Wolframite +Molybdenite+Chalcopyrite
Styles of alteration	Tourmaline, quartz, chlorite, topaz
Structures	Joints, Joint Intersections
Mines	Empire Mine, Clarke's Mine, Watson's Mine, Trembath's Mine, Drumlish Mine, Temora Mine, Syndicates Mine, Big Bygoo Mine, Lone Hand Tin Mine, the Titanic Mine, Bulgarian Mine, the Vulcan Mine

3. The Killarney group of Mines

Mining methods	Shafts, Shallow Pits, Open Cut
Period of mining	1912-1918?
Mineralization	Cassiterite+Molybdenite+Bismuth +Sulphides
Total Production	Minor
Styles of alteration	Quartz, tourmaline
Structures	Joints
Mines	Killarney Mine, McDermotts Mine, Ward and Mahoney's Mine, Rob Roy Mine, Card and House Mine, Buchanan Lease

4. The Taylor's Hill group of Mines

Mining method	Shafts, Drives, Open Cut
Period of mining	1912-1918?
Mineralization	Cassiterite+Arsenopyrite +Sulphides+Wolframite +Molybdenite
Total production	Minor
Styles of alteration	Tourmaline, quartz, muscovite, chlorite, fluorite, topaz
Structures	Joints, Joint Intersections
Mines	Ruby Tin Mine, the Outcast Mine, the Commonwealth Tin Mine, Welcome Stranger Mine, Perseverance Mine, Kia-Ora Mine, Austra Lease, Currajong Lease, Williatt and Party Lease, McCrase, Lease, Colarado Lease

5. The Bald Hill group of Mines

Mining method	Shafts, Open Cut, Shallow Pits
Period of mining	1912-1918
Total production	1.5 metric tons
Mineralization	Cassiterite+Arsenopyrite +Sulphides+Molybdenite +Wolframite
Alteration	Quartz, tourmaline, muscovite, Chlorite
Structures	Joints, Joint intersections

Mines	Bald hill Syndicate Mine, Maratholi Mine, Freemans lease, Ranchoeroo Syndicate Mine, Fisher and Party lease
Remarks	Very strong chlorite alteration in host rocks

6. The Carpathia group of Mines³

Mining method	Shafts, Drives, Crosscuts, Winzes Stoping, Adits, Open Cuts, Shallow Pits
Periods of mining	912-1956, 1956-1963
Total production	39,100 metric tons
Mineralization	Cassiterite+Wolframite +Stannite+Molybdenite +Sulphides+Bismuth
Styles of alteration	Quartz, tourmaline, topaz, chlorite, muscovite, kaolinite
Structures	Joints, Joint intersection, Reefs, Pipes

1 Data from Markham (1980)

2 Tin concentrate

3 Exclude the production by Aberfoyle Pty Ltd. during 1964-1987

Fig. 1-1 Structural geology map of New South Wales, Australia
(after Scheibner, 1975).

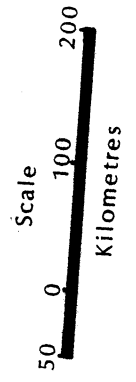
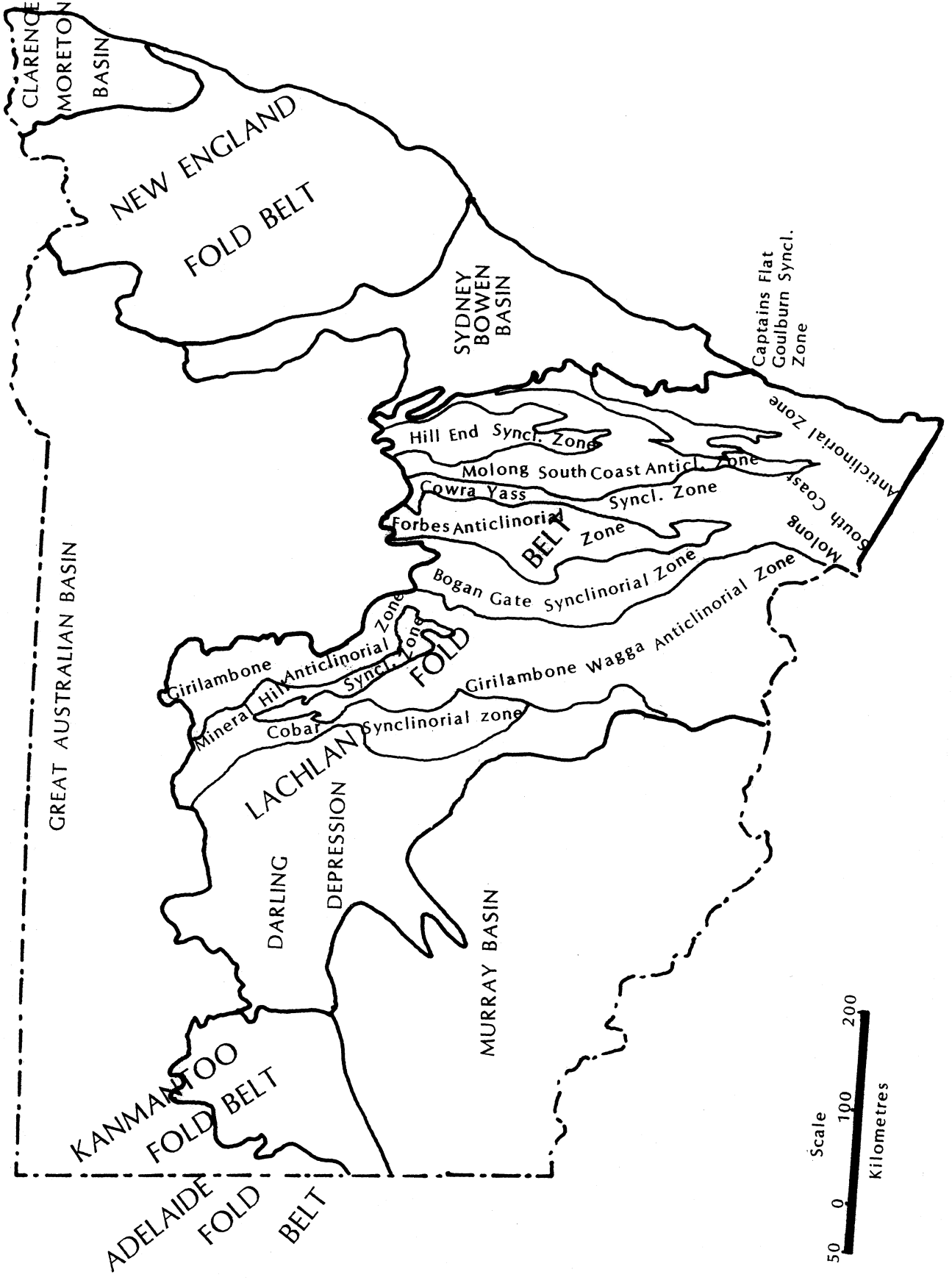


Fig. 1-2 Tin granites of southeastern Australia (compiled from data provided by the Aberfoyle Pty Ltd.).

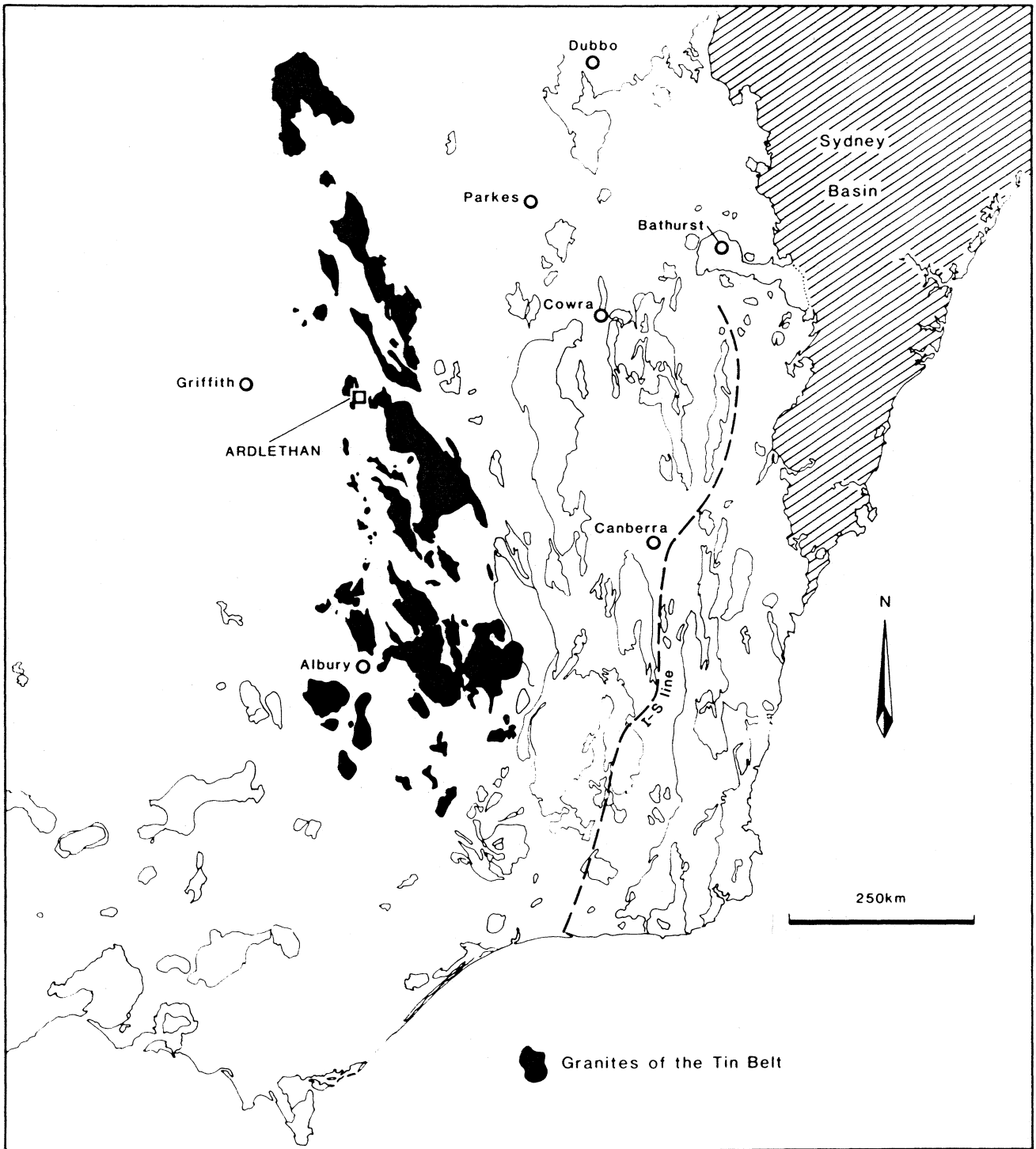


Fig. 1-3 Mineralization of the Girilambone-Wagga Anticlinorial zone, New South Wales, Australia (after Markham, 1980).

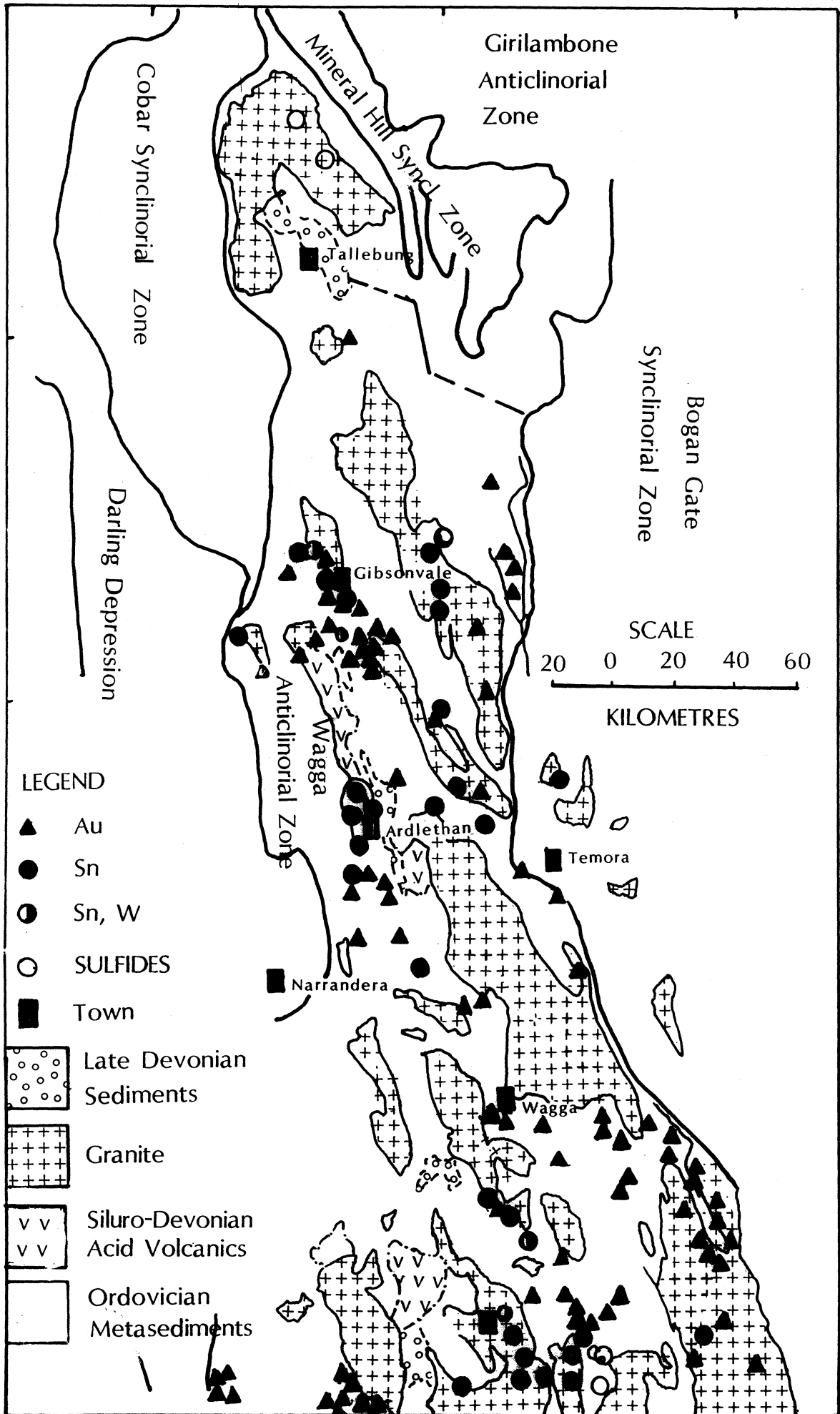
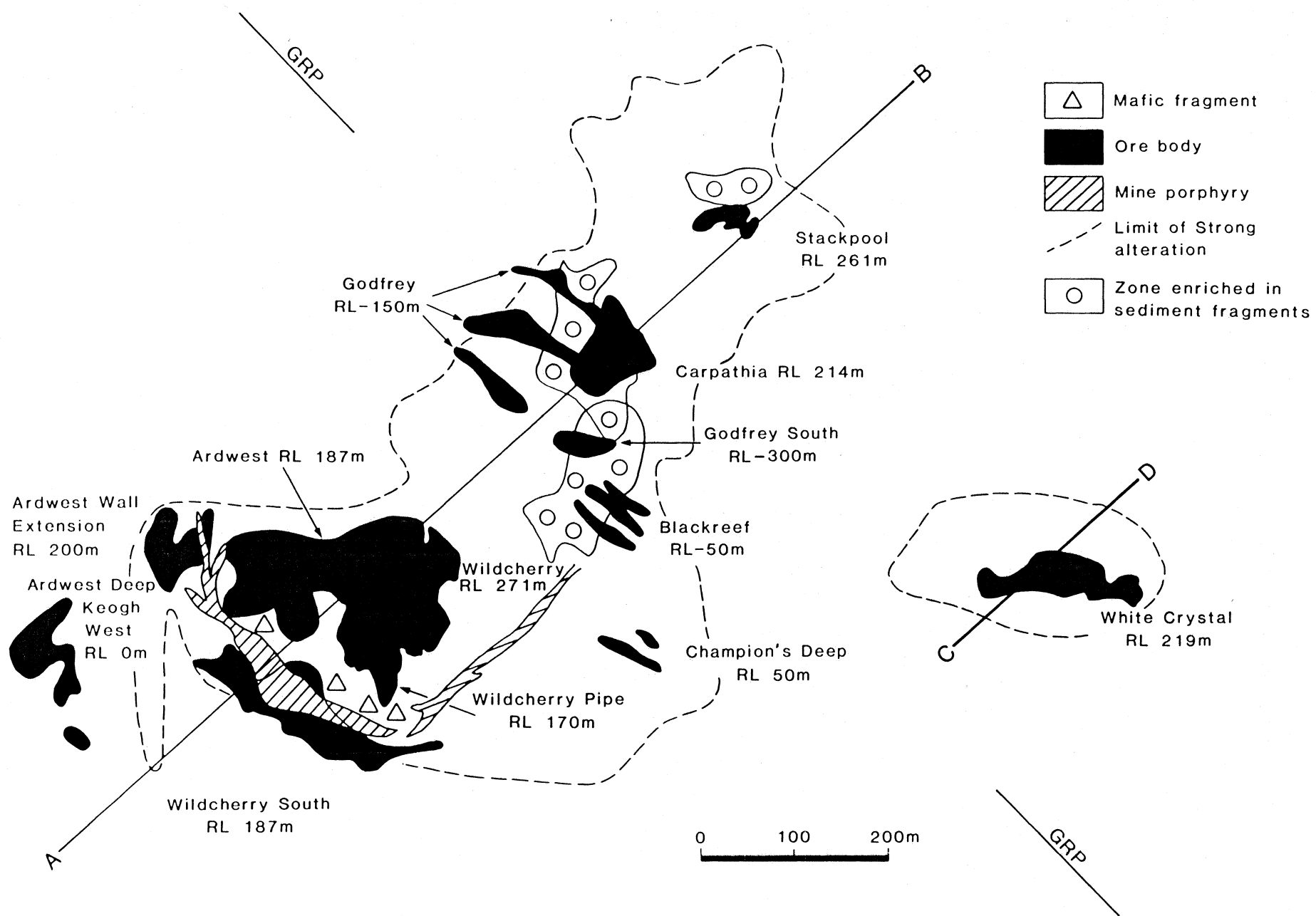


Fig. 1-4 Projected locations of tin deposits of the Ardlethan Tin Field, New South Wales, Australia . RL: Relative Level; GRP: Godfrey Reference Plane. Orientation is shown in Fig. 4-1.



Chapter 2

GEOLOGY AND PETROLOGY

Five main geological units occur in the Ardlethan Tin Mine area. They are the Ordovician metasedimentary rocks, the Mine Granite, the Garnet-Bearing Quartz-Feldspar Porphyry (GQFP), the Ardlethan Granite, and the Devonian sedimentary rocks (Fig. 2-1). They cover an area of about 300 km² around the Ardlethan Tin Mine bounded by latitudes 34°15'-34°22'S and longitudes 146°45'-147°00'E. In addition, a pyroclastic volcanic rock outcrops between the Mine Granite and the Ardlethan Granite, and the Mine Porphyry is exposed in the Wildcherry-Ardwest open cut. Intersections of the Mine Porphyry, microgranite and mafic dykes were encountered in cores from diamond drilling in and around the Ardlethan Tin Mine area.

2.1 The Ordovician and Devonian Metasedimentary Rocks

In the Lachlan Fold Belt the Ordovician metasedimentary rocks generally are comprised of a sequence of quartzites, slates, schists, phyllites, siltstones, sandstones, and fine-grained conglomerates. Only siltstones, sandstones, quartzites, phyllites and schists are exposed in the Girilambone-Wagga Anticlinorial Zone. In the mine area, the exposed Ordovician metasedimentary rocks are mainly siltstones, fine-grained sandstones and slates. They occur to the south of the Mine Granite and east of the Ardlethan Granite (Fig. 2-1).

The Ordovician metasedimentary rocks in the mine area are bi-mineralic, consisting of fine-grained (average grainsize 0.05 mm) quartz and sericite. Individual quartz crystals are angular to sub-angular. Most surface outcrops have a brown colouration due to iron oxide (mainly limonite) staining (Stone, 1969).

The Ordovician metasedimentary rocks in the mine area are folded into a N to N30°E trending direction.

The Devonian sedimentary rocks are conglomerates, sandstones, quartzites and shales.

2.2 The Mine Granite

The Mine Granite is grey to cream-grey, medium- to coarse-grained, and weakly foliated. It contains about 25% quartz, 35% K-feldspar, 25% plagioclase, 10-15% biotite and 0-2% muscovite. Accessory minerals include apatite, zircon, cordierite (Paterson, 1976), ilmenite and rarely rutile. There are no outcrops of fresh Mine Granite, however, weakly to moderately altered Mine Granite is exposed in the Wildcherry-Ardwest open pit and the White Crystal open pit. Relatively fresh Mine Granite samples were obtained from diamond drillcores.

The diamond- and percussion-drill holes in and around the Ardletha Tin Mine area indicate that the contact between the Mine Granite and the Ordovician sedimentary rocks is flat with numerous Mine Granite tongues in the sedimentary rocks. Clots of various size from several millimetres to 10's of centimetres composed of biotite and plagioclase crystals are common in Mine Granite along its contact with the Ordovician sedimentary rocks. They could be xenoliths (N. Higgins, pers. comm., 1989) or partially digested inclusions (R. Paterson, pers. comm., 1984).

In the mine area the Mine Granite is homogeneous in texture and mineralogy. K-feldspar crystals are mostly subhedral; plagioclase crystals are subhedral; and quartz crystals are anhedral. Biotite crystals are weakly orientated. Euhedral K-feldspar megacrysts (>1 cm in size) commonly occur in the Mine Granite. They contain abundant biotite flakes aligned parallel to growth zones. The volume proportions of the K-feldspar megacrysts range between 0.5 to 5%. Large coarse flakes of primary (?) muscovite also occur in the Mine Granite.

The occurrence of euhedral K-feldspar megacrysts in the Mine Granite may imply that some K-feldspar crystallized very early in the cooling history. Similarly, the biotite inclusions in those K-feldspar megacrysts indicate that some biotite also crystallized very early. Therefore the Mine Granite melt was probably over saturated with both biotite and K-feldspar.

Rb-Sr dating using muscovite samples by Richards *et al.* (1982) yielded a value of 417 ± 2.5 ma, corresponding to a Late Silurian age.

2.3 The Ardlethan Granite

The Ardlethan Granite out crops well along its eastern margin forming low elevation hills, for example, the Taylor's hill close to the Ardlethan Tin Mine. However, out crops are very rare to the west into the Ardlethan Granite body. As a result, its western margin is poorly located.

The Ardlethan Granite ranges from pink to white, porphyritic to nonporphyritic, and medium- to extremely coarse-grained. It also varies greatly in texture but average grainsizes range between 0.5 and 10 mm. The average abundances of major minerals are 35% quartz, 35% K-feldspar, 23% plagioclase, 1-4% biotite, 0-2% muscovite and up to 3% tourmaline. However, for individual samples K-feldspar may vary between 30 and 38%, plagioclase between 19 and 25%, and quartz between 33 and 40%. Primary accessory minerals include apatite, ilmenite and zircon. Pyrite, chalcopyrite, fluorite and cassiterite occur in weakly altered Ardlethan Granite, particularly along its eastern margin.

The porphyritic parts of the Ardlethan Granite contain about 15% phenocrysts of subhedral quartz and K-feldspar crystals mostly 0.5 to 1.5 cm in size. The groundmass contains anhedral quartz, K-feldspar, plagioclase and micas of varying grain sizes between 0.5 and 1.0 mm. There are some extremely coarse-grained porphyritic Ardlethan Granite outcrops at Taylor's Hill (Fig. 2-1) in which K-feldspar phenocrysts are as big as 5 cm. The nonporphyritic parts of the Ardlethan Granite also varies greatly in grainsize from 0.5 to 1.0 cm on average. Generally, the quartz, K-feldspar and plagioclase crystals are mostly subhedral. Primary biotite and muscovite flakes are subhedral to anhedral mostly along mineral boundaries.

There are commonly no distinctive boundaries between the porphyritic and nonporphyritic phases and transitions are gradual. Pods of porphyritic Ardlethan Granite may occur in nonporphyritic Ardlethan Granite and *vice versa*.

Numerous quartz and tourmaline nodules, varying in size from a few millimeters to approximately 20 centimeters, are common in the Ardlethan Granite along its eastern margin. They are composed of massive black coloured tourmaline and euhedral quartz crystals up to a few centimeters in size. These nodules may form 1-3% of the rock by volume and there is no apparent variation of the nodules from the porphyritic to the nonporphyritic Ardlethan Granite. Cores from diamond drilling in the Taylor's Hill and Big Bygoo areas (Fig.2-1) indicate that the abundance of the nodules decreases both towards the west and with depth in the Ardlethan Granite.

All of the known tin deposits in the Ardlethan Tin Field occur along the eastern margin of the Ardlethan Granite.

The Ardlethan Granite also was dated by Richards *et al.* (1982) who obtained an age of 410 ± 2.5 Ma, suggesting a very late Silurian to early Devonian age. This is in agreement with geological observations that the Ardlethan Granite intrude the Mine Granite.

2.4 The GQFP

The GQFP is a light-coloured rock, containing about 30-40% phenocrysts of subhedral to euhedral K-feldspar, quartz and plagioclase between 0.5 to 2.0 cm in a fine-grained matrix ranging from 0.001 to 0.1 mm in grain size. Accessory minerals are apatite, ilmenite, garnet and zircon. Garnet crystals observed range up to 0.5 cm in size. Tourmaline occurs in the GQFP as a secondary phase.

Spatially, the GQFP occurs in a narrow strip between the Mine Granite and the Ardlethan Granite (Fig. 2-1) and as discontinuous pods or stocks intruding a pyroclastic rock. One such stock outcrops in the mine area close to the contact of the Ardlethan Granite. According to Paterson (1976), outcrops of the GQFP also occur to the north and south of the mine area along the eastern contact of the Ardlethan Granite (Fig. 2-1). A diamond drill hole (B1120) in the Spring Valley area intersected a zone of the GQFP which merged gradually into the Ardlethan Granite, suggesting that it probably represents a marginal phase.

2.5 The Pyroclastic Volcanics

The Pyroclastic Volcanics outcrop between the Ardlethan Granite and the Mine Granite in the same fashion as the GQFP, but generally poorly exposed.

Textural and mineralogical characteristics of the Pyroclastic Volcanics are very different from the intrusive rocks in the region. The Pyroclastic Volcanics are dark-coloured, with a very small proportion of fine-grained K-feldspar phenocrysts and dark-coloured glass-like matrix. The phenocrysts are weakly aligned. Autobreccia textures are a common feature with fragments ranging between several millimeters to over 50 centimeters. A banded texture is very apparent in the matrix which consist of dark-coloured glass.

The intrusive relationship between the GQFP and the Pyroclastic Volcanics suggests that the formation of the latter predated the GQFP.

The relative age of the Pyroclastic Volcanics and the Mine Granite is not known.

2.6 The Microgranite Dykes

The microgranite dykes are white, fine-grained rocks containing about 30% quartz, 45% K-feldspar and 25% plagioclase. Accessory minerals are ilmenite, apatite and zircon with secondary fluorite and tourmaline. Grain sizes of major minerals range between 0.5 and 1.5 mm. Like the Ardlethan Granite, the microgranite contains quartz and tourmaline nodules (Sample RD107 from DDH B1185).

The microgranite dykes occur in the Ardlethan Granite, the Pyroclastic Volcanics and the Mine Granite. Thin bands, generally 3 to 5 cm thick, of quartz, tourmaline and topaz alteration commonly occur in the host Ardlethan Granite along contacts with microgranite dykes. Several microgranite dykes in the Mine Granite are disrupted by the brecciation (see Chapter 4). Fragments derived from microgranite dykes were found in the Mine Granite, Carpathia-Blackreef, Stackpool-Godfrey and White Crystal Breccia Pipes.

One microgranite dyke intersected by several diamond-drill holes (DDHs B1135, B1170, B1175, B1176, B1185 and B1198) on section 12N (see Chapter 4 and Appendix 2) was intruded by a Mine Porphyry dyke at a depth of about 300 m below the surface. This indicates that the Mine Porphyry dyke postdated the microgranite dyke. As microgranite dykes occur in the Ardlethan Granite, it is a clear that the Mine Porphyry dykes are later than the main Ardlethan Granite emplacement.

Although generally the microgranite is homogeneous in texture and mineralogy, the bottom part of the microgranite dyke intersected by diamond drill hole B1185 (see Appendix 2) contains over 85% euhedral K-feldspar megacrysts by volume.

2.7 The Mine Porphyry

The Mine Porphyry forms a swarm of Mine Porphyry dykes in the Ordovician sedimentary rocks and the Mine Granite in the Ardlethan Tin Mine area. The largest body of the Mine Porphyry is exposed in the main open cut (Fig. 1-4). Many smaller bodies ranging in lengths between several and hundreds of meters occur in the mine area. Several of them are disrupted by the Carpathia-Blackreef and the Stackpool-Godfrey Breccia Pipes (see Chapter 4).

The Mine Porphyry consists of varying amounts of euhedral phenocrysts of quartz and K-feldspar, from 15 to 30% by volume, in a very fine-grained matrix. The primary accessory minerals within the Mine Porphyry are not well known as the Mine Porphyry dykes are almost always associated with strong hydrothermal alteration. However, zircon and apatite are present in most of the Mine Porphyry samples.

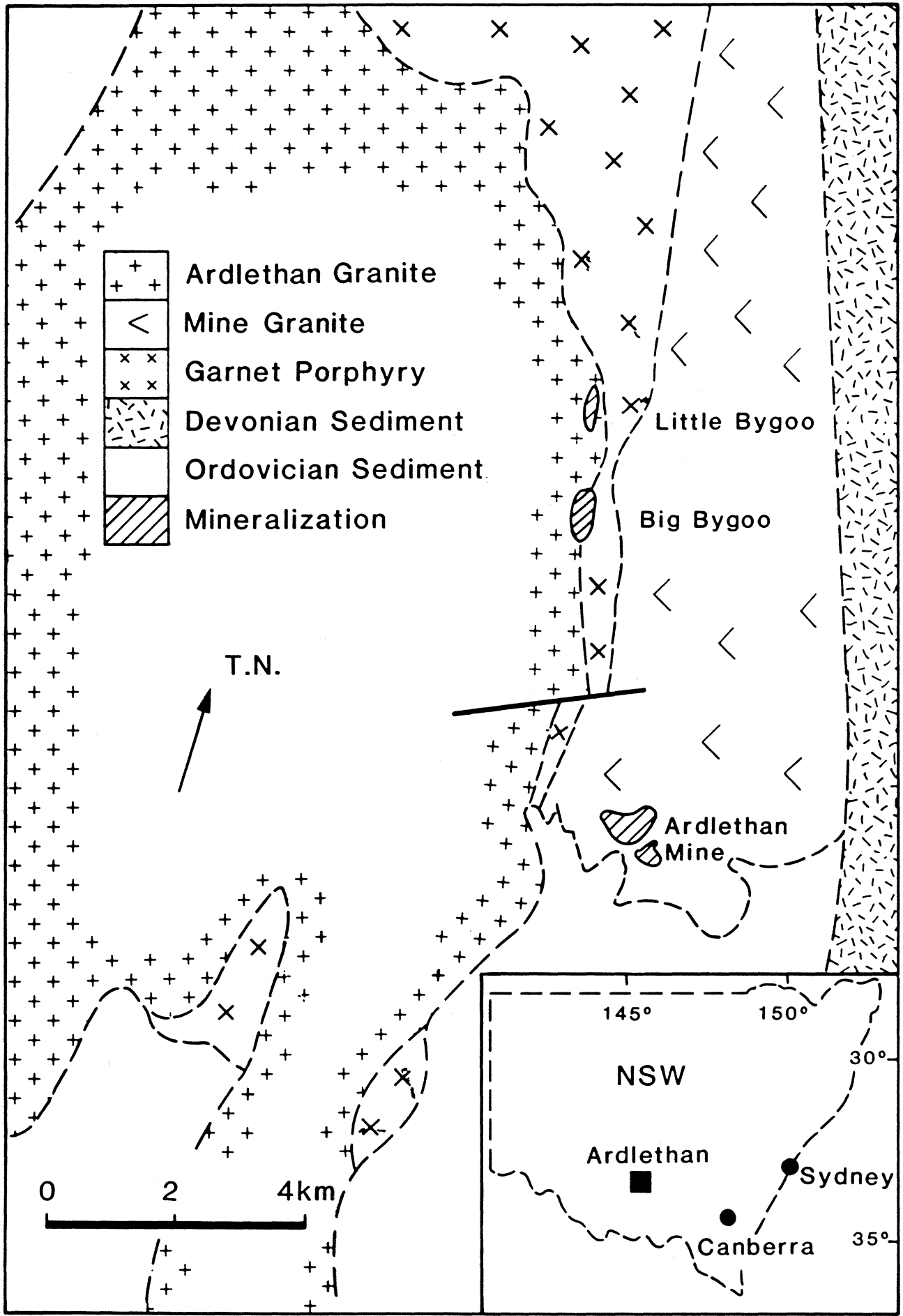
The Mine porphyry is the youngest known felsic igneous intrusion in the Ardlethan Tin Mine area.

2.8 The Mafic Dykes

The mafic dykes are composed of fine-grained, dark-coloured dolerite. The extent of mafic igneous activity is unknown. Fragments of mafic dykes occur in the Mine Granite Breccia Pipe within the Wildcherry South deposit (see Chapter 4) suggesting that they postdated the emplacement of the Mine Granite and preceded the brecciation.

2.9 Summary

The main rock types in the Ardlethan area are the Ordovician sedimentary rocks, the Mine Granite, the Ardlethan Granite and the Devonian sedimentary rocks. The GQFP occurs as a marginal phase to the Ardlethan Granite. The microgranite and the Mine Porphyry postdate the Ardlethan Granite. Fig. 2-2 illustrates the geological history of the igneous events in the Ardlethan area.



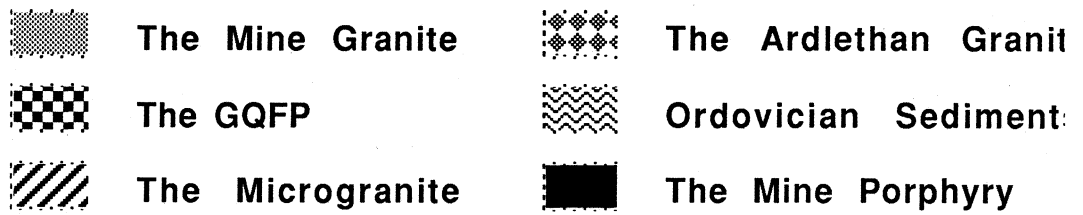
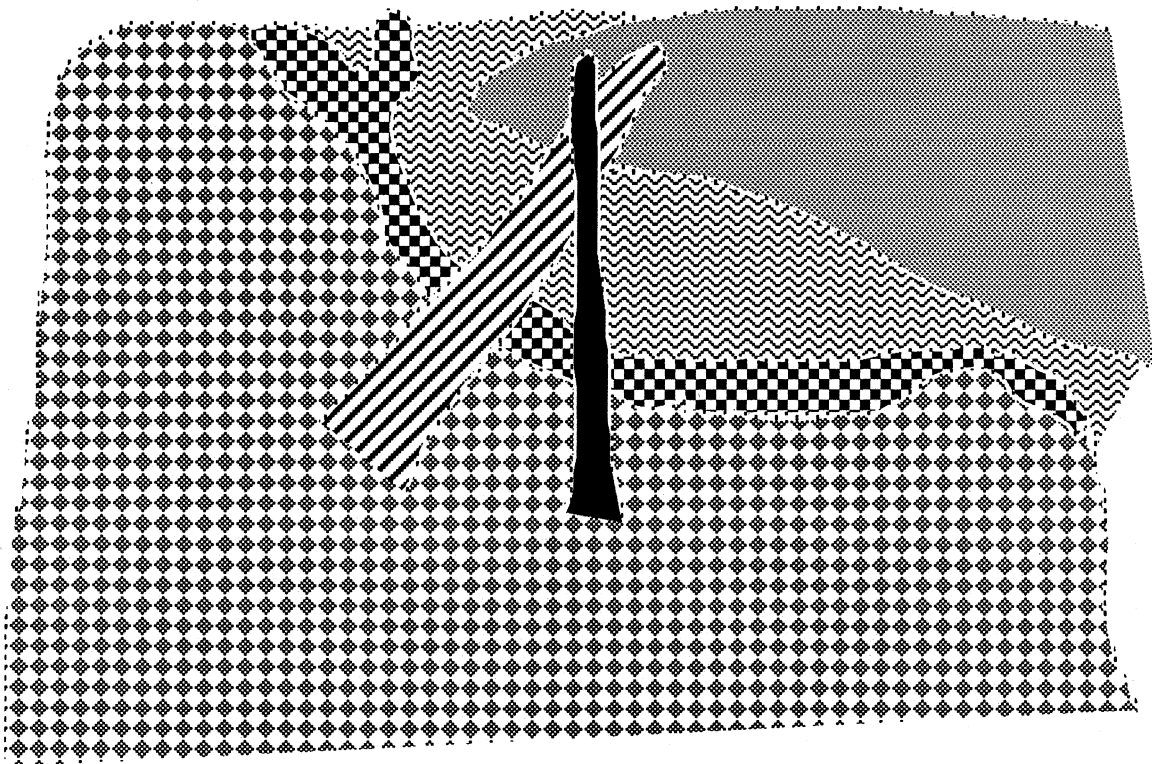


Fig. 2-2 Timing relations of the igneous events in the Ardlethan area

Chapter 3

GEOCHEMISTRY OF THE GRANITOIDS

As described in Chapter 2, granitoids that occur in the Ardlethan area include the Mine Granite, the Ardlethan Granite, the GQFP, the microgranite and the Mine Porphyry. In this chapter their geochemical characteristics are discussed in order to understand their genetic relationship.

3.1 Samples

The geochemical data for the granitoids exposed in the Ardlethan Tin Field were made available to the author by R. Paterson. Whole rock samples were collected by R. Paterson and J. A. McDonald prior to 1981. Samples Ard1 to Ard99 were analyzed by the Geology Department, Australian National University and samples Ard100 to Ard148 by the Geology Department, University of New England. These samples included relatively fresh to strongly altered rocks. The data (see Appendix 1) used here were obtained from samples described as fresh specimens of the Mine Granite, the Ardlethan Granite, the GQFP, the microgranite and the Mine Porphyry (total 49 samples).

It must be pointed out that the Mine Granite and Mine Porphyry samples described by R. Paterson as relatively fresh could be weakly altered. Values of some of the highly mobile elements, such as Sn, F and As, may have been modified by the alteration.

3.2 Types of the Granitoids

Chappell and White (1974) and White and Chappell (1977) divided the granitoids in the Lachlan Fold Belt into S- and I-type granitoids on the basis of their geochemical characteristics. The Mine Granite, the Ardlethan Granite and related phases all fall into the category of S-type granitoids according to their criteria of classification (Table 3-1).

Table 3-1: Characteristics of I- and S-type granitoid

I-type	S-type
1 Relatively high sodium, Na ₂ O normally >3.2% in felsic varieties, decreasing to >2.2% in more mafic types	Relatively low sodium, Na ₂ O normally <3.2% in rocks with approximately 5% K ₂ O, down to <2.2% in rocks of 2% K ₂ O
2 Mol Al ₂ O ₃ /(Na ₂ O+K ₂ O+CaO)<1.1	Al ₂ O ₃ /(Na ₂ O+K ₂ O+CaO)>1.1
3 CIPW normative diopside or <1% normative corundum	>1% CIPW normative corundum
4 Broad spectrum of composition from felsic to mafic types	Relatively restricted in compositions to high SiO ₂
5 Regular inter-element variations within pluton; linear or near linear variation diagrams	Variation diagrams more irregular

From Chappell and White (1974)

Table 3-2A: Whole rock compositions (Major Components in wt%) of the Mine Granite (MG), the Ardlethan Granite (AG), the garnet bearing quartz-feldspar porphyry (GQFP), the microgranite (Mic.G) and the Mine porphyry (MP) in comparison to the averages of I- and S-type granitoids of the Lachlan Fold Belt

No. anal.	I-Type*	S-type	MG	AG	GQFP	Mic.G	MP
	532	316	8	20	7	4	4
SiO ₂	67.98	69.08	70.22	75.78	72.48	75.72	76.30
TiO ₂	0.45	0.55	0.45	0.10	0.38	0.07	0.07
Al ₂ O ₃	14.49	14.30	14.87	12.86	13.41	13.15	12.15
Fe ₂ O ₃	1.27	0.73	0.52	0.34	0.93	0.28	0.40
FeO	2.57	3.23	2.53	0.98	1.75	0.77	1.17
MnO	0.08	0.06	0.05	0.03	0.04	0.03	0.02
MgO	1.75	1.82	1.26	0.11	0.50	0.19	0.17
CaO	3.78	2.49	1.41	0.44	1.58	0.49	0.52
Na ₂ O	2.95	2.20	2.24	3.11	2.66	3.40	2.24
K ₂ O	3.05	3.63	4.56	4.82	4.77	4.24	5.06
P ₂ O ₅	0.11	0.13	0.19	0.13	0.17	0.19	0.06
SO ₂			0.04	0.01	0.00	0.05	0.08
H ₂ O+			1.37	0.70	0.85	0.67	0.89
H ₂ O-			0.17	0.14	0.22	0.24	0.25
CO ₂			0.27	0.22	0.12	0.45	0.48
total	98.48	98.22	100.15	99.77	99.86	99.91	99.79

* Data for S- and I-type granitoids are from Chappell and White (1983)

The average Na₂O contents of the Mine Granite and the Ardlethan Granite are 2.24 % and 3.11%, respectively, while their average K₂O contents are 4.56% and 4.82%. The calculated Al₂O₃/(Na₂O+K₂O+CaO) of the Mine Granite is 1.33, and the Ardlethan Granite 1.14. Both the Mine Granite and the Ardlethan Granite are corundum normative according to CIPW normative calculations, and of high SiO₂ contents averaging 70.22% and 75.78%, respectively (Table 3-2A).

However, comparisons of the whole rock chemistry, particularly the trace element chemistry (Table 3-2B), suggest that both the Mine Granite and the Ardlethan Granite differ significantly from the average chemistry of S-type granitoids in the Lachlan Fold Belt summarized by White and Chappell (1983).

Table 3-2B: Whole rock compositions (Trace elements in ppm) of the Mine Granite (MG), the Ardlethan Granite (AG), the GQFP, the microgranite (Mic.G) and the Mine Porphyry (MP) in comparison to the averages of I- and S-type granitoids of the Lachlan Fold Belt

	I-Type [*]	S-type	MG	AG	GQFP	Mic.G	MP
No. anal.	532	316	8	20	7	4	4
Ba	520	480	341	106	680	93	183
Rb	132	180	307	652	237	43	618
Sr	253	139	131	36	128	33	35
Pb	16	27	35	21	37	30	25
Th	16	19	18.2	28.1	23.2	2.5	63.0
U	3	3	6.9	27.0	5.1	6.4	24.0
Zr	143	170	137	92	250	22	210
Nb	9	11	19	34	19	7	125
Y	27	32	21	65	31	9	94
La	29	31	33	25	44	5	54
Ce	63	69	69	38	104	7	89
Nd	23	25	17	6	40	1	15
Sc	15	14	6	2	6	1	7
V	74	72	49	4	18	2	11
Cr	27	46	28	4	6	5	11
Co	12	13	6	5	4	8	4
Ni	9	7	10	4	3	7	6
Cu	11	12	19	13	4	14	36
Zn	52	64	69	40	73	40	36
Ga	16	17	19	23	19	18	26
Li			57	155	58	11	21
B			56	84	26	545	10
Mo			0	1	1	0	0
Sn			29	35	7	37	59
F			356	3400	914	425	2385
As			11	5	3	7	8
Sb			3	1	1	0	3
Ta			4	6	1	7	5
W			14	22	4	9	41
Bi			4	5	2	1	6

* Data for S- and I-type granitoids are from Chappell and White (1983)

The Mine Granite has higher Rb, Cu, Nb and U; and lower Ba, Y, Nd, Cr and Ni than the average composition of S-type granitoids in the Lachlan Fold Belt (White & Chappell, 1983). Similarly for the Ardlethan Granite, Rb, Th, U, Nb, Y and Ga contents are higher than the average of S-type granitoids (Table 3-2B) while most of other trace elements analyzed are lower in varying degrees. The chemical compositions of the microgranite and the Mine porphyry are similar to the Ardlethan Granite. However, the chemical composition of the GQFP differs significantly from the Ardlethan Granite. It appears to be intermediate in composition between the Mine Granite and the Ardlethan Granite and this will be discussed again below.

3.3 Harker Diagrams

Harker diagrams of major and trace elements are constructed to compare their variations with the most important major component, SiO₂. Most plots show a continuous variations in compositions between the granitoid units. The GQFP exhibits the largest range in SiO₂, between 69.4 and 74.4 wt%. The Ardlethan Granite, microgranite and Mine Porphyry plot at the high silica end of the GQFP trend; the Mine Granite samples plot at the lower SiO₂ end. Harker diagrams of selected major and trace components are presented in Figs. 3-1 to 3-5.

The trends for a variety of components, such as TiO₂, Al₂O₃, Fe₂O₃, FeO, Na₂O, K₂O Sr and Sc, show a high linear correlation between all granitoid units ($r > 0.75$) with increasing SiO₂ (Figs. 3-1A & 3-1B). Harker diagrams of a number of components, including MgO, CaO, Ba, Zr, Ce, Nd, V and Cr, however show trends in which the Ardlethan Granite, GQFP, microgranite and Mine Porphyry samples define a common linear trend (Figs. 3-2A & 3-2B) but the Mine Granite samples exhibit a separate linear trend.

A third group of components, including Rb, Th, U, Nb, Y, Li, Sn, F, As, Ta and W, crudely form typical Rayleigh fractionation trends with increasing SiO₂ (Fig. 3-3A to Fig. 3-4B). The Ardlethan Granite, microgranite and Mine Porphyry samples define the enriched, high SiO₂ portion of the trend. There is also a tendency for the most enriched samples to show a limited decrease in SiO₂. The Mine Granite samples exhibit a wide scatter in Sn concentrations which probably reflects a weak overprinting of the mineralizing fluids associated with the main ore-forming event.

A fourth group of components, including MnO, P₂O₅, Pb, Co, Ni, Cu, Zn, Ga, B, Mo, Sb and Bi, does not define good linear trends. The Mine Granite and GQFP samples generally poorly define a linear trend

which intersects at the high end a diffuse field defined by the Ardlethan Granite, microgranite and Mine Porphyry samples (Figs. 3-5A & 3-5B).

Other geochemical plots such as Rb vs Sr, Rb vs Ba, U vs Ba and Th vs Ba, illustrate similar Rayleigh fractionation trends as defined by many of the Harker variation plots (Fig. 3-6A to Fig. 3-7B).

3.4 Discussion

The geochemical characteristics of the Mine Granite, Ardlethan Granite, GQFP, microgranite and Mine Porphyry exhibited by Fig. 3-1A to Fig. 3-5B can all be explained by a simple fractionation process. The separate trends defined by the Mine Granite samples (Figs. 3-2A & 3-2B) from the trend defined by the Ardlethan Granite, the GQFP, microgranite and Mine Porphyry could mean that the Mine Granite represents a mixture of cumulate and melt (Higgins *et al.*, 1985), while the others represent a dominantly melt trend. This interpretation implies that all the granitoids in the Ardlethan Tin Field have a comagmatic origin: the Mine Granite and the GQFP represent the early phases while the Ardlethan Granite, microgranite and Mine Porphyry the late fractionated phases. The Mine Granite samples fall on the fractionation curves on Figs. 3-6A, 3-7A and 3-7B in regions suggesting that the Mine Granite is a moderately fractionated phase if it is part of a whole fractionation process. This contradicts the previous conclusions. Because the Mine Granite is significantly older than all the other granitoids in the area (Chapter 2), it can not be more fractionated than the GQFP if they formed by a common fractionation process.

An alternative interpretation is that the Ardlethan Granite, GQFP, microgranite and Mine Porphyry represent products of a common fractionation process and the Mine Granite represents an earlier event not related to other granitoids in the area. This suggests that the GQFP represents an early crystallized phase, the Ardlethan Granite, microgranite and Mine Porphyry represent progressively fractionated phases of a common fractionation process. This interpretation is supported by the timing relationship that Mine Granite is older than all granitoids; the GQFP is an early crystallized marginal phase to the Ardlethan Granite, the microgranite is later than the main Ardlethan Granite body, and the Mine Porphyry is the latest intrusive in the Ardlethan Tin Field (Chapter 2). Because the Mine Granite represents a separate event, the Mine Granite samples can fall anywhere relative to the fractionation trend defined by the Ardlethan Granite, GQFP, microgranite and Mine Porphyry samples. Apparently, this interpretation implies that the GQFP, microgranite and Mine Porphyry are daughter phases of the main Ardlethan Granite.

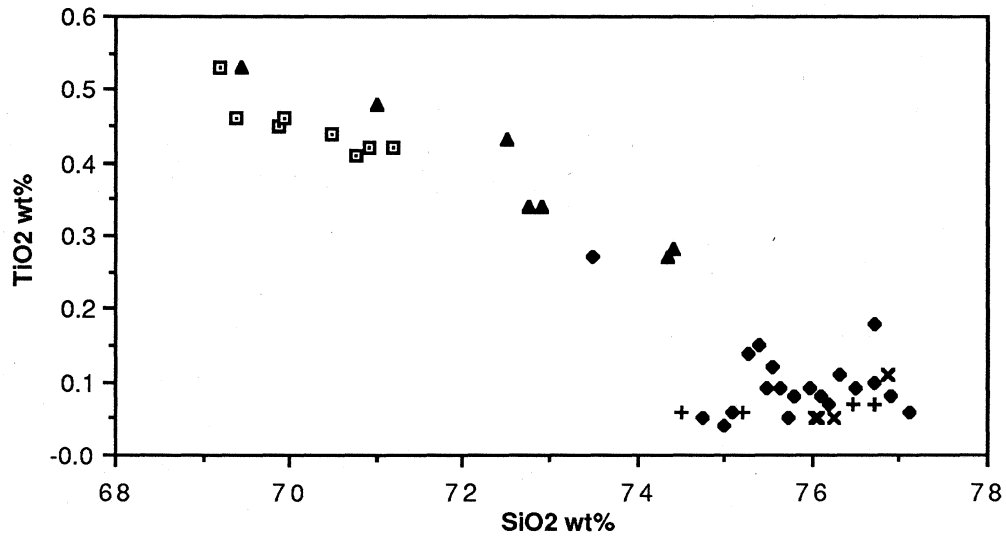


Fig. 3-1A: Harker diagram TiO₂ vs SiO₂

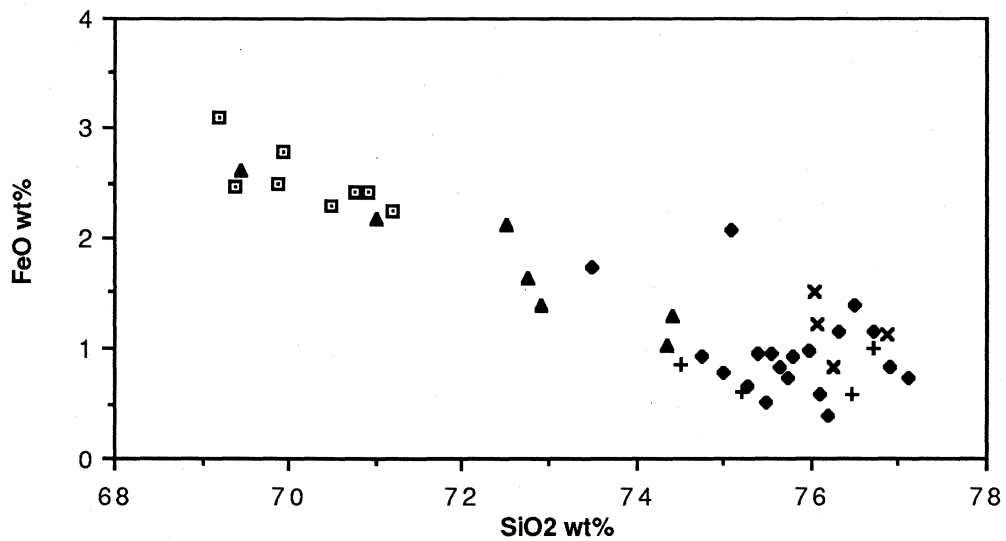


Fig. 3-1B: Harker diagram FeO vs SiO₂

Open square: the Mine Granite; filled diamond: the Ardlethan Granite; filled triangle: the GQFP; +: the microgranite and X: the Mine porphyry.

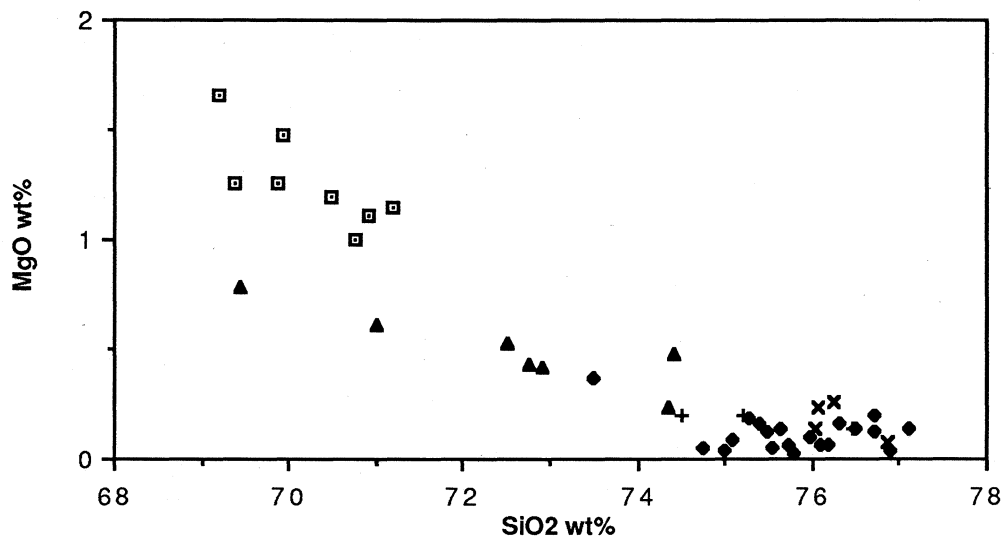


Fig. 3-2A: Harker diagram MgO vs SiO2

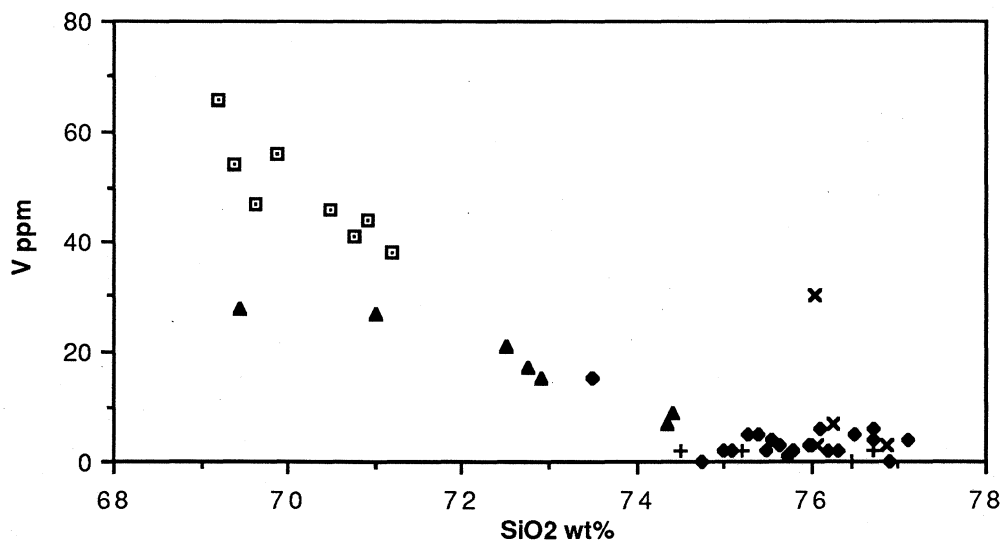


Fig. 3-2B: Harker diagram V vs SiO2

Open square: the Mine Granite; filled diamond: the Ardlethan Granite; filled triangle: the GQFP; +: the microgranite and X: the Mine porphyry.

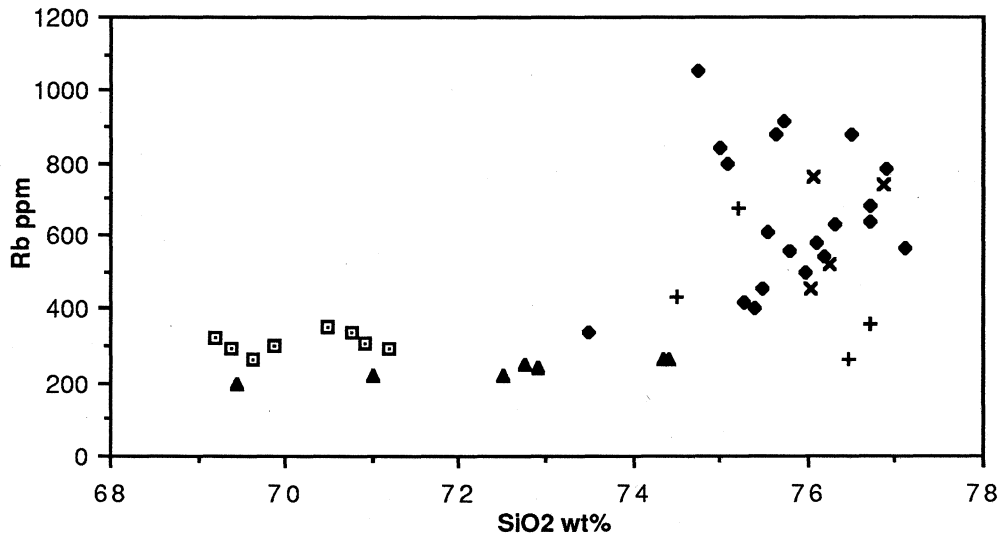


Fig. 3-3A: Harker diagram Rb vs SiO2

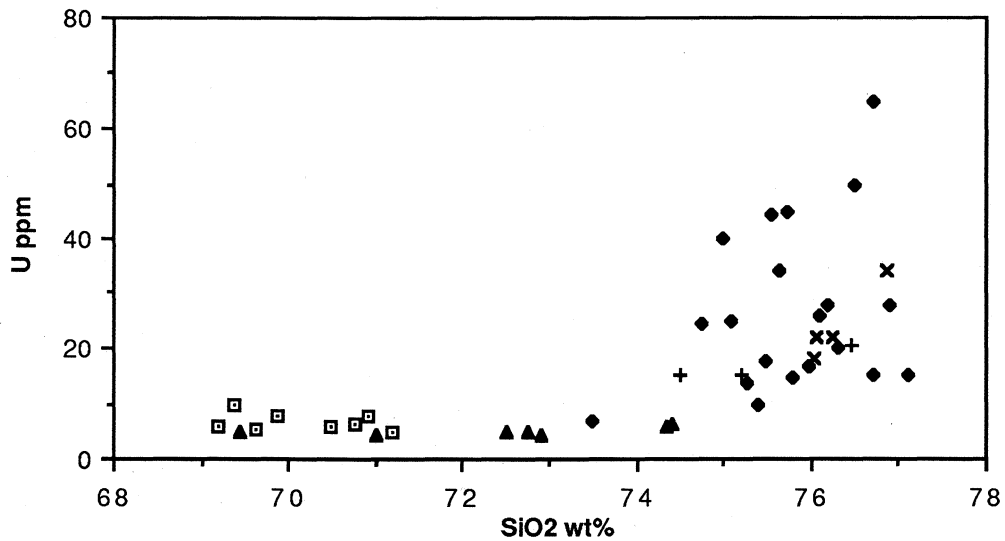


Fig. 3-3B: Harker diagram U vs SiO2

Open square: the Mine Granite; filled diamond: the Ardlethan Granite; filled triangle: the GQFP; +: the microgranite and X: the Mine porphyry.

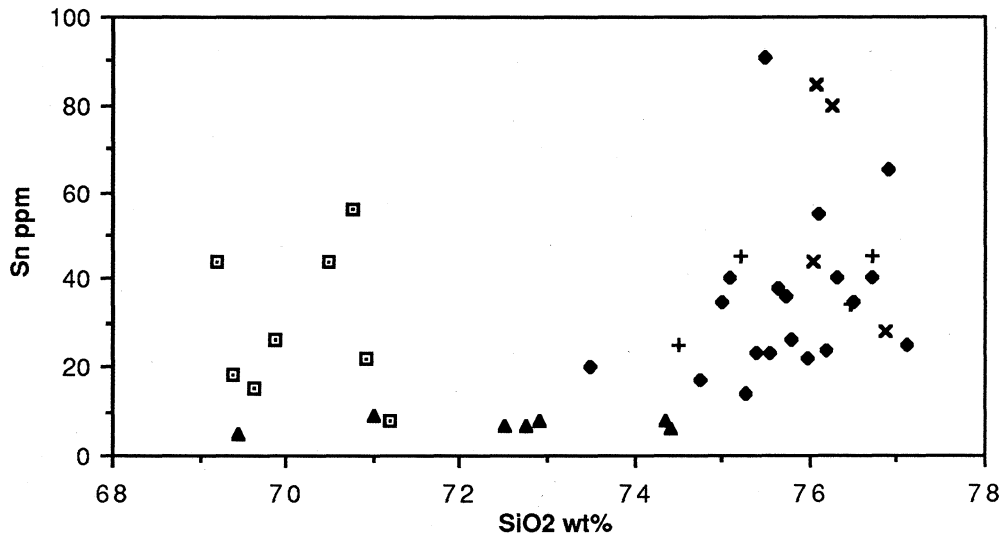


Fig. 3-4A: Harker diagram Sn vs SiO2

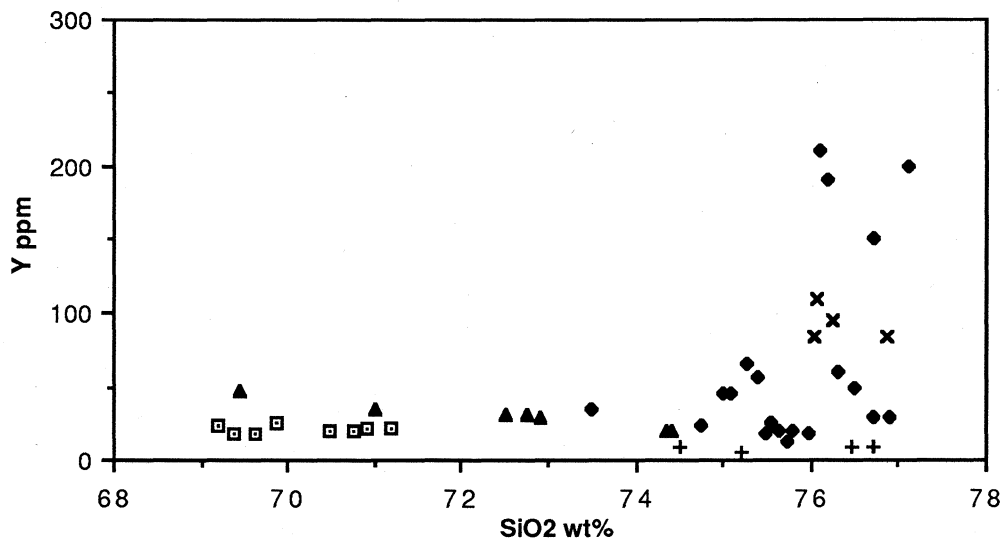


Fig. 3-4B: Harker diagram Y vs SiO2

Open square: the Mine Granite; filled diamond: the Ardlethan Granite; filled triangle: the GQFP; +: the microgranite and X: the Mine porphyry.

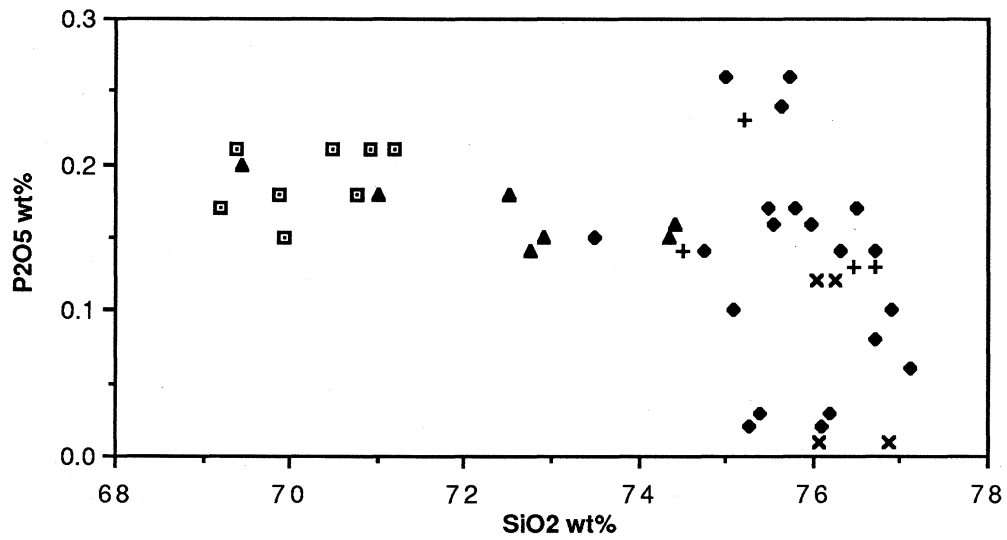


Fig. 3-5A: Harker diagram P₂O₅ vs SiO₂

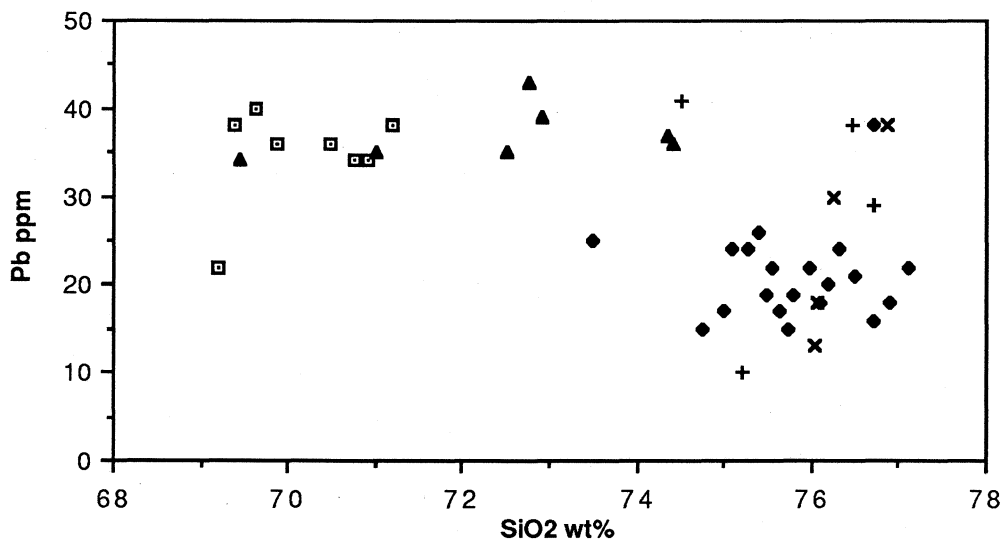


Fig. 3-5B: Harker diagram Pb vs SiO₂

Open square: the Mine Granite; filled diamond: the Ardlethan Granite; filled triangle: the GQFP; +: the microgranite and X: the Mine porphyry.

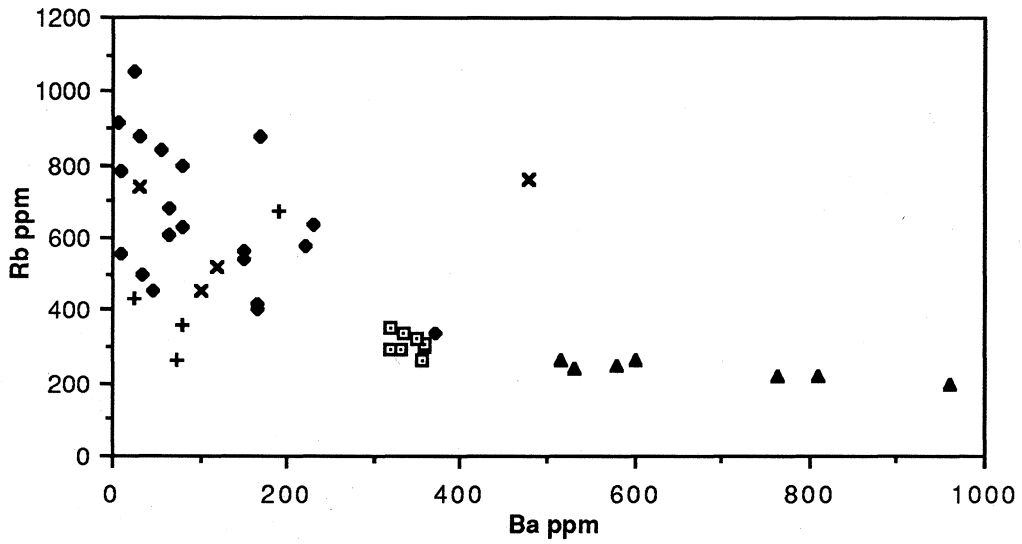


Fig. 3-6A: Variation diagram Rb vs Ba

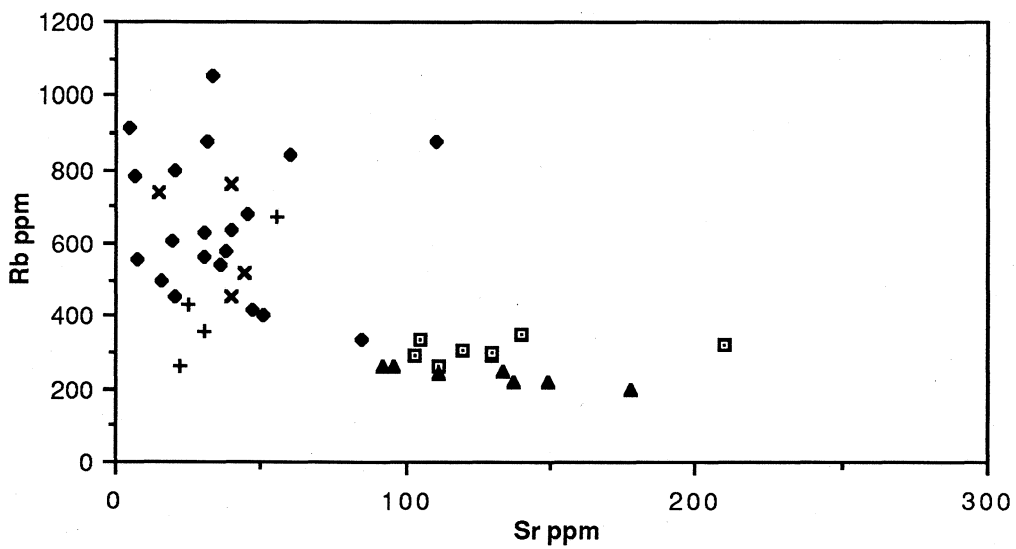


Fig. 3-6B: Variation diagram Rb vs Sr

Open square: the Mine Granite; filled diamond: the Ardlethan Granite; filled triangle: the GQFP; +: the microgranite and X: the Mine porphyry.

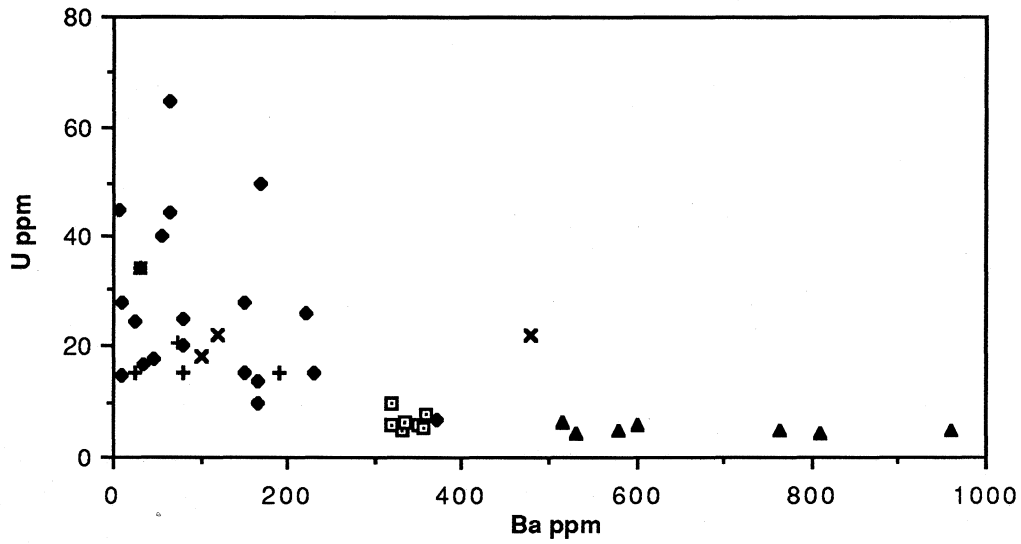


Fig. 3-7A: Variation diagram U vs Ba

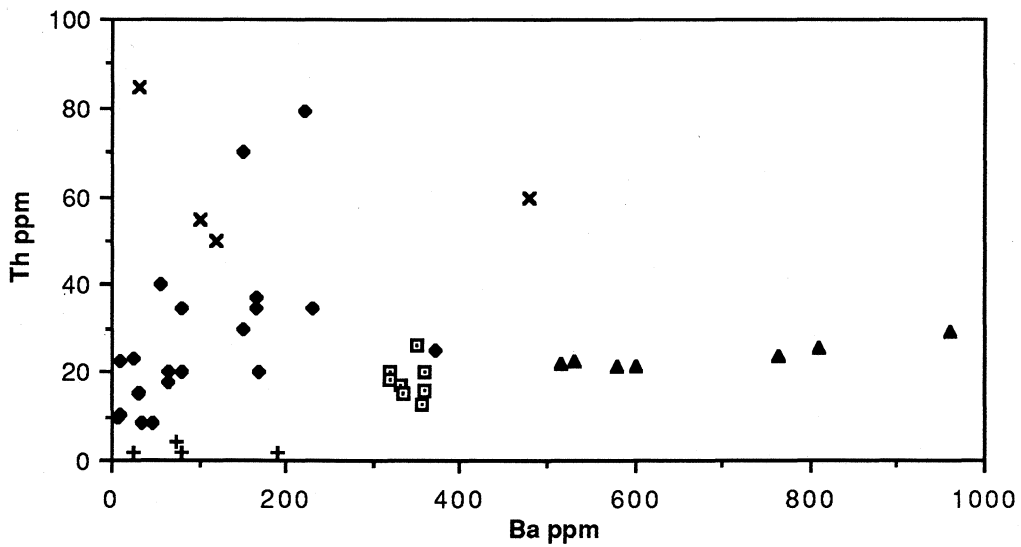


Fig. 3-7B: Variation diagram Th vs Ba

Open square: the Mine Granite; filled diamond: the Ardlethan Granite; filled triangle: the GQFP; +: the microgranite and X: the Mine porphyry.

The occurrences and the geochemical characteristics of the granitoids of the Ardlethan Tin Field are very similar to those of the Blue Tier Batholith, Northeastern Tasmania (Higgins *et al.*, 1985, Turner *et al.*, 1986, Higgins *et al.*, 1986, Mackenzie *et al.*, 1988, Higgins, 1989). Whilst there is a debate about the origin of the tin granites within the Devonian Blue Tier Batholith, in the Ardlethan Tin Field fractionation is clearly an important process which was responsible for tin enrichment in the Ardlethan Granite, microgranite and Mine Porphyry. This is similar to the fractionation model presented by Higgins *et al.* (1985; 1986).

3.5 Potentials of Tin Enrichment

A study of tin enrichment process during granitoid fractionation (Appendix 3) has shown that the granitoids with the following characteristics:

1. high in quartz and K-feldspar, low in plagioclase, biotite and muscovite, and free of sphene;
 2. high in volatiles and radioactive elements;
 3. emplacement at a high level in the crust;
 4. crystallized slowly under a high temperature gradient;
- and
5. early crystallization of quartz and K-feldspar rather than plagioclase and micas

have a better chance to enrich tin into their late stage fractionates.

The characteristics of the Mine Granite: high in biotite (up to 15% by volume) and low in quartz, early crystallization of K-feldspar and biotite, and relatively low concentrations of radioactive elements, suggests its potential to enrich tin into its late stage fractionates is very low.

The characteristics of the Ardlethan Granite: low in biotite and muscovite (<7% by volume), high in quartz and K-feldspar, early crystallization of quartz and K-feldspar, high in radioactive elements, and high level of emplacement (Stone, 1969), suggest that its potential to enrich tin into its late stage fractionates is high. This is supported by Harker diagram (Fig. 3-4A) which indicates strong tin enrichment with the degree of fractionation in the Ardlethan Granite.

As primary tin mineralization is almost always genetically related to granitoids, there are two possible tin sources in the Ardlethan Tin Field: the Mine Granite and the Ardlethan Granite. The above discussion

suggests that the Mine Granite has a low and the Ardlethan Granite has a high potential of producing tin rich fractionates. Therefore the tin mineralization in the Ardlethan Tin Field is probably related to the Ardlethan Granite.

3.6 Summary

The whole rock geochemistry data suggest that both the Mine Granite and the Ardlethan Granite are S-type granitoids. The Ardlethan Granite is strongly fractionated and the GQFP, microgranite and Mine porphyry are its daughter phases: the GQFP is an early marginal phase; the microgranite is a moderately fractionated phase, and the Mine Porphyry is a strongly fractionated phase. The Ardlethan Granite has a high potential to enrich tin during fractionation. Tin is enriched in the Ardlethan Granite and its fractionated phases: the microgranite and Mine Porphyry. It is likely that the tin mineralization in the Ardlethan Tin Field is related to the fractionation in the Ardlethan Granite.

Chapter 4

BRECCIA PIPES AND THEIR FORMATION

The Mine Granite, Carpathia-Blackreef, Stackpool-Godfrey and White Crystal Breccia Pipes (Fig. 4-1) are the four main breccia pipes in the Ardlethan Tin Field. They are located in an elongate zone about 0.5 km wide extending from the contact of the Ardlethan Granite northeast for about 1.5 km. The alteration halos of the Mine Granite, Carpathia-Blackreef and Stackpool-Godfrey Breccia Pipes overlap, forming an elongated common zone of alteration (Fig. 4-1). The White Crystal Breccia Pipe is separated from the zone at the surface but its alteration halo joins the main alteration halo at depth.

The geology of the Mine area is illustrated on a series of plans and cross sections (Fig. 4-2 to 4-15. See figure caption 4-1).

4.1 General Descriptions

4.1.1 The Mine Granite Breccia Pipe

The Mine Granite Breccia Pipe corresponds roughly to the main open pit developed to mine the Wildcherry, Ardwest and Wildcherry South deposits. It has a triangular shape on plans and the Wildcherry, Ardwest and Wildcherry South deposits are situated at the three sides in anticlockwise order (Fig. 4-10). As defined by the styles of brecciation and limit of alteration and mineralization, the Mine Granite Breccia Pipe dips about 60° WNW (Fig. 4-16).

The variations of styles of brecciation in the Mine Granite Breccia Pipe are difficult to map out in detail because of the strong hydrothermal alteration. Generally, there is a zonation from fragment supported breccia around the margins to rock-flour supported breccia (Plates 4-1 & 4-2) in the centre. The fragment supported breccia is composed of angular fragments with abundant vug spaces. The rock-flour supported breccia is composed of rock flour with or without vug spaces and minor elongated fragments. The transition between the two types of breccia is gradual with

fragment abundance decreasing and rock flour abundance increasing towards the central zone. The abundance of rock-flour and the lack of vug spaces in the central zone make it less permeable than the marginal zone.



Plate 4-1: Rock flour supported breccia in the Mine Granite Breccia Pipe. This interval contains rounded Mine Granite fragments (slide 9-19, from diamond hole B1110 at down hole depth of 350 m)

Fragments in the breccia pipe are mainly of the Mine Granite. They mostly range from several centimetres to several 10's of centimetres in size. Angularity is highly variable. Large fragments, up to a couple of metres across, occur in the marginal zone of the breccia pipe, for example, along the southern wall of the Wildcherry South open pit. The fragments are commonly cut by quartz tourmaline veins. A number of large, 10-30 cm, angular dark coloured mafic fragments were found within the Wildcherry South and Ardwest deposits. They appear to represent a disrupted mafic dyke (Fig. 4-9 to Fig. 4-15) along the southwestern margin of the breccia pipe.



Plate 4-2: Rock flour rich breccia in contact with the Mine Porphyry. Sample the central zone of the Mine Granite Breccia Pipe. This contact relationship indicates that the Mine Porphyry was later than the brecciation (Sample WY1, Ardwest open pit)

Rock-flour is composed of extremely fine-grained mineral debris, generally less than 1 mm in size. In thin section it consists of very angularly broken minerals of quartz and feldspars which are commonly strongly altered to biotite, sericite or chlorite (Plate 4-3 & 4-4). Garnet debris has been found in rock flour-supported breccia (sample RDW83). Generally more chlorite occurs in samples from the upper zone. In the central part of the breccia pipe the altered Mine Granite fragments cannot readily be distinguished from rock-flour. However, the presence of subangular clots of chlorite after K-feldspar phenocrysts and megacrysts, which are characteristic of the fresh Mine Granite, and dislocated quartz tourmaline veins are two useful field criteria. Also Clarke (1979) used hydrofluoric acid etching on polished surfaces to highlight the boundaries between fragments and rock flour dominated matrix.

Although the main Mine Porphyry dyke extends into the central zone of the Mine Granite Breccia Pipe near the surface (Fig. 4-9 to 4-15), it is not brecciated in this intensely brecciated zone. Contacts of the main Mine Porphyry dyke within the breccia pipe are very irregular and it is common to see numerous dykelets emanating from the main dyke into the



Plate 4-3: Strongly chlorite altered rock flour-rich breccia and nonbrecciated Mine porphyry (Sample WY10, Wildcherry South open pit)

rock-flour dominated matrix of the breccia. The Mine Porphyry also forms thin coating (thickness < 1 cm) on the surface of Mine Granite fragments. Samples from the central zone also show a limited degree of mixing of rock flour and the quenched margins of the Mine Porphyry dykes (Plates 4-2 & 4-3). These observations suggest that the emplacement of the main Mine Porphyry dyke post-dates the main stage of brecciation in the Mine Granite Breccia Pipe.

Small angular fragments of the Mine Porphyry only occur in several small zones in the Ardwest deposit (Fig. 4-9 to 4-15). These fragments are very angular, mostly ranging between 1 and 10 cm in size, and commonly make up a large proportion (up to 60%) of the total fragments (Plate 4-5) in these zones. Their distribution indicates several small secondary breccia pipes (Clarke, 1979) postdating the emplacement of the Mine Porphyry dykes. In these small pipes the vug spaces are filled with large amounts of massive, black-coloured tourmaline crystals, which are characteristic features of the Carpathia-Blackreef Breccia Pipe. This suggests that their formation may be contemporaneous with the Carpathia-Blackreef Breccia Pipe.

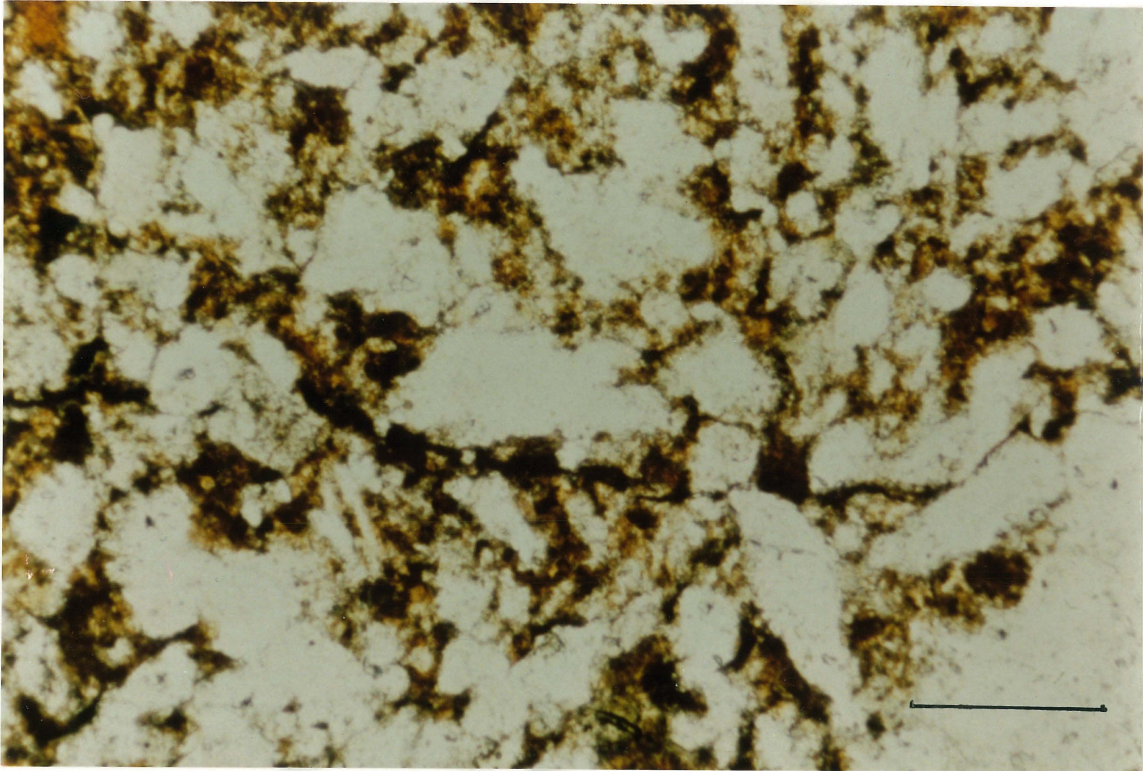


Plate 4-4: Secondary biotite alteration in rock flour zone. This sample is from the depth of the Mine Granite Breccia Pipe. It consists of mainly quartz and K-feldspar debris rimmed by secondary biotite (From sample RDW80, scale bar=0.5 mm).

Microgranite fragments are locally present in the southwestern corner of the Wildcherry South deposit. This indicates that the microgranite dykes predated the main stage brecciation in the Mine Granite Breccia Pipe.

In summary, cross-cutting relationships suggest that two stages of brecciation occurred in the Mine Granite Breccia Pipe. The first and main stage formed the Mine Granite Breccia Pipe. The second stage occurred only in several small secondary breccia pipes within the Ardwest deposit. The emplacement of the microgranite dykes predated first stage and the emplacement of the Mine porphyry dykes separated the two stages of brecciation.

4.1.2 The Carpathia-Blackreef and Stackpool-Godfrey Breccia Pipes

The Carpathia-Blackreef and Stackpool-Godfrey Breccia Pipes are exposed east of the Mine Granite Breccia Pipe. The central zones of these breccia pipes are characteristically enriched in fragments of sediment fragments (Plate 4-6). Fragment-supported breccia of mainly Mine Granite fragments occurs in marginal zones. Dark-coloured massive acute tourmaline alteration occurs in association with all the tin deposits in these breccia pipes.



Plate 4-5: Angular Mine porphyry fragment supported breccia. Sample from the secondary Breccia Pipes in the Ardwest deposit. The matrix is mainly acute tourmaline (Sample WY24; Ardwest open pit).

The Carpathia-Blackreef Breccia Pipe consists of a number of roughly N-S orientated subvertical zones which appear to coalesce and diverge over at least a vertical distance of 500 metres (Fig. 4-4 to 4-7 and

Fig. 4-17). The complex boundaries make it difficult to map precisely in three dimensions, however data collected from surface exposures, mining developments and diamond and percussion drill holes indicate that there are many daughter breccia pipes ranging from less than one metre to several tens of metres in diameters (Fig. 4-17). Two blind breccia pipes, i.e. pipes not opening to the surface, occur as parts of the Carpathia-Blackreef Breccia Pipe.

The Stackpool-Godfrey Breccia Pipe dips 60° WNW. It is exposed at the small Stackpool open pit.



Plate 4-6: Breccia enriched in sediment fragments. This is from the central zone of the Stackpool-Godfrey Breccia Pipe (Stackpool open pit)

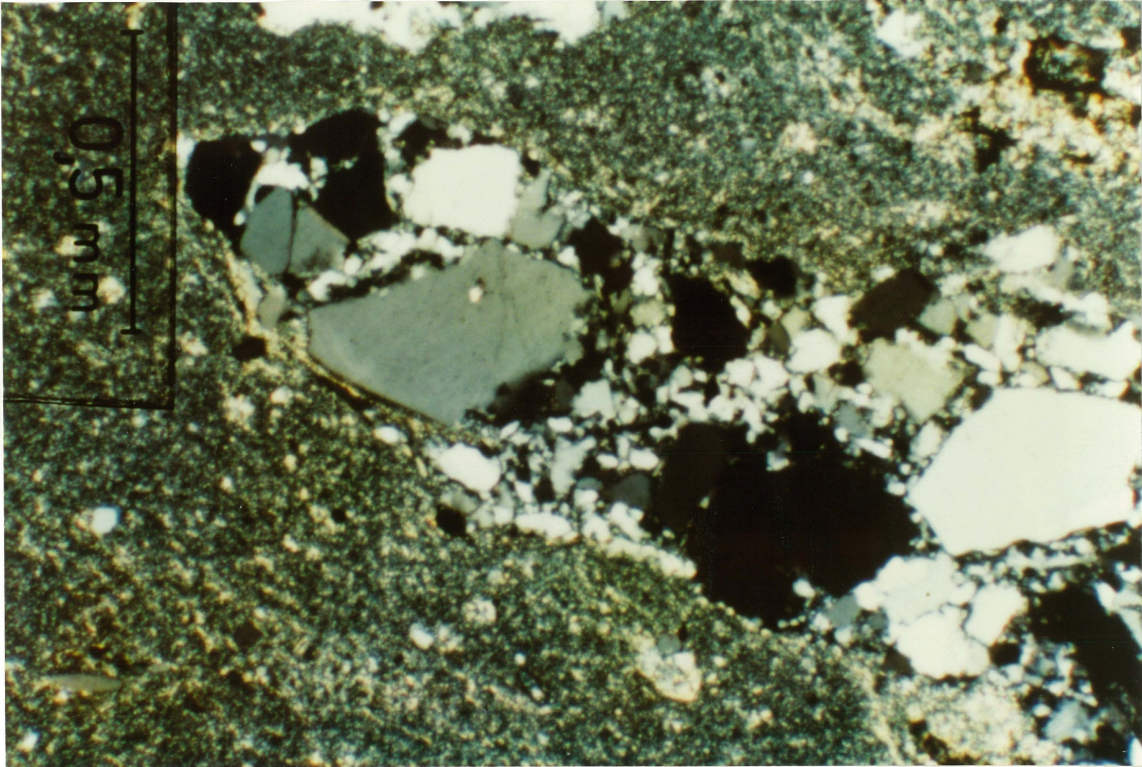


Plate 4-7: A rock flour pocket in the Mine Porphyry. This is from the contact of the Carpathia-Blackreef Breccia Pipe (sample RD128, scale bar=0.5 mm)

The Carpathia-Blackreef and Stackpool-Godfrey Breccia Pipes join together at a depth of about 700 metres below the surface (Fig. 4-15). Schematically, the overall geometry of these two breccia pipes is similar to a tree, with a common trunk at depth. The Stackpool-Godfrey Breccia Pipe represents a regular branch extending to the surface while the Carpathia-Blackreef Breccia Pipe has many smaller sub-branches, some of them extend to the surface, others are blind.

There are many rock flour pockets ranging from less than a centimetre to several centimetres in diameter (Fig. 4-18) along the hanging wall of the Carpathia-Blackreef Breccia Pipe. They extend into the nonbrecciated host rock like the blind daughter breccia pipes and open downwards into the Carpathia-Blackreef Breccia Pipe (Plate 4-7). They appear to be streams of rock flour injected into the nonbrecciated host rock.

As mentioned previously, the central zones of the Carpathia-Blackreef and Stackpool-Godfrey Breccia Pipes consist mainly of

fragments and matrix derived from sedimentary rocks (Plate 4-6). In the Stackpool open pit it is not difficult to recognize that they are fragments of fine-grained sandstone, siltstone and shale. The fragments range from several millimetres to about 10 cm and are mostly subangular in shape. Vug space is very rare within the zone enriched in sediment fragments and the breccia appears to be rock flour-supported. It is also common to see large fragments surrounded by smaller ones in the Stackpool open pit. An extremely large sediment fragment, at least 10 m across, was intersected by the decline linking the main open pit and the Carpathia deposit. Diamond and percussion drill hole information suggest that it occurs at the top closure of a blind daughter breccia pipe located about 120 m below surface between the Carpathia and Wildcherry deposits (Fig. 4-3).

Vertical variations in styles of brecciation were observed in both the Carpathia-Blackreef and Stackpool-Godfrey Breccia Pipes. Samples from depth contain more angular fragments and less rock flour than those near surface. Thus at depths greater than 300 m the breccias are dominantly fragment-supported.

The Carpathia-Blackreef and Stackpool-Godfrey Breccia Pipes all have marginal zones containing predominantly Mine Granite fragments (Plate 4-8). These marginal zones vary from less than 1 m to over 50 m in width and form a transitional phases to the nonbrecciated Mine Granite. The characteristics of these marginal zones are very similar to the marginal zone in the Mine Granite Breccia Pipe. There are abundant vugs with vug infill minerals and exhibit intense hydrothermal alteration. The footwall of the Stackpool-Godfrey Breccia Pipe lacks such a transitional zone.

Mine Porphyry fragments occur in both the Carpathia-Blackreef and Stackpool-Godfrey Breccia Pipes. Diamond drill hole information indicates that they were derived from several Mine Porphyry dykes which were disrupted during brecciation (Fig. 4-4 to Fig. 4-7 and Fig. 4-12 to Fig. 4-14).

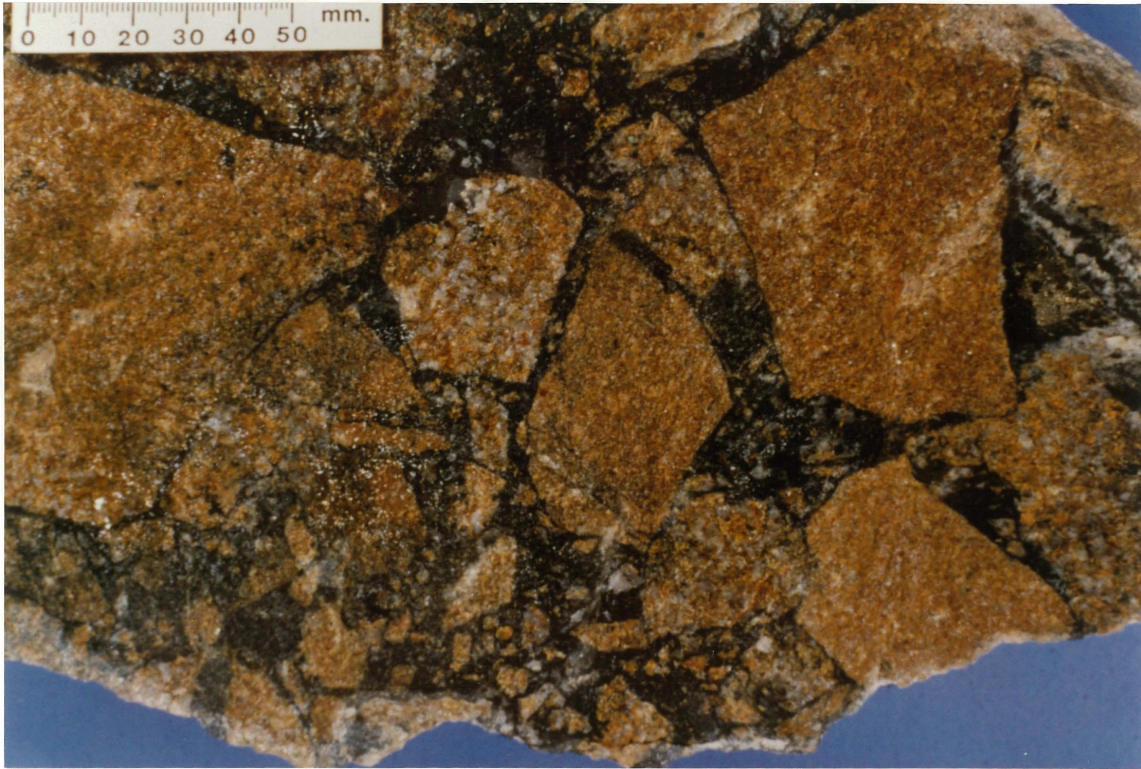


Plate 4-8: Mineralized breccia of mainly angular Mine Granite fragments. This sample is from the Blackreef deposit. The vugs are filled by tourmaline, cassiterite and sulphides; the fragments are strongly altered to sericite (Sample RB32)

It appears that the Mine Porphyry dykes immediately adjacent to the Breccia Pipes are the sources of the Mine Porphyry fragments in the breccia pipes. Diamond drill cores suggest that the Stackpool-Godfrey Breccia Pipe intersects two Mine Porphyry dykes, one at about 700 metres below surface and the other at about 300 metres below surface (Fig. 4-2). Samples from the surface exposure in the Stackpool open pit and diamond drill cores at depth of 460 metres or more below surface all contains about 1-3% Mine Porphyry fragments by volume whilst the section between 300 and 460 metres below surface contains very few Mine Porphyry fragments (Fig. 4-2). Such a distribution suggests upward transport of Mine Porphyry fragments during brecciation. Very similar features were found in the Carpathia-Blackreef Breccia Pipe (Fig. 4-4 to 4-7). Mine Porphyry fragments close to their parental dykes are larger and more angular than those further away.

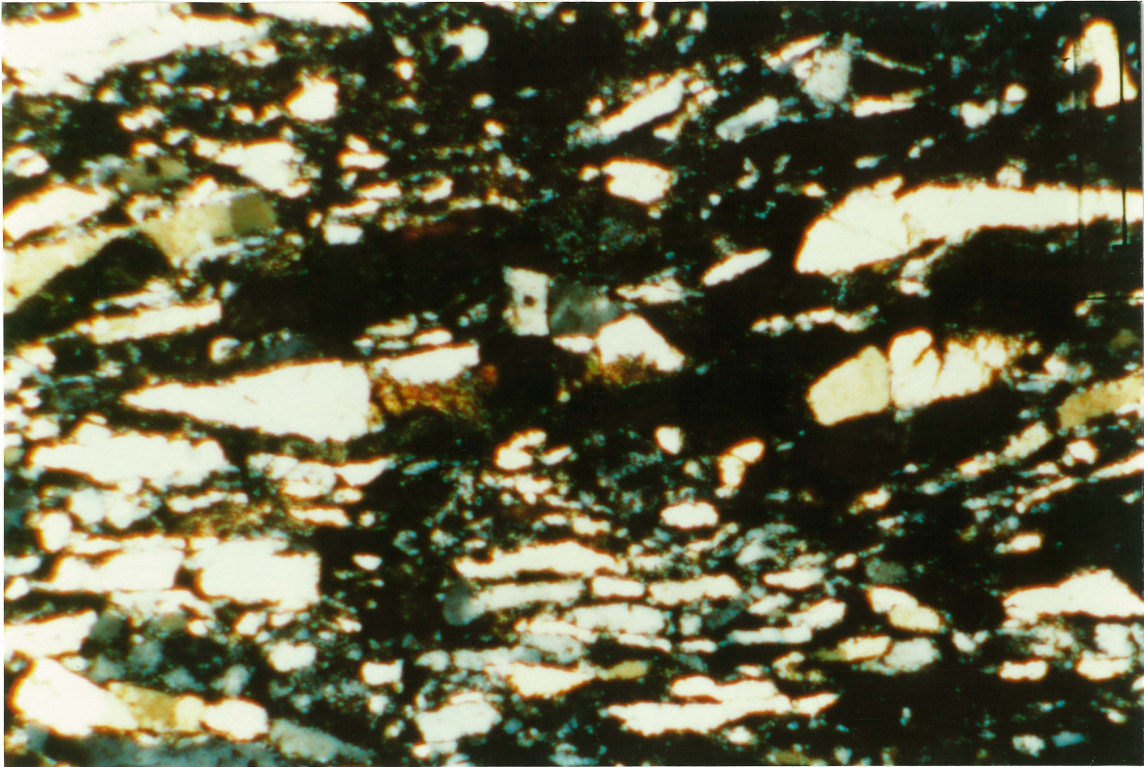


Plate 4-9: Laminar mass flow patterns. This is from the rock flour-rich zones in the Carpathia-Blackreef Breccia Pipe. Examinations of orientated thin sections indicate that the flow was upwards (Sample RD196, scale bar=2 mm).

Microgranite fragments also occur in the Carpathia-Blackreef and Stackpool-Godfrey Breccia Pipes. Most microgranite fragments occur in marginal zones. They range from a few centimetres to several metres in size, significantly larger than most of the other fragment types. Diamond drill core also indicates that there are microgranite dykes which were also disrupted by the Stackpool-Godfrey Breccia Pipe (Fig. 4-2).

Samples from the hanging wall of the Carpathia-Blackreef Breccia Pipe at depth of about 600 metres below surface contain mass-flow textures made up of laminated rock and mineral debris, and elongated fragments commonly less than 5 mm in size. They are regularly orientated and parallel to the contact of the breccia pipe (Plate 4-9). Orientated thin sections indicate that irregular pressure shadows occur behind convex corners to fragments and on the tops of coarser fragments, suggesting an upward flow direction. Similar features were also found at depth in the Mine Granite and Stackpool-Godfrey Breccia Pipes.

Another characteristic feature of the Carpathia-Blackreef and Stackpool-Godfrey Breccia Pipes is the large amount of black tourmaline crystals associated with cassiterite mineralization. This type of tourmaline alteration is very typical of the Blackreef deposit where high-grade ore contains more than 40% tourmaline. In the Stackpool deposit, this type of tourmaline occurs in subvertical pipes around the central zone of the Stackpool-Godfrey Breccia Pipe. Numerous massive tourmaline bands were intersected by diamond drill holes in the zones around the Godfrey deposit. Although tourmaline alteration is common in the Ardlethan Tin Field, this type of tourmaline is characteristic of the Carpathia-Blackreef, Stackpool-Godfrey Breccia Pipes, and the small secondary breccia pipes in the Ardwest deposit.

4.1.3 The White Crystal Breccia Pipe

The White Crystal Breccia Pipe (Figs. 4-1 & 4-8) occurs in a separate zone away from the other breccia pipes. It is characterized by the occurrence of extremely large, angular to tabular, and inward dipping Mine Granite fragments, large vugs and abundant vug infill minerals (Paterson, 1976; Clarke, 1979; Clarke *et al.*, 1984). The fragments are mostly derived from the host Mine Granite. There are some microgranite fragments.

The size of the Mine Granite fragments ranges from several centimetres to several metres. The large fragments near the original surface outcrop were commonly tabular in shape and dipped towards the center. This feature points to a "collapse breccia" pipe structure (Paterson, 1976; Clarke *et al.*, 1984).

The Mine Granite fragments, although of a wide range of size, are all very angular and unlike other breccia pipes in the Ardlethan Tin Field, there is no rock-flour. The breccia is always fragment supported which led to the formation of numerous vugs which may be up to 30x10x10 cm³ in size. The main vug infill minerals are tourmaline and quartz in association with cassiterite, wolframite, arsenopyrite, pyrite, chalcopyrite, sphalerite, galena, fluorite, and patches of cookeite (Plate 4-10).

Microgranite fragments also occur in the White Crystal Breccia Pipe. They are very similar to Mine Granite fragments in terms of size and angularity.



Plate 4-10: Large vug in the White Crystal Breccia Pipe. The vug is filled by sulphides (dark minerals) and cookeite (white patches). The fragments are strongly altered and contain mainly topaz+tourmaline (from White Crystal dump).

Fragments in the White Crystal Breccia Pipe are strongly altered to an assemblage of topaz, tourmaline, quartz and sericite. Topaz alteration is a unique characteristic of this breccia pipe.

4.2 Correlation Between Igneous and Brecciation Events

The igneous events in the Ardlethan Tin Field were in the following order: the Mine Granite, GQFP, Ardlethan Granite, microgranite and Mine Porphyry dykes (see Chapter 2). The timing of the mafic dyke emplacement is unknown except that it is not found cutting units other than the Mine Granite.

The Mine Granite Breccia Pipe, excluding the small secondary breccia pipes in the Ardwest deposit, does not contain any Mine porphyry

fragments but is intruded by nonbrecciated Mine Porphyry dykes. This suggests that the main stage of brecciation predated the intrusion of the Mine Porphyry dykes.

The Carpathia-Blackreef and Stackpool-Godfrey Breccia Pipes contain abundant Mine Porphyry fragments, indicating that their formation postdated the Mine Porphyry intrusion. As the small secondary breccia pipes in the Ardwest deposit also contain Mine Porphyry fragments and have a similar type of black-coloured acute tourmaline alteration, they were probably formed at the same time as the Carpathia-Blackreef and Stackpool-Godfrey Breccia Pipes.

There is no direct evidence to define the timing of formation of the White Crystal Breccia Pipe in relation to other breccia pipes in the Ardlethan Tin Field. However, the collapse features and lack of intensive brecciation possibly reflect a lower energy regime compared to the other breccia pipes. This, together with mineralogy and alteration studies (see Chapter 5), has led to the tentative interpretation that the White Crystal Breccia Pipe was the last one to form in the Ardlethan Tin Field.

In summary, three brecciation events are recognized in the Ardlethan Tin Field. The first event was the formation of the Mine Granite Breccia Pipe. This was followed by the the emplacement of the Mine Porphyry dykes, development of the Carpathia-Blackreef, Stackpool-Godfrey Breccia Pipes, and the limited secondary brecciation in the Ardwest deposit. The White Crystal Breccia Pipe is thought to be the third event. Each brecciation event contains unique characteristics: the Mine Granite Breccia Pipe is characterized by a rock flour-rich core; the Carpathia-Blackreef and Stackpool-Godfrey Breccia Pipes by central zones enriched in sediment fragments; and the White Crystal Breccia Pipe by its large, angular, tabular and inward-dipping fragments, large vugs and vug infill minerals.

4.3 Sources of the Sediment Fragments

The sediment fragments occurring in the Carpathia-Blackreef and Stackpool-Godfrey Breccia Pipes are clearly foreign and must have been transported into the breccia pipes during brecciation. There are only two possible sources. Either they were derived from depth being transported upwards during brecciation or they were derived from overlying sedimentary rocks. The data support an interpretation that the sediment fragments have been brought up into the breccia pipes from depth for the following reasons.

Firstly, studies of the compositions of rock flour and the distributions of microgranite fragments and Mine Porphyry fragments in the Carpathia-Blackreef and Stackpool-Godfrey Breccia Pipes (see above) all indicate general upward movement. The occurrence of garnet debris in rock flour-supported breccia in the central zone of the Mine Granite Breccia Pipe strongly indicates that some contents of the rock flour were derived from the GQFP at depth. The distribution of microgranite fragments and mafic fragments in the Mine Granite Breccia Pipe also suggests upward movements. A similar conclusion was made by Clarke (1979) in his study of the source of the Mine Porphyry fragments in the small secondary breccia pipes in the Ardwest deposit. In these locations Mine Porphyry fragments occur only above the level where Mine Porphyry dykes are disrupted by the secondary brecciation (Fig. 4-9 to Fig 4-15).

Secondly, the well preserved flow texture (Plate 4-9) observed in samples from the Carpathia-Blackreef Breccia Pipe indicate upward movement. More importantly, the occurrence of sediment fragments in blind breccia pipes negates the possibility of a collapse mechanism.

Thirdly, many Mine Granite fragments in the Mine Granite Breccia Pipe, and sediment fragments in the Carpathia-Blackreef and Stackpool-Godfrey Breccia Pipes, contain tourmaline veins. These veins occur only within and do not pass fragments which indicate that they formed prior to brecciation. Therefore the fragments must be derived from a place where tourmaline alteration occurred prior to brecciation. As described in chapter 2, the contact between the Mine Granite and sediments is generally fresh and tourmaline alteration occurs only along the contact of the Ardlethan Granite. DDH B1188 intersected zones of tourmaline alteration at depth greater than 500 m in the nonbrecciated Mine Granite, suggesting that the source of these fragments was likely beneath the breccia pipe.

The presence of rock flour-supported breccias in the Mine Granite, Carpathia-Blackreef and Stackpool-Godfrey Breccia Pipes also suggests a high energy regime, conditions unlikely to be met in a "collapse" breccia pipe, such as the White Crystal Breccia Pipe.

Finally, it is difficult to envisage that the narrow elongated breccia pipes could form by just a collapse process. Generally, a collapse occurs by withdrawing support. If the support withdrawal was over a large area, the whole area would probably tend to sink rather than form several narrow pipes. If the support withdrawal was localized, gravity itself would hardly be sufficient to overcome the strength of the rock to initiate brecciation, unless the host rock was very strongly fractured. There is no evidence to suggest that those narrow sub-vertical pipes had a more

strongly fractured precursor. Also as the breccia pipes all dip about 60° WSW, large scale downward movement of materials in these pipes is difficult.

4.4 Structural Control of Brecciation

Although there are no large major faults, there are many small faults and joints in the Ardlethan Tin Field. Measurements of strike and dip show that these faults and joints define three linear trends (Figs. 4-19 & 4-20).

The first lineament (ESE) corresponds to the linear occurrence of the GQFP stock, Mine Granite and Carpathia-Blackreef Breccia Pipes. It extends further east southeasterly (Fig. 4-19) to Brown's and Paterson's Knobs, two possible breccia pipes containing fragments of sedimentary rocks stannite and sulphide mineralization. Between the GQFP stock and the Mine Granite Breccia Pipe occurs another possible breccia pipe, the Wheat Field Breccia Pipe (?) suggested by auger drill holes. A number of creeks and alluvial deposits are sub-parallel to this trend (Fig. 4-19).

The second major lineament (NE) corresponds to the alignment of the Taylor's Hill breccia zone, Carpathia-Blackreef and Stackpool-Godfrey Breccia Pipes (Fig. 4-19). Again the orientations of several creeks and parts of the tin anomalous area and an alluvials are sub-parallel to this trend.

The third lineament (NNW) runs through the Little Bygoo, Big Bygoo and Ardlethan Tin Mines. It is also expressed by the overall distribution of areas of anomalous tin. It extends to the largest alluvial deposit in the field (Yithan). There are several creeks align with this trend (Fig. 4-19).

These data suggest that the brecciation in the Ardlethan Tin Field is localized along these lineaments or at their intersections. The Mine Granite Breccia Pipe has a triangular shape because it formed at the conjunction of the three trends (Fig. 4-19). A fracture control to mineralization is evident at Big Bygoo, Little Bygoo and Taylor's Hill where mineralization occurs along joints or joint intersections (see Chapter 1).

The White Crystal deposit does not lie on any of the major lineaments discussed above but it does have an elongated aspects to its distribution suggesting there are probably other minor lineaments in the area.

4.5 The Process of Brecciation

The importance of the relationship between mineralization and breccia pipes has been recognized since the late 19th century (Hunt, 1887). Many models of breccia pipe formation have been proposed over the last one hundred years and recent comprehensive review of breccia pipes and processes of breccia pipe formation was given by Sillitoe (1985). The processes which can lead to breccia pipe formation can be summarized into seven categories:

1. Explosive brecciation by expanding volatiles (Walker, 1928; Norton & Cathles, 1973; Burnham 1979 & 1985)

Fluid overpressure is often the result of volatile exsolution from a magma. Explosive brecciation is caused when the fluid pressure exceeds the lithostatic pressure plus the strength of the overlying column of rocks. The quick release of the over pressured volatiles (Norton and Cathles, 1973) usually results in near vertical circular opening breccia pipes. Burnham's (1979 & 1985) modelling of magmatic crystallization showed that volatiles are accumulated during fractional crystallization. When these fluids are exsolved there is sufficient pressure to brecciate the pre-consolidated rock explosively. The mechanism is similar to that associated with volcanic eruptions. Brecciated rock fragments can be significantly dislocated. Matrix-rich breccias could form if grinding or milling was initiated by multiple pulses of brecciation. Fragments in the breccia pipe could be of source rocks as well as country rocks. Explosion by other mechanisms, such as cool ground water pool being heated by intruding magma described as "phreatomagmatic" (Sillitoe, 1985) may also lead to breccia pipe formation through volatile overpressure.

2. Brecciation by fault movements (Walters and Campbell, 1935; Mitcham, 1974)

Breccia is often formed during fault movement and multiple movements on a fault plane or series of fault planes may generate large masses of breccia. The characteristics of the breccia mass depends on the nature of the rocks and on the style of fault movement. As fragments are generally derived from the fault surface, the breccia is made up of the same rock type as the host. Grinding and milling of fragments can be very marked. The breccia mass is usually bounded by fault planes and dislocations of fragments is related to the movement of the fault are evident. This type of brecciation is not necessarily associated with igneous or hydrothermal activity.

3. Brecciation associated with igneous intrusion (Walters and Krauskopf, 1941; Sharp, 1979)

Igneous intrusion can result in intense local stress within the country rock and may result in brecciation. An early consolidated shell of the igneous body as well as the country rock may be brecciated by continued intrusion of melt from below. The resulting breccia is generally located along the contact with the igneous intrusive and is not pipe-like in form. Such brecciation is often associated with hydrothermal alteration. The size and angularity of fragments may be extremely variable.

4. Collapse brecciation by magma chamber withdrawal (Bryant, 1968; Sillitoe and Sawkins, 1971)

Collapse breccias may result from a number of processes, for example, the retreat of a magma chamber by thermal contraction (Bryant, 1968). The negative pressure formed by such support withdrawal can cause the overlying rocks to collapse when their strength can no longer hold their weight (Norman and Sawkins, 1985). The model of forming breccia pipes by vapor stoping (Norton and Cathles, 1973) is a development of this model. Generally, collapse brecciation is driven by gravity and proceeds in a tensional environment. The resulting breccias generally do not display any strong grinding or milling of fragments.

5. Brecciation by fluidization process (Reynolds, 1954; McCallum, 1985; Shelnutt and Noble, 1985);

Fluidization occurs when a large volume of fluid flows through a channel and transports rock fragments. This concept was originally established to describe an industrial process utilized in large part to accelerate mixing and chemical reaction in a bed of fine grained particles (Wilson, 1980), and was introduced to geology to describe the similarities between such a process and many aspects of breccias (McCallum, 1985). The driving force is the flowing fluids. The rock fragments can move in the same or opposite direction as the fluid flow depending on the velocity and the density of the fluid and the density and size of the rock fragments. McCallum (1985) performed a series of experiments to examine the behaviour of fine-grained particles in a cylinder when compressed air was blown through the bottom of the cylinder at different speeds. He described seven fluidization states: fixed bed state, quiescent fluidized bed state, aggregative bubbling state, aggregative slugging state, dispersed suspension state, channelling state and spouting state with increasing flux of air. Of the seven states described, only the spouting state involves strong particle convection sufficient to produce matrix-rich breccia by grinding of the fragments. Apart from the fluid, a pre-existing fracture channel is apparently all that is required to initiate a fluidization process.

6. Brecciation by solution and replacement (Bulter, 1913)

Solution and replacement breccias are developed through the alteration modification of fractured rocks by hydrothermal fluids. The edges, sharp rims and smaller fragments in this situation are replaced by secondary minerals. Such breccias generally lack dislocations and rock flour. Pre-existing fractures are also needed to initiate such a process.

7. Chemical brecciation (Sawkins, 1969)

Chemical brecciation was suggested by Sawkins (1969). The process involves differential expansion of minerals in the rock in response to a change of physical or chemical conditions and the expansion could be responsible for the brecciation. Breccias formed this way are composed of very angular fragments which can be matched to adjacent fragments indicating little dislocation.

Although many different processes may lead to breccia pipe formation, most of them require a pre-existing structure and therefore they may not be an independent process. Consequently, a breccia pipe may have a dynamic history involving different processes at different times, or at different locations in the breccia pipe, forming breccias of very different characteristics.

The characteristics of the breccia pipes in the Ardlethan Tin Field can be briefly summarized as follows:

- 1. Fragments are of a variety of lithologies;*
- 2. Rock flour is a very common constituent except in the White Crystal Breccia Pipe;*
- 3. There were multiple events of brecciation;*
- 4. There are nonbrecciated Mine Porphyry dykes in the Mine Granite Breccia Pipe;*
- 5. Fragments in the Mine Granite, Carpathia-Blackreef and Stackpool-Godfrey Breccia Pipes were strongly dislocated upwards;*
- 6. All the breccia pipes dip to the same direction suggesting that they may converge at depth;*
- 7. Brecciation was probably controlled by three or more major lineaments and their intersections.*

These characteristics in the Mine Granite, Carpathia-Blackreef and Stackpool-Godfrey Breccia Pipes suggest that the processes which caused the brecciation in the Ardlethan Tin Field were very complex. Explosive

brecciation is likely to be a significant mechanism but the abundance of rock flour indicates a complex evolution. Collapse brecciation probably played an important role in the formation of the White Crystal Breccia Pipe.

The very poorly sorted nature of the breccias in the Mine Granite, Carpathia-Blackreef and Stackpool-Godfrey Breccia Pipes suggest that fragments were not transported by, or at least not only by, fluid suspension as developed in a fluidization process. The transporting power of a fluidized mass depends on the speed of the fluid flow. The finer the sizes of the particles, the easier they are to be transported by fluid. When the speed of fluid flow decreases, the larger fragments tend to deposit first and the smaller ones deposit only with further decrease of the speed of fluid flow. This initiates a sorting process like that commonly seen in fluvial systems. The existence of garnet debris also negates a simple fluidization process, as garnet would have been reacted out easily had the system been fluid dominated. The dislocations in these breccia pipes was probably caused by forces with little sorting ability. Such a force could be provided by intrusion of a magma. As nonbrecciated and brecciated Mine Porphyry are present in the breccia pipes they may well represent the highest expression of the breccia-forming intrusion.

These discussions lead to a general four stage model (Fig. 4-21) to explain the formation of the breccia pipes. The first stage involves the fluid exsolution and accumulation in the source magma chamber (differentiates of the Ardlethan Granite). Stage two involves explosive brecciation, at the weakest zones in the overlying rocks, along pre-existing fractures or fracture intersections. Stage three is a collapse stage which may follow the release of fluids and possible magma withdrawal. The fourth stage is an intrusive stage. Apparently, not all the four stages are required to form a breccia pipe. The Mine Granite, Carpathia-Blackreef and Stackpool-Godfrey Breccia Pipes probably evolved through stages one, two and four. The White Crystal Breccia Pipe evolved through stages one, two and three.

4.6 Summary of the Magmatic and Brecciation Events

The brecciation and mineralization in the Ardlethan Tin Field is interpreted to be the result of the hydrothermal events associated with the intrusion and fractionation of the Ardlethan Granite.

The Ardlethan Granite intruded into the area following the Mine Granite. Before most of the Ardlethan Granite had been crystallized, fluid exsolution started which created overpressure and caused explosive brecciation. The Mine Granite breccia pipe was formed. At this stage the

crystallized shell of the Ardlethan Granite was probably not very thick, melt from depth of the magma chamber followed the fluids and intruded into the newly formed breccia pipe. Strong stressing was generated by the intrusion, as well as by possibly multiple pulses of overpressured fluids. Fragments in the breccia pipe were milled, ground and pushed upward. Continuation of the fractional crystallization at depth in the magma chamber kept a steady supply of fluids, which were focused into the permeable marginal zones of the breccia pipe, resulting in the hydrothermal alteration and mineralization.

Continual mineral deposition in open spaces in the Mine Granite breccia pipe may have resulted in a reduction of permeability which led to the second event of overpressure. This consequently resulted in the brecciation of the Carpathia-Blackreef and Stackpool-Godfrey Breccia Pipes and mineralization. When these two breccia pipes had been sealed up by mineral deposition, a third brecciation event occurred which formed the White Crystal Breccia Pipe. Finally the crystallization of the Ardlethan Granite was probably complete. The White Crystal Breccia Pipe collapsed when the overpressure was depleted.

Fig. 4-1 The major Breccia Pipes in the Ardlethan Tin Field and reference of cross sections. The Wheat field Breccia Pipe has not been explored.

Note about plans and sections

- Fig. 4-1 Dashed lines show the approximate boundary of intense alteration.
- Fig. 4-2 Dashed lines show the zone enriched in sediment fragments. The solid line on the righthand side shows the boundary of intense alteration. Boundaries of breccia pipes are not marked due to lack of information.
- Fig. 4-3 Boundaries of breccia pipes are not marked.
- Fig. 4-5 Boundaries of breccia pipes are not marked
- Figs. 4-9 to 4-15 Filled triangles represent mafic fragments. Boundaries of breccia pipes are not marked.
- Fig. 4-16 The Perseverance deposit and part of the Ardwest deposit are projected to this section to illustrate the relations between brecciation and mineralization.

The author apologizes for any inconvenience.

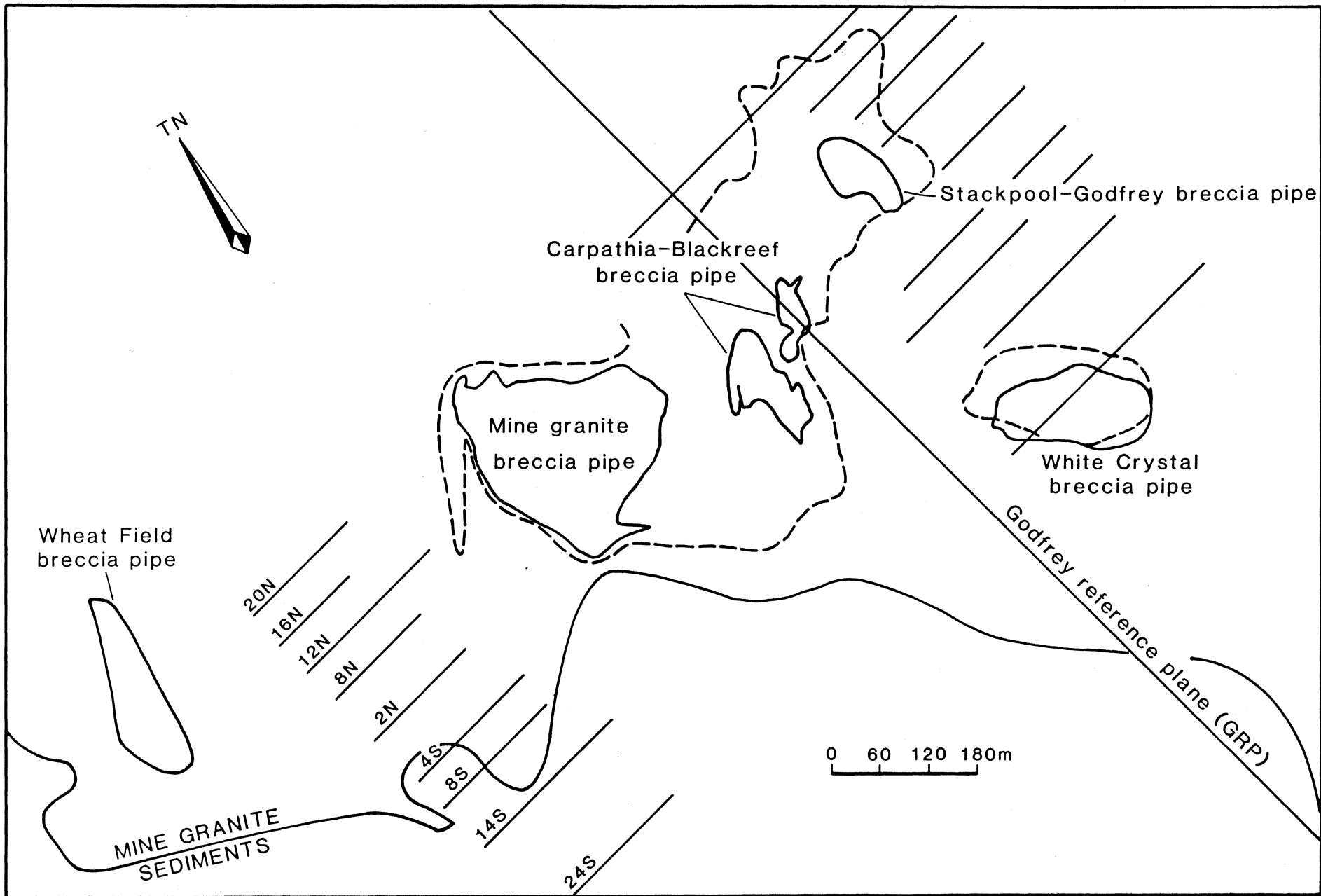
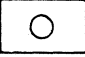

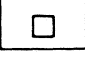
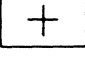



Fig. 4-2 Cross section 12N. The Godfrey deposit consists of five subvertical lenses at the depth of the Stackpool-Godfrey Breccia Pipe. The cross-cut relationship between the microgranite and Mine porphyry dyke indicates that the Mine porphyry is later than the microgranite. The distribution of microgranite and Mine porphyry fragments indicate the contents of this breccia pipe have moved upwards (GRP: Godfrey Reference Plane. Vertical scale in metres).

-  Sedimentary, Mine porphyry microgranite fragments
-  Orebody
-  Sedimentary & microgranite fragments
-  Microgranite dyke
-  Mine porphyry

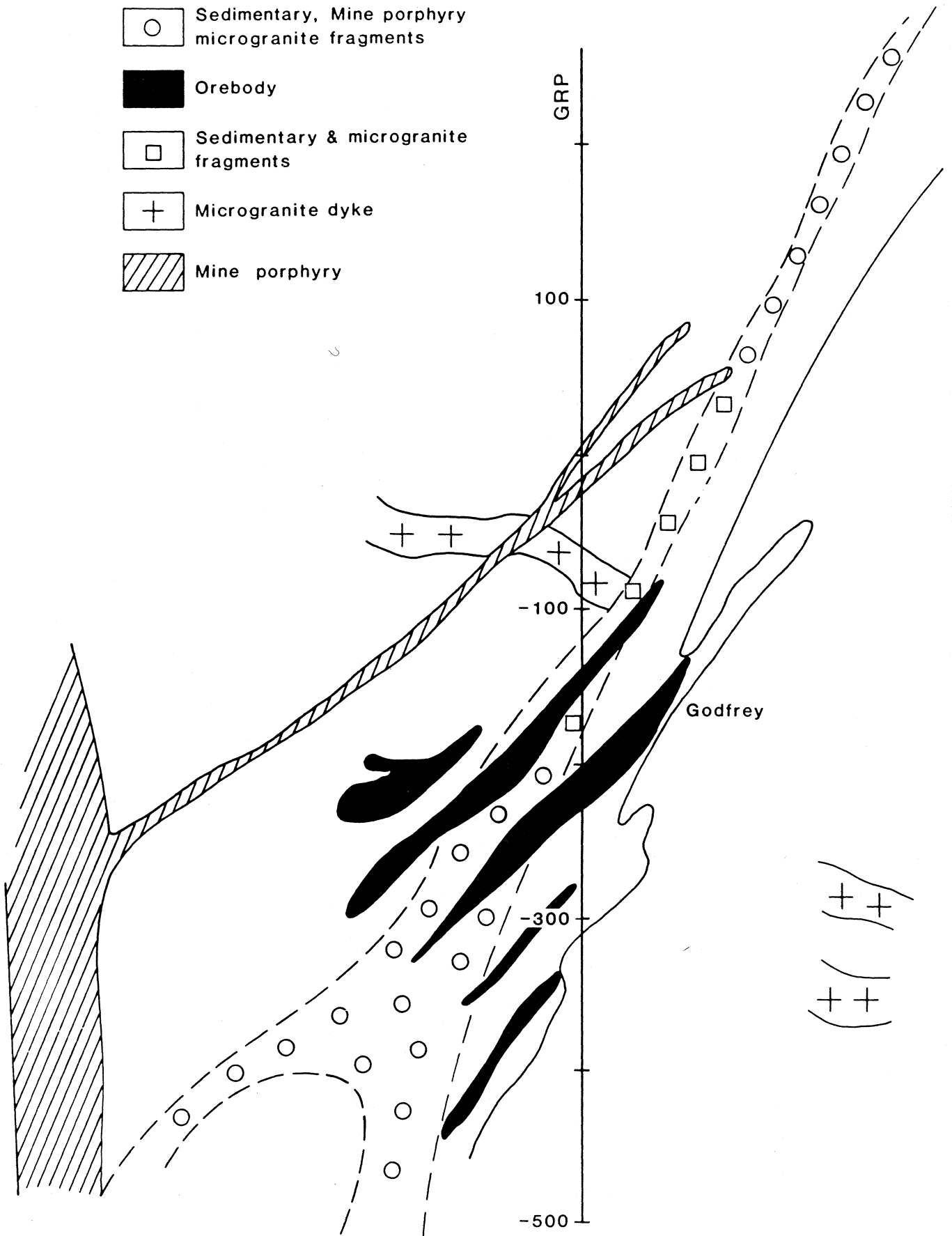


Fig. 4-3 Cross section 8N. The major Mine porphyry dyke is not brecciated in the Mine Granite Breccia Pipe (GRP: Godfrey Reference Plane. Vertical scale in metres).

A

B

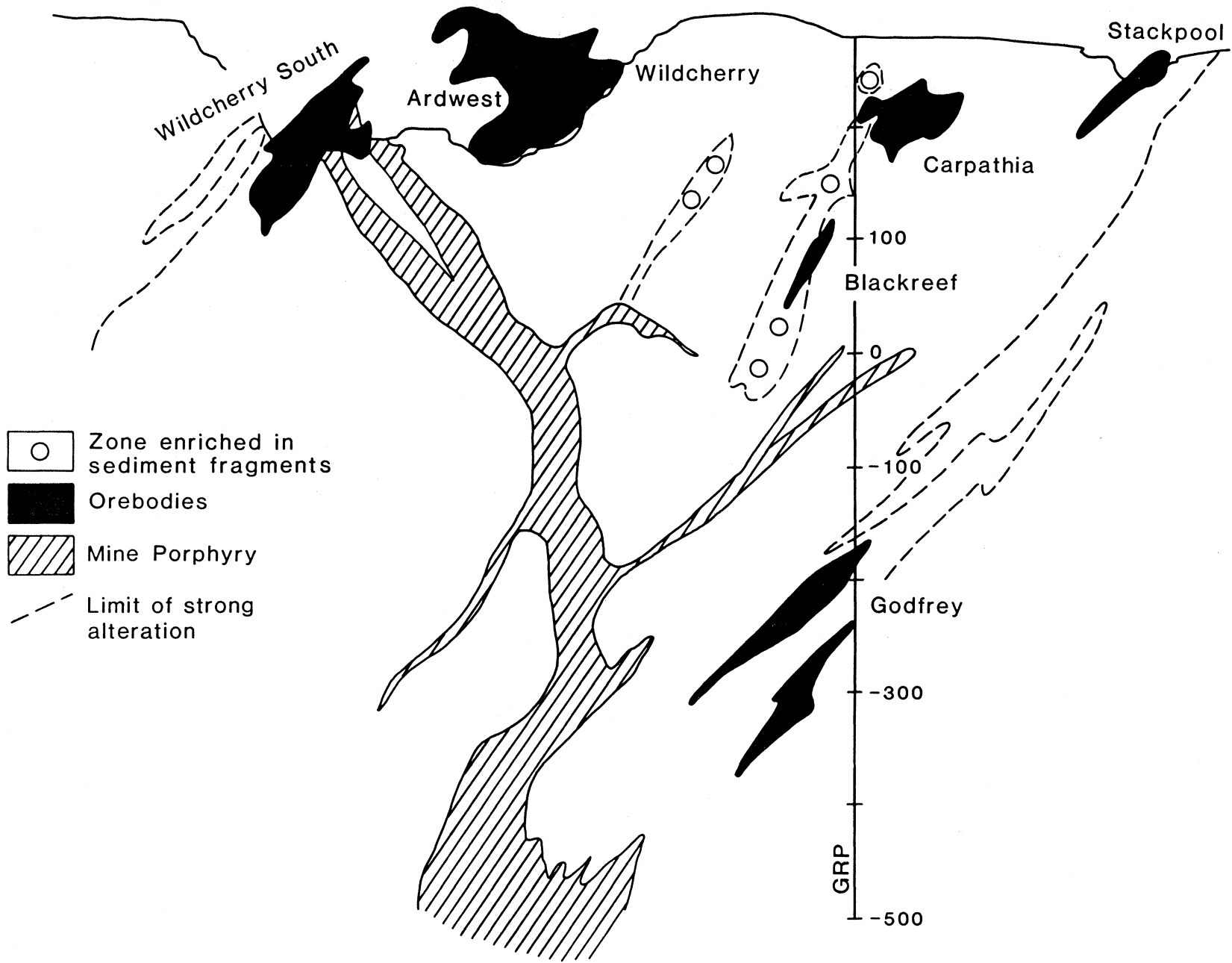


Fig. 4-4 Cross section 3N. This is part of the Carpathia-Blackreef Breccia Pipe. The distribution of Mine porphyry fragments in relation to the two parental dykes indicate a general upwards movement (GRP: Godfrey Reference Plane. Vertical scale in metres).

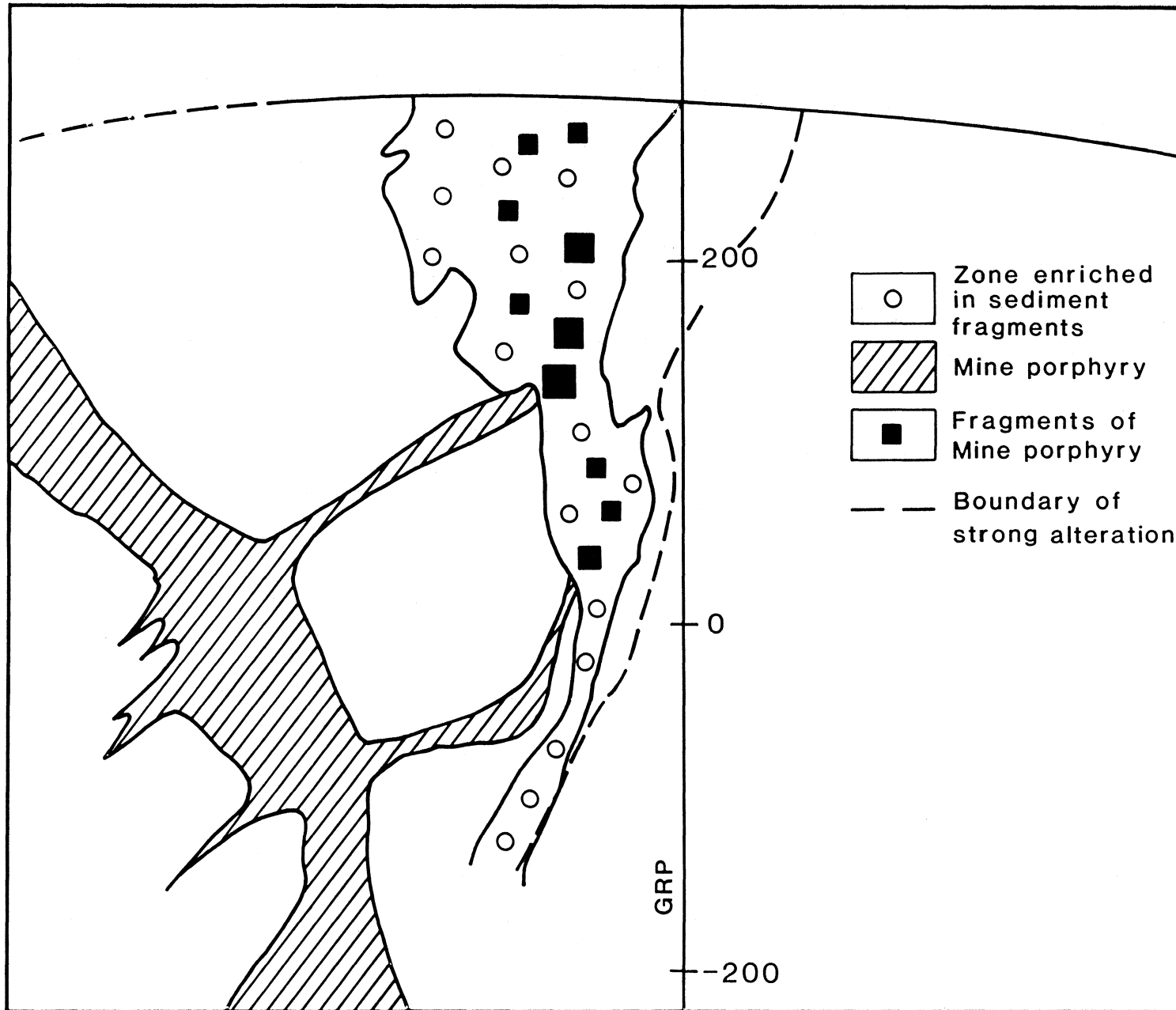


Fig. 4-5 Cross section 2N. The main Mine Porphyry dyke and its small branches were disrupted by the Carpathia-Blackreef Breccia Pipe and the distribution of Mine porphyry fragments indicates an upwards movement in this breccia pipe (GRP. Godfrey Reference Plane. Vertical scale in metres).

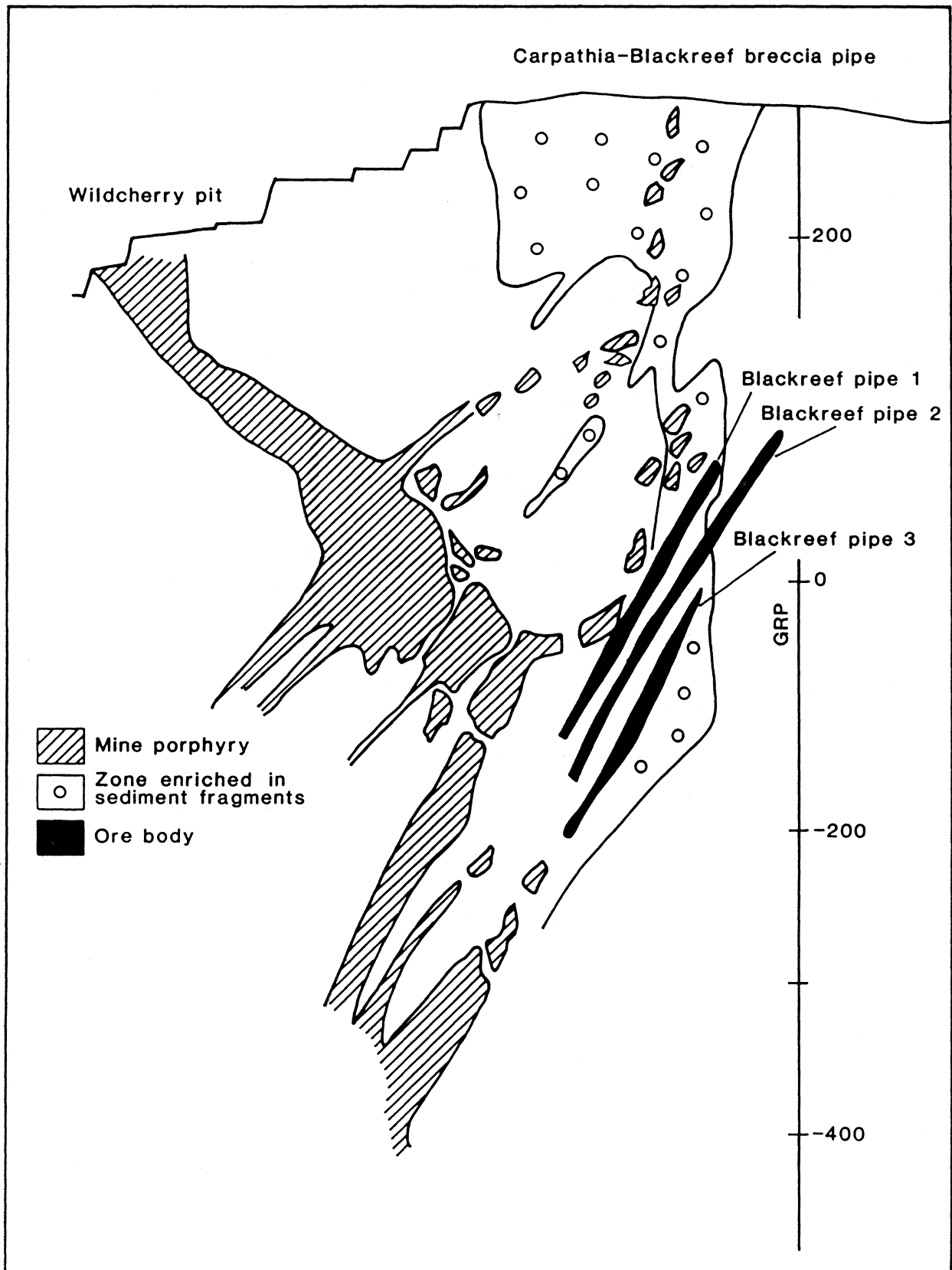


Fig. 4-6 Cross section 0 N. The Carpathia-Blackreef Breccia Pipe and disrupted Mine Porphyry dykes (GRP: Godfrey Reference Plane. Vertical scale in metres).

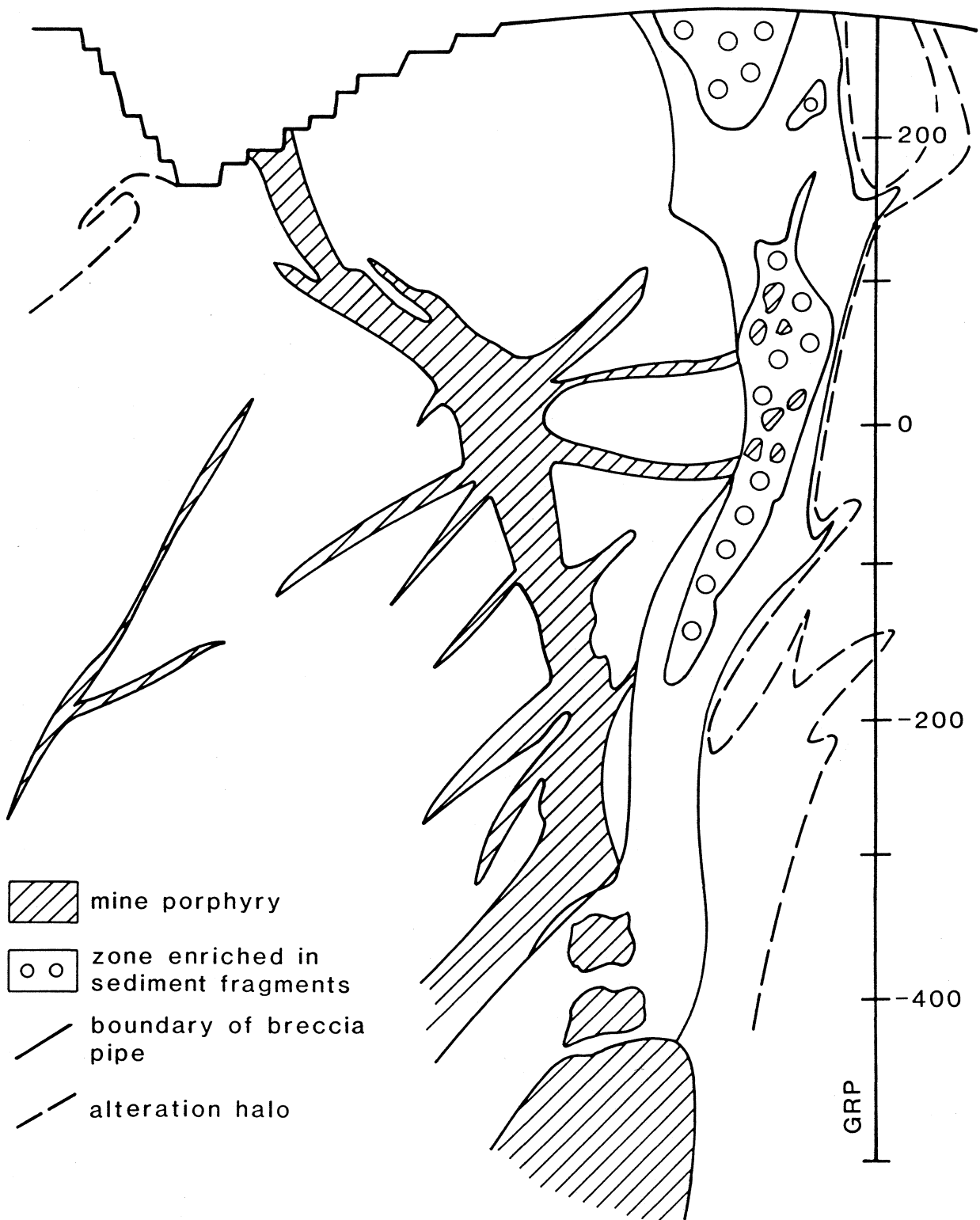


Fig. 4-7 Cross section 4S. Several small Mine Porphyry dykes were disrupted by the Carpathia-Blackreef Breccia Pipe and Mine Porphyry fragments were dislocated upwards. The Godfrey South deposit is the deepest in the Ardlethan Tin Field (GRP: Godfrey Reference Plane. Vertical scale in metres).

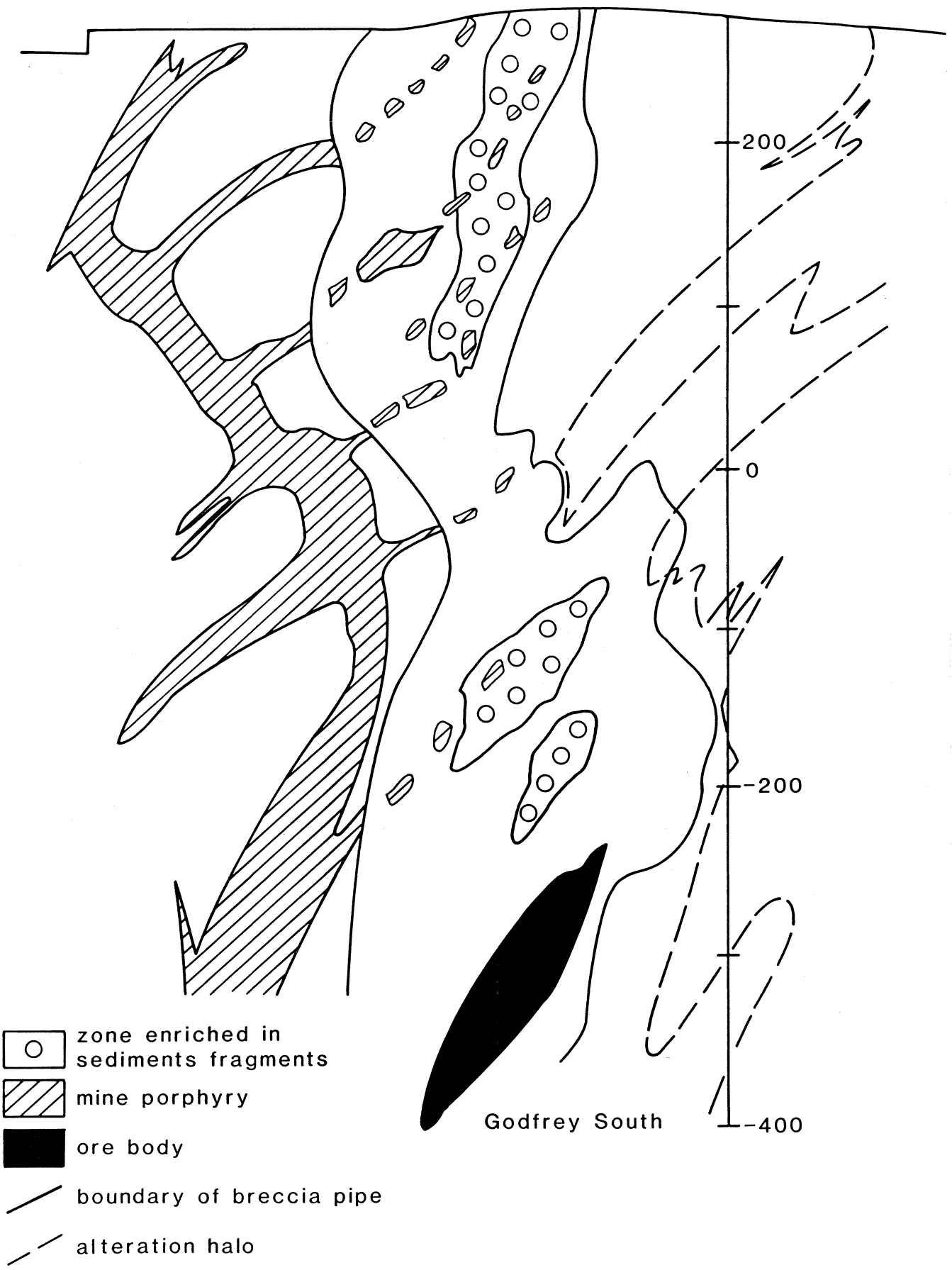
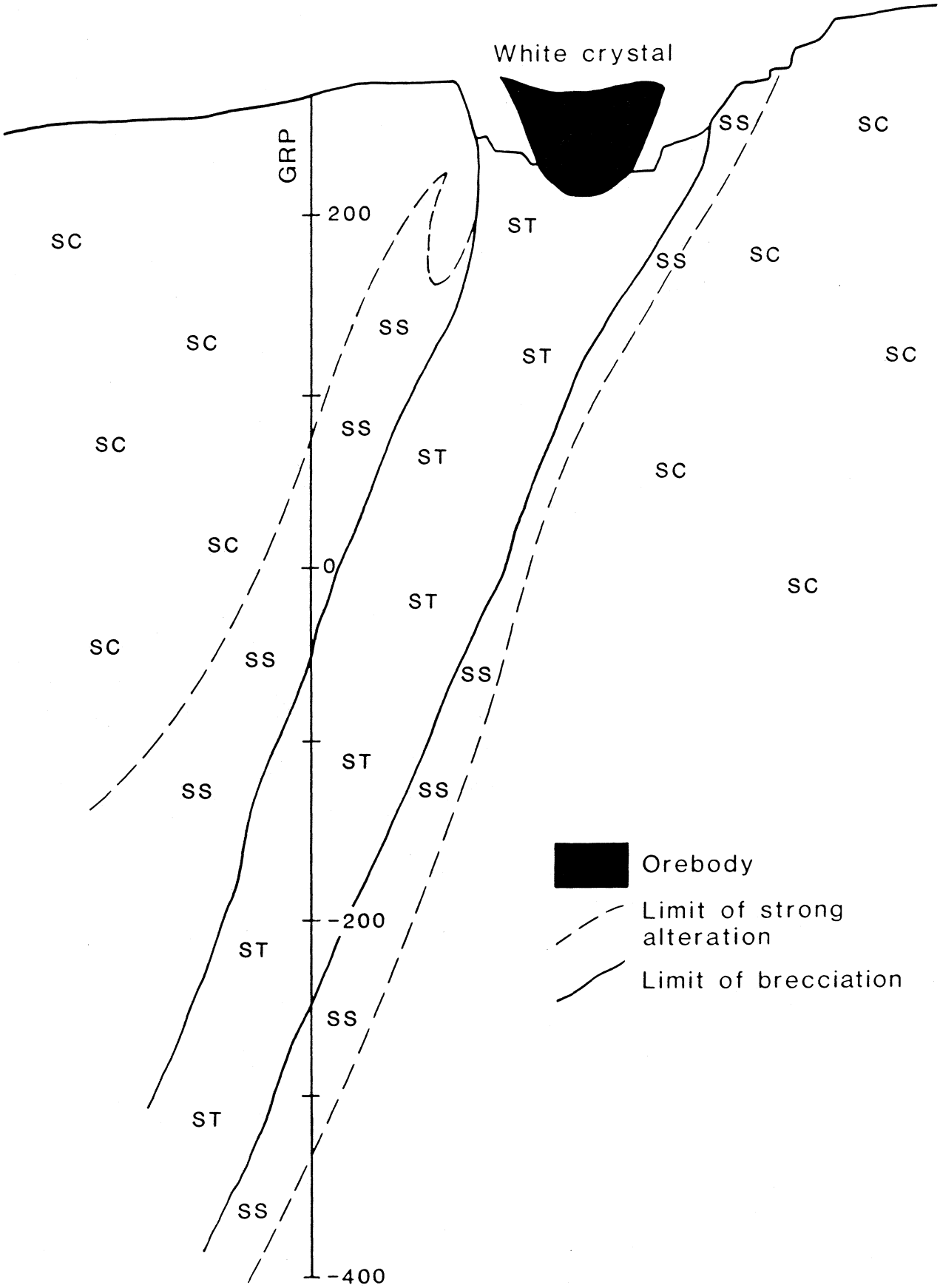


Fig. 4-8 Cross section 24S. The White Crystal Breccia Pipe and its alteration zonations are illustrated. CD refers to Fig. 1-4. (SC: weak sericite and chlorite alteration. SS: strong sericite alteration with siderite. ST: strong sericite, topaz and tourmaline alteration. GRP: Godfrey Reference Plane. Vertical scale in metres).

C

D

White crystal




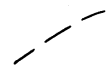

-  Orebody
-  Limit of strong alteration
-  Limit of brecciation

Fig. 4-9 Geological plan at RL 250 m. The Wildcherry, Stackpool, Carpathia and White Crystal deposits occur as a ring of mineralization in the Mine Granite Breccia Pipe. The Carpathia-Blackreef Breccia Pipe has two openings, zones 2 and 3 (GRP: Godfrey Reference Plane).

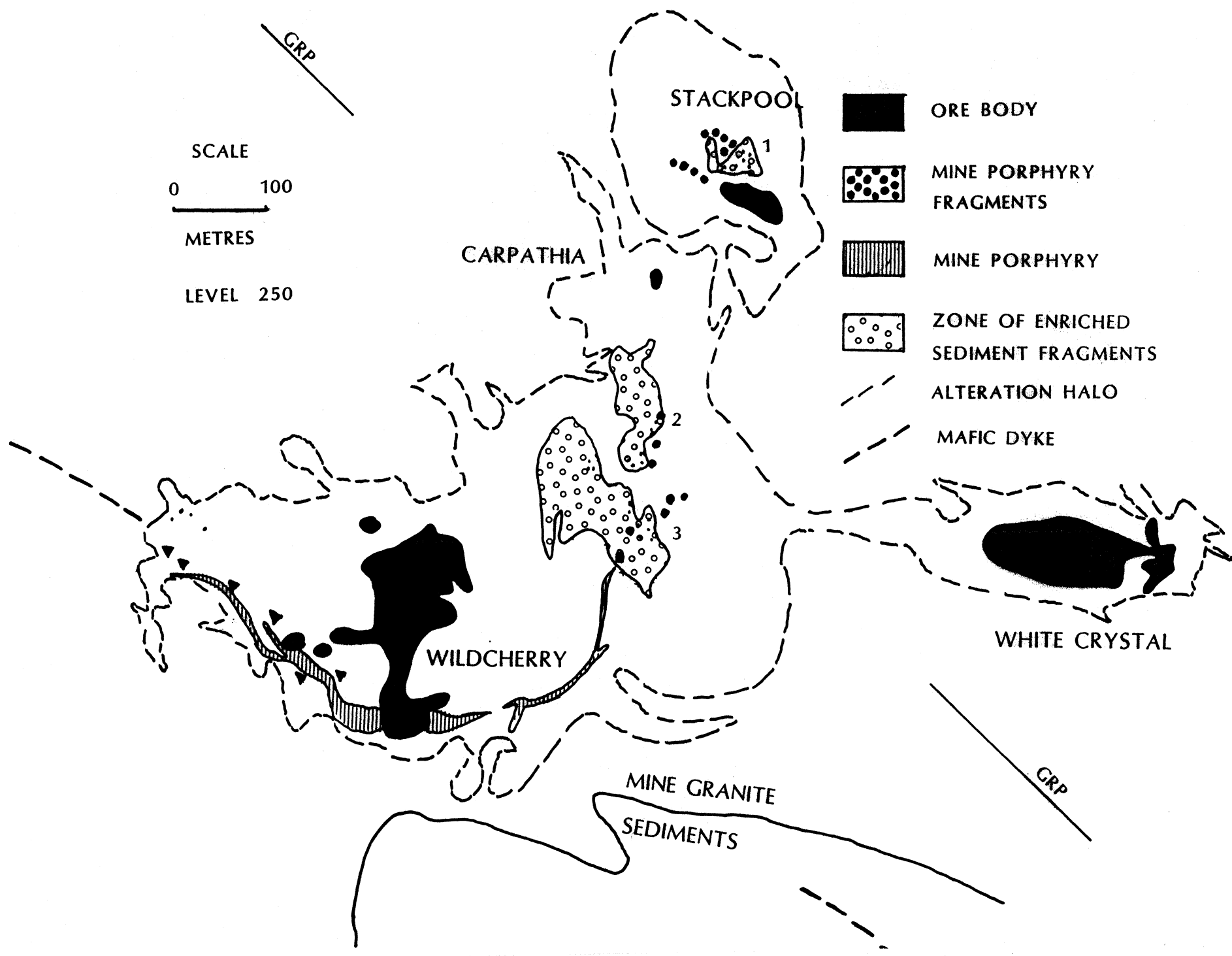
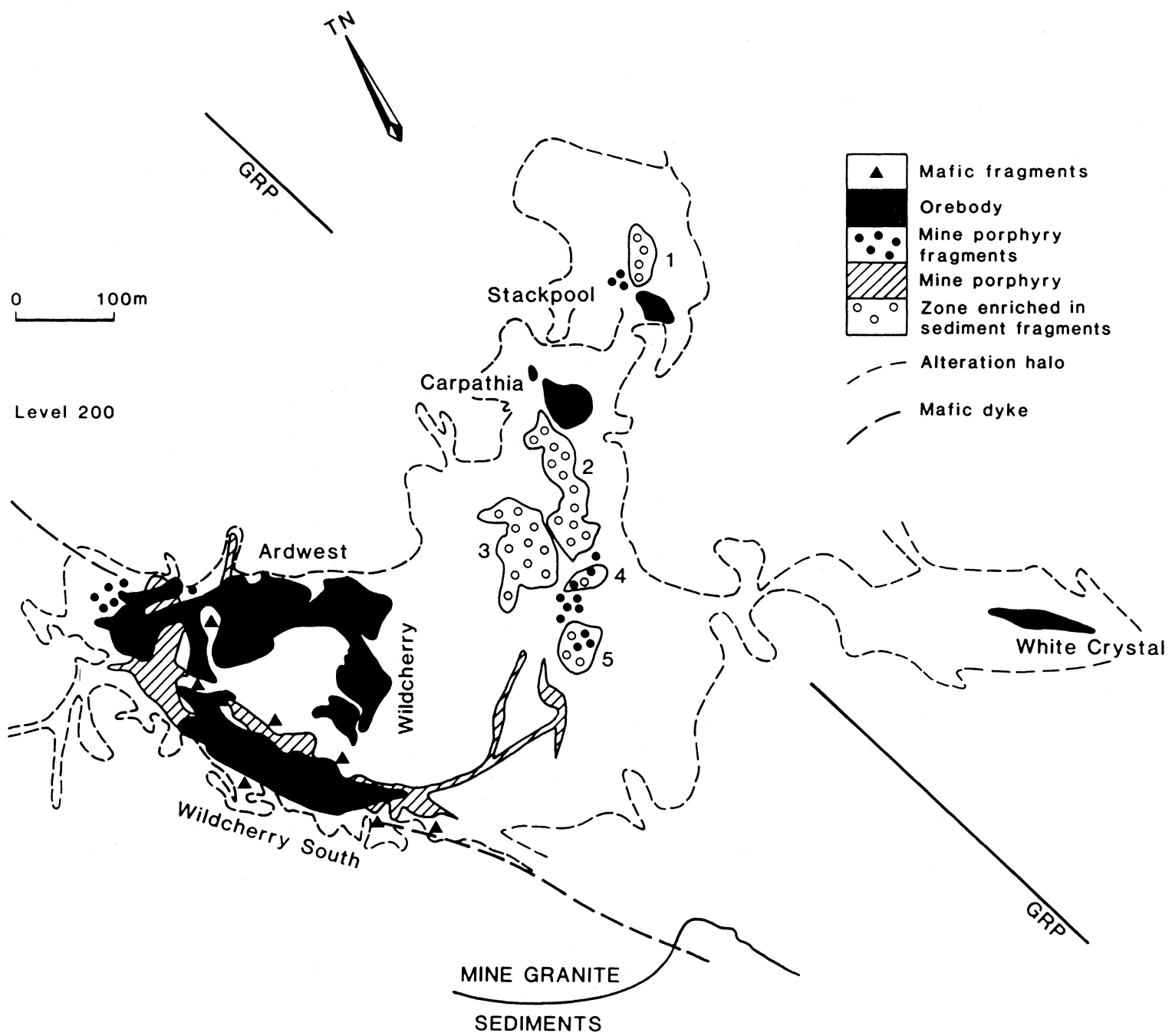


Fig. 4-10 Geological plan at RL 200 m. Two small blind daughter breccia pipes, zones 4 and 5, occur on this plan (GRP: Godfrey Reference Plane).



0 100m

Level 200

- ▲ Mafic fragments
- Orebody
- Mine porphyry fragments
- ▨ Mine porphyry
- Zone enriched in sediment fragments
- - - Alteration halo
- - - Mafic dyke

MINE GRANITE
SEDIMENTS

Fig. 4-11 Geological plan at RL 150 m. Blind daughter breccia pipe zones 4 and 3 join together. Mine Porphyry and mafic fragments occur mainly southwest to the main Mine Porphyry dyke in the Mine Granite Breccia Pipe (GRP: Godfrey Reference Plane).

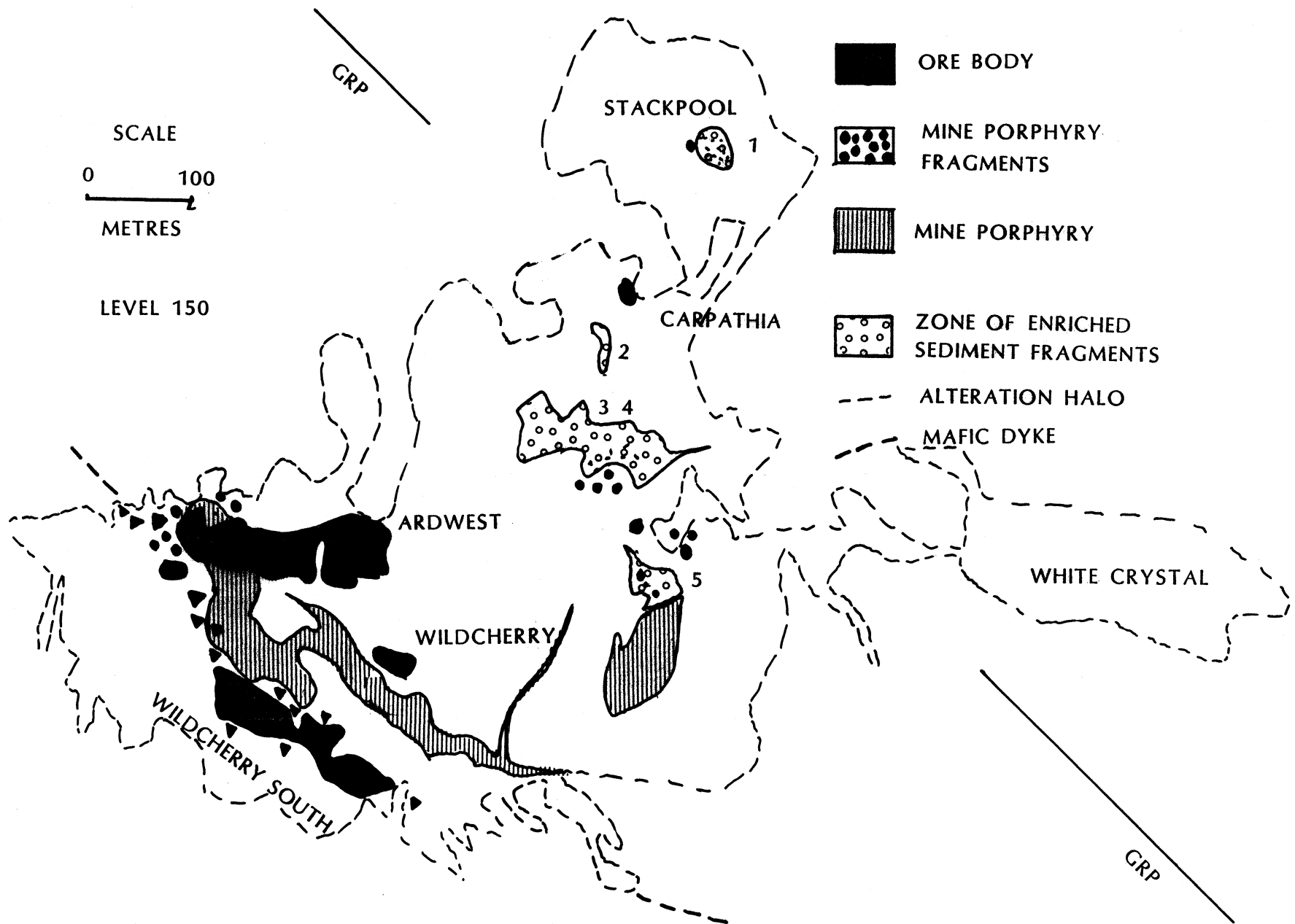


Fig. 4-12 Geological plan at RL 100 m. Zones 3 and 4 of the Carpathia-Blackreef Breccia Pipe are separated. The main Mine Porphyry dyke was penetrated by small secondary brecciated pipes in the Ardwest deposit. This is suggested by the occurrence of Mine porphyry fragments changing from its southwestern side (Fig. 4-10) to northeastern side (GRP: Godfrey Reference Plane).

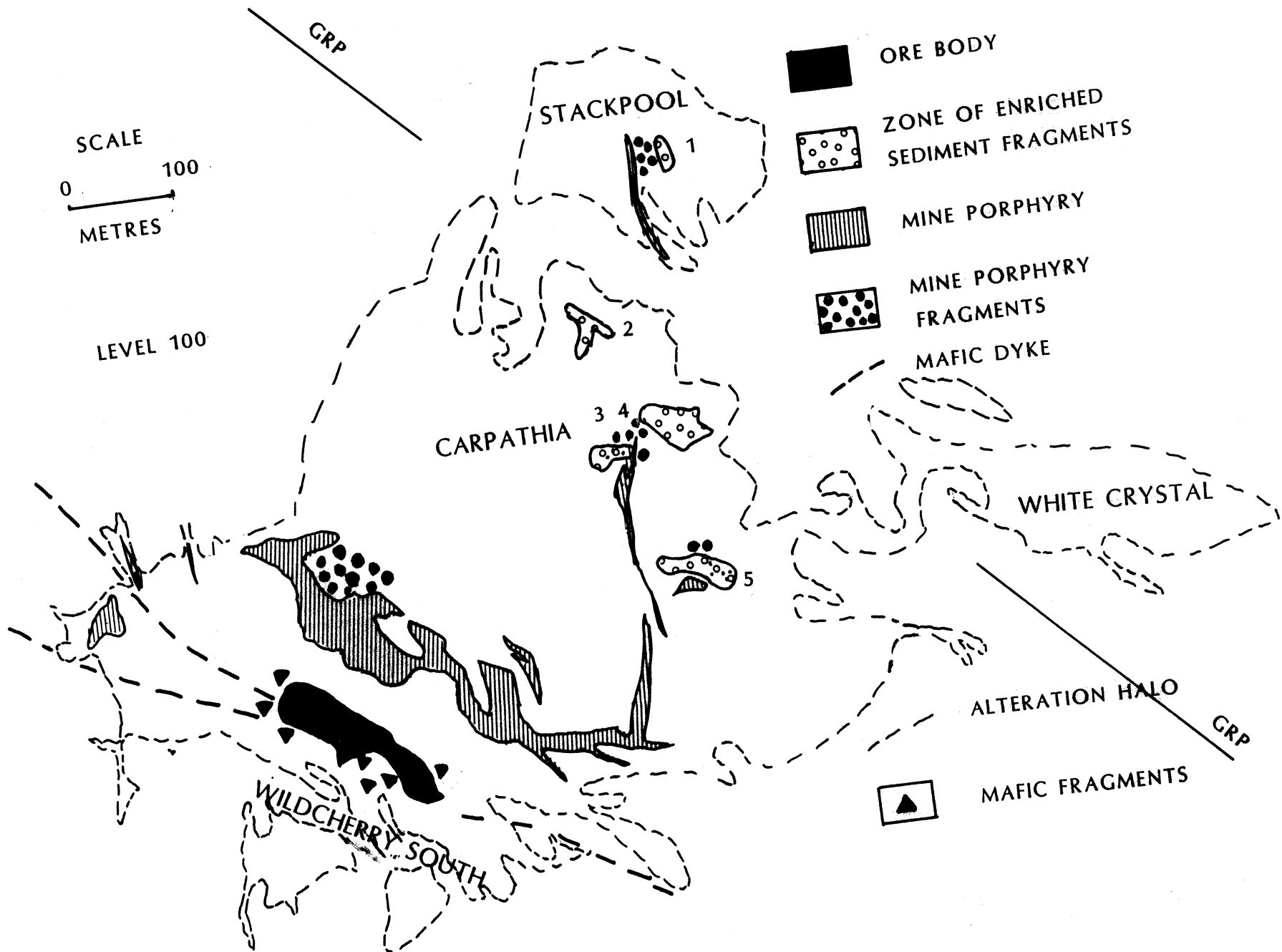







Fig. 4-13 Geological plan at RL 50 m. Another blind daughter breccia pipe, zone 6, occurs on this plan. Zones 3 and 4 join again (GRP: Godfrey Reference Plane).

-  ORE BODY
-  ZONE OF ENRICHED SEDIMENT FRAGMENTS
-  MINE PORPHYRY
-  MINE PORPHYRY FRAGMENTS
-  MAFIC FRAGMENTS

SCALE
0 100
METRES

LEVEL 50

ALTERATION HALO

MAFIC DYKE

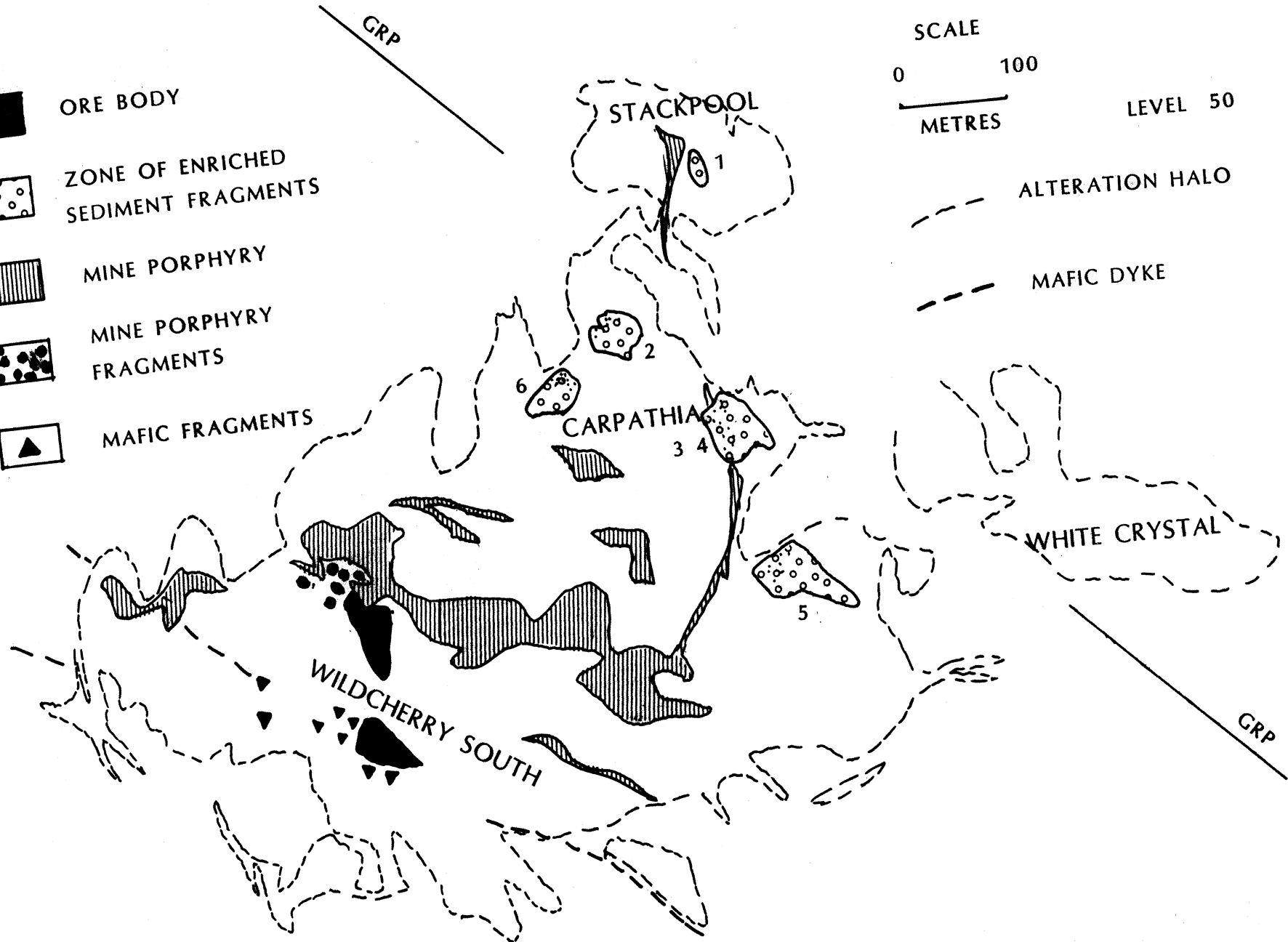


Fig. 4-14 Geological plan at RL 0 m. Blind daughter breccia pipe zone 6 joins zone 2. There are three zones within the Carpathia-Blackreef Breccia Pipe are enriched in sediment fragments on this plan (GRP: Godfrey Reference Plane).



ORE BODY



MINE PORPHYRY



MINE PORPHYRY FRAGMENTS



ZONE OF ENRICHED
SEDIMENT FRAGMENTS



MAFIC FRAGMENTS



MAFIC DYKE



ALTERATION HALO

SCALE

0 100



METRES

LEVEL 0

GRP

GRP

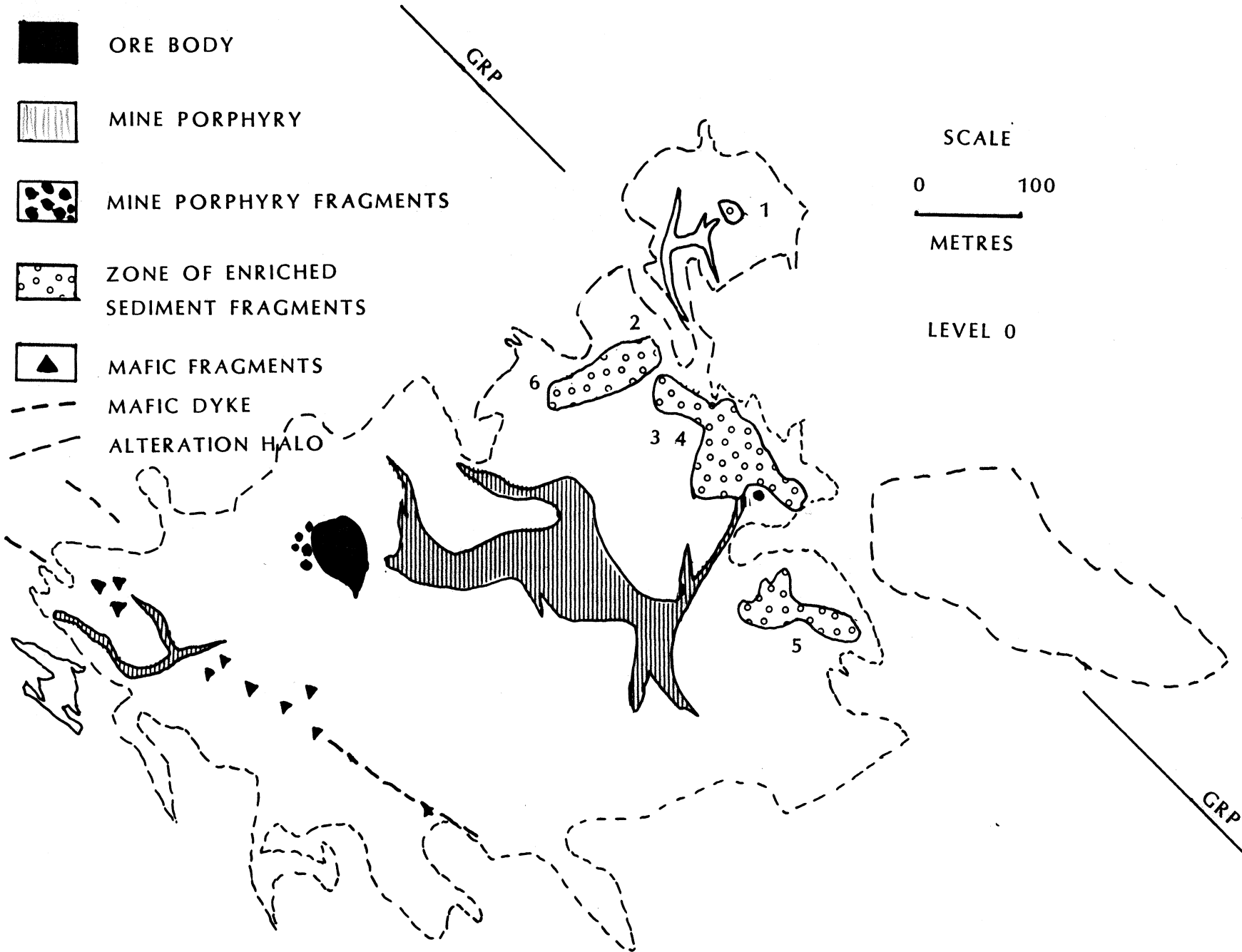


Fig. 4-15 Geological plan at RL -100 m. The Stackpool-Godfrey Breccia Pipe is almost indistinguishable from the Carpathia-Blackreef Breccia Pipe. Some cassiterite mineralization occur in the White Crystal Breccia Pipe (GRP: Godfrey Reference Plane).

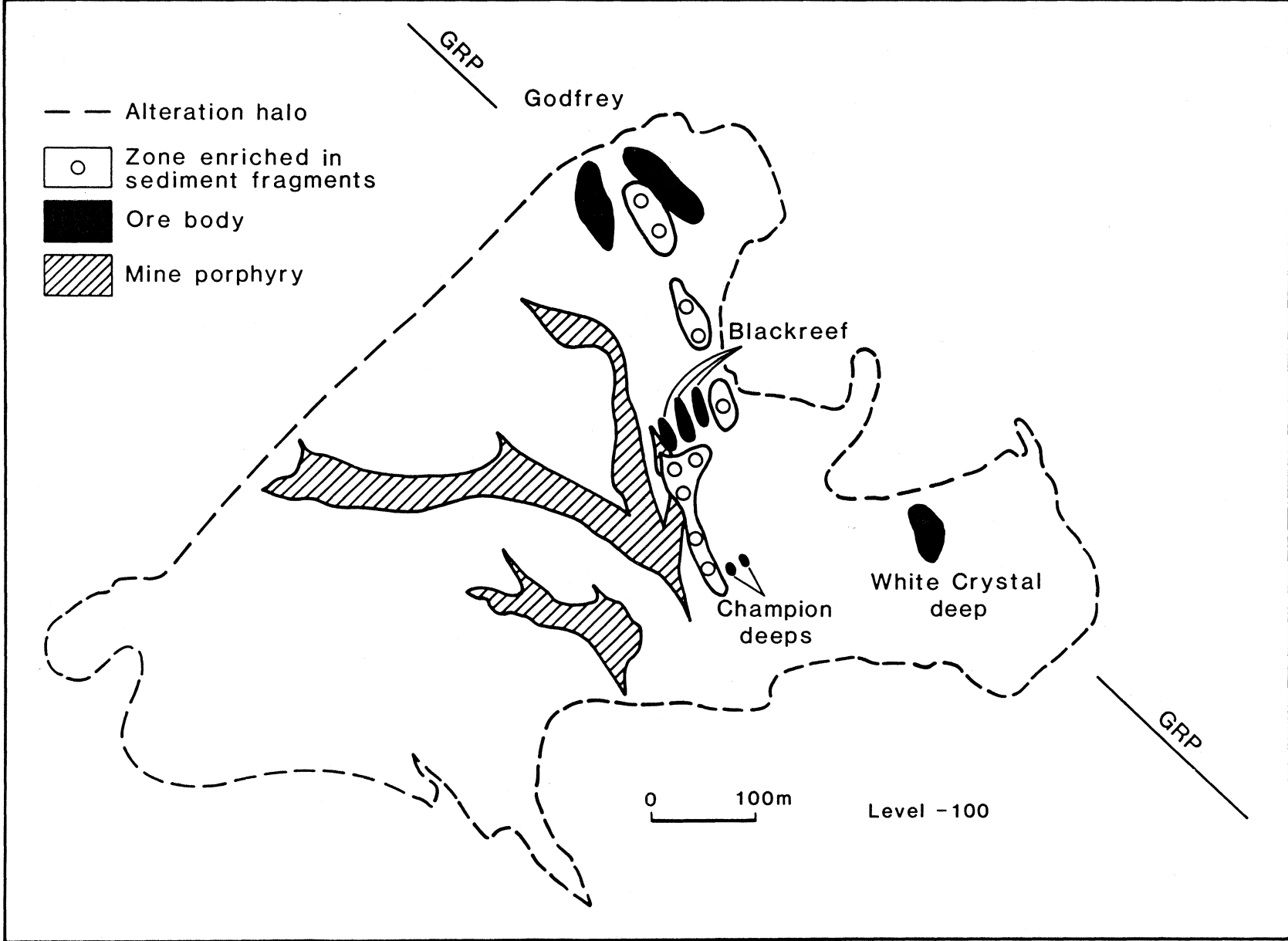


Fig. 4-16 Styles of brecciation and Mineralization in the Mine Granite Breccia Pipe (Cross section 8N). The marginal zones of the Mine Granite Breccia Pipe are mainly fragment supported breccia and host most of the mineralization (GRP: Godfrey Reference Plane).

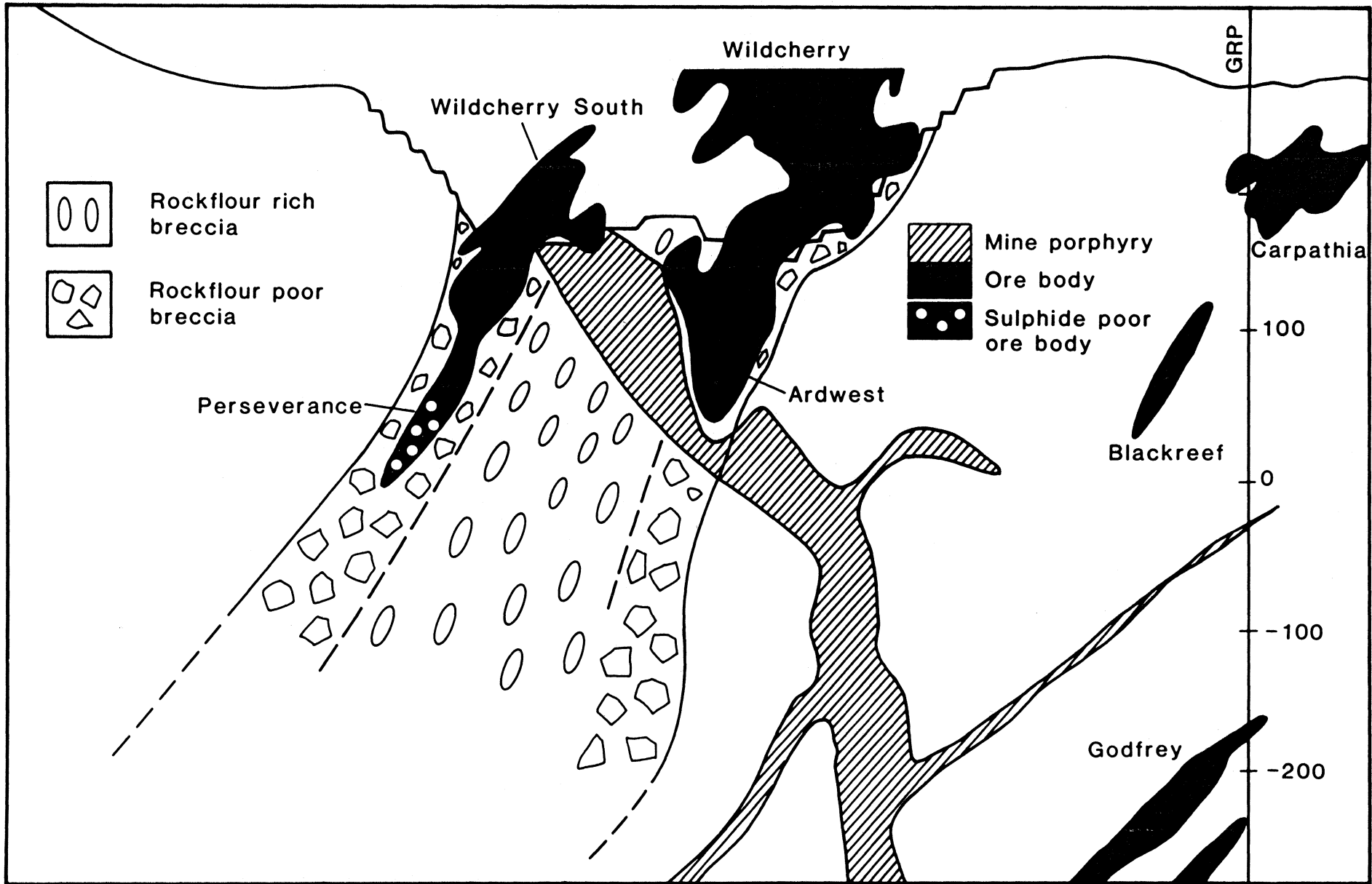


Fig. 4-17 Schematic 3-d diagram of the breccia pipes in the Ardlethan Tin Field. The irregularity and blind daughter Breccia Pipes of the Carpathia-Blackreef Breccia Pipe are outlined (the vertical interval is 50 m).

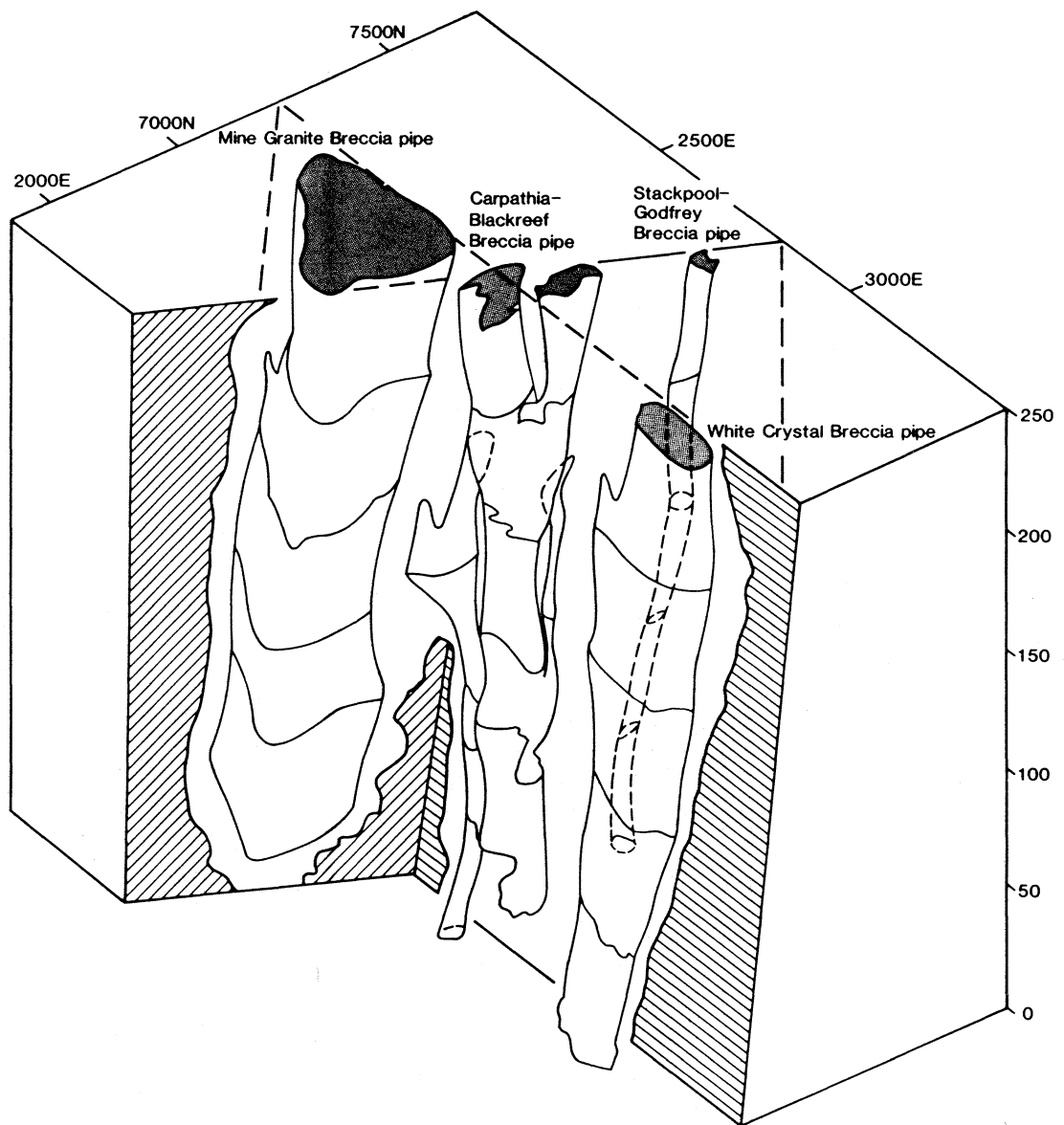


Fig. 4-18 Schematic diagram showing the irregular contact of the Carpathia-Blackreef Breccia Pipe (modified from Clarke, 1979)

SCALE
0 0.7
METRE

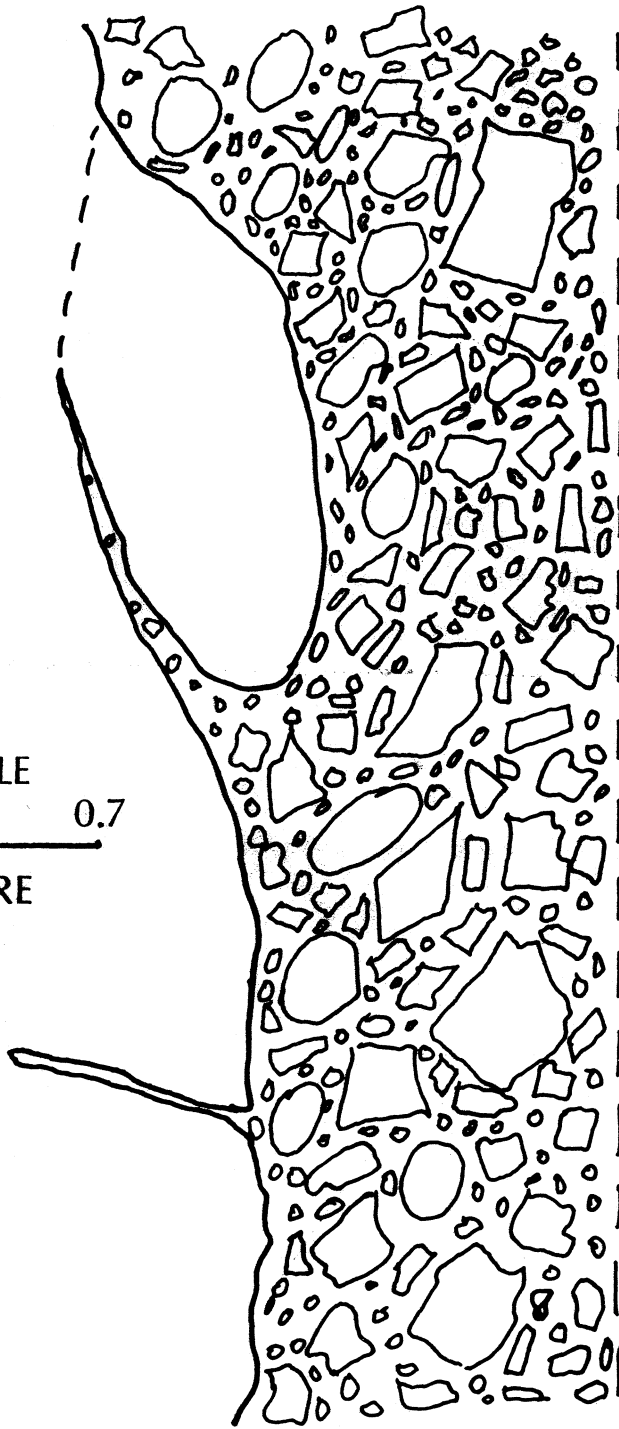


Fig. 4-19 Three major lineaments in the Ardlethan Tin Field. These are indicated by geochemical anomaly, alluvials, creeks and distribution of breccia pipes. 1: the wheat field Breccia Pipe; 2: the Taylor's Hill breccia zone; 3: the Mine Granite Breccia Pipe; 4: the Carpathia-Blackreef Breccia Pipe; 5: the Stackpool-Godfrey Breccia Pipe; 6: the White Crystal Breccia Pipe; 7: Brown's knob; 8 Paterson's knob. The Brown's knob and Paterson's knob could be another two Breccia Pipes similar to the Stackpool-Godfrey Breccia Pipe.

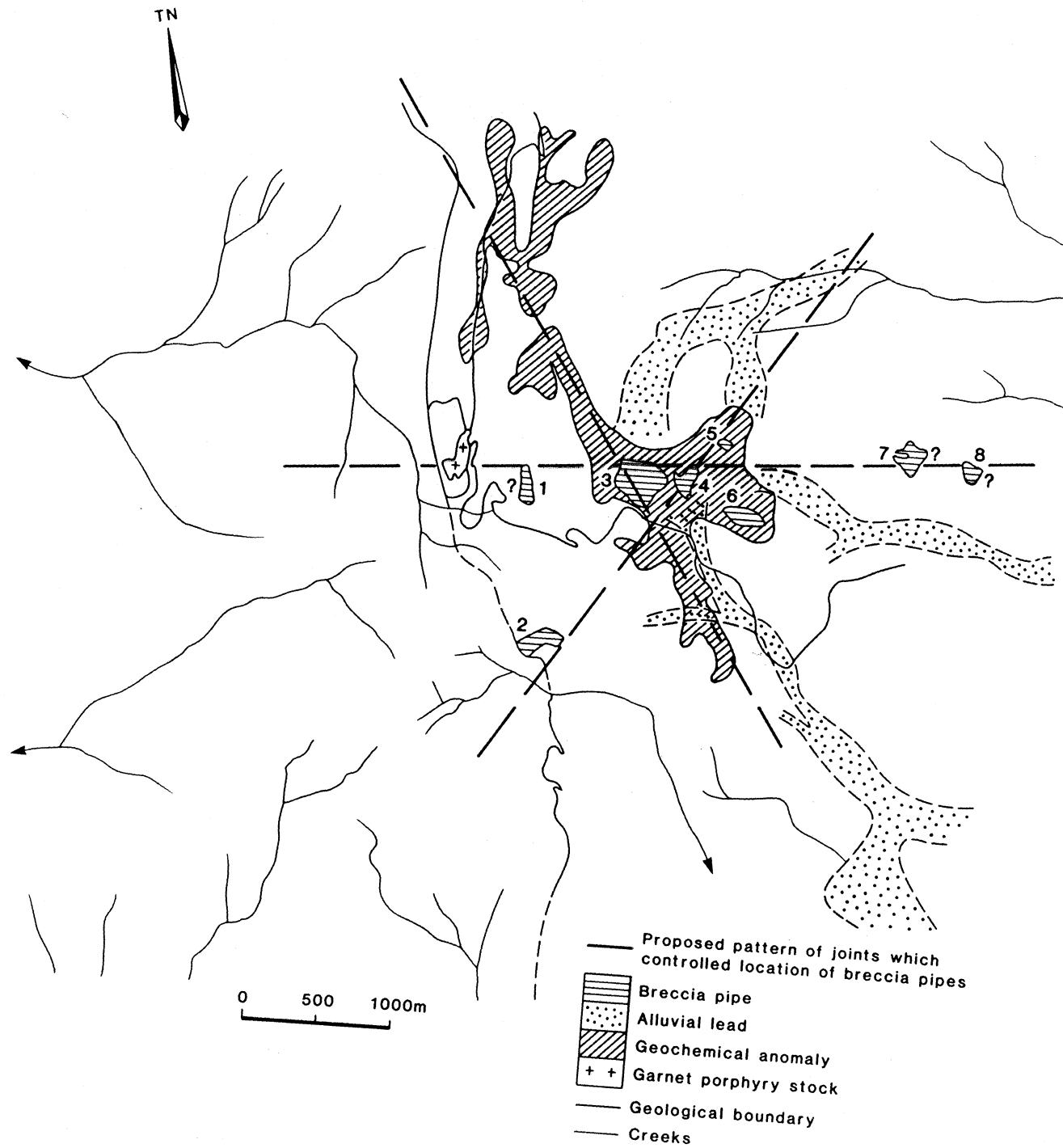


Fig. 4-20, Stereo plot (equal area) of the measured linears in the Ardlethan Mine area.

ROCK UNIT:
LOCATION:
DATE:

MEASURED BY:
EQUAL AREA
EQUAL ANGLE

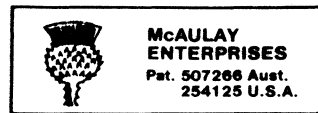
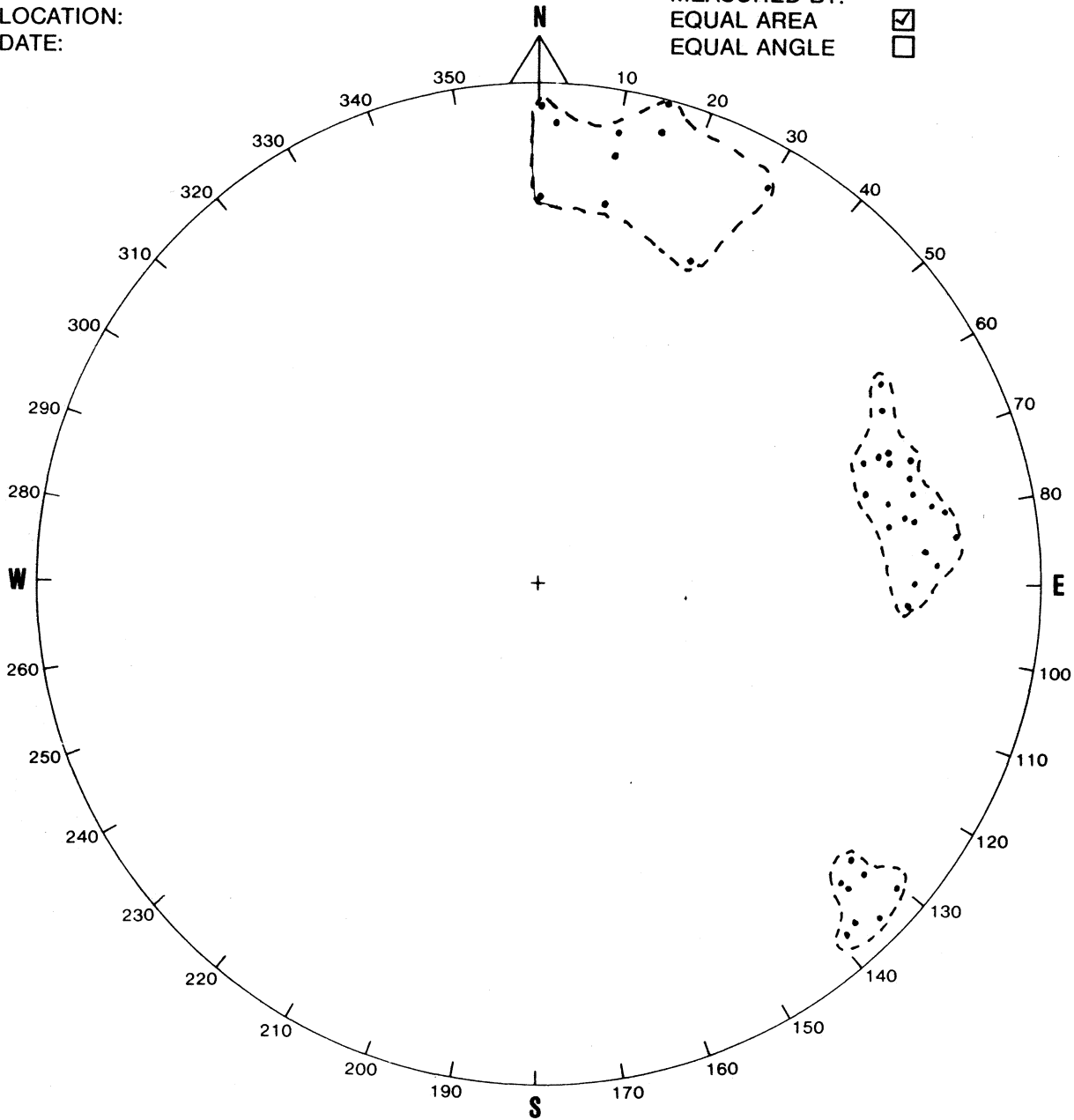
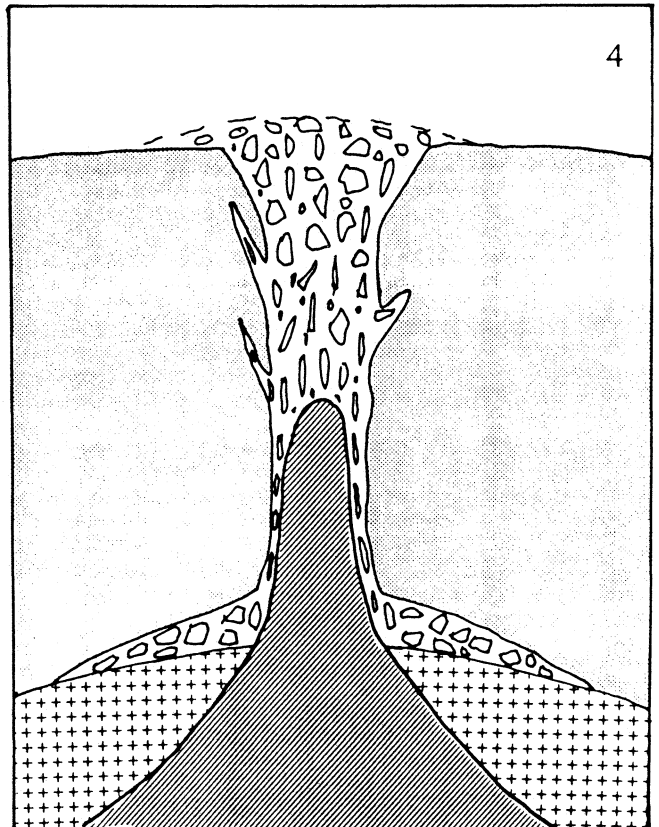
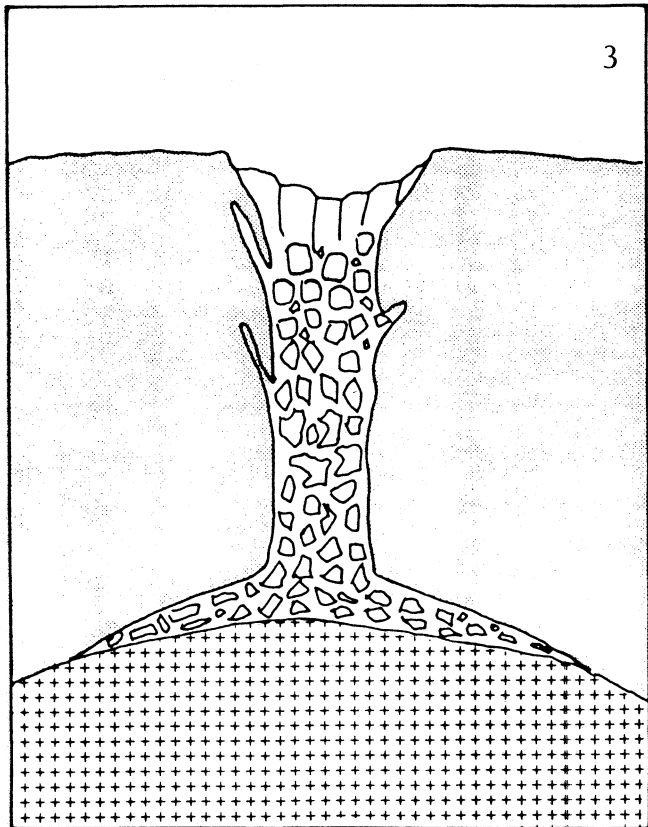
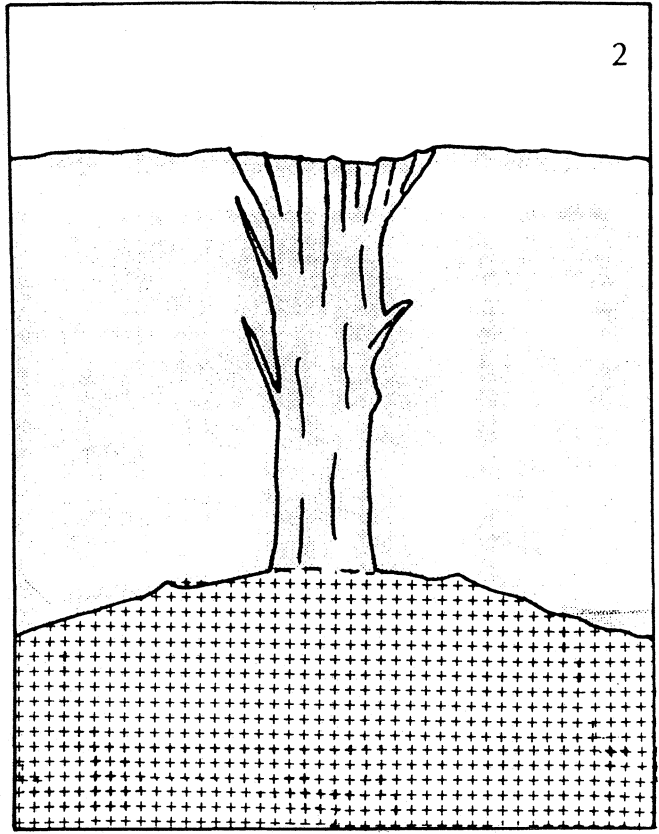
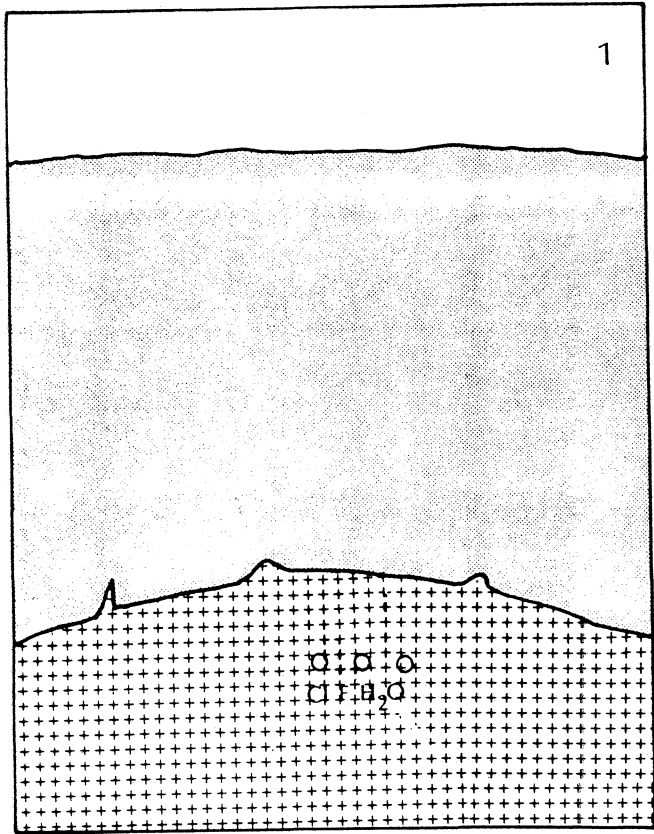


Fig. 4-21 Schematic diagram showing the evolution during Breccia Pipe formation: stage 1: volatile accumulation; stage 2: explosion; stage 3: collapse; stage 4: intrusion.



Chapter 5

MINERALIZATION, HYDROTHERMAL ALTERATION AND PARAGENESIS

Cassiterite mineralization in breccia pipes in the Ardlethan Tin Field is associated with various amounts of rutile, arsenopyrite, wolframite, pyrite, chalcopyrite, sphalerite and galena. Biotite, quartz, tourmaline, topaz, sericite and chlorite occur as hydrothermal alteration products within the ore bodies and their alteration halos. On the basis of their major styles of hydrothermal alteration and associated minerals the ore bodies are classified into the following three groups:

1. The Ardwest group, including the Ardwest, Wildcherry, Wildcherry South, Perseverance and Keogh West deposits;
2. The Carpathia group, including the Carpathia, Stackpool, Blackreef, Godfrey and Godfrey South deposits;
3. The White Crystal deposit.

Each group is hosted by a particular breccia pipe(s) and represents one of the three events of hydrothermal activity which followed the three events of brecciation (see Chapter 4, Ren & Walshe, 1986) in the Ardlethan Tin Field.

5.1 The Ardwest Group of Deposits

5.1.1 General Descriptions

The Ardwest group of deposits is hosted by the Mine Granite Breccia Pipe, including the Wildcherry, Ardwest, Wildcherry South, Perseverance and Keogh West deposits and their extensions. The Wildcherry, Ardwest and Wildcherry South deposits occurred from about 280 m RL (the surface) to 150 m RL (Figs. 1-4 & 4-3). They were the three largest deposits in the Ardlethan Tin Field and accounted for more than 70% of the total tin production. They appear to be the main sources

of the Yithan alluvial deposit, the largest of this type in the Ardlethan Tin Field. The typical mineral assemblage in these deposits is cassiterite+sulphides+tourmaline+quartz+sericite+chlorite. Relicts of biotite and K-feldspar may occur. The Perseverance and Keogh West deposits, occurring between 150 m RL and -100 m RL in the same breccia pipe, are characterized by an assemblage of cassiterite+sulphides+tourmaline+quartz+sericite+siderite.

The grades of the Ardwest group of deposits range from 0.2 to 3.0 wt% Sn with an average of 0.5 wt% Sn. The Wildcherry, Ardwest, Wildcherry South and Perseverance deposits have produced about 50,000 tonnes of tin concentrate. The Keogh West deposit contains approximately 15 tonnes of ore at approximately 0.35 wt% Sn on average.

The Wildcherry deposit occurred along the eastern margin of the Mine Granite Breccia Pipe (Fig. 4-10). It extended vertically from the surface (280 m RL) to about 180 m RL with a length of about 150 m, and a variable width, but generally around 100 m. The ore body narrowed at depth and terminated into a tail-like extension called the Wildcherry pipe (Fig 1-4). Mine Granite fragments were mostly altered to an assemblage of quartz, tourmaline, sericite and/or chlorite. However, relict crystals of K-feldspar, plagioclase and biotite were found in cores of large Mine Granite fragments. Rutile, arsenopyrite, pyrite, chalcopyrite, sphalerite and galena occurred with the cassiterite. Small amounts of fluorite and siderite also occurred in vugs with euhedral, toothy quartz crystals.

The degree of chlorite alteration in the Wildcherry deposit is variable within the deposit. Generally, the inner western rim of the ore body appears strongly chloritized. The bulk chlorite contents on hand specimen scale range from 5% to 25% by volume. Vertically, the upper levels of the ore body, from the surface to RL 200 m, contain more chlorite than at depth (R. Paterson, pers. comm., 1988). Sericite alteration appears to be more strongly correlated to cassiterite mineralization than chlorite alteration. The high-grade zones of cassiterite mineralization in the Wildcherry deposit were strongly sericite altered. Tourmaline and quartz alteration occurs mainly in fractures, veins, and interfragmental open spaces. Rarely pervasive tourmaline alteration occurs. Minor amounts of topaz were recorded during the early mining operation (P. Eadington, pers. comm., 1986).

The Ardwest deposit was located in an elongated zone from the northern end of the Wildcherry deposit to the western corner of the Mine Granite Breccia Pipe, extending about 200 m with a variable width around 70 m extending vertically between 240 m RL and 140 m RL. The ore body had several depth extensions and the major one was called the Ardwest Deep, occurring between 140 m RL and -50 m RL (Fig. 1-4).

Similar to the Wildcherry deposit, chlorite alteration is very intense along the inner rim of the ore body and decreases towards the margins. The high-grade zones of mineralization are again very strongly correlated to pervasive sericite alteration. The major opaque minerals are arsenopyrite, pyrite, chalcopyrite, sphalerite and galena. Small amounts of pyrrhotite, bismuthinite, wolframite and molybdenite have been identified in samples from the Ardwest deposit (Scott, 1980). In the Eastern Extension of the Ardwest deposit, a significant amount of fluorite (2-3%) occurs in late-stage vugs with toothy quartz and cookeite. There are several small secondary breccia pipes characterized by black tourmaline alteration and strong sericite alteration overprinting the main brecciation event and mineralization in the Mine Granite Breccia Pipe (see Chapter 4).

The Wildcherry South deposit forms the hypotenuse of the ore body triangle in the Mine Granite Breccia Pipe (Fig. 4-10). It extends from the southern end of the Wildcherry deposit northwesterly to the western extremity of the Ardwest deposit. Compared to the Wildcherry and Ardwest deposit, the outlines of the Wildcherry South deposit are irregular, particularly along its inner rim. Styles of hydrothermal alteration and mineralization are similar to those of the Wildcherry and Ardwest deposits. The Wildcherry South deposit also has an extension at depth, called the Perseverance deposit, extending from the bottom of the Wildcherry South open pit to about -50 m RL along the hanging wall of the Mine Granite Breccia Pipe (Fig. 4-16). The typical alteration assemblage in the Perseverance deposit is sericite+siderite+tourmaline+quartz. The sericite+siderite alteration occurs within the deposit, the alteration halo and also inside large Mine Granite fragments in strongly quartz-tourmaline altered high-grade zones. The tourmaline+quartz alteration corresponds closely to high-grade cassiterite ore. Opaque minerals in the Perseverance deposit include rutile, wolframite, arsenopyrite, pyrite, chalcopyrite, sphalerite and galena. Large patches of cookeite occur together with siderite and toothy quartz crystals in large vugs formed between angular fragments. The Perseverance deposit shows a marked variation in total sulphide content from 5-10% in its upper levels to less than 1% at its lower termination although the grade of cassiterite does not change significantly (Fig. 4-16).

The Keogh West deposit is the deepest ore body defined in the Mine Granite Breccia Pipe (Fig. 1-4). Diamond drill cores indicate that it is similar to the Perseverance deposit in terms of hydrothermal alteration and mineralization. However, there is not enough information to describe it in more detail.

In general, the styles and degree of hydrothermal alteration in the Mine Granite Breccia Pipe are variable although it appears that zones of strong sericite alteration commonly correspond to high grade ore. The

general alteration assemblage is quartz+tourmaline+sericite/chlorite. The degree of alteration decreases towards the host Mine Granite and towards the centres of large Mine Granite fragments.

Opaque ore minerals occur mostly in the interfragmental spaces in the zones of fragment-supported breccia. It is common to see layer textures from cassiterite barren cores inside large fragments, which are surrounded by a layer of milky quartz and tourmaline and then a layer of clear quartz and sulphides. Large vugs are filled by toothy quartz, fluorite, cookeite and possibly siderite. Cassiterite occur mainly with the milky quartz and tourmaline. In the highly altered zones these layers may not be apparent, however, weakly altered barren cores are commonly preserved inside large Mine Granite fragments. This indicates that cassiterite mineralization and associated hydrothermal alteration resulted from hydrothermal events postdating the breccia pipe formation.

5.1.2 Hydrothermal Alteration

The styles of hydrothermal alteration of the Mine Granite Breccia Pipe can be classified into the following four assemblages

1. *Biotite*
2. *Sericite*
3. *Chlorite*
4. *Tourmaline-quartz*

according to the distinctive minerals in each assemblage.

The zone of biotite alteration is restricted to the deepest part of the Mine Granite Breccia Pipe (Fig. 5-1) below 0 m RL. Above the biotite alteration zone there is a complex distribution of sericite alteration and chlorite alteration within and around the ore bodies. Broadly chlorite is more abundant in the upper level of the Mine Granite Breccia Pipe in the Ardwest, Wildcherry and Wildcherry South deposits particularly on the inner margins of the ore bodies. Strong chlorite alteration is more confined at depth forming alteration envelopes around Mine Porphyry dykes (Fig. 5-1). Sericite with siderite forms the main pervasive alteration in association with mineralization at depth of the Mine Granite Breccia Pipe. This leads to a subdivision of upper and lower zones of mineralization in the Mine Granite Breccia Pipe as following

1. The upper zone of mineralization, characterized by strong sericite and chlorite alteration: including the Wildcherry, Ardwest and Wildcherry South Deposits;

2. The lower zone of mineralization characterized by strong

sericite alteration with siderite: including the Perseverance, Ardwest depth extensions, Wildcherry pipe and Keogh West deposits.

Weak sericite and chlorite alteration occurs in the marginal zones in the Mine Granite around the Mine Granite Breccia Pipe (Fig.5-1). Tourmaline and quartz alteration occurs in association with all of the known mineralization.

Biotite Alteration

The zone of biotite alteration occurs at depth in the Mine Granite Breccia Pipe below the lower zone of mineralization (Figs. 4-3 & 5-1). No secondary biotite was found in other breccia pipes in the field.

Under the microscope, crystals of secondary biotite are brown or green in colour and mostly very fine grained (0.001 to 0.1 mm in size), occurring as clusters around primary minerals of K-feldspar, plagioclase or biotite. Clusters of relatively large crystals (up to 2 mm in size) of radiating secondary biotite may occur in open spaces. Mineral debris other than quartz in the rock flour-dominated zone may be rimmed by secondary biotite (Plate 4-4).

Biotite alteration, superficial, may appear to be pervasive, but is generally not very intense. The highest contents of secondary biotite rarely exceed 5% by volume. Some samples from -100 to -400 m RL in the Mine Granite Breccia Pipe contain fresh plagioclase, K-feldspar and biotite with minor fine secondary biotite crystals along mineral boundaries.

Textures, such as biotite altering rock flour-rich breccia, coarse flakes of secondary biotite infill of open spaces and fractures, and the strict occurrence of secondary biotite within the Mine Granite Breccia Pipe, indicate that the biotite alteration cannot be earlier than the formation of the Mine Granite Breccia Pipe. However, as only the primary minerals were replaced or rimmed by secondary biotite, biotite alteration was probably the earliest major alteration in the Mine Granite Breccia Pipe.

Sericite Alteration

Sericite alteration is widespread within the Mine Granite Breccia Pipe and its alteration halo. In the upper levels of the Wildcherry, Ardwest and Wildcherry South deposits, very intense sericite alteration occurs in several discrete zones corresponding to the high grade portions of the ore bodies. Sericite abundance decreases towards the central core of

the Mine Granite Breccia Pipe. Outside the margins of the breccia pipe, the abundance of sericite also decreases gradually to a zone of weak sericite+chlorite alteration in the host Mine Granite. As mentioned above, intense sericite alteration occurs in the lower zone of mineralization in the Mine Granite breccia pipe. A limited amount of sericite occurs below the secondary biotite line coexisting with secondary biotite (Fig. 5-1).

Samples from the Perseverance deposit and its alteration halo suggest that the sericite alteration over prints the biotite alteration. Sericite pervasively replaces biotite, plagioclase and K-feldspar crystals. Sericite crystals after plagioclase form clusters of fine flakes only distinguishable under the microscope. Those formed after K-feldspar crystals are generally much smaller in size than those after plagioclase crystals. Systematic sampling of rocks with varying degrees of sericite alteration indicates that sericite replaces firstly biotite, then primary K-feldspar and plagioclase crystals along mineral margins or microfractures. With increased degrees of sericite alteration primary minerals are replaced completely. Rarely, relicts of secondary biotite flakes were found within clusters of sericite ghosting K-feldspar crystals. Primary biotite crystals with partial rims of muscovite are common in the relatively weakly altered samples. A gradual transition from primary biotite crystals to large flakes of muscovite was observed, indicating that at least some of the coarse muscovite was formed by replacement of primary biotite.

Small amounts of siderite (generally between 0.5 to 3% by volume), occurring as fine crystals are closely associated with sericite or as relatively large crystals inside fractures or open spaces in zones of intense sericite alteration. Supergene oxidation of the siderite-bearing rock results in a reddish brown colouration which is a distinctive feature of the sericite altered rocks in the field.

Chlorite Alteration

The main zone of strong chlorite alteration in the Mine Granite Breccia Pipe extends from the surface exposure to about -400 m RL. It covers most of the inner parts of the Wildcherry, Ardwest and Wildcherry South deposits at the surface but is confined to very narrow zones along the contacts of the Mine Porphyry dykes at depth. This spatial distribution is also shown by the strong chlorite alteration along the contacts of other Mine Porphyry dykes in the Ardlethan Tin Mine area (Fig. 5-1). The boundaries between zones of sericite alteration and chlorite alteration are always irregular. There is no correlation between the intensity of chlorite alteration and cassiterite mineralization. Furthermore, the intensely chloritized central zone of the Mine Granite Breccia Pipe is not mineralized.

Under the microscope, the strongly chloritized rocks show chloritization to form at its most an assemblage of chlorite+quartz with few relicts of primary minerals. Relicts of fine flakes of sericite, however, were found in chloritized samples, suggesting that the strong chlorite alteration occurred after the sericite alteration and mineralization. The commonly observed texture that chlorite fills microfractures in tourmaline crystals supports this interpretation because tourmaline deposition was directly associated with cassiterite mineralization elsewhere in the Ardlethan Tin Field.

Minor chlorite occurs at the top of the Perseverance deposit and the outer margins of the alteration halo. Chlorite rims deeply sericitized plagioclase or K-feldspar crystals. Commonly relicts of primary biotite with thin rims of sericite and thick rims of chlorite were seen, illustrating that the alteration process was from biotite to sericite and then to chlorite (Plate 5-1).

Samples from the strongly chlorite altered zones along the margins of the Mine Porphyry dykes are similar to those from the surface exposures inside the main open pit. They have an assemblage of chlorite and quartz with small amounts of accessory minerals, and relicts of pre-existing minerals.

In summary, the textures observed support an interpretation that the chlorite alteration in the Mine Granite Breccia Pipe overprints the sericite alteration and cassiterite mineralization. The spatial correlation between intense chlorite alteration and Mine Porphyry dykes suggests that chlorite alteration may have followed the contact of the Mine Porphyry dykes instead of the breccia pipe conduits.

Tourmaline and Quartz Alteration

Tourmaline and quartz alteration occurs widely in the Mine Granite Breccia Pipe but is concentrated in zones of high-grade mineralization. The tourmaline in the Mine Granite Breccia Pipe may be classified into three types: patchy tourmaline, granular tourmaline and acute tourmaline.

Patchy tourmaline occurs in veins in some large Mine Granite fragments. Patchy tourmaline bearing fractures and veins also occur in the nonbrecciated Mine Granite in the mine area with spatial correlation with the occurrence of microgranite dykes. Under the microscope, patchy tourmaline forms brown coloured patches, up to several centimetres in size, similar to tourmaline in the quartz-tourmaline nodules in the Ardlethan Granite. The length/width ratios of patchy tourmaline are about unity.

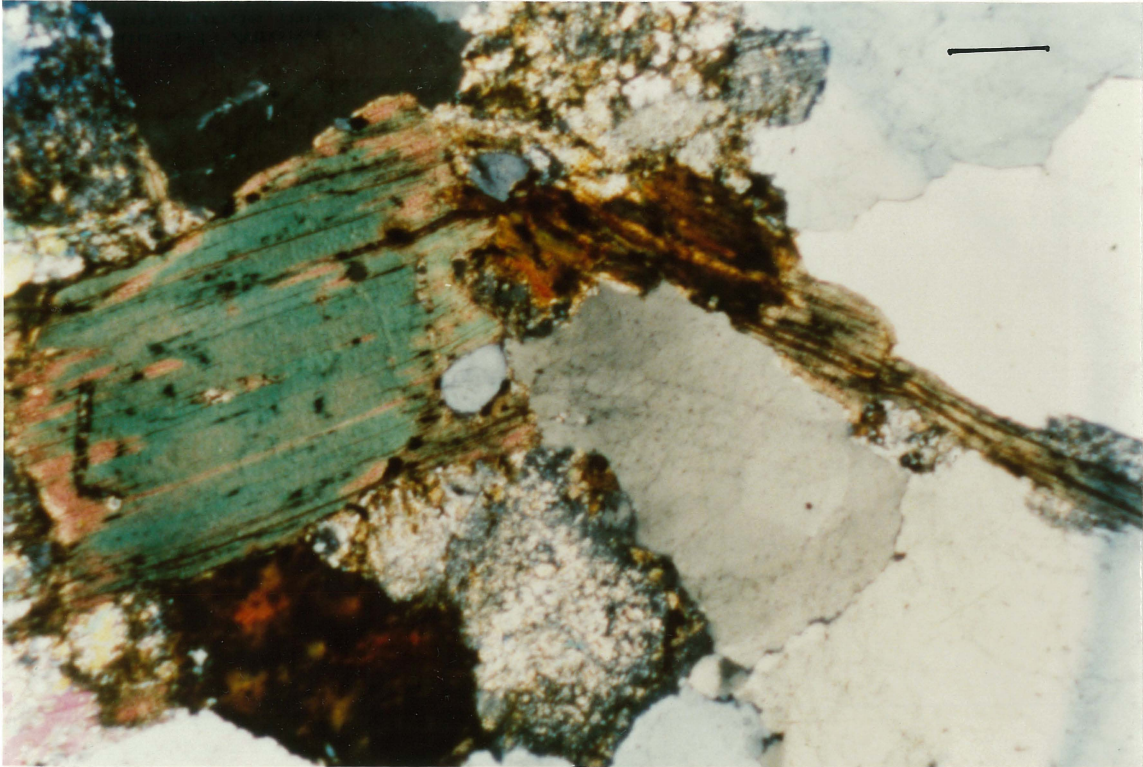


Plate 5-1: Altered Mine Granite. A primary biotite (green) crystal has thin discontinuous muscovite and chlorite rims. Sericite altered plagioclase (top left corner) and K-feldspar (central top and central bottom are partially chloritized (From sample RD21, scale bar=1mm).

Granular tourmaline occurs in the Wildcherry, Ardwest and Wildcherry South deposits and their extensions at depth in association with cassiterite and sulphide mineralization. Granular tourmaline is black or grey in colour and has length/width ratios between 1.5 and 3. It predominantly occurs as interfragmental, open-space infill with milky quartz and cassiterite closely rimming sericite-altered Mine Granite fragments. Semipervasive granular tourmaline and milky quartz occurs in the Perseverance deposit. The cassiterite grade is strongly correlated to the abundances of granular tourmaline in the Wildcherry, Ardwest and Wildcherry South deposits and their extensions at depth.

Acute tourmaline occurs in the small secondary breccia pipes in the Ardwest deposit. Its colour is usually dark black. Crystals of acute tourmaline are commonly with length/width ratios between 2 and 5. It

occurs with cassiterite, arsenopyrite, wolframite, and other sulphide minerals. Pure blocks of acute tourmaline up to several centimetres in size are common in the small secondary breccia pipes. They can rim Mine Granite and Mine Porphyry fragments, partially or completely, replace pre-existing minerals or selectively replace feldspars.

These three types of tourmaline represent three generations of alteration, namely pre-brecciation, post-brecciation and a late overprint on the main brecciation. Veins filled by patchy tourmaline and quartz within Mine Granite fragments in the Mine Granite Breccia Pipe always terminate at fragment boundaries, indicating that they are pre-brecciation. Their spatial correlation with microgranite dykes indicate that patchy tourmaline formation maybe part of the contact alteration of microgranite dykes, similar to that which occurs at the contact of the Ardlethan Granite. Granular tourmaline, occurring with quartz, cassiterite and sulphides, must postdate the main brecciation of the Mine Granite Breccia Pipe. As acute tourmaline occurs in the small secondary breccia pipes in the Ardwest deposit, it is clearly later again. However, with all the information available it is not possible to conclude whether the three types of tourmaline in the Mine Granite Breccia Pipe represent three discontinuous hydrothermal events or one evolving hydrothermal event.

Tourmaline has a complex relationship with other styles of alteration. In the alteration halo of the Perseverance deposit, tourmaline and sericite occur in the following relationships: tourmaline crystals penetrating through sericite-altered K-feldspar or plagioclase; sericite flakes rimming granular tourmaline crystals, and sericite growing in microfractures inside tourmaline crystals. Tourmaline also selectively replaces K-feldspar megacrysts, partially or completely, in intense sericite altered rocks. These complex and somewhat contradictory textural relationships are interpreted to imply contemporaneous tourmaline and sericite alteration although sericite alteration occurs as pervasive alteration of Mine Granite fragments, while tourmaline (\pm quartz) is more related to open spaces.

Characteristics of Quartz

In addition to the tourmaline association classified above, abundant quartz occurs in association with the cassiterite and sulphide mineralization in the Ardlethan Tin Field. There are three types of quartz, namely, milky quartz, clear quartz, and toothy quartz.

Milky quartz is the earliest open space infill quartz in association with tourmaline rimming fragments. It is characterized by its milky white colour and commonly forms massive patches without apparent crystal

boundaries. Microscopically, the milky quartz crystals are full of microfractures (Eadington & Paterson, 1984) and fluid inclusions. Milky quartz is almost always associated with tourmaline and can be associated with cassiterite, wolframite and arsenopyrite may occur in association with milky quartz.

Clear quartz forms open space infill after milky quartz. Clear quartz crystals are generally better crystallized than milky quartz. Crystal boundaries can be seen and most clear quartz crystals are subhedral to euhedral, although their roots may be massive. There are no distinct boundaries between milky quartz and clear quartz: transition is mostly very gradual. Microscopically, microfractures are less abundant and fluid inclusions are larger. Clear quartz crystals are commonly associated with pyrite, chalcopyrite, sphalerite, galena and tourmaline but rarely with cassiterite.

Toothy quartz is the last generation of open-space infill quartz and occurs only in large open vugs. Crystals of toothy quartz may be as long as several centimetres, lining open vugs and forming a "dog teeth" texture and are associated with fluorite and cookeite.

Marginal Sericite/Chlorite Alteration

Sericite and chlorite selectively alter the nonbrecciated Mine Granite in the mine area. Sericite replaces primary plagioclase and chlorite replaces or rims primary biotite. The sericite-altered plagioclase crystals have commonly a green colour and waxy lustre due to the formation of crowded microflakes of sericite. K-feldspar crystals appear fresh in hand specimen, but some may appear dusty under the microscope due to very weak sericite alteration.

Towards the alteration halo of the Mine Granite Breccia Pipe, sericite replaces biotite and K-feldspar. Variable amounts of chlorite may also occur in these zones but it appears that the chlorite replaces biotite only. Rarely sericite occurs between chlorite rims and relicts of biotite, indicating that the chlorite alteration overprints sericite alteration. The marginal sericite altered Mine Granite typically is pale-cream to pale-grey in colour and can be observed along the walls of the Ardwest pit and Wildcherry South pit.

5.1.3 Cassiterite and Sulphide Mineralization

Cassiterite in the Ardwest group of deposits is associated with pyrite, chalcopyrite, sphalerite, galena and small amounts of wolframite and arsenopyrite, where they occur as interfragmental, open space infill.

Cassiterite, wolframite and arsenopyrite are concentrated in tourmaline and milky quartz zones which closely rimming fragments. The majority of cassiterite crystals are subhedral to anhedral granular grains between 0.05 and 0.5 mm long. They occur very close to the margins of fragments although a significant proportion may be disseminating in strongly altered breccia matrix. Some euhedral to subhedral coarse grained cassiterite crystals also occur within or close to the small secondary breccia pipes in the Ardwest deposit. They are up to 5 mm in size with well developed knee twins and growth zonations (Plate 5-2). The coarse-grained cassiterite also occurs as open space infill with tourmaline and milky quartz. Trace amount of rutile occurs in the Perseverance deposit.

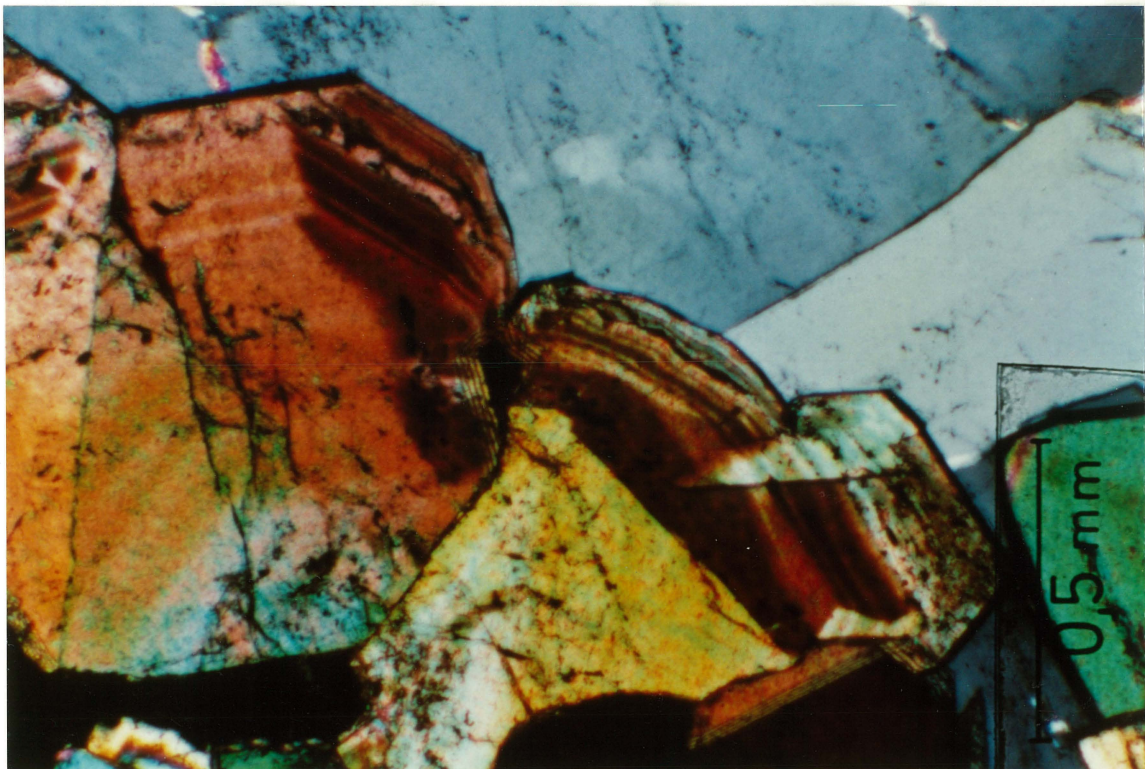


Plate 5-2: Coarse cassiterite crystals in association with milky quartz in the Wildcherry deposit (From sample WY12, scale bar=0.5 mm).

Pyrite, chalcopyrite, sphalerite and galena crystals occur as sulphide patches in interfragmental open spaces and fractures with clear quartz. There are also sulphide filled fractures cutting tourmaline and cassiterite

crystals, indicating that sulphides are later than cassiterite deposition. Sulphides exhibit complex intergrowth textures: such as chalcopyrite rimming pyrite, inclusions of chalcopyrite in sphalerite, and chalcopyrite filling fractures cutting through pyrite crystals. These are interpreted broadly as the results of one continuous stage of sulphide deposition, although the sphalerite and galena may be slightly later than pyrite and chalcopyrite.

Although sulphides occur in all the deposits in the Ardlethan Tin Field, cassiterite mineralization is not always associated with sulphide mineralization. In the very deep zone of the Perseverance deposit the ore is mainly sericite-tourmaline-quartz-cassiterite (Fig. 4-16). There are many sulphide rich zones in the Ardlethan Tin Mine area which contain only rare cassiterite (D. Barrell, pers. comm., 1987).

5.1.4 Toothy Quartz, Fluorite and Cookeite

In the Perseverance deposit and the deep parts of the Ardwest and Wildcherry deposits, there are some large open vugs partially filled by toothy quartz, fluorite and cookeite. Fluorite occurs as purple-coloured cubes and cookeite as white-coloured waxy patches (Ren *et al.*, 1988). They were deposited after cassiterite and sulphide mineralization.

5.1.5 Paragenesis of the Ardwest Group of Deposits

The paragenesis of each of the Ardwest group of deposits can be generalized as follows: biotite alteration; cassiterite mineralization with sericite, tourmaline and milky quartz; sulphide mineralization with tourmaline and clear quartz; toothy quartz, fluorite and cookeite filling vug spaces; and then chlorite overprinting. This sequence was overprinted by the brecciation and mineralization in the small secondary breccia pipes in the Ardwest deposit.

However, local variations are common and one or two events may be missing in a particular deposit. In the upper zone of the Wildcherry, Ardwest and Wildcherry South deposits, the paragenetic sequence is interpreted to be cassiterite mineralization with sericite, tourmaline and milky quartz; followed by sulphide mineralization with tourmaline and clear quartz; and then chlorite overprinting. The existence of chlorite rich ore is interpreted as the result of strong chlorite alteration of previous assemblages. The low abundances of toothy quartz, fluorite and cookeite in the Wildcherry, Ardwest and Wildcherry South deposits is interpreted to be due to the lack of vug spaces remaining after the earlier mineralizing events.

Chlorite alteration, although occurring with the main Mine Porphyry dyke to a depth of -400 m RL, is very poorly developed in the lower zone of mineralization. For example, no chlorite has been found in the Perseverance ore body. Samples from the zone between the Perseverance and Wildcherry South deposits show good textures of chlorite overprinting sericite and tourmaline (see above description of chlorite alteration). Sericite overprinting secondary biotite have been observed in the Perseverance deposit. The toothy quartz, fluorite and cookeite are relatively better developed in the Perseverance deposit and the deep portions of the Ardwest deposit. The deeper portions of the Perseverance deposit lack sulphides, which may suggest a termination of hydrothermal events in the deposit after cassiterite, sericite, tourmaline and milky quartz deposition.

It is suggested by R. Paterson (pers. comm., 1988) that mineralization in the Wildcherry, Ardwest and Wildcherry South deposits was related to intense chlorite alteration, and the mineralization in the Perseverance deposit was related to sericite alteration. This interpretation considers that the zone between the Perseverance and Wildcherry South deposit is a transitional zone between the two styles of mineralization. However, this interpretation cannot account for the following observations: (1) the high grade portions of the Wildcherry, Ardwest and Wildcherry South deposits are strongly sericitized and not chloritized; and (2) the most strongly chloritized zones in the Mine Granite Breccia Pipe are of very low tin grades.

The second phase of brecciation in the Ardwest deposit resulted in a second generation of cassiterite mineralization in association with acute tourmaline. The characteristics of this second generation of mineralization in the Mine Granite Breccia Pipe are very similar to that of the Blackreef deposit which will be discussed later in this chapter.

In summary, a sequence of events from biotite alteration; cassiterite mineralization with sericite, tourmaline and milky quartz; sulphide mineralization with tourmaline and clear quartz; toothy quartz, fluorite and cookeite vug infill; and finally to chlorite overprinting is the generalized paragenesis for deposits in the Mine Granite Breccia Pipe. But this does not imply that the cassiterite mineralization at depth of the Perseverance deposit was earlier in time than the sulphide mineralization in the Wildcherry deposit. Both temporal and spatial factors have to be considered in modelling the overall process and this will be discussed further in Chapter 10.

5.2 The Carpathia Group of Deposits

5.2.1 General Descriptions

The Carpathia group of deposits is hosted by the Carpathia-Blackreef and Stackpool-Godfrey Breccia Pipes (Fig.1-4) and includes the Carpathia, Blackreef, Stackpool, Godfrey and Godfrey South deposits. There are also a number of small mineralized veins and fractures adjacent to these two breccia pipes (Clarke, 1979). Ore bodies occur from the surface (280 m RL) to a depth of -400 m RL. The Carpathia, Stackpool and Blackreef deposits together have produced about 20,000 tonnes of tin concentrate.

The Carpathia deposit was in the irregular transitional zone around the central zone enriched in sediment fragments of the Carpathia-Blackreef breccia pipe between 220 and 120 m RL (Figs. 1-4 & 4-3). Various styles of mineralization in the Carpathia deposit were described by Clarke (1979), including zones of pyrite-rich, vug-rich and tourmaline-rich ores. The transitions between the ore styles are sharp and irregular. Opaque minerals identified in the Carpathia deposit include cassiterite, arsenopyrite, pyrite, chalcopyrite, sphalerite and galena, and very small amounts of rutile and wolframite (Clarke, 1979). The alteration mineralogy includes tourmaline, milky quartz, clear quartz, sericite, siderite and chlorite. As with the Ardwest group of deposits, tourmaline and quartz are mainly related to interfragmental open spaces, veins and fractures. Chlorite alteration is patchy in the Carpathia deposit. Sericite is the main pervasive replacement alteration mineral. There are generally more residual primary minerals of K-feldspar and plagioclase present in the Carpathia deposit than in the Ardwest group of deposits. Weak selective chlorite/sericite alteration also occurs in the host rocks forming a wide halo linking with that of the Ardwest group of deposits (Fig. 5-1).

The Stackpool deposit was small and it occurred at the surface exposure of the Stackpool-Godfrey Breccia Pipe. It extended downwards in a pipe-like configuration from the surface (280 m RL) to about 200 m RL (Figs. 1-4 & 4-3). Cassiterite mineralization occurs in the transitional zone of the breccia pipe where fragments are mainly from the Mine Granite. The central zone enriched in sediment fragments is barren. The Stackpool deposit is very similar to the Carpathia deposit in terms of styles of hydrothermal alteration and mineralization (Stone, 1969).

The Blackreef deposit is comprised of three tabular lenses (Figs. 1-4 & 4-6). The lenses penetrate through the central zone of the breccia pipe subvertically between -100 m RL to 80 m RL, with a common WSW dip of approximately 60°. The Blackreef deposit is characterized by the

occurrences of pervasive, massive to semimassive, dark-coloured, acute tourmaline particularly in the top portions of the lenses. The name "Blackreef" was termed to describe the strongly tourmalinized rocks associated with the cassiterite mineralization. Intense sericite alteration with or without siderite, occurs pervasively in the Blackreef deposit both inside Mine Granite fragments and in the alteration halo immediately enclosing the ore bodies. Massive patches of tourmaline crystals pseudomorph K-feldspar phenocrysts inside Mine Granite fragments, and in the sericite-altered rocks form sericite-tourmaline altered zones without destroying the primary texture of the Mine Granite. Inside the Blackreef ore body cassiterite is associated with arsenopyrite, wolframite, pyrite, chalcopyrite, sphalerite and galena. The Blackreef deposit has the highest tin grade of all the main deposits, ranging between 2 and 23 wt% Sn and averaging around 8%. The sulphide grade of the Blackreef deposit is also among the highest in the field reflected by the occurrence of massive arsenopyrite, pyrite, sphalerite and less commonly galena. The three varieties of quartz, namely milky quartz, clear quartz and toothy quartz all occur in the Blackreef deposit. Coarse-grained siderite and patches of cookeite also occur in vugs.

There are Blackreef-style mineralized fractures and veins in the Carpathia deposit and overprinting the main Carpathia-style mineralization. They extend downwards to join the Blackreef deposit, indicating that the mineralization in the Blackreef deposit postdates that in the Carpathia deposit.

Based on limited information from several diamond drill holes the Godfrey deposit is composed of five subvertical lenses between -100 m RL and -450 m RL in the Stackpool-Godfrey Breccia Pipe (Figs. 1-4 & 4-2). They dip between 55 and 65° to WSW. Identified opaque minerals are cassiterite, wolframite, arsenopyrite, pyrite, chalcopyrite, sphalerite and galena. Mineralization is associated with hydrothermal alteration products of sericite, tourmaline, quartz, siderite, and chlorite. The detailed zonation of these styles of alteration is difficult to construct as there is only limited drilling information. However, it is apparent that chlorite alteration is very patchy in the Godfrey deposit and cassiterite occurs mainly in zones of strong sericite, tourmaline and milky quartz alteration.

The Godfrey South deposit occurs between -230 m RL and -400 m RL within the Carpathia-Blackreef Breccia Pipe (Figs. 1-4 & 4-7). Cassiterite mineralization is associated with wolframite, arsenopyrite, pyrite, sphalerite and galena, and hydrothermal alteration products of sericite, tourmaline and quartz. The Godfrey South deposit contains relatively large amounts of fluorite (2-3% by volume). It is the only deposit in the Ardlethan Tin Field in which the colour of fluorite is variable from colourless, to white, brown and green.

The Carpathia group of deposits is partially overprinted by a later stage of mineralization of cosalite, native bismuth, bismuthinite, pyrite and chalcopyrite. Their occurrence is patchy and more detailed work is needed to quantify the resource potential.

5.2.2 Hydrothermal Alteration

Hydrothermal alteration phases in the Carpathia group of deposits include sericite, kaolinite, tourmaline, quartz, and chlorite. Upper and lower zones of mineralization can be defined on the basis of dominant style of hydrothermal alteration. The upper zone of mineralization includes the Carpathia and Stackpool deposits and many mineralized tourmaline veins and pipes; the lower zone includes the Blackreef, Godfrey and Godfrey South deposits. Stronger sericite+siderite alteration occurs in the lower zone. As with the Ardwest group of deposits, the styles of alteration are classified as

1. *Sericite*
2. *Kaolinite*
3. *Chlorite*
4. *Tourmaline*

according to the dominant mineral in each assemblage.

Sericite Alteration

Sericite in the Carpathia-Blackreef and Stackpool-Godfrey Breccia Pipes is similar to that in the Perseverance deposit in the Mine Granite Breccia Pipe. Sericite replaces plagioclase selectively in weakly altered zones, and pervasively replaces plagioclase, biotite, and K-feldspar in the mineralized zones.

Coarse flakes of sericite, up to 2 mm in size, occur in the Godfrey and Godfrey South deposits. These flakes of sericite generally form circular clusters interlocked in a kaolinite altered matrix. They are of very limited occurrence and spatially related to several upper closures of blind daughter breccia pipes along the hangingwall of the Carpathia-Blackreef and Stackpool-Godfrey Breccia Pipes.

There is always a small amount of siderite in association with the strong sericite alteration in the Carpathia, Blackreef, Godfrey and Godfrey South deposits. Siderite also occurs as large patches in vugs in the Blackreef, Godfrey and Godfrey South deposits.

Kaolinite Alteration

As mentioned above, kaolinite alteration which occurs in the Godfrey and Godfrey South deposits spatially correlates with the upper closures of blind daughter breccia pipes. Under the microscope, kaolinite altered samples indicate very intense pervasive alteration and no primary textures can be observed. Kaolinite crystals are very fine. Circular clusters of sericite and coarse flakes of chlorite may occur in fractures in the kaolinite-altered rocks along with wolframite and cassiterite.

Chlorite Alteration

The zone of strong chlorite alteration in the Mine Granite Breccia Pipe extends into the Carpathia-Blackreef and Stackpool-Godfrey Breccia Pipes following the small Mine Porphyry dykes. This further emphasizes the correlation between Mine Porphyry and intense chlorite alteration (Fig. 5-1). The characteristics of the strongly chlorite altered rocks are identical to those in the Mine Granite Breccia Pipe. Several large strongly chloritized blocks occur within the Carpathia-Blackreef and Stackpool-Godfrey Breccia Pipes, particularly in areas close to parental Mine Porphyry dykes. This implies that some of the intensely chloritized blocks could be fragments from pre-existing Mine Porphyry dyke contacts.

There are also a number of massive chlorite bands up to a metre thick in the deeper portions of the Carpathia-Blackreef Breccia Pipe. Microscopic examination indicates that relicts of acute-tourmaline crystals are common in these massive chlorite bands (Plates 5-3 & 5-4), suggesting that they are formed by replacing tourmaline bands. Two types of chlorite occur: a fine-grained type with light grey or green interference colours and a relatively coarse-grained type in clusters or veins with a deep purple interference colour (Plate 5-5).

Tourmaline Alteration

Two types of tourmaline are recognized in the Carpathia group of deposits: patchy and acute tourmaline. They are texturally identical to the same styles of tourmaline recognized in the Mine Granite Breccia Pipe. The patchy tourmaline occurs in veins in some large fragments of sedimentary rocks. The acute tourmaline is the main type of tourmaline in the Carpathia-group of deposits.

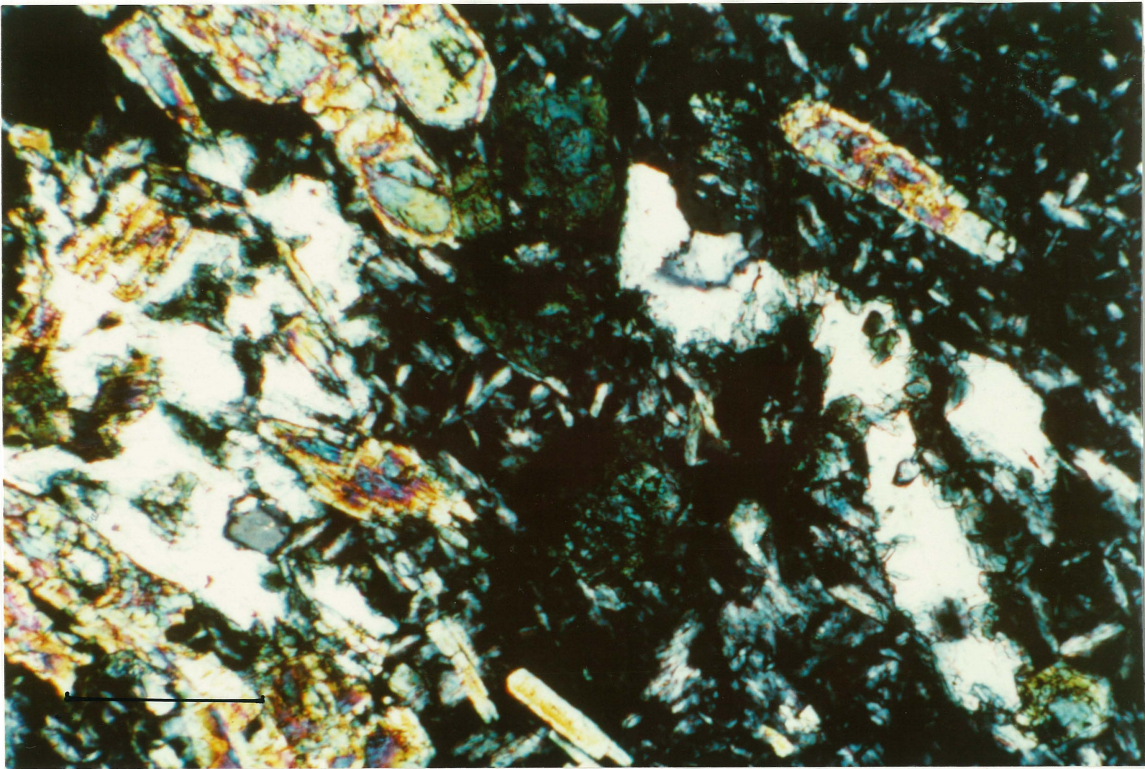


Plate 5-3: Relicts of tourmaline (bright) in massive chlorite (grey) bands (From sample RD193, scale bar=0.5 mm).

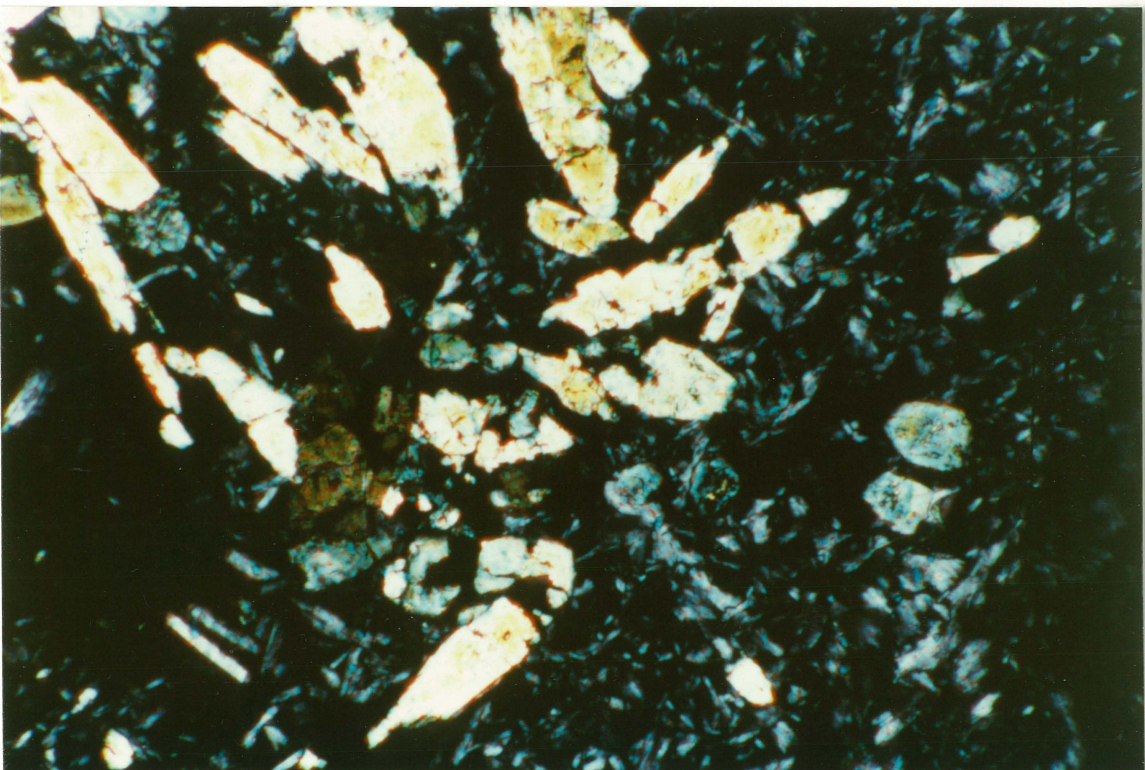


Plate 5-4: Relicts of tourmaline (bright) and cassiterite in massive chlorite bands (From sample RD193; scale bar=0.5 mm).

The acute tourmaline crystals exhibit needle like habits with length/width ratios between 2 and 5. Although acute tourmaline in the Blackreef deposit may occur as semipervasive to pervasive alteration, in the Carpathia, Stackpool, Godfrey and Godfrey South deposits, it occurs mainly as interfragmental open space infill with milky or clear quartz. In the semipervasively tourmalinized samples from the Blackreef deposit, acute tourmaline forms thick rims around Mine Granite fragments and is accompanied by milky quartz, cassiterite and arsenopyrite (Plate 5-6). Acute tourmaline also selectively replaces K-feldspar megacrysts inside Mine Granite fragments (Plate 5-6) and in the sericite-altered alteration halo around the Blackreef deposit.

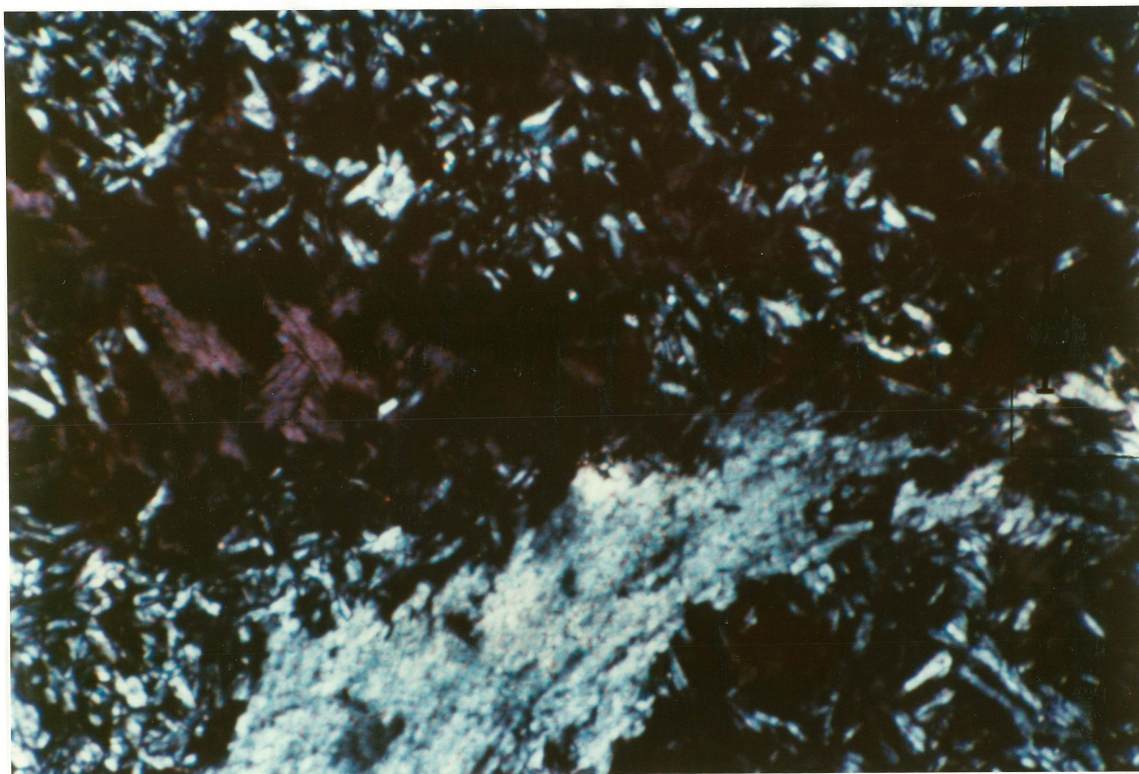


Plate 5-5: Two types of chlorite (purple or light grey) in massive chlorite bands (From sample RD194; scale bar=0.5 mm).

Massive acute tourmaline bands occur in the Carpathia-Blackreef and Stackpool-Godfrey Breccia Pipe. They contain a relatively simple assemblage of tourmaline, cassiterite, arsenopyrite and wolframite. Chlorite veins were found in samples of massive tourmaline bands.

5.2.3 Cassiterite and Sulphide Mineralization

There are various styles of cassiterite mineralization in the Carpathia deposit. Cassiterite mostly occurs as fine grains with sericite, tourmaline and milky quartz. Cassiterite may occur with chlorite, however, the textures suggest chlorite overprinting previous assemblages of cassiterite-sericite and cassiterite-tourmaline. Small amounts of arsenopyrite and wolframite occur with cassiterite. Sulphides, mainly pyrite, chalcopyrite, sphalerite and galena, infill open spaces with clear quartz after cassiterite and milky quartz. Rare molybdenite occurs in the Carpathia deposit as a late-stage open-space infill. Based on very limited information the Stackpool deposit is similar to the Carpathia deposit.

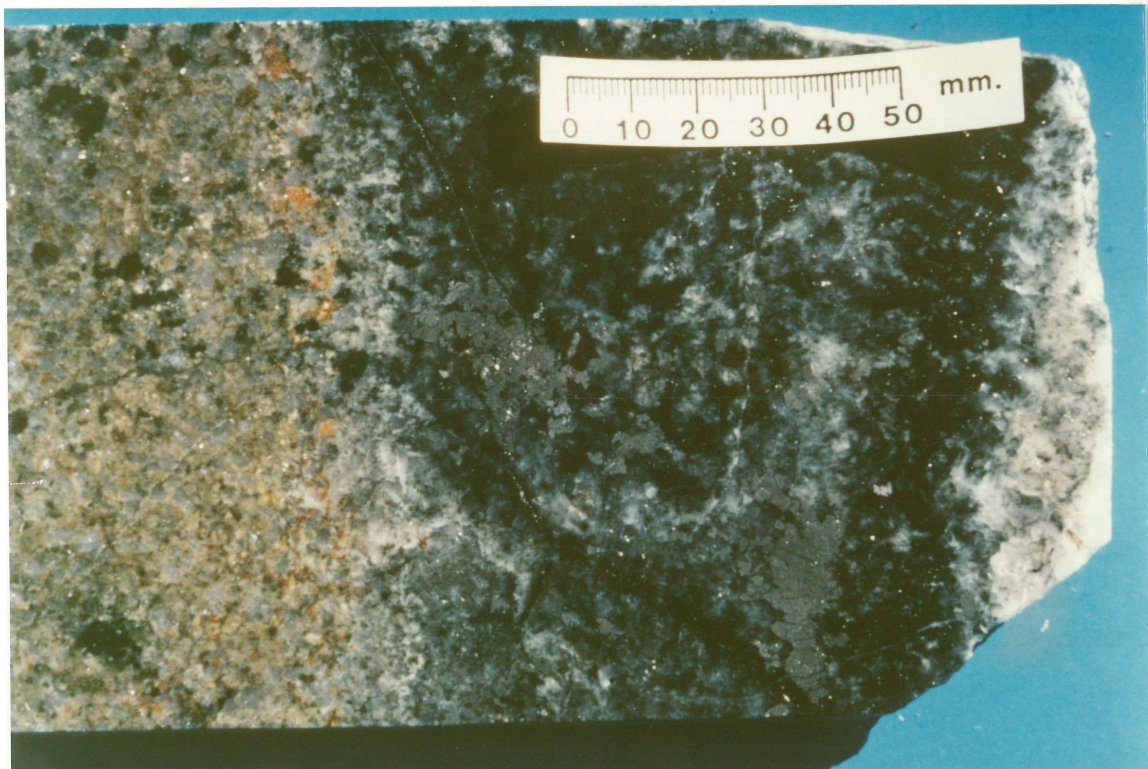


Plate 5-6: Zonation of alteration around a large Mine Granite Fragment. The core (left) was strongly altered by sericite and tourmaline, then there is a thick rim of tourmaline and milky quartz with unusually rich cassiterite and arsenopyrite (middle), and further out a layer of clear quartz (sample RB16).

Coarse- and fine-grained cassiterite crystals, cassiterite and tourmaline intergrowth occur commonly with acute tourmaline, sericite,

milky quartz and arsenopyrite in the Blackreef deposit (Plate 5-7). Cassiterite crystals are mostly subhedral and granular with grainsize between 0.05 to 0.5 mm, but occasionally up to 2 mm. Growth zonations occur within coarse cassiterite (Plates 5-7 & 5-8). The arsenopyrite content of ore from the Blackreef deposit may be up to 5% by volume, which is also the highest in the Ardlethan Tin Field. Pyrite, chalcopyrite, sphalerite and galena may also occur as massive patches up to hundreds of cubic centimetres in size, infill open spaces (Plate 5-8) in association with tourmaline and clear quartz. Like in the Ardwest group of deposits, cassiterite, milky quartz, arsenopyrite and wolframite are commonly enriched in layers closely enclosing sericite altered fragments. They are enclosed by layers of pyrite, chalcopyrite, sphalerite and galena with clear quartz. Toothy quartz, fluorite and cookeite infill the vugs. Such textures clearly indicate that, as with the Ardwest group of deposits, cassiterite deposition was later than the brecciation and was followed by sulphide deposition and then by toothy quartz, fluorite and cookeite deposition.



Plate 5-7: Coarse cassiterite (white to brown) and tourmaline (grey to green) intergrowth in the Blackreef deposit (From sample RD145, scale bar=0.5 mm).

The cassiterite and sulphides in the Godfrey and Godfrey South deposits are similar to the Blackreef deposit, but of much lower average grades ranging between 0.4 and 0.7 wt% Sn. The Godfrey South deposit contains the higher than average wolframite (up to 1 wt% W). Relatively

coarse (up to 2 mm in size) euhedral cassiterite crystals (Plate 5-9) were found in the Godfrey South deposit.

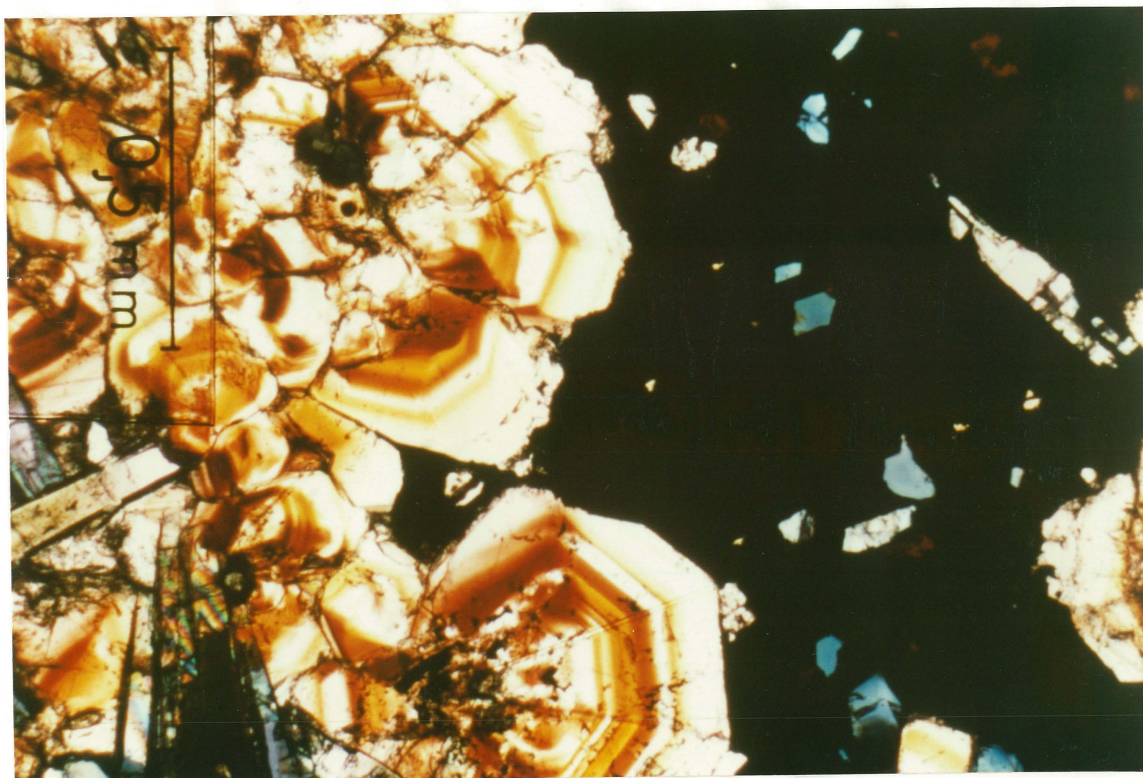


Plate 5-8: Sulphides (dark area) filling open spaces after cassiterite and tourmaline mineralization in the Blackreef deposit (From sample RD145, scale bar=0.5 mm).

5.2.4 Toothy quartz, Fluorite and Cookeite

Toothy quartz, fluorite and cookeite occur in the Carpathia group of deposits similar to those in the Ardwest group of deposits. Patches of brown-coloured siderite may occur in vugs in association with toothy quartz in the Blackreef deposit. The Carpathia, Stackpool and Godfrey deposits contain less toothy quartz, fluorite and cookeite than the Blackreef and Godfrey South deposits.

5.2.5 Cosalite Mineralization in the Blackreef deposit

A late stage of mineralization consisting of cosalite, bismuthinite, native bismuth, pyrite and chalcopyrite occurs in the Blackreef deposit and nearby zones. It overprints the main cassiterite and sulphide mineralization in the Blackreef deposit and nearby zones.

Cosalite is a Pb and Bi sulphosalt. In the Ardlethan tin field it has a peculiar composition and contains up to 2 wt% Ag and significant amount of copper. It occurs mainly in mineral cracks, microfractures (Plate 5-10) and microveins. Cosalite has a silvery colour and is intergrown with irregular patches of bismuthinite and native bismuth. In microveins cosalite is generally associated with brown-coloured siderite, cubic pyrite up to 5 mm in size, and a minor amount of chalcopyrite. Cosalite, bismuthinite and native bismuth infill almost all the microfractures within cassiterite and sulphides, but are especially prevalent in arsenopyrite (Plate 5-10), probably because of the high abundance of microfractures. One arsenopyrite-rich sample (RB10) from the Blackreef deposit contains approximately 15% cosalite by volume, but generally, the cosalite content of the Blackreef deposit and nearby zones is mostly lower than 3% by volume.

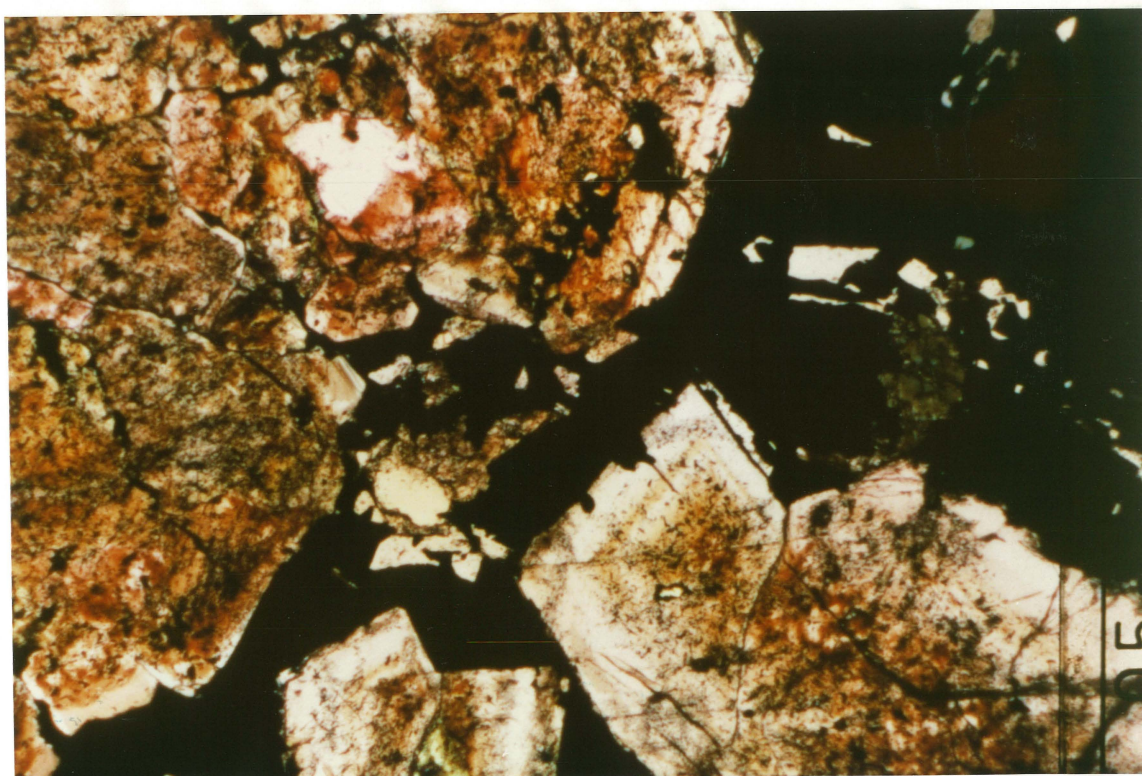


Plate 5-9: Cassiterite(white to brown) and interstitial sulphides (dark) in the Godfrey deposit (From sample 195, scale bar=0.5 mm)

As cosalite occurs mainly in microfractures and microveins within minerals formed during the main stage mineralization, it is clear that the hydrothermal event responsible for the cosalite deposition overprinted the main cassiterite and sulphide mineralization.

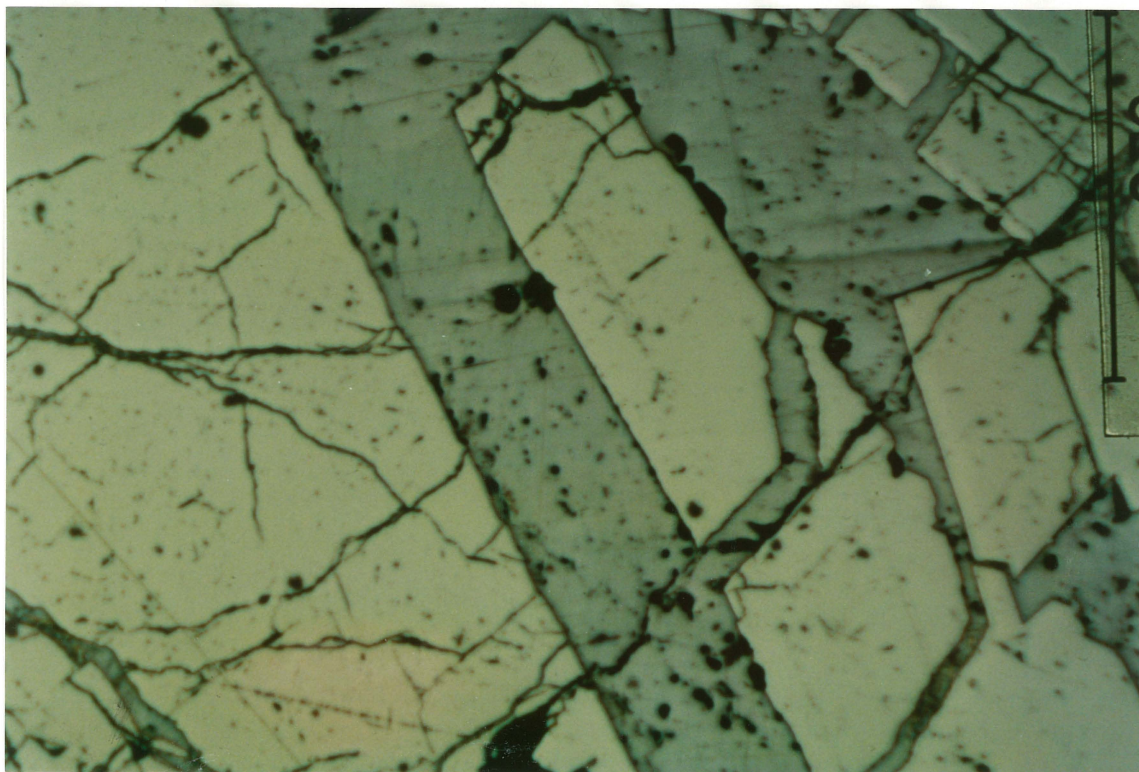


Plate 5-10: Cosalite (grey with black pits) in fractures in arsenopyrite in the Blackreef deposit (From sample RB10, scale bar=0.25 mm).

5.2.6 Parageneses of the Carpathia Group of Deposits

The brecciation, hydrothermal alteration and mineralization in the Carpathia-Blackreef and Stackpool-Godfrey Breccia Pipes are contemporaneous with the secondary breccia pipes in the Ardwest deposit and therefore later than the main stage mineralization in the Mine Granite Breccia Pipe. This is suggested by the abundant acute tourmaline like that in the secondary breccia pipes in the Ardwest deposit, and observations that the Mine Granite Breccia Pipe predated, and the Carpathia-Blackreef and Stackpool-Godfrey Breccia Pipes postdated the Mine Porphyry dykes. The parageneses of the Carpathia group of deposits are from cassiterite mineralization with sericite, tourmaline and milky quartz; to sulphide mineralization with tourmaline and clear quartz; and then to toothy quartz, fluorite and cookeite as open space infill. Weak chlorite alteration followed mineralization in each deposit. The Blackreef deposit and nearby

zones were overprinted by a later stage hydrothermal event which generated cosalite, bismuthinite, native bismuth, pyrite and chalcopyrite mineralization.

As with the Mine Granite Breccia Pipe, mineralization in the lower levels in the Carpathia-Blackreef and Stackpool-Godfrey Breccia Pipes appears later than that in the upper levels. This is illustrated by the partial overprinting relationship of the Blackreef style mineralization to the Carpathia mineralization. Also chlorite alteration replaces the Blackreef style massive black tourmaline bands in the Godfrey region (Plates 5-3 & 5-4).

It is recognized that the contents of wolframite, fluorite and cookeite increase steadily with the evolution of the system. The main Wildcherry, Ardwest and Wildcherry South deposits contain negligible amounts of wolframite, fluorite and cookeite. The Perseverance deposit contains around 0.2 % wolframite, up to 0.4% fluorite and cookeite. The Carpathia deposit contains about 0.4% wolframite, 0.5% fluorite and cookeite. In the Blackreef and Godfrey deposits the wolframite content is about 0.5% and fluorite and cookeite up to 1%. The Godfrey South deposit contains about 1% wolframite, 2-3% fluorite and cookeite. It is postulated that the fluorite- and cookeite-rich style mineralization in the Godfrey South deposit was the last to form in the Carpathia-Blackreef and Stackpool-Godfrey Breccia Pipes.

5.3 The White Crystal Deposit

5.3.1 General Description

The White Crystal deposit occurs in the White Crystal Breccia Pipe from the surface (280 m RL) to about 180 m RL (Fig. 4-8). Hydrothermal alteration products include topaz, tourmaline, sericite, quartz, and siderite. The White Crystal deposit is the only one of its type in the Ardlethan Tin Field. Primary textures of the Mine Granite have been completely destroyed by alteration. Wolframite, rutile, and arsenopyrite occur with tourmaline and milky quartz, and pyrite, chalcopyrite, sphalerite and galena with clear quartz. Minor cassiterite occurs as disseminated in association with topaz. Euhedral coarse-grained toothy quartz crystals (up to 3 cm) line large empty vugs with fluorite and patches of cookeite. The White Crystal deposit contains the highest abundances of wolframite (up to 1.5 wt% W), cookeite (up to 5% by volume) and fluorite (up to 3% by volume). It is the only deposit in the Ardlethan Tin Field with extensive development of topaz alteration.

5.3.2 Hydrothermal Alteration

The styles of hydrothermal alteration in the White Crystal deposit are

- 1 *Topaz alteration;*
- 2 *Sericite alteration;*
- 3 *Tourmaline and quartz alteration.*

Intense topaz alteration occurs in the central zone of the White Crystal Breccia Pipe. Topaz crystals are anhedral and granular, mostly growing from the margins of Mine Granite fragments inwards to form semipervasive topaz alteration. Small fragments may have been completely altered but topaz free cores are common within fragments larger than 10 cm in diameter. The margins of topaz crystals are very irregular and show evidence of etching by sericite. Microfractures within topaz crystals are commonly filled by sericite. The absolute abundance of topaz decreases from around 25% by volume at surface to about 5% at depth in the breccia pipe.

Sericite alteration occurs within the White Crystal deposit with topaz and tourmaline as well as in the alteration halo around the White Crystal Breccia Pipe. As described above, sericite replaces or rims topaz crystals. In the centers of large Mine Granite fragments sericite pervasively replaces all preexisting minerals forming massive patches. Sericite abundance increases with depth at the expense of topaz. Semipervasive sericite occurs in the nonbrecciated Mine Granite enclosing the White Crystal Breccia Pipe (Fig. 4-8) with some siderite, a pattern akin to the zonation around the Perseverance deposit. The alteration halo in the nonbrecciated Mine Granite, based on drill core information, is only several metres thick and grades into the relatively fresh Mine Granite with only weak sericite/chlorite alteration, again a pattern similar to the marginal alteration around the Ardwest group of deposits.

Tourmaline in the White Crystal deposit has a radiating texture and is classified as radiating tourmaline. It occurs in a different habit to the patchy, granular and acute tourmalines which occur in the Wildcherry, Ardwest, Wildcherry South, Carpathia and Blackreef deposits. Radiating tourmaline crystals occur as numerous long radiating needles, with length/width ratios in excess of 10. They have a light green colour and are associated with topaz or quartz. Generally, tourmaline alteration in the White Crystal deposit shows strong preference for the margins of fragments. The absolute abundance of tourmaline decreases from more than 30% by volume to about 10% with depth.

5.3.3 Cassiterite, Wolframite and Sulphide Mineralization

Cassiterite in the White Crystal deposit is fine-grained, usually enriched around the margins of fragments with tourmaline and milky quartz. A small proportion of cassiterite occurs with topaz and sericite. Very coarse-grained wolframite, up to 3 cm in size, occurs with cassiterite and associated tourmaline and milky quartz in the White Crystal deposit, and there is a good correlation between Sn and W grades. Arsenopyrite is closely associated with cassiterite.

Because the White Crystal Breccia Pipe is characterized by very large open vugs, patches of pyrite, chalcopyrite, sphalerite and galena may be as large as several centimetres in dimension. They occur with clear quartz and radiating tourmaline.

5.3.4 Toothy Quartz, Fluorite and Cookeite

Toothy quartz, fluorite and cookeite are the outstanding features of the White Crystal deposit. Toothy quartz crystals are up to several centimetre long and occur in all the vugs. Purple coloured fluorite crystals are also abundant in these vugs. Large cookeite patches, up to several cubic centimetres in size, occur in vugs and open spaces (Ren *et al.*, 1988). Very fine veinlets of silvery coloured galena may occur in fractures in patches of cookeite.

5.3.5 Paragenesis of the White Crystal Deposit

The observations that sericite rims granular topaz crystals, and grows in microfractures within topaz crystals, indicate that sericite alteration postdates topaz alteration in the White Crystal deposit. Tourmaline and quartz deposition at the marginal zones of fragments also postdates the topaz alteration because radiating tourmaline crystals penetrate topaz crystals. Briefly, the paragenesis of the White Crystal deposit can be simply described as topaz alteration with minor cassiterite; followed by cassiterite mineralization with sericite, tourmaline and milky quartz deposition; followed by sulphide mineralization with tourmaline and clear quartz deposition, and then followed by toothy quartz, fluorite and cookeite deposition in vugs.

5.4 Overall Paragenesis of the Ardlethan Tin Field

The evidence discussed in this chapter suggest that the Ardwest, Carpathia and White Crystal groups of deposits represent a sequence of three brecciation and mineralization events in the overall development of

the Ardlethan Tin Field. From the character of the brecciation, the tourmaline alteration, the mineralization, and their relationships to Mine Porphyry dykes, it is concluded that the Carpathia-Blackreef and Stackpool-Godfrey Breccia Pipes are later than the Mine Granite Breccia Pipe and its mineralization. But their relationship with the White Crystal Breccia Pipe is not clear. However, a number of features, such as,

1. The increasing proportions of wolframite, toothy quartz, fluorite and cookeite from the Ardwest, Carpathia group of deposits to the White Crystal deposit,
2. The increasing length/width ratios of tourmaline crystals from the Ardwest, Carpathia groups of deposits to the White Crystal deposit (According to Chen *et al.* (1985), increasing length/width ratios of tourmaline crystals occur in the Dachang Tin Field, South China from earliest to latest deposits),
3. The increasing proportions of remaining large open vugs from the Ardwest, Carpathia groups of deposits to the White Crystal deposit,
4. The collapse feature of the White Crystal Breccia Pipe (Chapter 4),

all suggests that the White Crystal Breccia Pipe was the last one to form.

5.5 Geometry of Ore Bodies

The ore bodies in the Ardlethan Tin Field have a common feature of lense- or pipe-like geometry or have lense- or pipe-like depth extensions. The Wildcherry, Ardwest and Wildcherry South ore bodies are relatively irregular but they all have pipe-like extensions at depth: the Perseverance deposit extends the Wildcherry South deposit; the Ardwest Deep extends the Ardwest deposit and the Wildcherry Pipe extends the Wildcherry deposit (Fig. 1-4).

The Carpathia deposit has two pipe-like extensions, called the Carpathia pipe 1 and 2. The lense-like Stackpool deposit, seems very likely that it is a down-dip extension of an eroded ore body. The Blackreef deposit has three lenses and Godfrey deposit has five (Figs. 4-2 & 4-6).

As discussed in Chapter 4, brecciation in the Ardlethan Tin Field was probably controlled by the intersections of the three linear structural patterns (Fig. 4-19). The locations and configurations of ore bodies are controlled by the host breccia pipes and are therefore related to the intersections of these linear patterns and their intersections.

5.6 Correlation Between Styles of Brecciation and Mineralization

Inside each breccia pipe, the locations of ore bodies are correlated with rock flour-poor breccia zones.

The Wildcherry, Ardwest, and Wildcherry South deposits all occur in the marginal zones of the Mine Granite Breccia Pipe. This is clearly shown both on plans and sections (Fig. 4-1 to Fig. 4-15). They form a circular zone of mineralization as an inner rim inside the Mine Granite Breccia Pipe encircling a barren core (Fig. 4-10). The down-dip extensions of these major ore bodies are also within the marginal zones of the Mine Granite Breccia Pipe.

This relationship also occurs in the Carpathia-Blackreef and Stackpool-Godfrey Breccia Pipes. The central cores of these breccia pipes contain abundant sediment fragments and rock flour at the surface while the marginal zones contain mainly Mine Granite fragments with minor rock flour. The Stackpool and Carpathia ore bodies are predominantly in the marginal zones of their respective breccia pipes. However, as there is only minor development of rock flour at the depth, the lenses of the Blackreef and Godfrey deposits penetrate the central zones. There is no rock flour in the White Crystal Breccia Pipe, the ore body occurs in the central zone.

This correlation is interpreted as the result of permeability control over fluid activity. As large volumes of fluid must flow through the rock to form an ore body, rock flour-poor zones are better conduits because of their higher permeability compared to rock flour-rich zones (Fig. 4-16). This is a simple but a common correlation in many breccia pipe hosted deposits, for example, in the copper-bearing breccia pipes in Chile (Sillitoe & Sawkins, 1971).

5.7 Summary and Conclusions

It is concluded that there was a sequence of three brecciation and mineralization events in the development of the Ardlethan Tin Field; they are represented by the Ardwest group of deposits, the Carpathia group of deposits and the White Crystal deposit.

The first event was the main stage brecciation and mineralization in the Mine Granite Breccia Pipe. Brecciation was followed by biotite alteration; cassiterite deposition with sericite, tourmaline and milky quartz; sulphide deposition with tourmaline and clear quartz; minor deposition of toothy quartz, fluorite and cookeite; and then chlorite

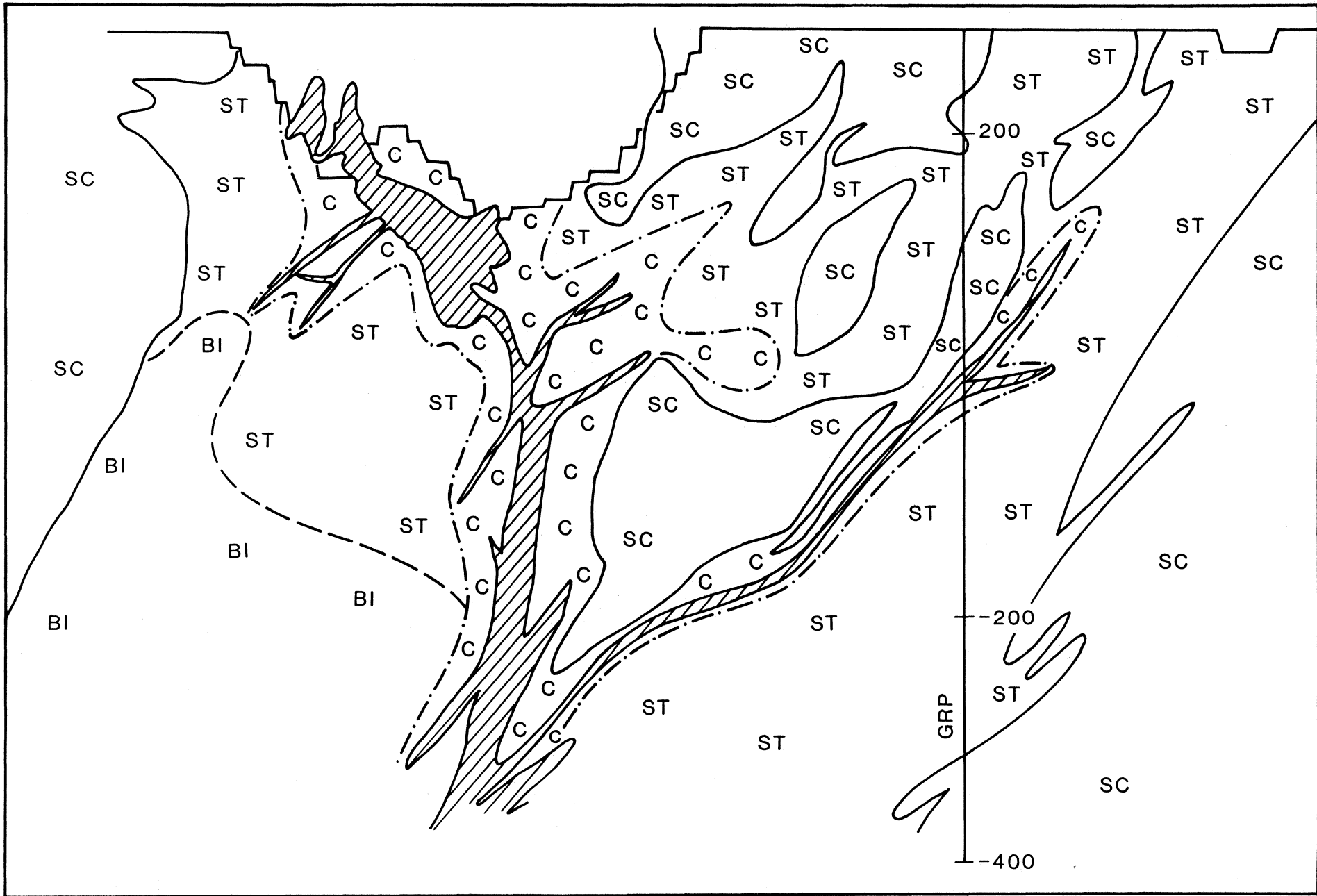
alteration.

The second event led to the formation of the Carpathia-Blackreef and the Stackpool-Godfrey Breccia Pipes and the Carpathia, Stackpool, Godfrey, Blackreef and Godfrey South deposits, as well as the mineralization in the secondary breccia pipes in the Ardwest deposit. The common paragenetic sequence of the second event was cassiterite deposition with sericite, tourmaline and milky quartz; sulphide deposition with clear quartz; and post-mineralization vug infill by toothy quartz, fluorite, and cookeite. This was followed by weak chlorite alteration and chlorite recrystallization in the Carpathia and Godfrey deposits.

The White Crystal deposit represents the third brecciation and mineralization event. Its paragenesis is as follows: topaz replaces primary minerals with minor cassiterite; cassiterite deposition with sericite, tourmaline and milky quartz; sulphide deposition with tourmaline and clear quartz; and toothy quartz, fluorite and cookeite vug infill.

Afterwards, the Blackreef, Godfrey deposits and nearby zones were overprinted by a later hydrothermal event which resulted in mineralization of cosalite, bismuthinite, native bismuth, pyrite, chalcopyrite and siderite.

Fig. 5-1 Zonation of alteration of cross section 8N. SC: marginal sericite/chlorite alteration; ST: sericite-tourmaline alteration; C: strong chlorite alteration; and Bi: biotite alteration. See Fig. 4-1 for references.



Chapter 6

MINERAL CHEMISTRY

Mineral analyses were done using the Energy Dispersive Electron Microprobe (EDM) and the Wave Dispersive Electron Microprobe (WDEM) in the Research School of Earth Sciences, Australian National University. Data reduction was carried out using the method of Reed and Ware (1975) and Ware (1981). Individual analyses are documented in Appendix 1.

6.1 Feldspars

Compositions of K-feldspar in both the Mine Granite and the Ardlethan Granite (Table 6-1) are close to ideal. Na₂O contents in K-feldspar vary between 0 and 4.5 wt% in the Mine Granite and between 0 and 1.04 wt% in the Ardlethan Granite. The compositions of K-feldspar in the microgranite and Mine Porphyry are very similar to the K-feldspar in the Ardlethan Granite.

Plagioclase in both the Mine Granite and the Ardlethan Granite is sodic, close to albite in compositions. In the Mine Granite plagioclase contains between 0 and 3.12 wt% CaO and in the Ardlethan Granite between 0 to 0.89 wt%.

The compositions of feldspars, particularly their contents of K₂O, Na₂O and CaO, reflects their whole rock compositions. The Mine Granite contains relatively more CaO than the Ardlethan Granite (see Chapter 3), this is reflected by the slightly higher CaO (1.90 wt%) in its plagioclase (Table 6-1) than those in the Ardlethan Granite.

6.2 Biotite

The mean compositions (Table 6-2) of 29 analyses of biotite in the Ardlethan Granite yielded a calculated structural formula of $K_{0.90}[Mg_{0.14}Mn_{0.03}Fe_{1.47}Ti_{0.07}Al_{0.89}][Si_{2.91}Al_{1.09}O_{10}][OH]_2$. It differs significantly from ideal biotite composition by its high total Al contents

and low total octahedral occupancy. The high Al and low Mg contents in biotite in the Ardlethan Granite are also reflections of the whole rock chemistry.

Table 6-1: Mean compositions of K-feldspar and plagioclase in the Mine Granite (MG) and the Ardlethan Granite (AG).

N. ana.*	K-feldspar		plagioclase		
	(MG)	(AG)	(MG)	(AG)	(AG)
	20	10	7	15	15
SiO ₂	64.21	64.77	65.35	68.03	
Al ₂ O ₃	18.65	18.27	22.05	19.74	
MgO	0.0	0.0	0.48	0.15	
CaO	0.06	0.01	1.90	0.13	
K ₂ O	14.17	15.79	0.86	0.19	
Na ₂ O	1.18	0.19	9.57	11.38	
total	98.26	99.18	100.28	99.63	
Calculated structural formula					
Si	2.99	3.01	2.87	2.98	
Al	1.02	1.00	1.14	1.02	
Mg	0.00	0.00	0.03	0.01	
Ca	0.00	0.00	0.09	0.01	
K	0.84	0.94	0.86	0.01	
Na	0.11	0.02	0.82	0.98	

*Numbers of analyses

The two types of biotite: primary and secondary, in the Mine Granite were also analyzed. The mean compositions (Table 6-2) of 86 analyses of primary biotite in the Mine Granite yielded a structural formula of $K_{0.91}[Mg_{0.86}Fe_{1.37}Ti_{0.21}Al_{0.37}][Si_{2.69}Al_{1.31}O_{10}][OH]_2$. It is apparently also high in Al compared to ideal biotite.

The secondary biotite contains moderate amounts of Al₂O₃, TiO₂ and MgO comparing to the primary biotites (Table 6-2). Octahedral Mg vs octahedral Ti and octahedral Al(O) vs Mg/Mg+Fe (Figs. 6-1 & 6-2) diagrams show clearly that the compositions of secondary biotite are between the two primary biotites from the Mine and Ardlethan Granites.

The high octahedral Al and low octahedral occupancy of the biotite in the Ardlethan Granite could not be interpreted as the result of undetected Li in a biotite with compositions such as $K[LiAl][Si_{3.0}AlO_{10}][OH]_2$. As described in chapter 3, Li content varies from several ppm to several hundred ppm in the Ardlethan Granite. No

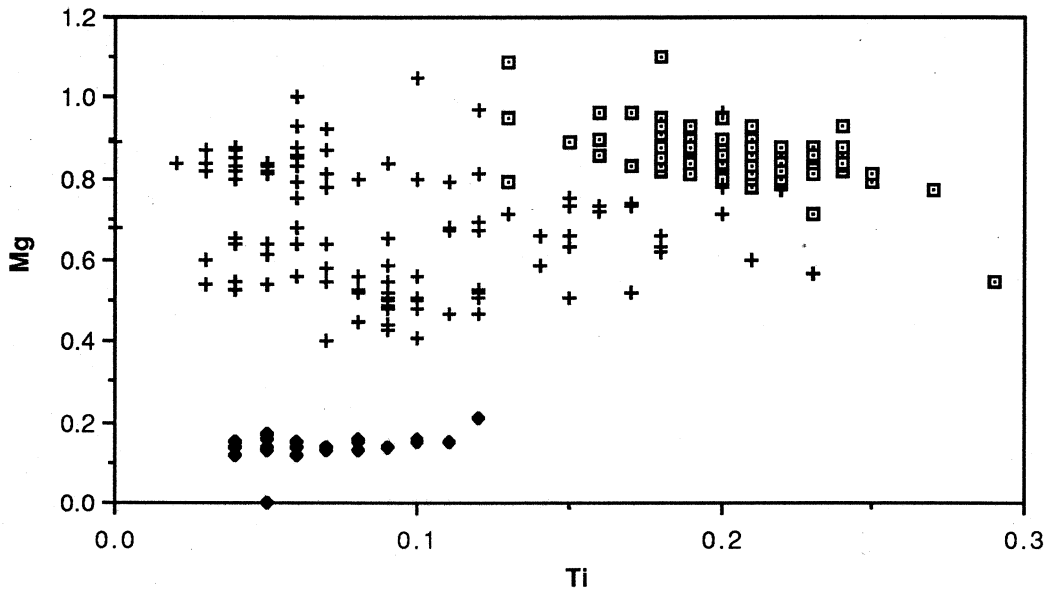


Fig.6-1 Octahedral Mg vs Octahedral Ti plot of biotites (open square: primary biotite in the Mine Granite, cross: secondary biotite in the Mine Granite, filled diamond: biotite in the Ardlethan Granite). The secondary biotite in the Mine Granite has moderate Mg and low to moderate Ti contents compared to primary biotites.

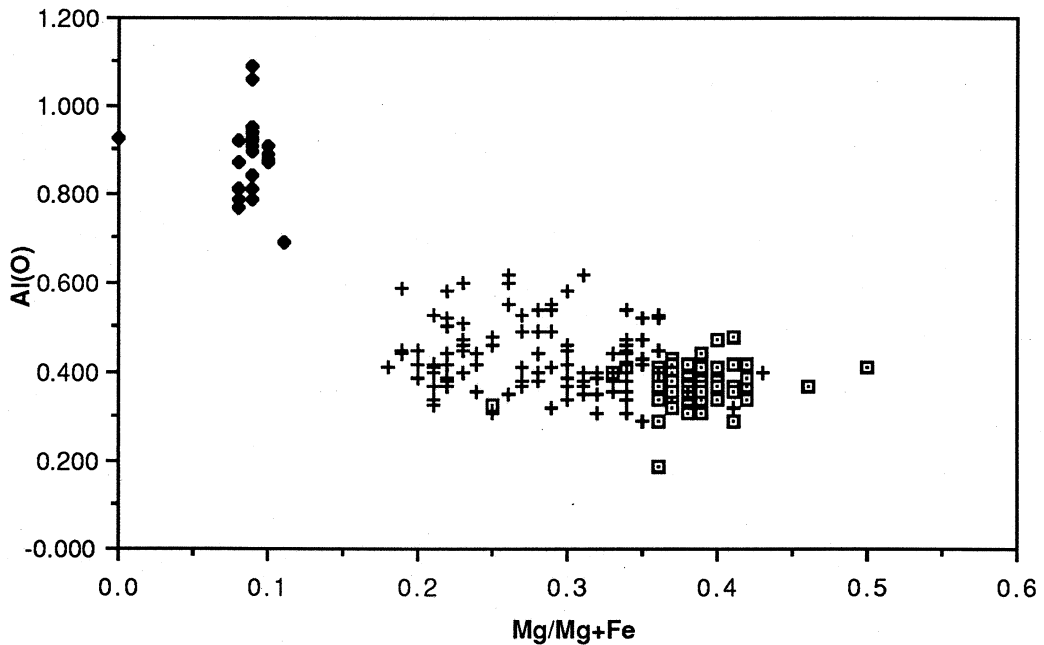


Fig. 6-2 Octahedral Al vs Mg/Mg+Fe plot biotites (open square: primary biotite in the Mine Granite, cross: secondary biotite in the Mine Granite, filled diamond: biotite in the Ardlethan Granite). The secondary biotite in the Mine Granite again shows moderate values of Mg/Mg+Fe and Al(O).

significant deviation in biotite compositions have been found in samples of very different Li contents. The possibility that the biotite may contain interlayers of muscovite due to partial muscovitization is ruled out by the somewhat consistent compositions. Consequently, it is more likely that such compositions are results of some unique conditions in the Ardlethan Granite, perhaps due to its high peraluminous chemistry.

Table 6-3: Mean compositions of biotite

N. ana.	Ardlethan Granite 29	Mine Granite (s) 109	Mine Granite(p) 86
SiO ₂	37.00	33.51	34.47
TiO ₂	1.14	1.51	3.50
Al ₂ O ₃	21.40	18.32	18.40
FeO	22.40	25.23	21.04
MnO	0.39	0.00	0.06
MgO	1.19	5.70	7.39
CaO	0.00	0.02	0.00
K ₂ O	8.96	8.67	9.11
Na ₂ O	0.00	0.00	0.00
total	92.48	92.94	93.98
Calculated unit cell			
Si(t)	2.91	2.69	2.69
Al(t)	1.09	1.31	1.31
Al(o)	0.89	0.43	0.37
Ti	0.07	0.09	0.21
Fe	1.47	1.70	1.37
Mn	0.03	0.00	0.00
Mg	0.14	0.68	0.86
Total(o)	2.60	2.90	2.81
Ca	0.00	0.00	0.00
K	0.90	0.89	0.91
Na	0.00	0.00	0.02

(t), tetrahedral; (o), Octahedral; (p), Primary; (s), Secondary

Tin contents in biotites were analyzed using the Wave-length Dispersive Electron Microprobe. To achieve a deviation around 100 ppm Sn, the Microprobe was set at beam current 35 nA, accelerating potential of 25 kv, 300 seconds counting time for Sn-L α , and metal Sn standard.

Seven analyses of the biotite in the Ardlethan Granite yielded tin contents between 245 and 394 ppm, and averaging 330 ppm. Six analyses of the primary biotite in the Mine Granite contains yielded between 100

and 362 ppm and an average of 202 ppm Sn. The secondary biotite in the Mine Granite has tin contents (for seven analyses), between 280 and 470 ppm averaging 335 ppm.

In summary, biotite in the Ardlethan Granite contains higher Al_2O_3 , lower TiO_2 and MgO than the biotite in the Mine Granite. Primary biotite in the Mine Granite contains the highest MgO and TiO_2 concentrations. There is a decrease of $\text{Mg}/\text{Mg}+\text{Fe}$ from primary biotite in the Mine Granite, to secondary biotite in the altered Mine Granite, and then to biotite in the Ardlethan Granite (Figs. 6-1 & 6-2). TiO_2 contents of biotite show the same decreasing trend (Table 6-3).

These compositional variations may imply that the formation of the secondary biotite in the Mine Granite was via a fluid from the Ardlethan Granite reacting with brecciated Mine Granite. As the Ardlethan Granite is high in Fe and low in Mg, it could have generated a Fe-rich, Mg-poor fluid which reacted with the high Ti and relatively high Mg Mine Granite to form the secondary biotite. The high tin contents of the secondary biotite also support such an interpretation.

6.3 Muscovite

Table 6-3 lists the average compositions of muscovite in the Ardlethan Granite, the microgranite and the Mine Granite. Apparently, the compositions of muscovite in the microgranite dykes are similar to those in the Ardlethan Granite. Muscovite (primary ?) in relatively fresh Mine Granite is close to ideal muscovite in composition. However, $\text{FeO}+\text{MgO}$ contents of muscovite in intensely altered Mine Granite are higher than those in relatively fresh Mine Granite but lower than those in the Ardlethan Granite (Fig. 6-3).

The tin contents of muscovite in the Ardlethan Granite range from 100 to 670 ppm. For 18 analyses the average is 328 ppm. Generally the high tin muscovite is associated with trace topaz and cassiterite. Muscovite in relatively fresh Ardlethan Granite mostly contains less than 300 ppm Sn. Muscovite in the Mine Granite contains between 100 and 350 ppm Sn. Similarly, muscovite in samples close to known mineralization contains higher tin than muscovite away from mineralization. Six muscovite analyses from a microgranite sample (RD96A) yielded tin contents between 150 and 462 ppm, averaging 305 ppm.

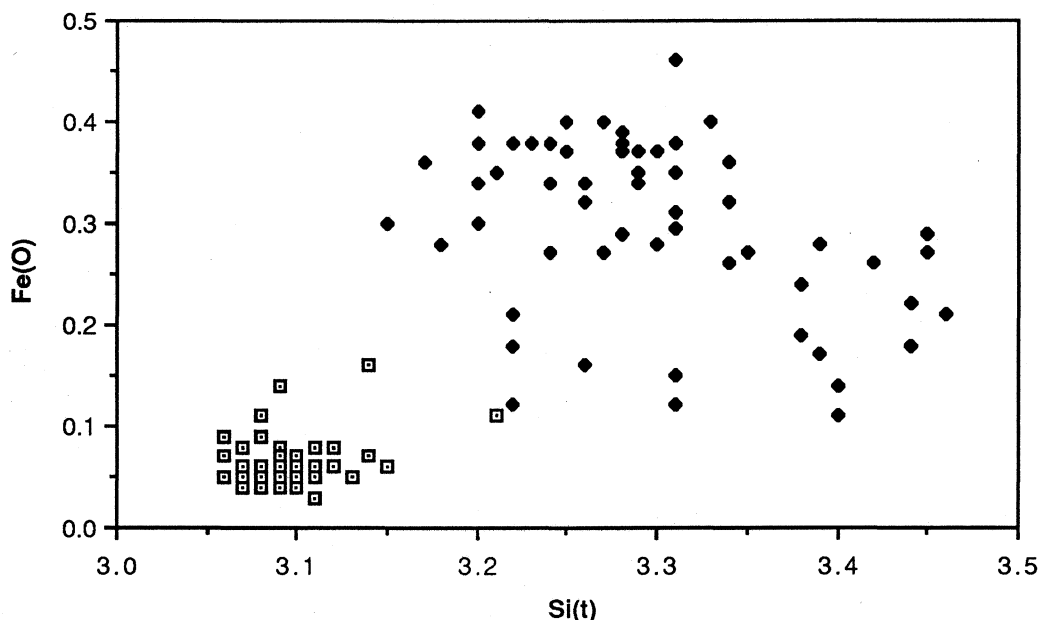


Fig. 6-3 Plot of octahedral Fe vs tetrahedral Si of muscovites (open square: muscovite in the Mine Granite, filled diamond: muscovite in the Ardlethan Granite).

Table 6-3: Chemistry of Muscovite

Hosts	A.G	MicroG	M.G
N. ana.	66	10	77
SiO ₂	47.83	45.84	45.91
Al ₂ O ₃	29.89	33.22	35.52
FeO	5.08	4.96	1.04
MgO	0.62	1.10	0.74
K ₂ O	10.13	10.59	10.49
Na ₂ O	0.23	0.25	0.21
total	93.61	95.96	93.95

Calculated structural formula

Si(t)	3.31	3.09	3.09
Al(t)	0.69	0.91	0.91
Al(O)	1.75	1.73	1.91
Fe	0.30	0.28	0.06
Mg	0.06	0.11	0.07
K	0.90	0.91	0.90
Na	0.03	0.03	0.03

*A.G. Ardlethan Granite; M.G. Mine Granite;

MicroG microgranite

6.4 Chlorite

Chlorite occurs in weakly altered Ardlethan Granite along its eastern margin. Two samples, one from Taylor's Hill and one from Little Bygoo, were analyzed. The data indicated that these are extremely high Fe chlorites with an average FeO content of 41.52 wt% (Table 6-4).

Analyses of chlorite in the altered Mine Granite, excluding those in the massive chlorite bands (see Chapter 5), yielded a range of compositions (Fig.6-4). Mg/Mg+Fe ranges from 0.33 to 0.55 and generally decreases in strongly altered samples. The values of Mg/Mg+Fe of chlorite in fresh samples are higher than that of chlorite in altered samples of the Mine Granite.

Table 6-4: Mean Compositions of Chlorite

Hosts NoS	A.G. 10	MicroG. 10	M.G. 2	M.P 6	A. M.G.# 68
SiO ₂	21.45	21.64	26.49	26.78	25.40
Al ₂ O ₃	21.34	21.64	19.53	20.97	19.98
FeO	41.52	42.52	28.90	31.62	30.64
MnO	1.19	1.24	0.26	0.10	0.35
MgO	2.11	1.84	10.34	5.43	10.91
CaO	0.00	0.00	0.16	0.00	0.00
K ₂ O	0.07	0.05	0.97	1.03	0.19
Na ₂ O	0.00	0.26	0.00	0.00	0.00
total	87.68	89.19	87.25	85.93	87.49
Calculated Unit Cell					
Si(t)	2.58	2.50	2.87	2.98	2.76
Al(t)	1.42	1.50	1.13	1.02	1.24
Al(O)	1.48	1.45	1.38	1.72	1.33
Fe	4.01	4.11	2.62	2.94	2.79
Mn	0.12	0.12	0.02	0.01	0.03
Mg	0.48	0.32	1.67	0.90	1.77
Ca	0.00	0.00	0.02	0.00	0.00
K	0.07	0.01	0.13	0.14	0.03
Na	0.00	0.06	0.00	0.00	0.00

*A.G. Ardlethan Granite; M.G. Mine Granite; MicroG. microgranite; M.P. Mine Porphyry;
A M.G. Strongly altered Mine Granite
#Chlorite in the massive chlorite bands are not included

The compositions of chlorite from the microgranite dykes are very similar to chlorites from the Ardlethan Granite. Chlorite in altered Mine Porphyry has low MgO contents, around 5.5 wt%, but other components are similar to those of the chlorite in altered Mine Granite (Table 6-4).

The chlorite with purple interference colour in massive chlorite bands has distinctively higher MgO contents, mostly between 10 and 13 wt% (Table 6-5), than other types of chlorite. But the coexisting fine chlorite with green or grey interference colours has compositions very similar to those of the chlorite in altered Mine Porphyry (Appendix 1). The relationship of the coarse-grained chlorite with purple interference colours to other chlorite has not been fully understood. Texturally it appears to be later than the fine chlorite (see Chapter 5), thus it may be related to the cosalite mineralization.

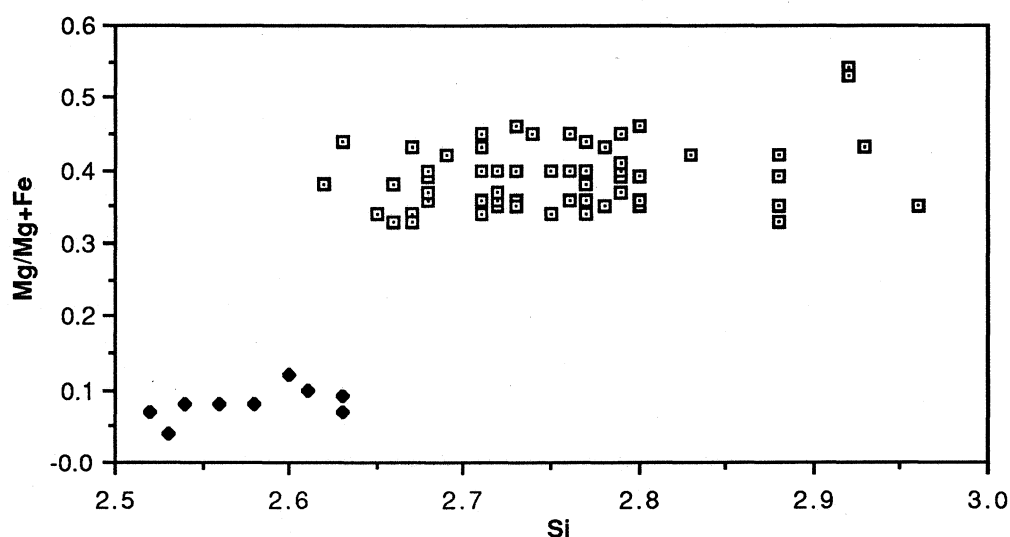


Fig. 6-4. Plot of Mg/Mg+Fe vs tetrahedral Si of chlorites (filled diamond: Chlorite in the Ardlethan Granite, open square: Chlorite in the Mine Granite). Chlorite in the Mine Granite has higher Mg/Mg+Fe than chlorite in the Ardlethan Granite.

Table 6-5: Summary and average compositions of chlorite with purple interference colours in massive chlorite bands from a total of 16 analyses (see appendix 1 for full analyses)

Components	wt%	Range
SiO ₂	25.38	24.00 -- 26.27
TiO ₂	0.01	0.00 -- 0.04
Al ₂ O ₃	21.52	19.13 -- 22.56
FeO	29.21	27.07 -- 31.80
MnO	0.13	0.00 -- 0.35
MgO	11.34	7.66 -- 13.05

The variation of FeO, MgO, and Mg/Mg+Fe from the relatively fresh Mine Granite, to altered Mine Granite, and to the Ardlethan Granite

supports the interpretation that the alteration in the Mine Granite was caused by fluid from the Ardlethan Granite.

6.5 Tourmaline

Based on textural characteristics tourmalines in the Ardlethan Tin Field can be classified into five types (see Chapters 2 & 5). They are the nodular tourmaline in the Ardlethan Granite, the patchy tourmaline in fractures in Mine Granite fragments in the Mine Granite breccia pipe and sediment fragments in the Carpathia-Blackreef and Stackpool-Godfrey breccia pipes, the granular tourmaline in the Mine Granite Breccia Pipe, the acute tourmaline in the Carpathia-Blackreef-Stackpool-Godfrey Breccia Pipes and the secondary breccia pipes in the Ardwest deposit, and the radiating tourmaline in the White Crystal Breccia Pipe.

The compositional variation in these five types of tourmaline can be described in terms of a solid solution between $\text{NaFe}_3\text{Al}_6[\text{Si}_6\text{O}_{18}][\text{BO}_3]_3[\text{OH},\text{F}]_4$ and $\text{NaMg}_3\text{Al}_6[\text{Si}_6\text{O}_{18}][\text{BO}_3]_3[\text{OH},\text{F}]_4$ if the variation of Si is omitted (Table 6-6).

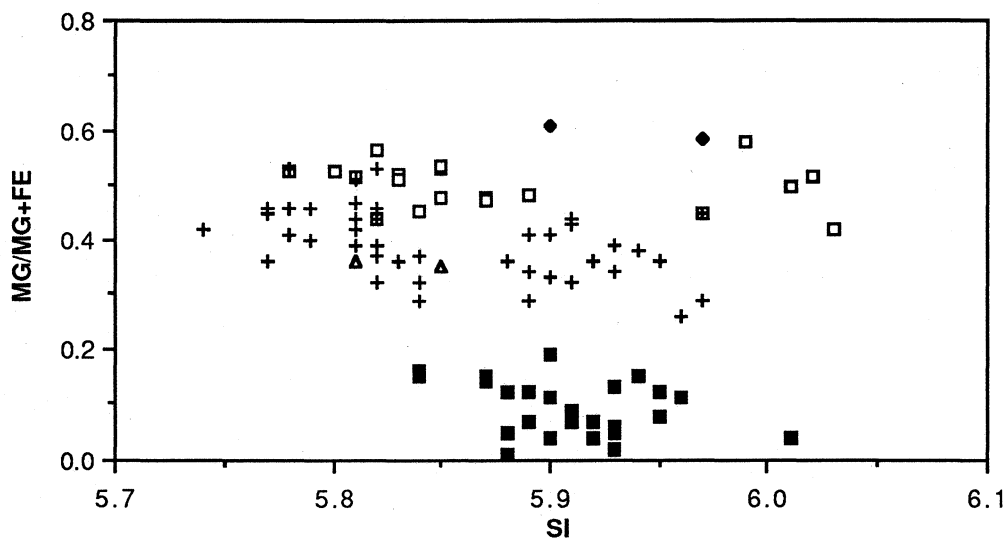


Fig. 6-5 Mg/Mg+Fe vs Si(t) plot of tourmalines (filled square: nodular tourmaline, cross: acute tourmaline, triangle: radiating tourmaline, open square: granular tourmaline and filled diamond: patchy tourmaline).

The nodular tourmaline in the Ardlethan Granite contains the lowest MgO and highest FeO (Table 6-6). The average FeO contents of the radiating and acute tourmalines are higher than the granular and patchy tourmalines (Table 6-6). This compositional variations may also support the interpretation that the hydrothermal alteration was caused by fluid from the Ardlethan Granite.

Table 6-6: Mean compositions of tourmaline

N. Ana.	N. tour.	R. tour	A. tour	G. tour	P. tour
	28	2	42	19	2
SiO ₂	35.39	35.71	34.47	36.04	35.61
TiO ₂	0.16	0.01	0.45	0.56	N.A.
Al ₂ O ₃	32.82	34.75	32.53	33.45	31.89
FeO	16.50	10.72	10.77	9.27	6.63
MnO	0.08	0.00	0.00	0.01	0.00
MgO	0.97	3.60	3.96	5.23	6.63
K ₂ O	0.04	0.05	0.04	0.02	0.00
Na ₂ O	2.44	1.74	2.05	2.05	1.72
CaO	0.00	0.25	0.27	0.50	0.24
Total	88.40	86.83	84.53	87.11	84.96

Calculated unit cell (based on 3 B and 31 O, OH and F)

Si	5.91	5.81	5.71	5.88	5.94
Ti	0.02	0.00	0.06	0.07	0.00
Al	6.46	6.69	6.35	6.43	6.27
Fe	2.30	1.58	1.49	1.27	1.10
Mn	0.01	0.00	0.00	0.00	0.00
Mg	0.24	0.88	0.98	1.27	1.65
K	0.01	0.01	0.01	0.00	0.00
Na	0.80	0.56	0.67	0.66	0.57
Ca	0.00	0.05	0.05	0.09	0.05

N.tour: Nodular tourmaline; R.tour: Radiating tourmaline; A.tour: Acute tourmaline; G.tour: Granular tourmaline and P.tour: Patchy tourmaline.
N.A. Not analyzed

6.6 Siderite

As described in Chapter 5, there are two generations of siderite in the Ardlethan Tin Field: an earlier generation formed during the cassiterite and sulphide mineralization, and a later generation formed during cosalite mineralization. Two samples (RD36 and RD33) were prepared for microprobe analyses. Sample RD33 contains the earlier generation siderite and sample RD36 contains both generations of siderite.

The two generations of siderite have distinctive compositions. The siderite formed during cassiterite and sulphide depositions contains around 47 wt% FeO, between 4 and 10 wt% MgO, and less than 1 wt% MnO (Table 6-7). The later siderite contains between 2.6 and 4.87 wt% MnO. The distinctively higher MnO contents of the latter siderite support the interpretation derived from isotope study that the cosalite mineralization is an independent event (see Chapter 8).

Table 6-7: Compositions of Siderite

Sample (G)	FeO	MnO	MgO	CaO
RD36 E*	46.38	0.74	9.31	0.80
E	46.99	0.48	8.94	0.95
E	44.20	0.40	8.64	0.82
L	45.46	4.87	7.46	0.08
L	44.51	4.84	7.27	0.11
L	45.85	3.97	7.71	0.00
L	47.73	2.60	7.62	0.00
L	48.06	2.80	6.95	0.00
RD33 E	46.88	0.17	4.26	0.71
E	46.10	0.00	5.14	0.20
E	47.94	0.00	4.10	0.36

E: the earlier generation, L: the later generation

6.7 Cookeite

Cookeite is a Li-Al chlorite. Most of the reported occurrences of cookeite are in weathering profiles or as inclusions in other minerals (Cerny, 1970). The occurrence of hydrothermal cookeite in the breccia pipes in the Ardlethan Tin Field has been documented in detail by Ren *et al.* (1988). The analyses of five samples (WX06, WX23, WX27, WX28 and WX29) are presented in Table 6-8.

The calculated structural formula for the White Crystal cookeite is $(\text{Li}_{0.66}\text{Al}_{4.02}\text{Fe}_{0.003}\text{Mg}_{0.013}\text{K}_{0.017})[\text{Si}_{3.27}\text{Al}_{0.73}\text{O}_{10}](\text{OH})_8$ based on 14 oxygen equivalent. Compared to the ideal cookeite composition given by Brammall *et al.* (1937), the White Crystal cookeite is significantly lower in Li, and consequently, has a low octahedral occupancy of 4.71, which is lowest of all reported values. The low Li is interpreted as the result of the substitution: $\text{Si}=\text{Al}+\text{Li}$, which may reflect its hydrothermal origin (Ren *et al.*, 1988).

6.8 Cosalite

Three samples of cosalite were analyzed using a WDEM and pure metal standards for Bi, Au, Pb, Cu, Ag, S and Sb. The data indicates that the ranges of variations of each components are all very narrow for all the analyses. Table 6-9 lists all the mean composition of the analyses. Compared to the ideal composition ($\text{Pb}_2\text{Bi}_2\text{S}_5$), cosalite from the Ardlethan Tin Field has a high Cu content and a very high Ag content (Table 6-9).

Table 6-8: Chemical analyses of cookeite from samples collected in the White Crystal deposit.

Oxides	WX06	WX23	WX27	WX28	WX29
SiO ₂	36.09	36.94	36.12	36.13	37.12
Al ₂ O ₃	45.06	45.34	45.36	44.84	44.91
FeO	<0.04	0.04	0.07	0.05	0.05
MgO	0.11	0.09	0.09	0.10	0.10
CaO	0.06	0.08	0.09	0.09	0.09
Na ₂ O	0.03	0.05	0.06	0.03	0.05
K ₂ O	0.14	0.13	0.19	0.16	0.14
Li ₂ O	1.87	1.82	NA	NA	NA
Total*	83.40	84.49	83.40	83.28	84.31

Calculated structural formula

Si(T)	3.241	3.267	3.288	3.249	3.294
Al(T)	0.759	0.733	0.712	0.751	0.706
Al(O)	4.010	3.993	4.005	4.002	3.991
Fe	0.000	0.003	0.005	0.004	0.004
Mg	0.015	0.012	0.012	0.013	0.013
Ca	0.006	0.008	0.009	0.009	0.009
Na	0.005	0.009	0.010	0.005	0.009
K	0.016	0.015	0.022	0.018	0.016
Li*	0.668	0.658	0.665	0.669	0.660

*Total and formula unit for analyses from WX27, WX28 and WX29 were calculated using the average of 1.85 wt% Li₂O. Li analysis was done by Atomic Absorption Spectroscopy. Other major components were analysed with a Wave Dispersive Electron Microprobe

Table 6-9: Chemical analyses of Cosalite

Sample	RB1	RB10	RD136
N. Ana.	2	9	4
Pb (wt%)	34.84	34.69	33.71
Bi (wt%)	44.79	45.00	44.65
Cu (wt%)	0.69	0.68	0.70
Ag (wt%)	2.20	2.21	2.16
Sb (wt%)	1.29	1.27	1.39
S (wt%)	17.33	17.05	16.90
total	99.85	100.9	99.51

6.9 Summary

The biotite, tourmaline, muscovite and chlorite in the Ardlethan Granite have higher FeO and lower MgO contents than those in the relatively fresh Mine Granite. Those formed in alteration zones in the Mine Granite through rock-fluid reactions are generally of intermediate composition. Those variations supports an interpretation that the fluid responsible for the alteration and mineralization was derived from the Ardlethan Granite.

Siderite in association with cosalite mineralization contains higher MnO than that in association with cassiterite and sulphide mineralization. This supports the interpretation from stable isotopes (Chapter 8) that cosalite mineralization was an independent hydrothermal event. The chlorite with purple interference colour in massive chlorite bands contains higher MgO than all the other types of chlorite. This may imply that the fluids which deposited this chlorite were not from the Fe-rich, Mg-poor Ardlethan Granite, therefore supporting the conclusion derived from the isotope evidence (see Chapter 8).

Chapter 7 FLUID INCLUSION STUDIES

7.1 Samples and Microthermometry

Thirty five doubly polished sections were prepared for microthermometry from samples which contain nodular quartz, milky quartz, clear quartz, toothy quartz, fluorite, topaz, sphalerite and cassiterite. They were sampled from the Wildcherry, the Ardwest, the Wildcherry South, the Blackreef and the White Crystal deposits and from the Ardlethan Granite. In addition, about 250 polished petrographic thin sections were examined for types of fluid inclusions trapped in quartz, siderite, fluorite and cassiterite. Special attention was given to the Blackreef and the White Crystal deposits.

A Linkam TH-600 heating and freezing stage was used to carry out the microthermometry measurements. It has a designed temperature range between -180°C and 600°C . The stage was calibrated using organic and metal alloy cells for temperatures between -70°C and 500°C . The standard deviation of a single temperature measurement is roughly $\pm 0.5^{\circ}\text{C}$ between -20 and 100°C and $\pm 5^{\circ}\text{C}$ above 100°C .

Most of the samples contain large numbers of fluid inclusions. It is common to see hundreds of fluid inclusions in a tiny piece of quartz but most are too small to be measured accurately. Their occurrence in clusters along fracture surfaces indicate that most of them are secondary (Konnerup-Masden, 1977; Eadington, 1977; Roedder, 1981).

The microthermometry study included identifying phases; visually estimating the relative abundances of each phase (V%) and measuring the temperatures of dry ice melting (T_{m,CO_2}); ice melting ($T_{m,\text{ice}}$); clathrate melting ($T_{m,\text{cl}}$); homogenization of liquid and gas CO_2 (T_{h,CO_2}); daughter NaCl dissolution ($T_{m,\text{NaCl}}$); and the complete homogenization of the fluid phases (T_H).

Measurements were obtained by firstly freezing the sample to very low temperatures and then heating it very slowly ($1^{\circ}\text{C}/\text{minute}$) to observe the various phase changes and record the temperatures.

7.2 Types of Fluid Inclusions

Five types of fluid inclusions (Fig. 7-1) were recognized in samples from the Ardlethan Tin Field (Table 7-1).

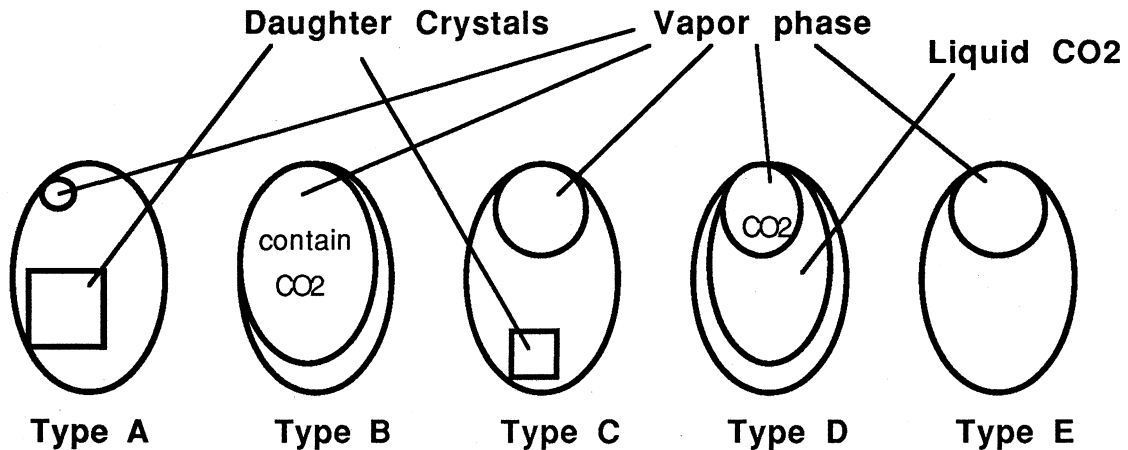


Fig. 7-1 Schematic diagrams of types of fluid inclusions in the Ardlethan Tin Field. The aqueous phase in each type is unmarked

7.2.1 Type A Fluid Inclusions

Type A fluid inclusions contain three phases: a NaCl daughter crystal which is indicated by the regular or slightly modified cubic shapes (up to 25% of the total volume); a vapor bubble (less than 10% of the total volume) which probably contains mainly CO₂; and an aqueous phase. Type A fluid inclusions occur only in the Ardlethan Granite (Table 7-1). They have irregular shape and some of them have sharp tails. They mostly occur as isolated inclusions suggesting a primary origin. However, their irregular shapes, especially the sharp tails suggests a high probability of change after trapping.

Table 7-1: Types of fluid inclusions and their hosts

Types	Descriptions	Hosts
Type A	Super saline	Quartz in the Ardlethan Granite
Type B	Vapor rich	Quartz in the Ardlethan Granite
Type C	Saline	Quartz in the Ardlethan Granite
Type D	CO ₂ rich	All samples
Type E	H ₂ O rich	All samples

The vapor bubbles in type A fluid inclusions decrease in size very

quickly when heated and homogenize into the aqueous phase at temperatures between 130 and 270°C (Table 7-2). The corners of the daughter crystals usually dissolve firstly and the crystals dissolve completely between 290 and 485°C (Table 7-2). Three exceptions were observed in samples TH08 and TH10 in which their large halite daughter crystals did not homogenize at the highest temperature achieved, about 500°C.

7.2.2 Type B Fluid Inclusions

Type B fluid inclusions contain two phases: a relatively large vapor bubble (55 to 80% by volume) and an aqueous phase. They occur in the Ardlethan Granite (Table 7-1). As with type A fluid inclusions, type B fluid inclusions also occur as isolated inclusions and have irregular shapes.

Type B fluid inclusions homogenize in a wide temperature range from 270 to 500°C. Most of them homogenized into aqueous phase but several appeared (see following) to homogenize into vapor phase. Several type B fluid inclusions failed to homogenize at the highest working temperature (500°C). Double freezings of clathrate and ice were observed in some cases, indicating that the vapor phase is mainly CO₂. The ice melting temperatures are mostly between -16 and -22.0°C (Table 7-2).

7.2.3 Type C Fluid Inclusions

Type C fluid inclusions contain an aqueous, a daughter crystal and a vapor phases. As with type A and type B, type C fluid inclusions occur only in the Ardlethan Granite (Table 7-1). The vapor bubbles in type C fluid inclusions are larger (10-16% of total volume) and the daughter crystals smaller than those of type A fluid inclusions. Type C fluid inclusions also occur as isolated and have regular elongated shapes suggesting that they are well preserved primary inclusions.

The population of type C fluid inclusions is extremely small and only three have been measured. The determined $T_{m,NaCl}$ is at $275 \pm 25^\circ\text{C}$ and T_H at $380 \pm 10^\circ\text{C}$ (Table 7-2).

7.2.4 Type D Fluid Inclusions

Type D fluid inclusions contain an aqueous phase, a CO₂-rich vapor phase and a liquid CO₂ phase. The proportions of vapor and liquid CO₂ phases range between 13 and 95% by volume (Table 7-2).

Table 7-2: Tabulated fluid inclusion data

The Ardlethan Granite: Type A					
ID	Sample/Host##	T _H (°C)	Vapor V%	T _{m,NaCl}	NaCl wt%
F213#	TH12/Q	260	5	410	40
F432#	TH1/Q	256	7	284	37
F452#	RDS65/Q	133	5	248	34
F453#	RDS65/Q	112	8	304	38
F454#	RDS65/Q	167	6	270	37
F457#	TH8/Q	141	8	251	34
F458#	TH8/Q	217	10		36
F459#	TH8/Q	134	5	420	49
F501#	TH1/Q	166	5	485	55
F502#	TH1/Q	203	10	385	45
F507#	TH1/Q	148	5	265	32
F508#	TH1/Q	169	7	367	46
F509#	TH1/Q	165	6	269	39
F607#	TH2/Q	205		381	65
The Ardlethan Granite: Type B					
ID	Sample/Host	T _H (°C)	CO ₂ V%	T _{m,ice}	NaCl wt%
F206#	TH12/Q	343	22		
F207#	TH12/Q	360	20		
F212#	TH12/Q	330	15		
F216#	TH12/Q	338	24		
F217#	TH12/Q	360	20		
F410#	TH4/Q	500	75	-16.0	19.7
F411#	TH 4/Q	498	75		
F421#	TH1/Q	488*	80		
F424#	TH1/Q	494	40		
F429#	TH1/Q	435	65	-11.1	15.2
F455#	RDS65/Q	435	50	-22.5	24.5
F503#	TH1/Q	304	30	-2.1	3.6
F504#	TH1/Q	311	26	-2.9	5.0
F602#	TH4/Q	328			
F606A#	TH4/Q	374	55		
F606B#	TH4/Q	374	60		
F606C#	TH4/Q	375*	65		
F615#	TH2/Q	381*	70		
F616#	TH2/Q	319	30		

Table 7-2: Continued

The Ardlethan Granite: Type C

ID	Sample/Host	T _H (°C)	Vapor V%	T _{m,NaCl}	NaCl Wt%
F404#	TH4/Q	377	10	268	29%
F405#	TH4/Q	390	14	298	31%
F619#	TH1/Q	385		251	28%

The Ardlethan Granite: Type D

ID	Sample/Host	T _{m,ice}	T _H	T _{h,CO2}	T _{m,CO2}	CO ₂ V%	T _{m,cl}	NaCl wt%
F407	TH4/Q	-23.2	209	23.0*		11		
F419	TH4/Q		336*		-56.8	85		
F425	TH4/Q	-8.9	197			10		
F426	TH4/Q		295	29.5*	-56.4	40	-0.1	15.4
F605	TH4/Q		336*	27.6	-56.8	90	1.7	13.4

The Ardlethan Granite: Type E

ID	Sample/Host	T _{m,ice}	T _H	Vapor V%	NaCl wt%
F201	TH12/Q		206	9	
F202	TH12/Q		209	10	
F203	TH12/Q		267	12	
F204	TH12/Q	-10.2	210	12	14.2
F205	TH12/Q	-10.6	210	8	14.7
F210	TH12/Q		280	17	
F211	TH12/Q	-10.1	210	11	14.0
F510	TH1/Q	-12.9	197	8	17.4
F511	TH1/Q	-9.3	184	8	13.3
F512	TH1/Q	-14.9	194	9	18.7
F406	TH4/Q	-22.3	265	13	24.4
F408	TH4/Q	-23.5	225	11	25.1
F409	TH4/Q	-25.7	222	12	26.6
F414	TH4/Q	-26.7	236	13	27.1
F415	TH4/Q	-22.4	226	12	24.4
F417	TH4/Q	-24.3	230	10	25.6
F430	TH1/Q	-25.5	393	31	26.5
F434	TH2/Topaz		254	15	
F436	TH2/Topaz	-15.2	199	10	19.1
F437	TH2/Topaz	-25.2	297	18	26.2
F439	TH2/Q	-9.1	213	11	13.0
F605	TH4/Q		317	10	
F617	TH4/Q	-13.5	259	30	17.0
F618	TH2/Q	-14.1	332	25	17.5

Table 7-2: Continued

The White Crystal Deposit: Type D

ID	Sample/Host	T _{m,ice}	T _H	T _{h,CO2}	T _{m,CO2}	CO ₂ V%	T _{m,cl}	NaCl wt%
F1#	WX27/TQ	174*	27.4		80	8.8	2.4	
F4#	WX27/TQ	168*	28.4		90	9.2	1.6	
F3#	WX27/CQ	252*	27.3		88	9.4	1.2	
F46	WX07/MQ	270*	20.8*		80			
F339#	WX28/MQ	316	26.5*		75	2.5	12.6	
F336#	WX28/MQ	361*			70			
F343	WX28/CQ	241*	21.8*		86	9.6	0.8	
F353#	WX28/MQ	360			-58.8 45			
F364#	WX29/CQ	270	25.0		60	5.0	9.0	
F380#	WX29/CQ	250	23.0*		17	7.1	5.6	
F401#	WX28/MQ	306*	26.9*		-57.5 80	9.0	2.0	
F402#	WX28/MQ	310	28.8*		13	3.5	11.2	
F448#	WX05/CQ	249	23.0*		-57.1	2.7	12.3	
F462	WX04/CQ	218	26.7		75	1.5	13.9	
F481	WX13/Topaz	243	26.1*		60			
F601#	WX07/MQ	348*	21.0*		-57.8 65	7.6	4.5	
F603#	WX07/MQ	347*	23.2*		-57.0 75			
F604#	WX07/MQ	345*	23.1*		85			

The White Crystal Deposit: Type E

ID	Sample/Host	T _{m,ice}	T _H	Vapor V%	NaCl wt%
F7	WX27/CQ	-0.2	233	16	0.3
F8#	WX27/CQ		243	16	
F9 #	WX27/CQ		248	17	
F12	WX27/CQ	-3.1	195	8	5.2
F13#	WX06/TQ	-9.9	197	11	13.8
F17	WX06/TQ	-2.7	194	10	4.5
F23#	WX06/MQ		329	47	
F24#	WX06/MQ		269		
F25	WX06/MQ	-1.7	215	15	3.0
F26#	WX06/MQ		326	16	
F27	WX06/MQ	-11.9	213	17	15.7
F28#	WX06/MQ		311	50	
F31#	WX06/MQ	-15.2	338	16	19.2
F47	WX07/MQ		275	25	
F218#	WX23/Fluorite	-10.5	157	6	14.7
F219#	WX23/Fluorite	-10.9	155	6	15.0
F221#	WX23/Fluorite	-10.1	160	10	14.2
F222#	WX23/Fluorite	-13.6	167	8	17.5

Table 7-2: Continued

The White Crystal Deposit: Type E

ID	Sample/Host	T _{m,ice}	T _H	Vapor V%	NaCl wt%
F246#	WX07/Fluorite	-9.9	206	8	13.9
F249	WX07/Fluorite	-7.9	161	11	11.8
F251	WX07/Fluorite	-9.2	167	12	13.1
F252	WX07/Fluorite	-9.1	169	12	13.0
F253	WX07/Fluorite	-9.1	176	14	13.0
F256	WX07/Fluorite	-8.8	145	12	12.7
F257	WX07/Fluorite	-8.9	138	13	12.8
F259	WX07/Fluorite	-12.3	140	15	16.3
F260#	WX25/Fluorite	-22.3	234	15	24.4
F261#	WX25/Fluorite	-22.1	239	15	24.2
F269	WX26/TQ	-9.2	201	12	12.7
F270#	WX26/TQ	-10.2	219	11	14.2
F271	WX26/TQ	-9.8	201	10	13.7
F272#	WX26/TQ	-11.6	221	11	15.7
F273#	WX26/TQ	-9.7	231		13.5
F274	WX26/TQ	-10.1	206	11	14.2
F275	WX26/TQ	-9.8	222	13	13.7
F276	WX26/TQ	-9.7	217	13	13.6
F277	WX26/TQ	-12.0	219	12	16.0
F278	WX26/TQ	-9.5	198	13	13.5
F279#	WX26/TQ	-9.8	223	16	13.7
F280	WX26/TQ	-9.9	235	16	13.9
F281	WX26/TQ	-9.9	212	16	13.9
F282	WX26/TQ	-9.7	170	13	13.6
F284	WX26/TQ	-9.7	197	13	13.6
F285	WX26/TQ	-9.9	175	13	13.9
F286	WX26/TQ	-1.9	168	19	3.2
F290#	WX26/CQ	-9.1	253	15	13.2
F292#	WX26/CQ	-13.2	246	13	17.0
F293	WX26/CQ	-9.0	180	14	12.7
F294	WX26/CQ	-9.6	173	6	13.5
F295	WX26/CQ	-9.7	169	9	13.6
F296	WX26/CQ	-10.7	223	10	14.8
F297	WX26/CQ	-9.8	184	10	13.7
F298#	WX26/CQ	-10.1	235	9	14.1
F301#	WX26/CQ	-8.9	223	18	12.7
F302	WX26/CQ	-1.9	175	16	3.2
F303	WX26/CQ	-2.0	174	16	3.5
F304	WX26/CQ	-2.0	175	13	3.5
F305	WX26/TQ	-12.2	169	13	16.2
F306	WX26/TQ	-12.1	163	14	16.1
F307	WX26/TQ	-12.3	157	12	16.3
F308	WX26/TQ	-12.3	154	12	16.3

Table 7-2: Continued

The White Crystal Deposit: Type E

ID	Sample/Host	T _{m,ice}	T _H	Vapor V%	NaCl wt%
F312	WX28/CQ	-10.4	227	12	14.5
F313	WX28/CQ	-10.1	224	12	14.1
F315	WX28/CQ	-11.1	222	12	15.0
F316	WX28/CQ	-10.3	221	12	14.4
F317	WX28/CQ	-10.4	223	13	14.5
F318	WX28/CQ	-11.3	223	10	15.2
F322#	WX28/CQ	-10.8	229	13	14.8
F323#	WX28/CQ	-10.2	226	12	14.1
F324#	WX28/CQ	-11.9	228	13	15.8
F335	WX28/MQ	-9.7	223	13	13.6
F337#	WX28/MQ		317		
F338#	WX28/MQ	-9.8	317	14	13.7
F342	WX28/CQ	-10.1	240	14	14.1
F345	WX28/CQ	-8.3	252	15	12.0
F346#	WX29/MQ	-7.9	365	35	11.7
F347	WX29/MQ	-8.3	215	12	12.0
F348#	WX29/MQ	-8.3	360	28	12.0
F349	WX29/CQ	-9.5	228	11	13.4
F350	WX29/CQ	-9.6	227	13	13.5
F352	WX30/MQ	-10.2	225	13	14.1
F354	WX30/MQ	-9.8	176	8	13.7
F355	WX30/MQ	-11.0	210	10	15.1
F356	WX30/MQ	-11.0	204		15.1
F357	WX30/MQ	-9.8	207	11	13.7
F365#	WX29/CQ	-10.8	260	18	14.8
F367#	WX29/CQ	-8.6	246	10	12.4
F368#	WX29/CQ	-9.9	244	15	13.8
F369#	WX29/MQ		360	60	
F370#	WX29/MQ	-12.4	317	19	16.2
F371#	WX29/MQ		337	55	
F374	WX29/MQ	-8.5	202	10	12.2
F375#	WX29/MQ		355		
F376	WX29/MQ	-9.6	256	16	13.2
F377	WX29/MQ	-10.0	225	14	14.1
F378	WX29/MQ	-10.5	224	12	14.6
F381	WX29/MQ	-11.0	257	15	15.1
F382#	WX29/MQ	-10.2	354	65	14.3
F383	WX30/TQ	-8.8	193	11	12.6
F384	WX30/TQ	-8.9	198	12	12.8
F385	WX30/MQ	-10.0	220	14	14.1
F387	WX30/MQ	-10.3	187	17	14.4
F388	WX30/MQ	-10.2	246	17	14.3
F389#	WX30/MQ	-12.3	330	26	16.2

Table 7-2: Continued

The White Crystal Deposit: Type E

ID	Sample/Host	T _{m,ice}	T _H	Vapor V%	NaCl wt%
F480#	WX13/Topaz		359	12	
F449	WX05/MQ	-5.2	180	8	7.9
F450	WX05/MQ	-4.9	200	10	7.5
F461	WX04/MQ	-15.3	216	12	19.2
F463	WX04/MQ	-3.4	215	11	5.5
F464	WX04/MQ	-8.7	221	12	12.5
F466	WX04/MQ	-9.4	226	12	13.4
F467	WX04/MQ	-9.8	225	12	13.7
F468	WX04/MQ	-8.0	182	9	11.7
F469	WX04/MQ	-8.6	201	10	12.5
F471	WX04/MQ	-17.9	205	10	21.2
F622a	WX23/MQ	-11.7	217		14.2
F622b	WX23/MQ	-12.1	221		16.1
F626	WX23/MQ		325		
F627#	WX07/Sphalerite	-10.1	248	18	14.2
F628#	WX07/Sphalerite	-9.9	265	17	13.8
F629#	WX07/Sphalerite	-9.9	258	17	13.8

The Blackreef Deposit: Type D

ID	Sample/Host	T _{m,ice}	T _H	T _{H,CO2}	T _{m,CO2}	CO ₂ V%	T _{m,cl}	NaCl wt%
F41	RB3/MQ		198*	27.0		83		
F70#	RB12/CQ		260			40	3.0	11.8
F71#	RB12/CQ		260			43	3.1	11.5
F75#	RB12/CQ	-9.1	254			20		12.5
F180	RB21/CQ		221			17		
F188#	RB9/MQ		345	27.4*		75		
F189#	RB9/MQ		333*	26.6*		80		
F190#	RB9/MQ		330*	25.5*		80		

The Blackreef deposit: Type E

ID	Sample/Host	T _{m,ice}	T _H	Vapor V%	NaCl wt%
F34A	RB3/MQ	-17.0	195	8	20.5
F38	RB3/MQ	-13.1	214	12	17.4
F39	RB3/MQ	-14.0	213	12	17.9
F40	RB3/MQ	-22.0	198	10	24.2
F50	RB1/CQ	-8.2	205	16	12.1
F51	RB1/CQ	-13.7	187	21	17.7
F52	RB1/CQ	-9.8	241	14	14.0

Table 7-2: Continued

The Blackreef deposit: Type E					
ID	Sample/Host	T _{m,ice}	T _H	Vapor V%	NaCl wt%
F53#	RB1/CQ	-14.5	266	18	18.3
F54	RB1/CQ	-12.4	197	16	16.2
F56	RB1/CQ	-13.0	185	14	16.8
F56a	RB1/MQ		237	17	
F58	RB1/MQ	-15.0	304	13	18.8
F59	RB1/MQ	-3.9	195	18	6.3
F60	RB1/MQ	-4.4	178	17	6.8
F73	RB1/CQ	-10.5	156	10	14.7
F74#	RB1/CQ	-10.6	236	14	14.8
F77#	RB12/CQ	-10.0	262	14	14.0
F107	RB25/TQ	-0.5	101	5	1.0
F108	RB25/TQ	-2.3	137	7	3.9
F109	RB25/TQ	-5.1	119	4	8
F116#	RB25/TQ	-14.5	226	13	18.4
F117#	RB25/TQ	-13.4	223	11	16.5
F120#	RB25/TQ	-13.6	199	10	17.5
F121	RB25/TQ	-10.2	197	12	14.3
F122#	RB25/TQ	-11.4	208	15	15.4
F123	RB25/TQ	-3.7	171	10	6.0
F124	RB25/TQ	-4.4	156	9	7.0
F125	RB25/TQ	-2.8	160		4.8
F126#	RB10/TQ	-13.8	201	10	17.7
F127	RB10/TQ	-14.4	181	8	18.3
F128#	RB10/TQ	-11.7	201	14	15.7
F129#	RB10/TQ	-12.7	223	11	16.5
F130#	RB10/TQ	-13.0	233	11	16.9
F131	RB15/TQ	-12.6	187	14	16.4
F132 #	RB15/TQ	-12.7	192	15	16.5
F133	RB15/TQ	-8.8	213	12	12.6
F134	RB15/TQ	-13.5	195	10	17.3
F135	RB15/TQ	-12.1	206		16.1
F136	RB15/TQ	-12.3	202		16.2
F137	RB15/TQ	-12.0	184	12	16.0
F138	RB15/TQ	-11.3	213		15.3
F139#	RB15/TQ	-9.3	216	18	13.2
F140#	RB15/TQ	-11.3	209	15	15.4
F141	RB15/TQ	-11.6	195	14	16.1
F143	RB15/TQ	-11.0	173	9	15.1
F148#	RB20/TQ	-13.0	223	12	16.8
F149#	RB20/TQ	-12.3	216	10	16.1
F152#	RB20/TQ	-11.5	221	17	15.5
F158#	RB20/CQ	-12.8	220	14	16.8
F159#	RB20/CQ	-16.6	247	17	20.2

Table 7-2: Continued

The Blackreef deposit: Type E					
ID	Sample/Host	T _{m,ice}	T _H	Vapor V%	NaCl wt%
F160#	RB20/CQ	-14.6	264	19	18.5
F161#	RB20/CQ	-17.1	245	16	20.6
F162#	RB20/CQ	-14.4	275	18	16.3
F163	RB20/CQ	-14.5	210	15	16.4
F164#	RB20/MQ	-10.9	327	12	15.0
F165	RB20/MQ	-12.5	223	12	16.4
F166#	RB20/MQ	-12.4	227	12	16.3
F167#	RB20/MQ		338	20	
F168	RB20/MQ	-10.3	385	25	14.5
F169	RB21/CQ	-13.8	235	14	17.7
F170	RB21/CQ	-12.8	236	14	16.8
F171	RB21/CQ	-9.5	251	19	13.4
F172	RB21/CQ	-9.9	262	16	13.9
F173	RB21/CQ	-10.0	238	14	14.0
F176	RB21/CQ	-14.0	257	17	17.8
F177	RB21/CQ	-15.1	225	13	18.9
F181	RB21/CQ	-14.4	221	14	18.2
F182	RB21/CQ	-15.4	233	18	19.3
F186	RB21/TQ	-13.8	217	10	17.3
F191	RB9/MQ	-10.8	246	15	14.9
F192	RB9/MQ	-13.7	225	10	17.7
F194	RB9/MQ	-10.9	270	18	14.9
F610	RB3/MQ		304		
F610a#	RB3/MQ		351		
F610b	RB3/MQ		263		
F610c	RB3/MQ		283		
F610d	RB3/MQ		296		
F610e #	RB3/MQ		298		
F611a #	RB3/MQ		328	20	
F611b #	RB3/MO		335		
F611c #	RB3/MQ		337		
F611d #	RB3/MQ		344		

The Ardwest Group of Deposits: Type D								
ID	Sample/Host	T _{m,ice}	T _H	T _{H,CO2}	T _{m,CO2}	CO ₂ V%	T _{m,cl}	NaCl wt%
F91#	WC1/CQ	-10.8	249					
F476 #	WC1/CQ				-57.5			
F478 #	WC1/CQ		283	26.0	-57.5	50	3.9	11.5
F479 #	WC5/CQ		249	28.0*	-57.6	18		

Table 7-2 Continued

The Ardwest Group of deposits: Type E					
ID	Sample/Host	T _{m,ice}	T _H	Vapor V%	NaCl wt%
F81	WC01/MQ	-9.0	218	9	21.9
F82	WC01/MQ	-13.2	233	10	17.2
F83	WC01/MQ	-11.5	229	13	15.5
F84#	WC01/MQ	-13.6	341	14	17.6
F85	WC01/MQ	-12.5	327	14	16.4
F88	WC01/MQ	-12.0	310	15	14.9
F89	WC01/MQ	-10.8	213	20	14.9
F90	WC01/MQ	-10.7	202	18	14.8
F223	WC01/MQ	-11.2	221	11	15.2
F225#	WC01/MQ	-12.8	325	19	16.7
F226	WC01/MQ	-11.8	193	11	21.2
F472	WC05/MQ	-10.9	226	14	14.9
F473	WC05/MQ	-11.4	237	14	15.5
F613#	WY17/MQ	-18.2	372		21.3
F630#	WY17/Cassiterite		366		
F631#	WY17/Cassiterite		331		
F632	WY17/Cassiterite		273		

primary fluid inclusions

##Q: Quartz; MQ: Milky quartz; CQ: Clear quartz; TQ: Toothy quartz;

* homogenization into the vapor phase.

Type D fluid inclusions are found in quartz and fluorite crystals (Table 7-1) in all the deposits. They occur as isolated primary inclusions and also as secondary inclusions along fractures. Type D fluid inclusions are commonly large (mostly between 10 and 60 microns) and ideal for both freezing and heating studies.

A total of 12 measurements of T_{m,CO₂} of type D fluid inclusions were obtained ranging between -61.1°C and -56.8°C (Table 7-2). These values are lower than the the triple point (solid-liquid-vapor equilibrium) temperature of pure CO₂ (-56.6°C), indicating the presence of at least another component, most likely methane (CH₄), common in CO₂-rich fluid under reduced conditions (Walsh *et al.*, 1988).

The range of T_{m,cl} of type D fluid inclusions is between 0 and 8°C (Table 7-2). Type D fluid inclusions which contain high proportions of CO₂ (liquid+vapor) tend to have high values of T_{m,cl} generally. The CO₂ phases may homogenize to either liquid or vapor phase, indicating a relatively wide range of density. Type D fluid inclusions may homogenize to CO₂-rich vapor phase or the aqueous phase, depending on their initial volume ratios. The measured range of T_H is between 174 and 361°C

(Table 7-2).

7.2.5 Type E Fluid Inclusions

Type E fluid inclusions contain an aqueous and a vapor phases, and are widely present in all the samples, comprising up to 95% of the total population of fluid inclusions in any given sample. The vapor bubbles occupy 10-18% of the inclusion by volume, but may be as low as 5%. Like type D fluid inclusions, type E fluid inclusion may occur in isolation as primary inclusions or along microfractures as secondary inclusions.

They homogenize to the aqueous phases at temperatures between 120 and 370°C, with the majority homogenizing in a range between 180 and 250°C (Table 7-2).

The $T_{m,ice}$ of type E fluid inclusions exhibits a wide range between -2 to -22°C with the majority between -9 to -16°C (Table 7-2). There is no apparent correlation between T_H and $T_{m,ice}$ for all type E fluid inclusions (Fig. 7-2).

7.3 Salinities of Fluid Inclusions

Salinities for type A and type C fluid inclusions were estimated using a volumetric method (Khaibullin *et al.*, 1980) based on the volume ratios of NaCl crystals and the aqueous phases and assuming NaCl saturation for the aqueous phases (Roedder, 1984). The estimated salinities are between 38 and 55 wt% NaCl for type A fluid inclusions and around 35 wt% NaCl for type C fluid inclusions (Table 7-2). The salinities of type A and type C fluid inclusions can also be estimated from $T_{m,NaCl}$ since the solubility of NaCl is a function of temperature. The results from the two methods are mostly consistent their ranges of uncertainty (about ± 5 wt% NaCl).

Roedder (1984) presented an empirical equation which can be used to calculate salinity from temperature depression of ice melting

$$\text{wt}\% = 1.7696\Delta T - 4.2384 \times 10^{-2} \Delta T^2 + 5.2788 \times 10^{-4} \Delta T^3 \pm 0.028 \quad (7.1)$$

in which wt% denotes the salinity in wt% NaCl, and ΔT the temperature depression of ice melting. Equation 7.1 is valid in the salinity range from 0 to 26 wt% NaCl. Fluid inclusions may contain constituents other than NaCl, such as KCl, CaCl_2 , CO_2 and etc, the temperature depressions of ice melting reflect the total effects of all the solutes in the aqueous phase

(Hedenquist & Henley, 1985b) and therefore the calculated salinity represents a NaCl equivalent salinity.

The majority of type E fluid inclusions from the Ardwest group of, Blackreef and White Crystal deposits has salinity between 12 and 18 wt% NaCl (Fig. 7-2). They occur in milky quartz, clear quartz, toothy quartz, fluorite and cassiterite crystals. There is no apparent correlation between salinities of fluid inclusions and their filling temperatures. Apparently, as cassiterite and sulphides are associated with milky and clear quartz, the salinity of the fluids responsible for cassiterite and sulphide deposition is approximately 16 wt% NaCl.

Some type E fluid inclusions from the White Crystal and the Blackreef deposits have low salinities between 2 and 9 wt% NaCl, their filling temperatures are mostly lower than 200°C (Fig. 7-2). They occur as primary inclusions only in toothy quartz and fluorite or as secondary inclusions in clear and milky quartz, suggesting that they are later than the cassiterite and sulphide deposition.

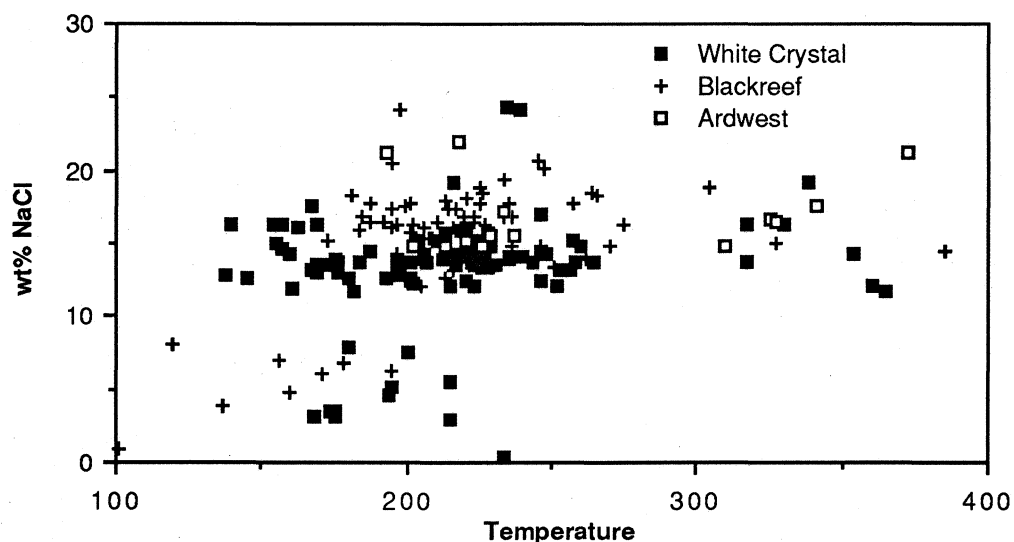


Fig. 7-2 Salinities and filling temperatures of type E fluid inclusions.

Equation 7.1 cannot be used to calculate salinities for type D fluid inclusions as the ice melting temperature are significantly affected by the formation of the gas hydrate (clathrate), which absorbs a significant amount of H₂O, therefore causing an increased salinity for the aqueous phase (Collins, 1979). Soluble CO₂ can depress the ice melting temperature even for fluid inclusions in which the amount of CO₂ is not large enough to form clathrate (Higgins, 1985). Hedenquist and Henley (1985b) reported a method for salinity calculation for fluid inclusions of known CO₂ concentrations. However, Collins' (1979) method of calculating the salinity from the temperature depression of clathrate

melting has been used for type D inclusions. Based on these calculations, type D fluid inclusions can be classified further into two groups: a low salinity, 0.2 to 3 wt% NaCl, group and a high salinity 14 and 17 wt% NaCl, group. The low salinity type D fluid inclusions have relatively large proportions of CO₂ and homogenize into the CO₂ phase, while the high salinity type D inclusions have relatively small proportions of CO₂ and homogenize to the aqueous phase.

Temperatures of clathrate melting of type B fluid inclusions were very difficult to measure and therefore their salinities cannot be estimated using the temperature depression of clathrate melting. The salinities calculated from temperature depressions of ice melting are up to 24.5 wt% NaCl (Table 7-2). These are apparently not precise salinities. However, as no liquid CO₂ presents in type B fluid inclusions, their mole fractions of CO₂ are probably not very high. Therefore the estimated salinities of type B fluid inclusions from temperature depressions of ice melting are probably not too much higher than real.

7.4 Type A, B and C Fluid Inclusions

Type A, B, and C fluid inclusions are all primary inclusions in the Ardlethan Granite. They coexist in quartz along the eastern margin of the Ardlethan Granite, particularly in the quartz-tourmaline nodules.

Type A fluid inclusions scatter above the NaCl-saturation line on salinity vs filling temperature plot (Fig. 7-3). Type C and type E fluid inclusions are below the NaCl-saturation line.

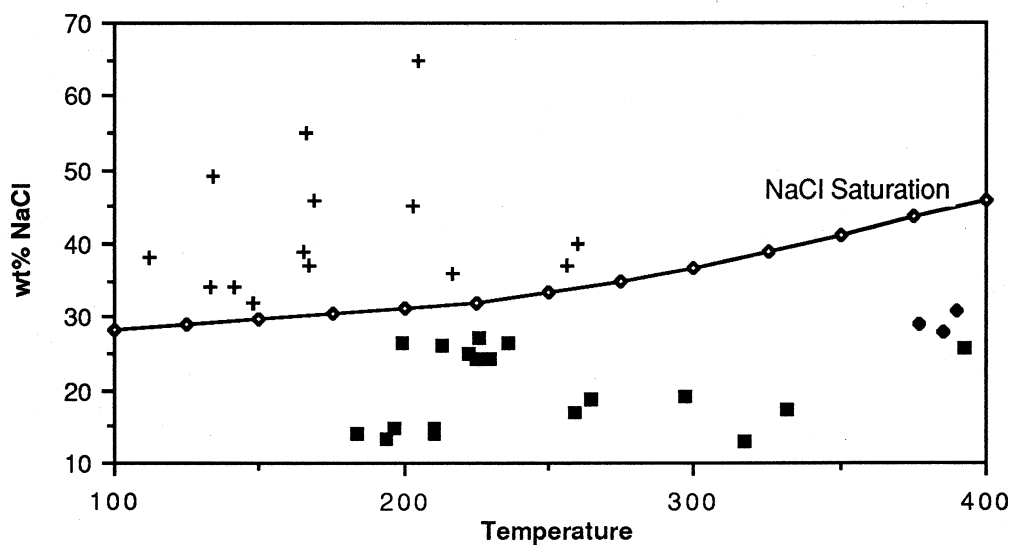


Fig. 7-3. Salinities and filling temperatures of fluid inclusions in the Ardlethan Granite. type A: +; type C: filled diamond; Type E: filled squares.

The wide ranges of filling temperatures and salinities of type A fluid inclusions, and their coexistence with type B and type C fluid inclusions indicate a complex genesis. The possibilities are:

1. heterogeneous trapping;
2. necking down;
3. pressure changes;
4. trapping of fluids below vapor saturation.

Ahmad and Rose (1982) discussed these possibilities and their trends in relation to NaCl-saturation line. According to their discussions, it is most likely that type A fluid inclusions have necked down.

The wide range of filling temperatures and relatively high salinities (up to 25 wt% NaCl) of some type B fluid inclusions indicate that they are not trapped vapor phase. They could be the results of heterogeneous trapping, or leaking or necking down. Consequently, the homogenization temperatures and salinities of type B fluid inclusions do not represent these of the parental fluid either.

Type C fluid inclusions are very scarce and only three were measured. Although their measured T_H and salinities show some consistency, there are not enough measurements to indicate whether or not they represent the characteristics of parental fluids.

In summary, type A, type B and type C fluid inclusions in the Ardlethan Granite probably all have suffered some change after trapping. These measurements do not represent the true characteristics of the parental fluids. However, they do reflect the complex geohistory of the Ardlethan Granite.

7.5 Temperatures of Mineralization

7.5.1 The Blackreef Deposit

Samples of quartz and fluorite from the Blackreef deposit contain type D and type E fluid inclusions. Examination of polished petrographic thin sections indicate that cassiterite, siderite and sphalerite in the Blackreef deposit also contain type D and type E fluid inclusions.

T_H of primary fluid inclusions, including both type D and type E, in milky quartz associated with cassiterite, arsenopyrite, tourmaline and

muscovite, are between 310 and 370°C, and mostly between 320 and 360°C. Large numbers of secondary type D and type E fluid inclusions also occur in these samples and they homogenize at much lower temperatures, between 150 and 300°C (Fig. 7-4). As type E fluid inclusions are H₂O-rich and type D CO₂-rich, their coexistence as primary inclusions in milky quartz implies that the system was CO₂ saturated and boiling during milky quartz deposition. Therefore no pressure correction is required. As cassiterite deposition was closely associated with milky quartz deposition (see Chapter 5) this indicates that the temperature of cassiterite deposition in the Blackreef deposit was between 310 and 370°C.

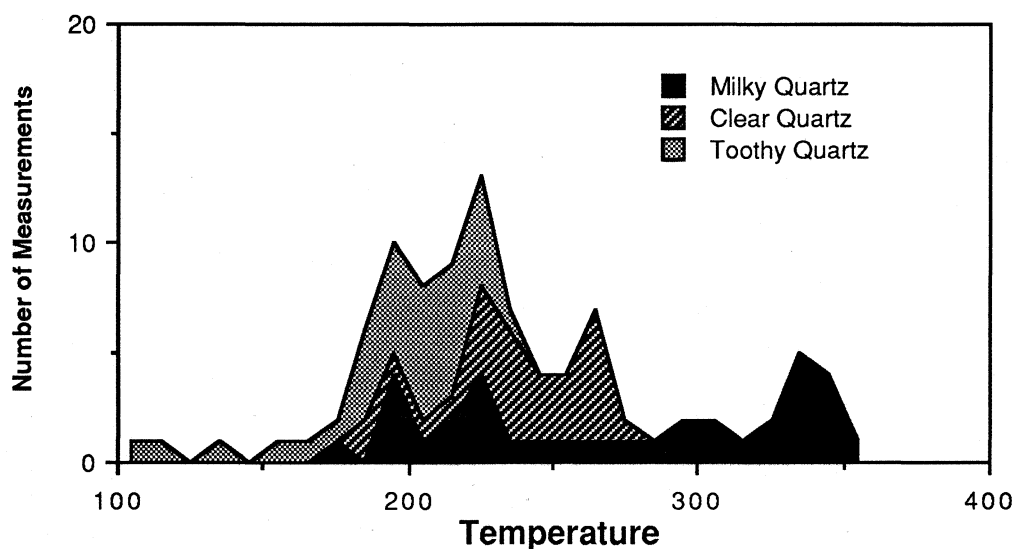


Fig. 7-4 Homogenization temperatures of fluid inclusions in the Blackreef deposit.

Measured T_H of primary type D and type E fluid inclusions in clear quartz are mostly between 220 and 270°C. No pressure correction is required either for the same reason. As clear quartz are associated with pyrite, chalcopyrite, sphalerite and galena (see Chapter 5), this indicates that the temperature of sulphide deposition in the Blackreef deposit was between 220 and 270°C. Clear quartz samples also contain secondary type D and type E fluid inclusions which homogenize at temperatures as low as 156°C (Table 7-2 & Fig. 7-4).

Homogenization temperatures of primary type D and type E fluid inclusions in toothy quartz and fluorite are mostly between 150 and 210°C. As mentioned above, many secondary fluid inclusions in milky and clear quartz also homogenize in this temperature range (Fig. 7-4), suggesting that they have been affected by the later hydrothermal fluids responsible for toothy quartz deposition.

It can be summarized that the homogenization temperatures of type D and type E fluid inclusions in the Blackreef deposit are strongly related to their host minerals (Fig. 7-4). The milky quartz contains inclusions trapped at in the whole temperature range but the primary ones were at high temperatures; the clear quartz contains primary inclusions trapped at intermediate temperatures and secondary ones at low temperatures, and the toothy quartz and fluorite contain only fluid inclusions trapped at low temperatures.

7.5.2 The White Crystal Deposit

Fluid inclusions in quartz, fluorite, topaz and sphalerite from the White Crystal deposit are type D and type E. Eadington (1985a) reported type C fluid inclusions with salinity up to 50 wt% NaCl in topaz from depth of the White Crystal breccia pipe.

Fourteen measurements of T_H of primary type E fluid inclusions in milky quartz samples in association with cassiterite are between 310 and 370°C. Seven type D fluid inclusions with the same association homogenized to CO₂-rich vapor phase at temperatures between 310 and 361°C. These data suggest that the temperatures of cassiterite mineralization at the White Crystal deposit were between 310 and 370°C. As with the Blackreef deposit, there are also large numbers of secondary type D and type E fluid inclusions which homogenize at lower temperatures in milky quartz and topaz (Fig. 7-5).

The homogenization temperatures of primary type E and type D fluid inclusions in clear quartz samples are between 210 and 270°C which are interpreted as the temperatures of sulphide deposition. Three primary type E fluid inclusions in a sphalerite sample homogenized at 248, 265 and 258°C respectively, which are in very good agreement with the above estimation. Again, there are many secondary fluid inclusions which homogenize at lower temperatures in the clear quartz samples (Fig. 7-5).

Primary fluid inclusions in toothy quartz and fluorite samples mostly homogenize at temperatures between 160 and 220°C for both type D and type E inclusions. Extremely low T_H were recorded in several type E fluid inclusions which homogenized between 110 to 150°C.

The T_H of secondary fluid inclusions of the White Crystal deposit are very similar to those from the Blackreef deposits. Milky quartz and topaz contain secondary fluid inclusions which give T_H values equivalent to these of the primary inclusions in the clear and toothy quartz, and the secondary fluid inclusions in the clear quartz give T_H values equivalent to

those of the primary inclusions in toothy quartz and fluorite.

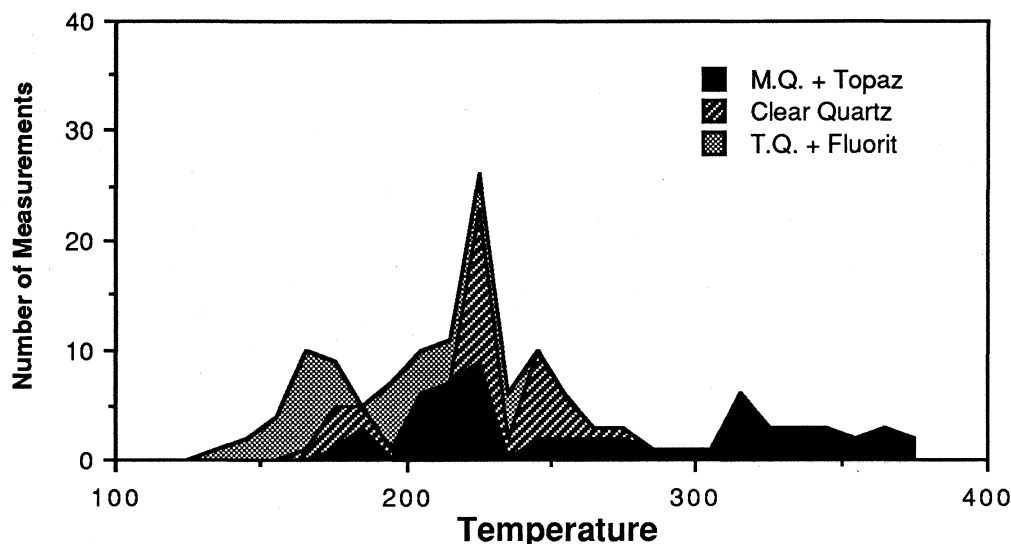


Fig. 7-5 Homogenization temperatures of fluid inclusions in the White Crystal deposit. M.Q. stands for milky quartz and T.Q. toothy quartz.

7.5.3 The Ardwest Group of Deposits

The types and homogenization temperatures of fluid inclusions in samples from the Ardwest group deposits are very similar to those from the Blackreef and the White Crystal deposits. Temperatures of cassiterite mineralization suggested by primary type E fluid inclusions in milky quartz are between 310 and 370°C, temperatures of sulphide mineralization suggested by primary inclusions in clear quartz samples are between 230 and 270°C, and the temperatures of toothy quartz, fluorite and cookeite deposition are between 160 and 230°C (Table. 7-2). Two primary and one secondary fluid inclusions in a cassiterite sample (WY17) yielded homogenization temperatures of 366, 331 and 273°C respectively, which are in good agreement with the above interpretation.

7.6 Pressure of Mineralization

The co-existence of CO₂-rich and H₂O-rich fluid inclusions in the White Crystal deposit enables an estimate of trapping pressure. Takenouchi and Kennedy (1964) experimentally studied the H₂O-CO₂ binary system at high temperature and pressure and constructed a series of phase diagrams in P-X-T space. A plot of T_H against X_{CO₂} could be used to estimate pressure.

A special procedure outlined as following was used to estimate

X_{CO_2} in type D fluid inclusions. Firstly fluid inclusions of regular shape were selected and heated very slowly to observe the homogenization of liquid CO_2 and vapor CO_2 phases. This temperature (T_{h,CO_2}) was recorded with the highest possible precision, and at the same temperature the fluid inclusion was photographed. Then the negative was used to produce an enlarged image on a sheet of squared graph paper. The numbers of squares covered by CO_2 phase (N_1) and H_2O phase (N_2) were counted. By assuming the fluid inclusion and the CO_2 phase were both roughly spherical, the volume ratios can be calculated from

$$V_{CO_2}/V_{H_2O}=(N_1/N_2)^{3/2} \quad (7.2)$$

Because the solubility of CO_2 in the aqueous phase and the partial pressure of H_2O at temperature lower than $30^\circ C$ are both low (Greenwood & Barns, 1966), these two phases can be assumed of essentially pure CO_2 and H_2O . The T_{h,CO_2} and the observation that whether the liquid CO_2 homogenizes to vapor phase or liquid phase are used to obtain the mean density of CO_2 phases from the phase diagram constructed by Hollister et al. (1981). Similarly, the density of H_2O at T_{h,CO_2} is obtained from Roedder and Bodnar (1980). The mole fraction of CO_2 in the fluid inclusion can be calculated from

$$X_{CO_2}=\frac{18D_{CO_2}}{44D_{H_2O}V_{H_2O}/V_{CO_2}+18D_{CO_2}} \quad (7.3)$$

in which D denotes the density of the subscribed phases. This method is similar to that used by Halley (1987), except that area counting is used instead of weighting in order to achieve a better precision. The precision of V_{CO_2}/V_{H_2O} estimation is improved for fluid inclusions with regular shapes as equation 7.2 is strictly valid for spherical inclusions.

Type D fluid inclusions of the White Crystal deposit are too scattered on T - X_{CO_2} plot (Fig. 7-6) to give a pressure estimate. However, they suggest pressures between 300 and 900 bars. After a salinity correction, by taking 3 wt% NaCl as the mean salinity, they become 450 and 1200 bars respectively using the data of Takenouchi and Kennedy (1964). This is similar to the results of Eadington and Paterson (1984) and Eadington (1985a).

7.7 Oxidation Conditions

The temperature depressions of solid CO_2 melting, T_{m,CO_2} , of type D fluid inclusions below $-56.6^\circ C$ suggest that methane is probably present.

The proportions of methane in CO₂ phase can be estimated using the experimental data of Arai *et al.* (1971) and phase diagram of Burrus (1981). This estimate can be used to calculate oxygen fugacities (Patterson *et al.*, 1981; Hedenquist and Henley, 1985b) from the following reaction



using

$$\log f_{\text{O}_2} = 0.5(\log f_{\text{CO}_2} - \log f_{\text{CH}_4} - \log K_{7.4}) \quad (7.5)$$

by assuming that the fugacity ratio of CH₄ and CO₂ equal to their mole fraction ratio. The value of logK_{7.4} at given temperature can be calculated from the thermodynamic properties of methane, CO₂, H₂O and O₂ and Helgeson's (1978) data were used in this study. The precision of this estimate depends much more on the measurement of temperature than the estimation of mole fraction ratios of methane and CO₂: an estimated error of X_{CH₄}/X_{CO₂} of 30% could only causes a consequent error of ±0.1 to the estimated logf_{O₂}, but a ±5°C uncertainty of measured T_H would cause an uncertainty of ±0.8 to the estimated logf_{O₂}.

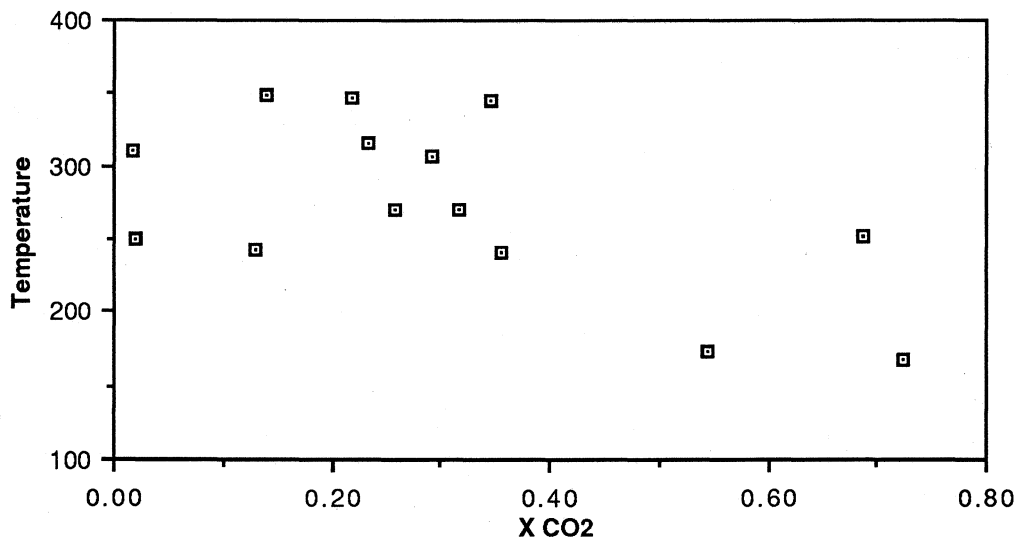


Fig. 7-6 Plot of homogenization temperatures vs estimated X_{CO₂} of type D fluid inclusions of the White Crystal deposit.

The calculated logf_{O₂} from fluid inclusions of the White Crystal, the Blackreef and the Wildcherry deposits are listed in Table 7-3. These values are below the hematite/magnetite buffer which is in good agreement with the mineral associations and other estimates (see Chapter 9).

Table 7-3: Oxygen fugacities estimated from fluid inclusions for the White Crystal, Wildcherry, and the Blackreef deposits

Run Id	T _H	CH ₄ %	logK _{7.4}	logf _{O₂}	Host
F71	260	2.1	74.0	-36.2	Blackreef
F401	306	4.1	68.8	-33.7	White Crystal
F478	283	4.1	71.4	-35.0	Wildcherry
F479	249	4.4	75.2	-36.9	Wildcherry
F353	360	10.8	63.4	-31.5	White Crystal
F623	298	16.0	69.8	-34.5	White Crystal
F625	326	6.2	67.0	-32.9	White Crystal

7.8 Summary and Conclusions

1. Fluid inclusion data suggest that in the Ardlethan Tin Field cassiterite deposition occurred between 310 to 370°C, sulphide deposition occurred between 220 and 270°C, and toothy quartz, fluorite and cookeite deposition occurred between 160 and 220°C.

2. Pressure estimate from type D fluid inclusions is not precise but it suggests a pressure between 450 and 1200 bars.

3. Temperature depressions of solid CO₂ melting suggest the presence of methane in type D fluid inclusions and yield a logf_{O₂} estimate of -31.5 at 360°C during cassiterite deposition, which is in agreement with the mineral association and those estimated from other methods (see Chapter 9).

Chapter 8

STABLE ISOTOPE STUDIES

Hydrothermal minerals, and fresh and altered Mine Granite were analyzed for oxygen, carbon, hydrogen and sulphur isotopes to study the origin and evolutions of the hydrothermal fluids responsible for the mineralization in breccia pipes in the Ardlethan Tin Field.

8.1 Carbon Isotopes

Eight siderite samples were analyzed for carbon and oxygen isotopes. Seven were vug infill siderite from the Wildcherry, Blackreef, Godfrey and White Crystal deposits and one was fracture infill siderite associated with cosalite, bismuthinite, native bismuth and cubic pyrite. The values of $\delta^{13}\text{C}$ relative to PDB standard (Craig, 1957) fall in a narrow range of 4.3 ± 1.0 per mil (Table 8-1).

Table 8-1: $\delta^{13}\text{C}$ values of siderite samples

Samples	Descriptions	$\delta^{13}\text{C}$ (per mil)
RD108	Vug infill siderite, Godfrey	-4.3
RB10	Vug infill siderite, Blackreef	-3.1
RB15	Vug infill siderite, Blackreef	-4.2
RB25	Vug infill siderite, Blackreef	-3.3
RB26	Vug infill siderite, Blackreef	-3.5
WY4	Vug infill siderite, Wildcherry	-5.1
WX29	Vug infill siderite, White Crystal	-4.5
RD35	Fracture infill with cosalite, Godfrey	-5.3

As vug infill siderite is associated with toothy quartz and fluorite, temperature of deposition is estimated to be in the range between around 180 and 240°C. The fractionation of carbon between siderite and aqueous CO_2 at such temperatures is not significant and therefore the values of $\delta\text{C}_{\text{siderite}}$ are approximately the same as those of CO_2 in the fluid.

According to Javoy *et al.* (1978), Ohmoto and Rye (1979) and

Taylor and Bucher-Nurminen (1986) and Taylor (1987), the fractionation between $\delta^{13}\text{C}_{\text{CO}_2}$ and $\delta^{13}\text{C}_{\text{fluid}}$ is strongly controlled by oxidation conditions and is very small at conditions which are not reduced enough for the formation of significant proportions of organic phases. Although methane occurs in CO_2 -rich fluid (see Chapter 7), its proportion is almost negligible compared to CO_2 . Therefore, the $\delta^{13}\text{C}_{\text{siderite}}$ values are very close to the values of $\delta^{13}\text{C}_{\text{fluid}}$ and are representative of the carbon source. The $\delta^{13}\text{C}$ values of -4.5 ± 1.0 per mil are within the range for magmatic carbon from a granitic source, but carbon from sedimentary or metamorphic rocks could have similar $\delta^{13}\text{C}$ values (Ohmoto & Rye, 1979).

8.2 Sulphur Isotopes

Table 8-2 is a list of the values of sulphur isotopes of sulphides from various deposits in the Ardlethan Tin Field. The $\delta^{34}\text{S}$ values of most of sulphide samples from the Ardlethan Tin Field fall in a narrow range between -2.0 and 2.5 per mil. Only five samples plot outside this range; two from pyrite associated with cosalite deposition have the highest values (12.2 and 10.4 per mil); the other three from pyrite and chalcopyrite from the Godfrey deposit exhibiting intermediate values (4.5 to 7.1 per mil). Based on mineragraphic data the latter appear to be mixtures of the two generations of sulphides, suggesting 'contamination' by the late cosalite mineralization.

The tight range of $\delta^{34}\text{S}$ values of the main stage sulphides indicates that they were deposited from hydrothermal solutions in which either H_2S was dominant or there was an exceptionally narrow range of physico-chemical conditions (Kelly and Rye, 1979). In this case the fluid appear to have been dominated by H_2S (see later discussion) so that the $\delta^{34}\text{S}$ of the total sulphur in the hydrothermal fluids was roughly equal to that of sphalerite (Ohmoto & Rye, 1979), which is about 0 per mil. This is a typical value for sulphur from an igneous source (Rye & Sawkins, 1974; Ohmoto & Rye, 1979; Taylor, 1987).

The much higher $\delta^{34}\text{S}$ values (>10 per mil) of pyrite and chalcopyrite formed during cosalite mineralization indicate that the fluid responsible for the cosalite mineralization contained much heavier sulphur. This implies a different source for the fluid, possibly from sedimentary rocks. As cosalite mineralization was late and overprinted the cassiterite and sulphide mineralization, it was likely to be an independent hydrothermal event which was not related to the cassiterite and sulphide mineralization.

Table 8-2: Sulphur isotope data#

Sample	Mineral	Deposit	$\delta^{34}\text{S}$ (per mil)
RD35*	FeS ₂	Godfrey	12.2
RB10	FeS ₂	Blackreef	1.0
RB26	FeS ₂	Blackreef	1.5
RD108	FeS ₂	Godfrey	0.2
WC25	ZnS	Wildcherry	0.8
RB4	ZnS	Blackreef	0.9
RB7	ZnS	Blackreef	-0.5
WX04	ZnS	White Crystal	-0.6
RD104	CuFeS ₂	Godfrey	-0.6
RB10	CuFeS ₂	Blackreef	0.7
RB33	PbS	Blackreef	-0.6
RD83*	CuFeS ₂	Godfrey	7.1
RB1	ZnS	Blackreef	-0.4
RB5	ZnS	Blackreef	0.8
RB5	PbS	Blackreef	-2.1
RB6a	ZnS	Blackreef	1.5
WX25	ZnS	White Crystal	-0.4
8382	FeS ₂	Wildcherry	-0.1
8417	CuFeS ₂	Wildcherry	0.4
8449	ZnS	Wildcherry South	1.0
DR7	FeS ₂	Godfrey	0.0
Dr9	FeS ₂	Godfrey	1.3
Dr10	FeS ₂	Godfrey	0.4
RD170*	CuFeS ₂	Godfrey	4.5
RD177	FeS ₂	Godfrey	0.8
RD188	FeS ₂	Godfrey South	2.4
RD191*	FeS ₂	Godfrey	6.2
RD192*	FeS ₂	Godfrey	10.4
RD195	FeS ₂	Godfrey	0.1
WX09	PbS	White Crystal	-2.1
75A2**	FeS ₂	White Crystal	1.6
75A7**	CuFeS ₂	White Crystal	2.0
75A11**	PbS	White Crystal	-1.6
75A11**	ZnS	White Crystal	0.8

#Sulphur isotope analyses were done by R. A. Both, Adelaide University

*Sulphides associated with cosalite mineralization

**S. S. Sun's unpublished data, 1985

The sulphide samples listed in Table 8-1 include two pairs of sphalerite and galena samples analyzed for sulphur isotope geothermometry (Ohmoto & Rye, 1979; Taylor, 1987). They gave temperatures of 260°C for the White Crystal deposit (sample 75A11) and 230°C for the Blackreef deposit (RB5). These temperatures are within the temperature ranges defined from fluid inclusion data (see Chapter 7).

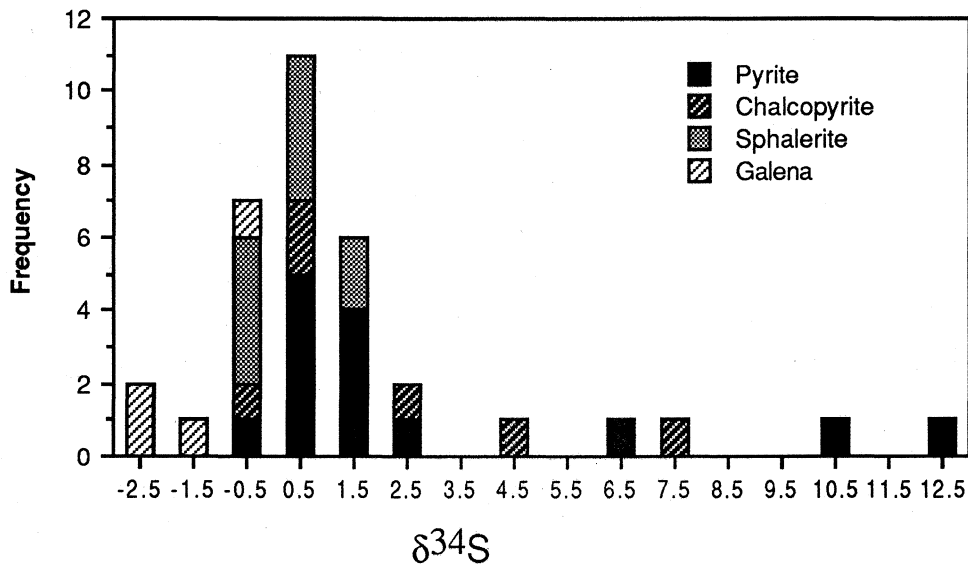


Fig. 8-1: Frequency plot of sulphur isotope values

The tight range of $\delta^{34}\text{S}$ values around 0 per mil of the main stage sulphur in the Ardlethan Tin Field is similar to the values for some other tin-tungsten deposits, for example, the Panasqueira tin-tungsten deposits, Portugal, and the Cleveland tin deposits, Tasmania. These are both interpreted as representing magmatic sulphur systems (Kelly & Rye, 1979; Collins, 1981). However, higher $\delta^{34}\text{S}$ values were reported in pyrrhotite-bearing tin deposits. Although the $\delta^{34}\text{S}$ values for pyrrhotite formed in the high temperature stage range between 0 and -2 per mil, these formed in the cassiterite stage range between 1 and 4.5 per mil (Halley 1987). The $\delta^{34}\text{S}$ values of pyrrhotite in association with the main stage of cassiterite deposition are around 6.3 ± 1 per mil at the Renison Bell tin deposit, Tasmania (Patterson *et al.*, 1981).

8.3 Oxygen Isotopes

8.3.1 Whole Rock Samples

Ten whole rock samples selected from the collection of Scott (1980) were analyzed for oxygen isotope compositions (unpublished data from S. S. Sun, 1985). Three of these were from the Ardlethan Granite, one from the Mine Porphyry and six from the Mine Granite. Table 8-3 lists the oxygen isotope compositions and gives brief descriptions of the samples.

The three fresh Ardlethan Granite samples have $\delta^{18}\text{O}$ values between 10.0 and 10.5 per mil, which are typical values for S-type granites (O'Neill and Chappell, 1977). The $\delta^{18}\text{O}$ value of 9.9 per mil for a Mine Porphyry sample suggests that it is isotopically very similar to the Ardlethan Granite. One fresh Mine Granite sample has a $\delta^{18}\text{O}$ value of

8.7 per mil, suggesting that the Mine Granite the oxygen isotope composition of the Mine Granite is probably lighter than the Ardlethan Granite and its daughter phases (Table 8-3).

Table 8-3: Oxygen isotope data of whole rock samples*

Sample	Rock	$\delta^{18}\text{O}_{\text{SMOW}}$	Description
67975	Ardlethan Granite	10.2	fresh
67961	Ardlethan Granite	10.0	fresh
67974	Ardlethan Granite	10.5	fresh
67962	Mine Porphyry	9.9	fresh
67961	Mine Granite	8.7	fresh
67901	Mine Granite	9.4	altered
67902	Mine Granite	10.4	altered
67886	Mine Granite	11.7	strongly altered
67889	Mine Granite	11.1	strongly altered
41070	Mine Granite	10.2	altered

*S. S. Sun's unpublished data, 1985

Five altered Mine Granite samples yielded $\delta^{18}\text{O}$ values between 9.4 to 11.7 per mil (Table 8-3). The highest $\delta^{18}\text{O}$ value corresponds to the most strongly altered sample which has a 3.0 per mil increase in $\delta^{18}\text{O}$ value in comparison to fresh Mine Granite. This clearly indicates that the result of rock-fluid isotope exchange is that the rock gained ^{18}O from the fluid.

8.3.2 Quartz Samples

Quartz samples were carefully selected for oxygen isotope analyses as follows: 1, doubly polished fluid inclusion sections were made; 2, microscopic examination of the fluid inclusions in each sample was undertaken and those containing good primary fluid inclusions were selected for oxygen isotope analyses; and 3, homogenization temperatures of the primary fluid inclusions were measured. Samples selected included the milky quartz in association with cassiterite and tourmaline, clear quartz in association with sulphides and the toothy quartz with fluorite and cookeite. One sample of quartz crystal within the quartz-tourmaline nodules in the Ardlethan Granite was also selected and analyzed. Table 8-4 lists the results of oxygen isotope analyses and descriptions of samples.

The values of $\delta^{18}\text{O}$ for all the quartz samples are very similar and fall in a very narrow range between 11.6 and 13.7 per mil regardless of the wide range of temperatures of deposition (Table 8-5), except for one

value of 8.2 per mil (RB26, Table 8-4). The $\delta^{18}\text{O}$ values of quartz from individual deposit are almost constant, 12.1 ± 0.5 per mil for the White Crystal deposit, 13.2 ± 0.7 per mil for the Blackreef deposit and 12.5 ± 0.6 per mil for the Wildcherry South deposit.

Table 8-4: Oxygen isotope## data of quartz samples

Sample*	Descriptions	Quartz types**	$\delta^{18}\text{O}_q$ (per mil)
TH12	Coarse Ard. Granite	Q. in Q-T nodule	11.9
WX06C	White Crystal ore	Clear quartz	12.1
WX23	White Crystal ore	Clear quartz	11.6
WX06T	White Crystal ore	Toothy quartz	12.1
WX25	White Crystal ore	Milky quartz	11.7
WX07	White Crystal ore	Milky quartz	13.1
67872	White Crystal ore	Toothy quartz	11.6
67968	White Crystal ore	Clear quartz	11.7
RD108	Godfrey ore	Milky quartz	12.4
RB26	Blackreef ore	Toothy quartz	8.2
RB20	Blackreef ore	Clear quartz	12.5
RB21	Blackreef ore	Toothy quartz	12.8
RB15	Blackreef ore	Toothy quartz	12.5
RB1	Blackreef ore	Clear quartz	12.9
RB9	Blackreef ore	Milky quartz	13.8
RB12	Blackreef ore	Clear quartz	13.2
RB3	Blackreef ore	Milky quartz	13.7
RB10	Blackreef ore	Clear quartz	13.4
RB23	Blackreef ore	Clear quartz	13.1
RB25	Blackreef ore	Clear quartz	12.5
RB15A	Blackreef ore	Toothy quartz	12.7
WY4	Wildcherry ore	Milky quartz	12.1
WY17	Wildcherry ore	Milky quartz	12.7
67883#	Wildcherry South ore	Clear quartz	12.3
67881#	Wildcherry South ore	Milky quartz	12.4
67853#	Ardwest ore	Clear quartz	12.9
67869#	Ardwest ore	Clear quartz	13.4
67880#	Ardwest ore	Milky quartz	13.2
67947#	Ardwest ore	Milky quartz	12.0

* Samples from which quartz were extracted for oxygen isotope analysis

**See chapter 5 for the definitions and descriptions of milky, clear and toothy quartz of the Ardlethan Tin Field

S. S. Sun's unpublished data, 1985

##Analyses done by Dr A. Andrew, CSIRO, Sydney

Plots of $\delta^{18}\text{O}$ values of quartz samples against the temperatures of depositions, i. e., the maximum fluid inclusion temperatures, show some correlations for the White Crystal and the Blackreef samples (Figs. 8-2 & 8-3).

The reason for a single low $\delta^{18}\text{O}$ value for toothy quartz sample

from the Blackreef deposit is not fully understood. However, as RB26 is very rich in cosalite (~5% cosalite by volume) this may reflect the characteristics of the fluid responsible for the cosalite deposition.

Table 8-5: Maximum fluid inclusion temperatures and calculated $\delta^{18}\text{O}$ values (per mil) for the fluids in equilibrium with quartz

Sample	T(°C)	$\delta^{18}\text{O}(\text{quartz})$	$\delta^{18}\text{O}(\text{H}_2\text{O})$
TH12	450	11.9	8.4
WX06	270	12.1	3.7
WX23	270	11.6	3.3
WX06A	200	12.1	0.1
WX25	330	11.7	5.4
WX07	348	13.1	7.3
67972	200	11.6	-0.4
67968	240	11.7	1.9
RD108	360	12.4	7.0
RB26	180	8.2	-5.2
RB20	223	12.5	1.8
RB21	217	12.8	1.8
RB15	210	12.5	1.1
RB1	266	12.9	1.4
RB9	333	13.8	7.7
RB12	260	13.2	4.3
RB3	330	13.7	7.4
RB10	233	13.4	3.1
RB23	260	13.1	4.2
RB25	226	12.5	2.0
RB15A	200	12.7	0.7
WY4	380	12.1	7.2
WY17	363	12.7	7.3
67883	270*	12.3	3.9
67881	360*	12.4	7.0
67853	270*	12.9	4.5
67869	270*	13.4	5.0
67880	360*	13.2	7.8
67947	360*	12.0	6.6

*These are the maximum temperatures of milky quartz and toothy quartz depositions as fluid inclusion temperatures are not available for S. S. Sun's samples

The calculated $\delta^{18}\text{O}$ values for fluids in equilibrium with quartz using the fractionation factor of Becker and Clayton (1976), except the lowest value from the cosalite rich sample (RB26), fall in a wide range between -0.4 and 7.7 per mil (Table 8-5). This mainly reflects the change of $\Delta_{\text{quartz-H}_2\text{O}}$ with temperature (Figs. 8-2 & 8-3).

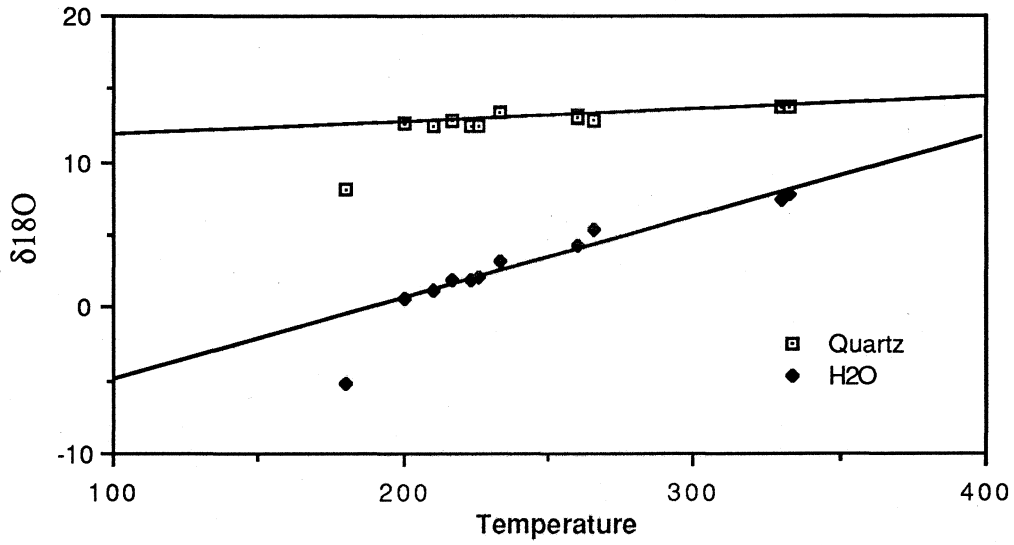


Fig. 8-2: Plot of $\delta^{18}\text{O}$ values of quartz (box) and calculated $\delta^{18}\text{O}$ of fluids (diamonds) against temperatures ($^{\circ}\text{C}$) of depositions of the Blackreef deposit.

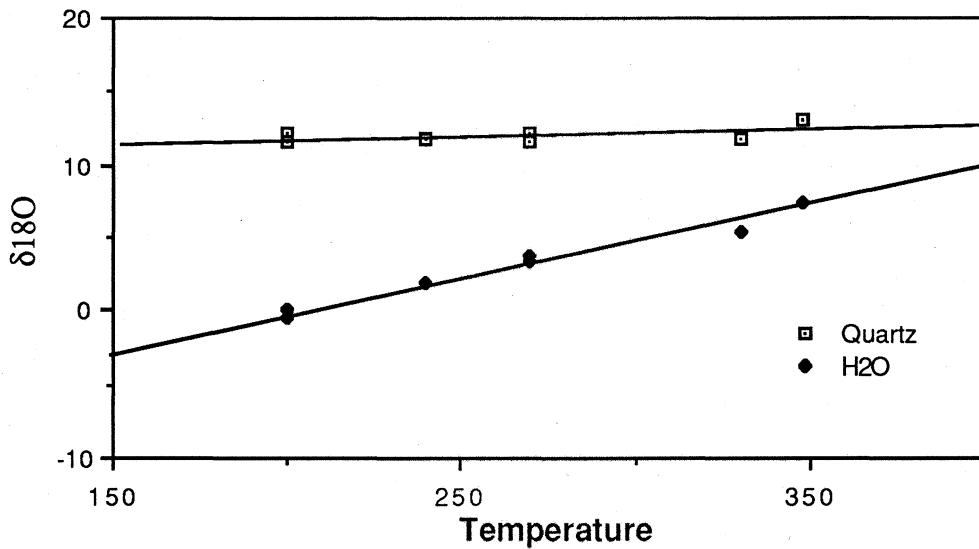


Fig. 8-3: Plot of $\delta^{18}\text{O}$ values of quartz (box) and calculated $\delta^{18}\text{O}$ of fluids (diamonds) against temperatures ($^{\circ}\text{C}$) of deposition of the White Crystal deposit.

8.3.3 Other Minerals

Five cassiterite samples were analyzed and they yielded $\delta^{18}\text{O}$ values in a very narrow range between 1.2 and 2.7 per mil (Table 8-6). These values are consistent with isotopic equilibrium between quartz and cassiterite at temperatures between 310 and 360°C using the fractionation factors proposed by Borshevskiy (1979), Patterson *et al.* (1981), Borshevskiy *et al.* (1983), and Sun and Eadington (1987).

Three chlorite samples from the Wildcherry South deposits yielded $\delta^{18}\text{O}$ values of 4.4, 5.9 and 7.2 per mil. A muscovite sample yielded a $\delta^{18}\text{O}$ value of 8.7 per mil and a cookeite (originally described as kaolinite) sample 8.5 per mil (Table 8-6). The $\delta^{18}\text{O}$ values of the eight siderite samples were also analyzed and they yielded $\delta^{18}\text{O}$ values between 9.8 and 11.3 per mil (Table 8-7).

Table 8-6: Oxygen isotope data of cassiterite, muscovite and chlorite samples

Sample	Description	Mineral	$\delta^{18}\text{O}$
67956*	Wildcherry Ore	Cassiterite	1.2
67947*	Wildcherry Ore	Cassiterite	1.8
67881*	Wildcherry Ore	Cassiterite	2.0
67878*	Wildcherry Ore	Cassiterite	1.8
WY4	Wildcherry South Ore	Cassiterite	2.7
67881*	Wildcherry Ore	Muscovite	8.7
67871*	Wildcherry Ore	Chlorite	4.4
WY17	Wildcherry South Ore	Chlorite	7.2
WY5	Wildcherry South Ore	Chlorite	5.9
67972*	White Crystal Ore	Cookeite**	8.0

*S. S. Sun's unpublished data, 1985

** This sample was originally called kaolinite and lately identified as cookeite

The muscovite sample (67881) was also analyzed for hydrogen isotopes which yielded a δD values of -76.6 per mil.

Table 8-7: Oxygen isotope data of siderite samples

Sample*	RD108	RD35	RB10	RB15	RB25	RB26	WY4	WX29
$\delta^{18}\text{O}$	9.8	9.6	11.3	10.7	11.1	9.8	10.2	11.3

* See Table 8-1 for sample descriptions

8.3.4 Oxygen Isotope Compositions of the Hydrothermal Fluids

The $\delta^{18}\text{O}$ compositions of the hydrothermal fluid are calculated from theoretical or experimental mineral-fluid fractionation factors as direct measurement of $\delta^{18}\text{O}_{\text{H}_2\text{O}}$ is difficult (Taylor, 1987). The analyzed $\delta^{18}\text{O}$ values of quartz, siderite, cassiterite, muscovite, chlorite and kaolinite samples of the Ardlethan Tin Field were used to calculate the $\delta^{18}\text{O}$ values of their coexisting fluid. The quartz-fluid and siderite-fluid oxygen isotope fractionation factors are from Becker and Clayton (1976), the muscovite-fluid and chlorite-fluid oxygen isotope fractionation factors are from Taylor (1987), and the cassiterite-fluid fractionation factor from Sun and Eadington (1987).

Trusdell (1974) tried to determine the salt effect on quartz-fluid fractionation for temperatures up to 270°C experimentally. His data suggested that a maximum of 2.0 per mil correction was needed for fluid of about 3 molal NaCl. But recent experimental investigations by Kendall *et al.* (1983) suggest that the salt effect is not significant. Studies of natural geothermal systems suggest that no correction for a "solute-effect" is needed to yield isotopic temperatures corresponding to those measured in drill holes (Taylor, 1987). Therefore, salinity corrections have not been considered in the following calculations.

The calculated oxygen isotope compositions from quartz-fluid fractionations for fluids of the Blackreef and White Crystal deposits are plotted together with those of quartz samples (Fig. 8-2 & 8-3). Reflecting the change of $\Delta_{\text{quartz-H}_2\text{O}}$, the calculated $\delta^{18}\text{O}$ values for fluid declined from around 8 per mil at around 360°C, to 5 per mil at around 260°C, and then to about 1 per mil at around 180°C. Similar results were obtained for the Wildcherry South deposit using Sun's unpublished data and the maximum fluid inclusion temperatures from milky quartz, clear quartz and toothy quartz.

As mentioned previously, the analyzed $\delta^{18}\text{O}$ values of cassiterite suggest that cassiterite was in equilibrium with milky quartz. Consequently, the $\delta^{18}\text{O}_{\text{H}_2\text{O}}$ values calculated from $\delta^{18}\text{O}_{\text{cass}}$ are consistent with those calculated from $\delta^{18}\text{O}$ of quartz. Using the average temperatures calculated from sheet silicate geothermometry for the formation of chlorite and muscovite (see Chapter 9), which are 240°C and 320°C respectively, the chlorite-fluid and muscovite-fluid fractionation factors of Taylor (1987), the calculated $\delta^{18}\text{O}$ values for fluid were about 4.0 per mil at 240°C and 6.6 per mil at 320°C, respectively. These are also in good agreement with the values calculated from quartz-fluid equilibrium. The $\delta^{18}\text{O}$ values for siderite also suggest similar $\delta^{18}\text{O}_{\text{H}_2\text{O}}$ values using the fractionation factors of Becker and Clayton (1976), and

the mean fluid inclusion temperatures of 210°C.

As the composition of cookeite ($\text{LiAl}_4\text{Si}_3\text{AlO}_{10}(\text{OH})_8$) is more akin to kaolinite than to the common Fe- or Mg-rich chlorite, the kaolinite-fluid fractionation (Taylor, 1987) was used to calculate the $\delta^{18}\text{O}_{\text{H}_2\text{O}}$. The calculated $\delta^{18}\text{O}_{\text{H}_2\text{O}}$ is 1.0 per mil at 180°C, which is consistent with the $\delta^{18}\text{O}_{\text{H}_2\text{O}}$ calculated from quartz-fluid fractionation for samples associated with the cookeite.

In summary, the $\delta^{18}\text{O}_{\text{H}_2\text{O}}$ calculated from mineral-fluid isotopic equilibrium suggests that the hydrothermal fluid responsible for the cassiterite and sulphide mineralization in the breccia pipes were very similar. $\delta^{18}\text{O}_{\text{H}_2\text{O}}$ values of fluid were between 6 and 8.0 per mil at high temperature (310 to 360°C), between 3 and 5 per mil at temperatures between 220 and 270°C, and about 1.0 per mil at temperatures between 170 and 200°C (Table 8-5). The fluid responsible for the cosalite deposition appears to be much lighter (-5.8 per mil).

8.4 Origin of the Hydrothermal Fluids

8.4.1 A Mixing Model

The continued decrease of $\delta^{18}\text{O}_{\text{H}_2\text{O}}$ from around 8.0 per mil down to about 0 per mil makes it difficult to assess the origin and evolution of the hydrothermal fluid. On the first glance, leaving aside the lowest values (-5.8 per mil) associated with cosalite deposition, it appears that the data can be interpreted by a simple fluid mixing model involving:

1: A dominantly magmatic fluid at the high temperature stage of cassiterite deposition,

2: A mixed fluid of about equal proportions of magmatic and meteoric fluids at the intermediate temperature stage of sulphide deposition,

3: A dominantly meteoric fluid at the low temperature stage of toothy quartz, fluorite and cookeite deposition,

if it can be assumed that the system was fluid-buffered.

The narrow ranges of oxygen isotope compositions of quartz, cassiterite, chlorite and siderite do not support a mixing model. The decrease of the calculated oxygen isotope compositions for fluid reflects apparently the change of $\Delta_{\text{mineral-H}_2\text{O}}$ with decreasing temperature only.

If there had been a fluid mixing and the system had been fluid-buffered, a decrease of $\delta^{18}\text{O}$ for hydrothermal minerals, such as quartz, would have produced. Apparently this does not occur with the cassiterite and sulphide deposition. The lowest $\delta^{18}\text{O}_{\text{H}_2\text{O}}$ value may suggest a different fluid, but this was very late and only responsible for the cosalite deposition.

Other evidence of fluid mixing is also lacking. The sulphur isotope and carbon isotope data representing the cassiterite and sulphide deposition all fall in very narrow ranges and therefore they do not support a simple mixing model either. Eadington (1985a) discussed fluid inclusion salinity data which he interpreted as results of a mixing of high saline magmatic fluid and very low saline meteoric fluid. However, as described in Chapter 7, the salinities of the fluid inclusions representing the fluid responsible for the cassiterite and sulphide deposition in the Ardlethan Tin Field do not show any apparent trend of change with temperature and therefore do not support a mixing model.

8.4.2 A Dynamic Evolution Model

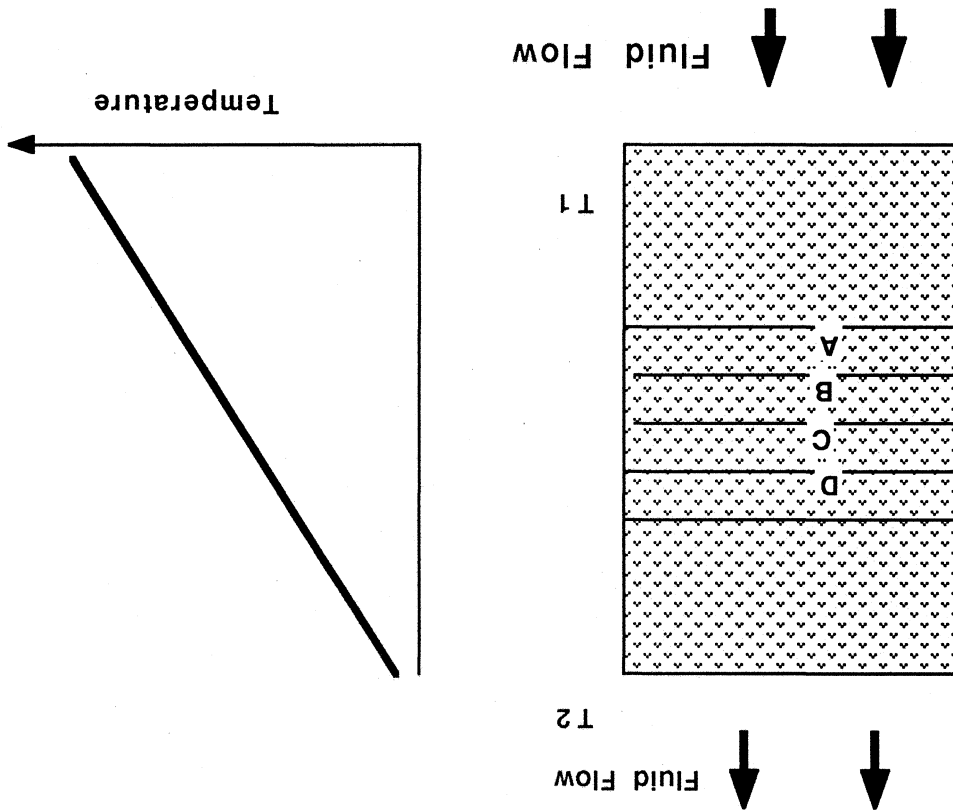
A dynamic model which assumes continuous equilibrium between a magmatic fluid and rock is used to interpret the near constant $\delta^{18}\text{O}$ values for quartz and the declining $\delta^{18}\text{O}$ values for fluid towards low temperatures. This model interprets the cassiterite and sulphide mineralization as a result of passing a large amount of magmatic fluid through the breccia pipes. As any packet of fluid flowed through a breccia pipe, it reacted with rocks, cooled and deposited sequentially cassiterite and milky quartz, sulphides and clear quartz, and fluorite, cookeite and toothy quartz. The breccia pipes were basically receptive media open to the fluid which entered the breccia pipes at depth and left the breccia pipes at higher levels (surface?). While the overall amount of fluid that passed through the breccia pipes could be very large, the instantaneous amount of fluid reacting with rocks was small as open space in the breccia pipes was limited. This is equivalent to a multi-stage process in which each stage has a very small fluid/rock ratio. The isotopic compositions of the fluid in the breccia pipes would under these circumstances tend to be buffered by the rocks in the breccia pipe and would decline with temperature as a result of the increase of $\Delta_{\text{rock-fluid}}$ with declining temperatures. The rocks would become isotopically heavier very slowly with the continuous fluid flow in the breccia pipes. Each packet of fluid that flowed through the breccia pipes contributed to a tiny increase in $\delta^{18}\text{O}$ of the rocks. These tiny increases were cumulative and resulted in the net increase of $\delta^{18}\text{O}$ for the altered Mine Granite.

To describe such a complex process quantitatively is difficult. The following is a much simplified discussion to illustrate the process. It

As the fluid is incompressible then the amounts of fluid flowing through each interval must be the same at any given period of time. Since each interval is very small, the volume of rocks in each interval can be

The magnitude of such changes depends on the mineralogical composition of the rock and the temperature gradient.

Fig.8-4 Schematic diagram illustrating the dynamic process of rock-fluid isotopic exchange (see text for discussion).



When a packet of fluid flows into interval A, it reacts with the volume of rock in this interval and achieves isotopic equilibrium. Then it flows to interval B. But as it has cooled ($T_B < T_A$) and therefore the $\Delta_{rock-fluid}$ has increased, it is out of equilibrium with the volume of rock in interval B initially, and therefore it continues to react with the volume of rock in interval B to achieve a new equilibrium at T_B . This process continues as the fluid flows upwards in the breccia pipe until it leaves the system. The fluid loses some $18O$ to the rock, causing changes in $\delta^{18}O$ to both the rock and the fluid.

assumes that A, B, C, and D are very tiny vertical intervals of the breccia pipe and each of them represents a homogeneous sub-system (Fig. 8-4). But because of the temperature gradient, temperature decreases from interval A, to B, to C, and to D ($T_A > T_B > T_C > T_D$).

considered homogeneous. The isotopic compositions of fluid and rock in each section are always constrained by

$$\delta^{18}\text{O}_{\text{H}_2\text{O}} = \delta^{18}\text{O}_{\text{r}} - \Delta \quad (8.1)$$

in which Δ is a function of temperature and the mineralogical composition of the rock.

If the isotopic composition of the volume of rock in interval B is $\delta^{18}\text{O}_{\text{r},m}$ after it reacted with m packets of fluids, when it reacts and achieves equilibrium with the fluid packet $m+1$, the isotope compositions of the volume of rock and the fluid in interval B are constrained by

$$\begin{aligned} N_{\text{r}}\delta^{18}\text{O}_{\text{r},m} + N_{\text{H}_2\text{O}}\delta^{18}\text{O}_{\text{H}_2\text{O},\text{A}} \\ = N_{\text{r}}\delta^{18}\text{O}_{\text{r},m+1} + N_{\text{H}_2\text{O}}\delta^{18}\text{O}_{\text{H}_2\text{O},\text{B}} \end{aligned} \quad (8.2)$$

and

$$\Delta_{\text{B}} = \delta^{18}\text{O}_{\text{r},m+1} - \delta^{18}\text{O}_{\text{H}_2\text{O},\text{B}} \quad (8.3)$$

where N_{r} and $N_{\text{H}_2\text{O}}$ are the number of oxygens in the volume rock in interval B and in a packet of fluid, respectively. The isotope composition of the fluid before it reacts with the volume of rocks in interval B is $\delta^{18}\text{O}_{\text{H}_2\text{O},\text{A}}$, as it has equilibrated with the volume of rock in interval A before it flows into interval B.

The solution to 8.2 and 8.3 are

$$\delta^{18}\text{O}_{\text{r},m+1} = \frac{\delta^{18}\text{O}_{\text{r},m} + N_{\text{H}_2\text{O}}/N_{\text{r}}(\delta^{18}\text{O}_{\text{H}_2\text{O},\text{A}} + \Delta_{\text{B}})}{1 + N_{\text{H}_2\text{O}}/N_{\text{r}}} \quad (8.4)$$

$$\delta^{18}\text{O}_{\text{H}_2\text{O},m+1} = \frac{\delta^{18}\text{O}_{\text{r},m} + N_{\text{H}_2\text{O}}/N_{\text{r}}(\delta^{18}\text{O}_{\text{H}_2\text{O},\text{A}} - \Delta_{\text{B}})}{1 + N_{\text{H}_2\text{O}}/N_{\text{r}}} \quad (8.5)$$

where footnote A and B stands for the corresponding term in intervals A and B, respectively.

The solution depends on the number of oxygens in the volume of rock in section (N_{r}), the number of oxygens in a packet of fluid ($N_{\text{H}_2\text{O}}$), the temperature, the isotope compositions of the volume of rocks in intervals A and B.

If the isotope compositions of the volumes of rocks in intervals A and B are roughly the same, equation 8.4 can be simplified to

$$\delta^{18}\text{O}_{\text{r},m+1} = \delta^{18}\text{O}_{\text{r},m} + N_{\text{H}_2\text{O}}/N_{\text{r}}(\Delta_{\text{B}} - \Delta_{\text{A}}) \quad (8.6)$$

Since $\Delta_B > \Delta_A$ as a result of the temperature gradient ($T_B < T_A$), the second term on the right hand side of 8.6, although very small in value, will always be positive. This suggests that there is only a tiny change in the isotope composition of the rock by reacting with a packet of fluid, thus the system keeps to be rock-buffered in terms of oxygen isotope. However, the change in the rock is cumulative and its $\delta^{18}\text{O}$ will increase significantly after reacting with a large number of packets of fluids.

It is clear that no matter how many packets of fluid flows through the breccia pipe, because the isotopic changes to the fluid are not cumulative as the fluid leaves the system after reacting with the rock, the system is always rock buffered in terms of oxygen exchange. It is also clear that, although we may say the system was buffered by the rock, it does not mean that the isotope composition of the rock does not change. On the contrary, as the rock accumulates the small changes caused by each packet of fluid, it became isotopically heavier and heavier.

Theoretically, the initial isotope composition of the fluid cannot be estimated by analyzing the hydrothermal minerals in such a system. However, the net result of the fluid-rock reaction in the breccia pipes was that the rocks gained ^{18}O from the fluid. This is indicated by the higher $\delta^{18}\text{O}$ values of the altered Mine Granite than fresh Mine Granite (see above). The initial $\delta^{18}\text{O}$ value of the fluid must have been greater than that calculated from quartz compositions, i.e., 7.7 per mil, which is greater than a fluid in equilibrium with fresh Mine Granite. Together with other characteristics of the fluid (see chapters 2, 3 and 6), it is logical to conclude that the fluid originated from the isotopically heavier Ardlethan Granite.

The $\delta^{34}\text{S}$ values of sulphides also suggest that a magmatic fluid was responsible for the main stage mineralization. There is no indication of the presence of sulphur from any other sources during the cassiterite and sulphide mineralization. However, the cosalite mineralization in the Blackreef and Godfrey area may represent an independent event caused by fluid from another source which is characterized by a much heavier sulphur ($\delta^{34}\text{S} > 10.0$ per mil).

The carbon isotopic compositions of siderite of $\delta^{13}\text{C}$ around -4.5 per mil are consistent with the above interpretation that the fluid responsible for cassiterite and sulphide mineralization and associated hydrothermal alteration was of magmatic origin.

The single δD analysis of a muscovite yielded a value of -76.6 per mil. Using the fractionation factor between muscovite and fluid of Taylor (1974) a δD value of -45.0 per mil is suggested for the fluid which is in

the range for magmatic fluid from granitic sources.

In comparison to other tin systems, the oxygen isotope data of the Ardlethan Tin Field are similar to those of the Panasqueira deposit (Kelly and Rye, 1979) which was interpreted as magmatic dominated system and the magmatic stage of the Renison Bell (Patterson *et al.*, 1981) deposit. Tin deposits associated with the Mole Granite are interpreted to have formed by mixed magmatic and meteoric fluids (Sun & Eadington, 1987) based on two types of quartz with distinctive oxygen isotope compositions. No such evidence has been found in the Ardlethan Tin Field.

8.5 Conclusions

Oxygen isotope compositions of fresh rocks indicate that the Mine Granite is isotopically lighter than the Ardlethan Granite and its differentiates. This supports the conclusion derived from the geochemical study that the Mine Granite is not genetically related to the Ardlethan Granite series.

Sulphur, carbon, oxygen and hydrogen isotope data either support or permit an interpretation that the cassiterite and sulphide mineralization and associated hydrothermal alteration in the Ardlethan Tin Field resulted from a dynamic process of passing large amounts of cooling magmatic fluids from the Ardlethan Granite through the breccia pipes. The fluid was in local equilibrium with and largely buffered by the rocks in the breccia pipes.

The cassiterite and sulphide mineralization was overprinted by an independent hydrothermal event that deposited cosalite, native bismuth and bismuthinite in association with euhedral pyrite and trace chalcopyrite in the Blackreef-Godfrey area. The sulphur isotopic compositions of sulphides deposited at this stage indicate a nonmagmatic fluid.

Chapter 9

CONDITIONS OF MINERAL DEPOSITION

In this chapter the conditions of cassiterite and sulphide mineralization and the causes of cassiterite deposition in the Ardlethan Tin Field are discussed.

9.1 Temperature

Temperatures of cassiterite and sulphide mineralization in the Ardlethan Tin Field have been estimated independently by fluid inclusion measurements, sheet silicate geothermometry and stable isotope geothermometry.

Fluid inclusion measurements (see Chapter 7) indicate that the temperatures of cassiterite deposition are between 310 and 370°C in the Wildcherry, the Ardwest, the Wildcherry South and the Perseverance deposits; between 310 and 360°C in the Blackreef and Godfrey deposits and between 320 and 370°C in the White Crystal deposit. Temperatures of sulphide deposition are between 230 and 270°C. Temperatures of toothy quartz, fluorite, and cookeite deposition in the Blackreef, the White Crystal, and the Godfrey South deposits are between 150 and 210°C.

The compositions of the secondary biotite in the altered Mine Granite have been used to calculate temperatures and $\log f_{O_2}$ conditions of secondary biotite formation using a biotite solid solution model (Appendix 4). The calculated temperatures are between 350 and 440°C and mostly between 360 and 420°C, peaking at 395°C (Figs. 9-1 & 9-2). Using the geothermometer calibrated by Hedges and Walshe (1986) the compositions of muscovite in the altered Mine Granite give temperatures between 290 and 330°C, peaking at 315°C (Fig. 9-2). Temperatures and redox conditions of chlorite formation have been calculated using the solution model of Walshe (1986) and the computer program provided by Walshe and Harrold. The calculated temperatures range between 105 and 290°C and peak at 200°C (Fig. 9-2).

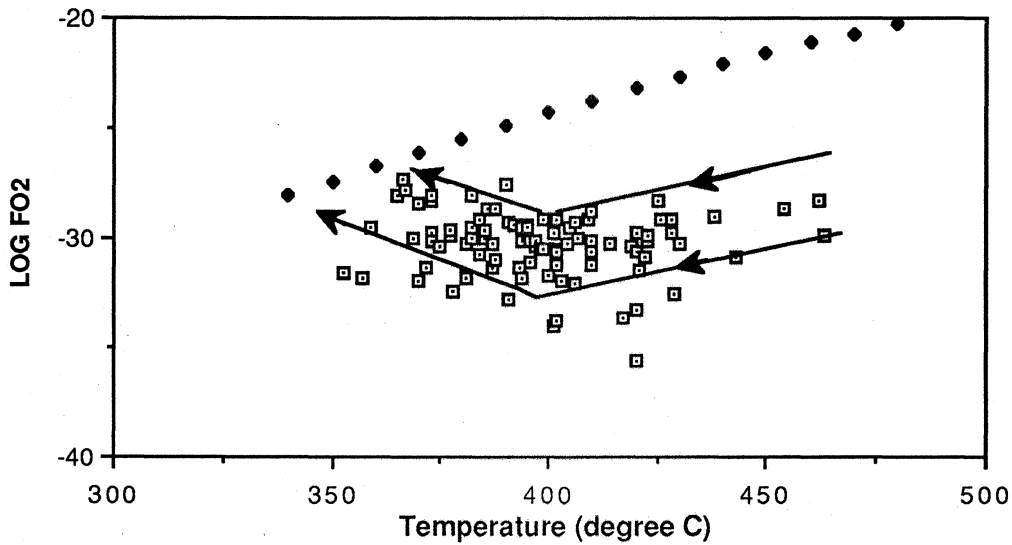


Fig. 9-1. Temperatures and $\log f_{O_2}$ calculated from secondary biotite compositions (square) in reference to hematite/magnetite $\log f_{O_2}$ buffer (filled diamond).

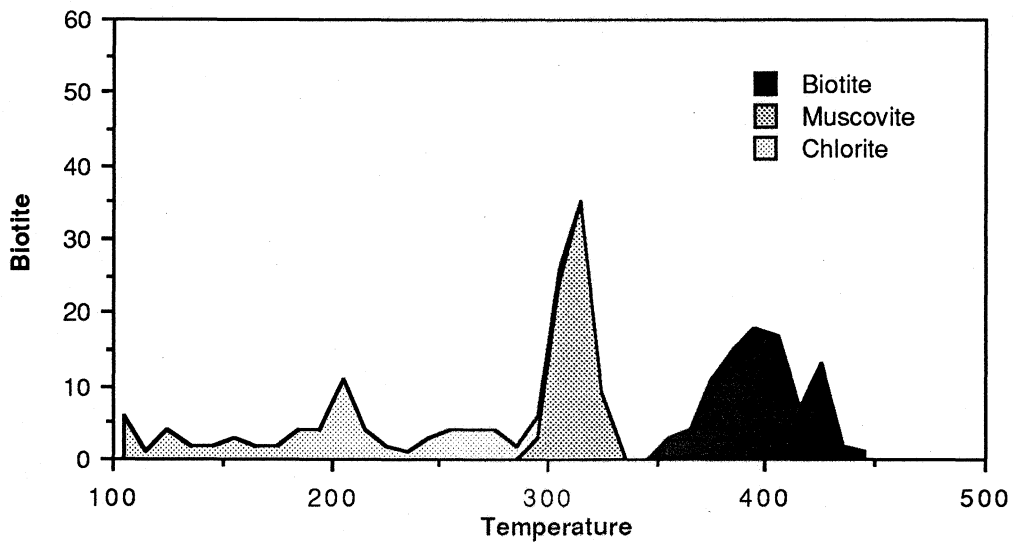


Fig. 9-2 Frequency plot of temperatures ($^{\circ}C$) calculated from biotite, muscovite and chlorite geothermometers.

It is apparent (Fig. 9-2) that the biotite temperatures are mostly higher than; muscovite temperatures are mostly in the range of; and chlorite temperatures are lower than the fluid inclusion temperatures of

cassiterite deposition defined by the fluid inclusion study. As described in chapter 5, biotite alteration proceeded below; sericite alteration proceeded in; and chlorite alteration proceeded above the zone of cassiterite deposition. These temperatures strongly support the interpretation that the fluid flowed upwards and cooled. The change in alteration styles of was in response to fluid cooling. The temperature of the fluid, when funnelled into the Breccia pipes at depth, should be higher than the maximum biotite temperature, i. e., higher than 450°C.

9.2 Pressure

Pressures during cassiterite mineralization in the White Crystal deposit have been estimated from fluid inclusions (Chapter 7). The pressures is between 450 bars and 1,200 bars. The pressures in the Mine Granite, Carpathia-Blackreef and Stackpool-Godfrey Breccia Pipes are assumed to be the same as those of the White Crystal Breccia Pipe.

9.3 Redox Conditions

Oxygen fugacity was estimated independently by sheet silicate calculations, CO₂/CH₄ ratios in fluid inclusions, and fluid-mineral equilibria.

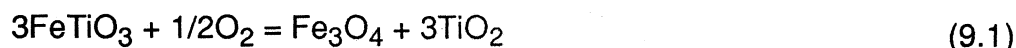
The f_{O_2} values calculated from secondary biotite compositions are mostly between 10⁻³³ and 10⁻²⁷ atm. The values of the most calculated f_{O_2} decrease with declining temperatures between 440 and 385°C and then increases slightly towards lower temperatures (Fig. 9-1). The average f_{O_2} value at 360°C is about 10^{-29.5±1.5} atm. The log f_{O_2} value is about 5 and 4 unit below the hematite/magnetite buffer at 440 and 380°C respectively. At 350°C the average value of log f_{O_2} is approximately 1.5 unit below the hematite/magnetite buffer (Fig. 9-1).

The direction change of the log f_{O_2} trend at 385°C could be caused by (a) change of mineral buffer; (b) fluid mixing; or (c) fluid boiling (unmixing). There is no change of mineral buffer. The possibility of fluid mixing is ruled out by the isotope evidence (see Chapter 8). Consequently, it is interpreted as the result of fluid boiling. This is supported by the fluid inclusion evidences. As the reduced components, such as H₂S, CH₄ and H₂ would go preferentially into the vapor phase during boiling, the remaining fluid would become relatively more oxidized.

The value of f_{O_2} was also estimated from the CO₂/CH₄ ratios in fluid inclusions (Chapter 7). The values estimated are from 10^{-31.5} atm at

360°C, decreased to 10^{-37} atm at 250°C. The value of $10^{-31.5}$ atm at 360°C is in good agreement with that calculated from biotite compositions.

Another estimate of f_{O_2} during cassiterite mineralization was made through the reaction:



Rutile and ilmenite are primary and secondary trace minerals in the altered Mine Granite therefore reaction 9.1 suggests

$$\log f_{O_2} = 2(\log a_{\text{mag}} - \log K_{9.1}) \quad (9.2)$$

where a_{mag} is the activity of magnetite. The activity of magnetite must be less than unit as it is not a stable phase in the altered rocks. Using the thermodynamic data of Robie *et al.* (1978) to calculate the $\log K_{9.1}$, equation 9.2 gives a f_{O_2} estimate of $10^{-30.08}$ atm at 330°C by assuming an activity of 0.1 for magnetite, this is in good agreement with those estimated from fluid inclusion and biotite compositions.

Fig. 9-3 plots the T- $\log f_{O_2}$ cooling path of the fluid responsible for the cassiterite mineralization in the Ardlethan Tin Field.

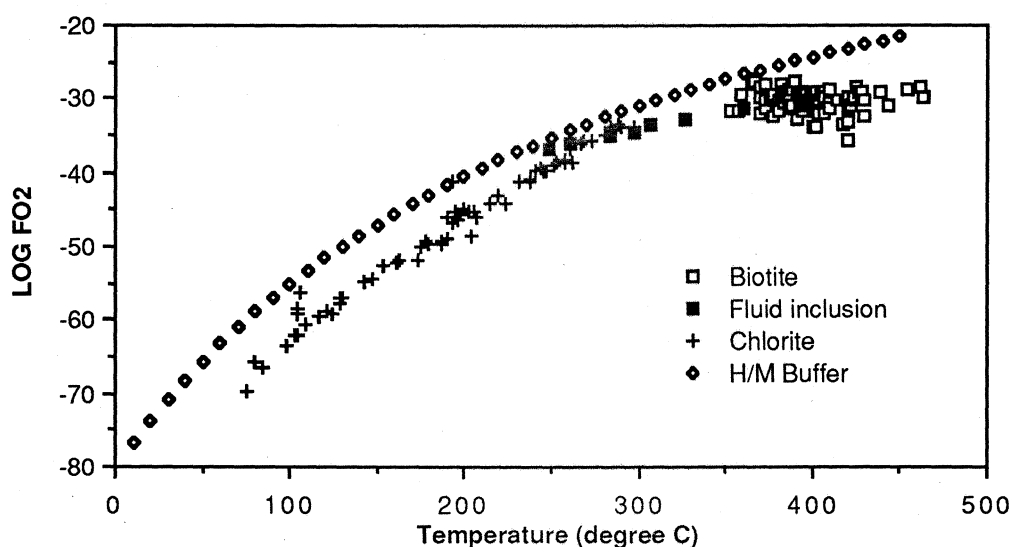


Fig. 9-3 T- $\log f_{O_2}$ cooling path of the fluid estimated by biotite geothermometry, fluid inclusions and chlorite geothermometry in reference to hematite/magnetite buffer

9.4 pH Condition

The pH condition is difficult to estimate. In the following fluid inclusion data and fluid-mineral equilibria are used to define the limits of pH variation during cassiterite deposition in the Ardlethan Tin Field.

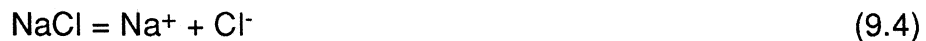
The value of pH can be calculated through

$$\text{pH} = \log a_{\text{Na}^+}/a_{\text{H}^+} - \log a_{\text{Na}^+} \quad (9.3)$$

from estimated $\log a_{\text{Na}^+}/a_{\text{H}^+}$ and $\log a_{\text{Na}^+}$.

Fluid inclusion measurements indicated that the average salinity of the fluids responsible for the cassiterite and sulphide mineralization in the Ardlethan Tin Field is about 15.5 wt% NaCl (approximately equivalent to 3 m NaCl).

The activity of Na^+ can be calculated through the equilibrium



which indicates that

$$\log K_{9.4} = \log a_{\text{Na}^+} + \log a_{\text{Cl}^-} - \log a_{\text{NaCl}} \quad (9.5)$$

and

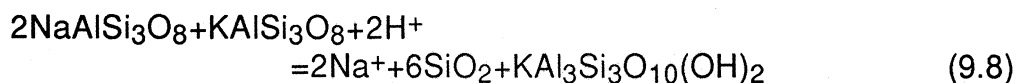
$$C_{\text{total}} = C_{\text{Na}^+} + C_{\text{NaCl}} \quad (9.6)$$

in which C is the concentration and a the activity of the footnoted component. Helgeson's (1978) data were used to calculate $\log K_{9.4}$ at various temperatures. Using the salinity data to substitute for C_{total} in equation 9.6, and Debye-Huckel equation to calculate the activity coefficient for Na^+ and Cl^- , then the activity of Na^+ can be calculated through 9.5 and 9.6 by assuming

$$C_{\text{Na}^+} = C_{\text{Cl}^-} \quad (9.7)$$

The calculated a_{Na^+} at 330°C is 0.16.

The value of $\log a_{\text{Na}^+}/a_{\text{H}^+}$ during cassiterite deposition in the Ardlethan Tin Field cannot be precisely defined due to the lack of major Na-bearing mineral in the cassiterite assemblage. However, in the following equilibrium



the activity of sericite and quartz can be taken as unity as cassiterite mineralization is associated sericite and quartz. As relicts of K-feldspar are commonly present, the average composition of K-feldspar in the Mine Granite, $\text{Na}_{0.11}\text{K}_{0.84}\text{Al}_{1.02}\text{Si}_{2.99}\text{O}_8$ (see Chapter 6), suggests that the activities of K-feldspar and albite were approximately 0.84 and 0.11 approximately during cassiterite deposition. The calculated value of $\log a_{\text{Na}^+}/a_{\text{H}^+}$ through

$$\log a_{\text{Na}^+}/a_{\text{H}^+} = 0.5 \log K_{9.8} + 0.5 \log a_{\text{Kf}} + \log a_{\text{Ab}} \quad (9.9)$$

is 3.6 at 330°C using the thermodynamic data of Helgeson (1978).

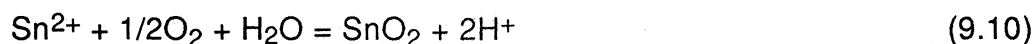
A pH value of 4.4 is obtained by replacing the estimated values of $\log a_{\text{Na}^+}/a_{\text{H}^+}$ and a_{Na^+} into equation 9.3 at 330°C. This is strictly a maximum value as K-feldspar is not always present. However, the relic occurrences of K-feldspar suggest that it is a realistic estimate.

9.5 Cassiterite Deposition

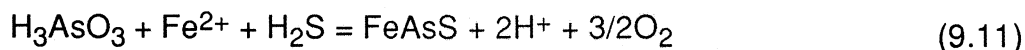
The solubility of cassiterite is a function of temperature, redox conditions and pH. Sn complexes with Cl^- , F^- and OH^- but quantitative calculations indicates that only Sn-Cl and Sn-OH complexes are important for Sn transport at most geological conditions (Patterson *et al.*, 1981; Eadington, 1982; Jackson & Helgeson, 1985a,b). Therefore the activity of Cl^- in the fluid is an important factor affecting the total solubility of Sn. The calculations of the solubility of cassiterite are briefly summarized in Appendix 5.

The calculated solubility of cassiterite declines from around 15 ppm Sn to less than 1 ppm Sn (Fig. 9-4) in response to the changes of f_{O_2} and declining temperature from 350 to 300°C at estimated pH. This is in good agreement with fluid inclusion results which indicate that cassiterite deposition was between 370 and 310°C.

The cassiterite deposition reaction



consumes oxygen and produces protons. The progress of this reaction depends on other associated reactions to buffer both oxygen fugacity and pH, otherwise consumption of oxygen and accumulation of H^+ in the fluid would stop cassiterite deposition. In the Ardlethan Tin Field, the pH and the redox conditions of the fluid were controlled by fluid-mineral equilibria, as discussed above, and boiling. The redox condition was probably also partly controlled by the reaction:



as arsenopyrite is commonly present. Heinrich and Eadington (1986) discussed the effectiveness of reaction 9.11 in buffering redox condition during cassiterite deposition.

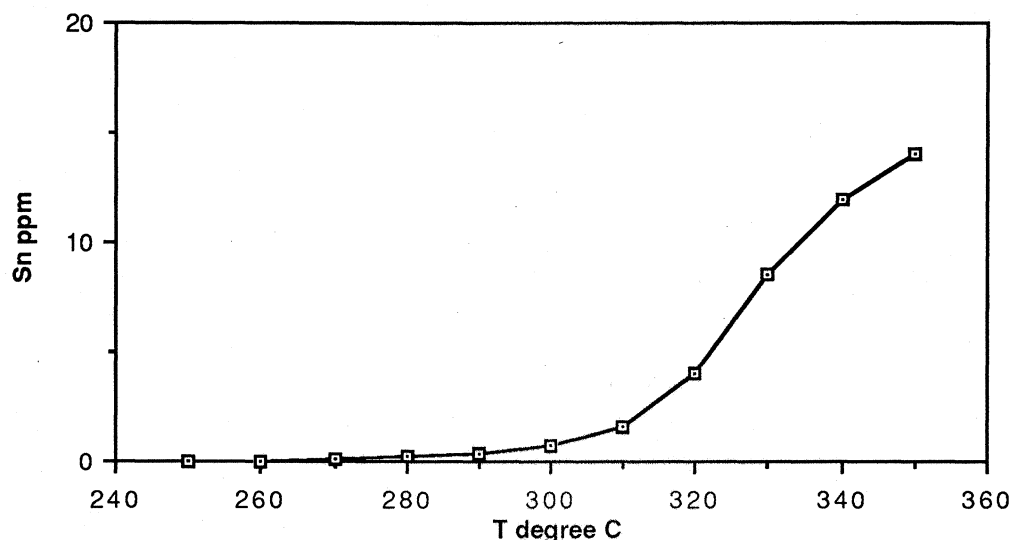


Fig. 9-4. Calculated cassiterite solubility (ppm Sn) with declining temperatures. The values of pH, salinity and redox conditions are set as discussed in the text. This diagram indicates that the tin concentration decreased from 15 ppm to 0.8 ppm when the fluid cooled from 350 to 300°C. This is in very good agreement with fluid inclusion and sheet silicate geothermometry results which suggest that the cassiterite deposition was mostly between 370 and 310°C (see text for discussion).

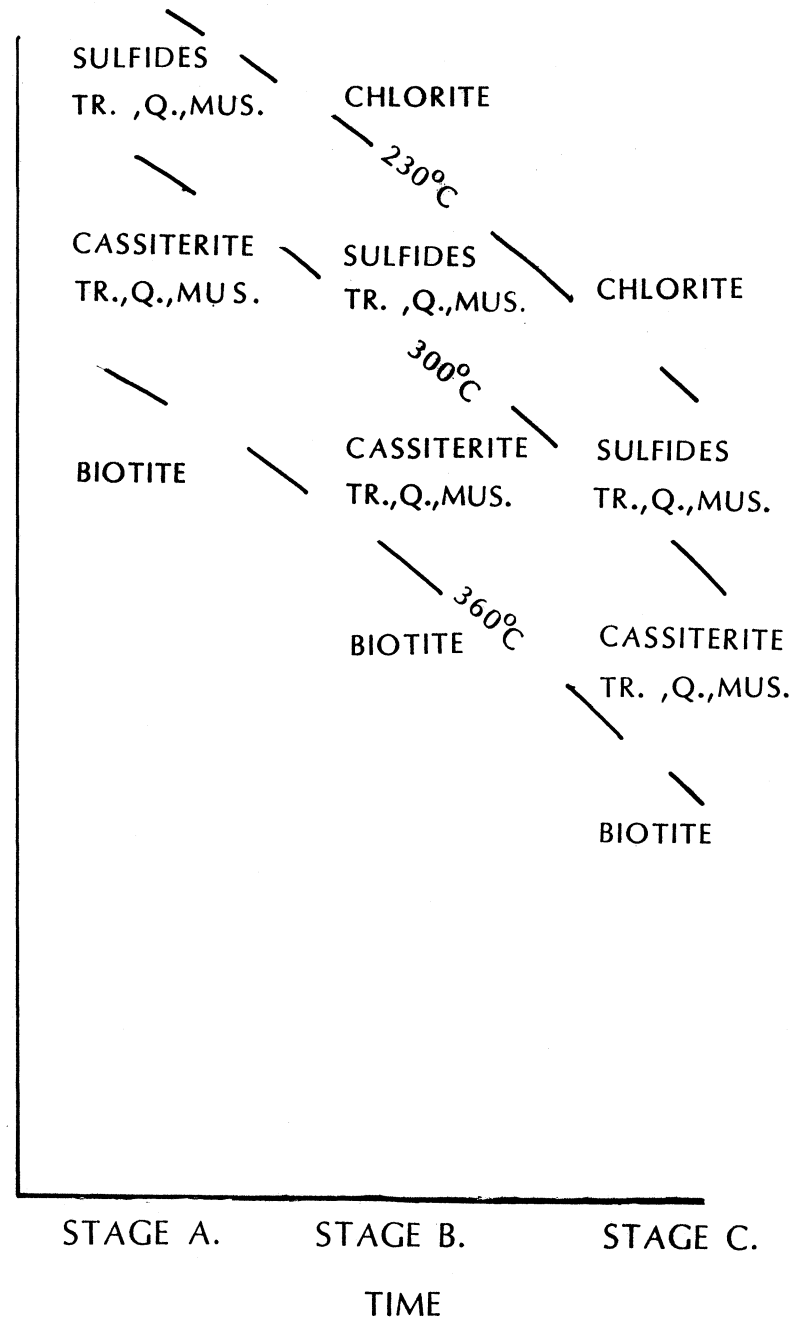
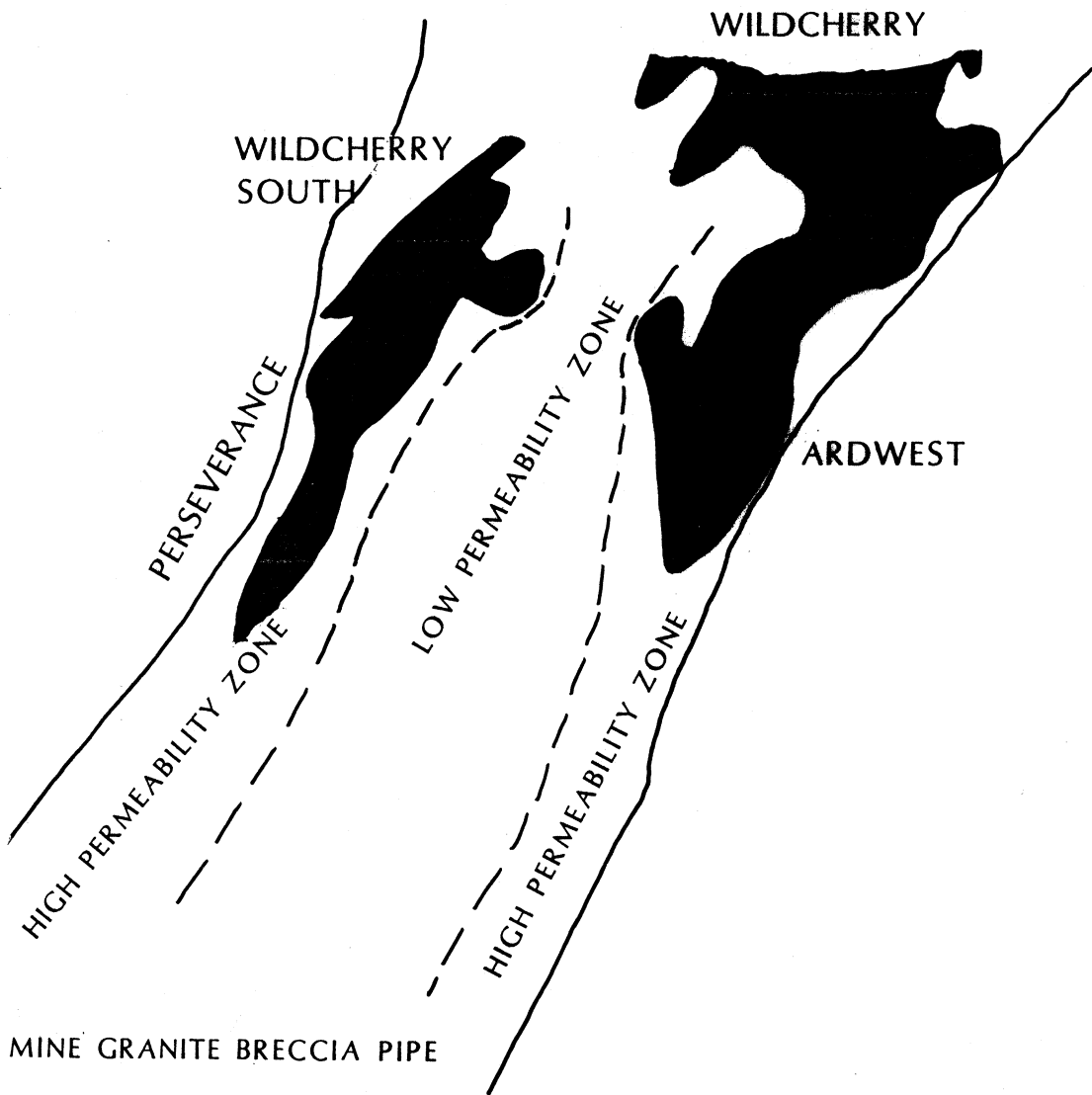
9.6 Summary and Discussion

In summary, cassiterite was deposited by a saline fluid at temperature between 370 and 300°C; pressure between 450 and 1200 bars; f_{O_2} around 10^{-31} atm; and pH around 4.4.

Cassiterite and sulphide mineralization in the breccia pipes in the Ardlethan Tin Field can be interpreted in terms of a dynamic process. The Mine Granite Breccia Pipe represents the first episode of brecciation, alteration and mineralization. The pH, $\log f_{\text{O}_2}$, a_{Cl^-} and fluid composition were buffered by the progress of complex fluid-rock reactions, fluid boiling, volatile and energy releases. Biotite alteration occurred in the high temperature zones at depth, cassiterite deposition occurred in the boiling zones at relatively higher temperature, sulphide deposition, toothy quartz, fluorite and cookeite deposition and chlorite alteration occurred in lower temperature zones. With deposition of minerals, the permeability of

the breccia pipes was reduced, causing a decrease of fluid flux. The various zones of mineral deposition and alteration retreated and sulphides and chlorite overprinted the upper zones of mineralization in the Mine Granite Breccia Pipe (Fig. 9-5). When the Mine Granite Breccia Pipe had been completely sealed up by mineral deposition, a new stage of pressure build up occurred at depth and resulted in the brecciation and mineralization of the Carpathia-Blackreef and Stackpool-Godfrey Breccia Pipes, and subsequently the White Crystal Breccia Pipe.

Fig. 9-5. Illustrative diagram showing the process of mineralization in the Mine Granite Breccia Pipe.



Chapter 10

SUMMARY AND CONCLUSIONS

Geological, geochemical, mineralogical, mineral chemical, fluid inclusion, stable isotope and thermodynamic methods have been used to study the genesis of the breccia pipes and mineralization in the Ardlethan Tin Field, New South Wales, Australia. The results and conclusions are summarized below:

The Ardlethan Tin Field is located within the Girilambone-Wagga Anticlinorial Zone towards the western extremity of the Lachlan Fold Belt. The Ordovician sedimentary rocks were metamorphosed, folded and intruded by granitoids. Tin mineralization occurs widely in association with granitoids in a north- to northwesterly-trending belt called the "Wagga Tin Belt". The Ardlethan Tin Mine was the largest hard rock tin mining operation within the belt.

Two main granitoids, the Mine Granite and the Ardlethan Granite, intruded the Ordovician sedimentary rocks consecutively in the Late Silurian. The Mine Granite extends from the Ardlethan Tin Mine northwards and is very poorly exposed. The Ardlethan Granite occurs to the west of the Tin Mine and is much larger than the Mine Granite. The GQFP and some pyroclastic volcanics occur between the two granites. There are also several microgranite dykes and Mine Porphyry dykes in the Ardlethan Tin Mine area.

The Mine Granite is a biotite-rich, homogeneous and weakly foliated S-type granite. The Ardlethan Granite is also a S-type granite but its texture, mineralogy and whole rock chemistry all vary widely from place to place indicating a very strong degree of fractionation. The fractionation of the Ardlethan Granite produced the GQFP, the microgranite and the Mine Porphyry at various stages.

Disseminated cassiterite and sulphide mineralization occurs along the eastern margin of the Ardlethan Granite from Little Bygoo to the south of Taylor's Hill in deep fractures and breccia pipes. The mineralized fractures can occur within the Ardlethan Granite; the volcanics; the GQFP; the sedimentary rocks as well as in the Mine

Granite. The four breccia pipes explored to date, however, are all hosted by the Mine Granite.

Examination of the styles of brecciation, their timing relationships to the intrusions of microgranite and the Mine Porphyry dykes, and characteristics of hydrothermal alteration and mineralization concluded that the four breccia pipes of the Ardlethan Tin Field were formed in three consecutive brecciation events. The first event resulted in the Mine Granite Breccia Pipe, the second event resulted in the Carpathia-Blackreef and the Stackpool-Godfrey Breccia Pipes, and the final event resulted in the White Crystal Breccia Pipe.

The breccias in the Ardlethan Tin Field are classified broadly into fragment-supported breccia and rock flour-supported breccia. The Mine Granite Breccia Pipe has a central zone of rock flour-supported breccia and an outer zone of mainly fragment-supported breccia. In the Carpathia-Blackreef and the Stackpool-Godfrey breccia pipes, the central zones are enriched in sediment fragments and consist mainly of rock flour-supported breccia in the upper levels. The White Crystal breccia pipe does not contain any rock flour-supported breccia.

The distribution of microgranite fragments, Mine Porphyry fragments and mafic fragments within the Mine Granite Breccia Pipe, the Carpathia-Blackreef and the Stackpool-Godfrey Breccia Pipes indicates that the contents within these three breccia pipes have moved upwards during brecciation. This conclusion is supported by many other observations: such as the common occurrences of blind daughter breccia pipes and rock flour pockets along the irregular contact of the Carpathia-Blackreef Breccia Pipe and flow patterns in rock flour-rich zones. Evidence for collapse is found only in the White Crystal Breccia Pipe.

The characteristics of the breccias of the Mine Granite Breccia Pipe, the Carpathia-Blackreef and the Stackpool-Godfrey Breccia Pipes indicate that brecciation was initiated by over-pressured volatiles, followed by the intrusion of magma plugs. The magma plugs were responsible for the upward moving and milling within the breccia pipes to form rock flour-rich breccia. A four-stage model of breccia pipe formation was formulated to interpret the process of breccia pipe formation in relation to magmatic fractionation in the parental magma chamber.

Structural analysis of the Ardlethan Tin Mine area showed that brecciation was controlled by three major linears and their intersections. The triangular shaped Mine Granite Breccia Pipe sits on the intersection of the three linears and the Carpathia-Blackreef Breccia Pipe was developed along one of the major linears. This analysis suggests that there

are potentially more breccia pipes in the area along these linears.

Each brecciation event was followed by a sequence of hydrothermal events: sericite-tourmaline-milky quartz alteration with cassiterite mineralization; tourmaline-clear quartz alteration with sulphides mineralization; vug infill with toothy quartz, fluorite and cookeite and chlorite alteration. Biotite alteration occurred at depth in the Mine Granite breccia pipe before cassiterite mineralization. A stage of topaz alteration with minor cassiterite occurred in the White Crystal Breccia Pipe following brecciation. The Wildcherry, the Ardwest, the Wildcherry South and the Perseverance deposits were formed following the first brecciation event, the Carpathia, the Blackreef, the Stackpool, the Godfrey and the Godfrey South deposits following the second event, and the White Crystal deposit following the final event.

Cassiterite and sulphide mineralization occurs mainly in zones of rock flour-poor breccia and zones of rock flour supported breccia are barren. This correlation indicates a strong permeability control over mineralization. The importance of permeability is further emphasized by the many occurrences of tin mineralization in fractures and fracture joints along the eastern margin of the Ardlethan Granite.

Chemical composition of tourmaline, biotite, chlorite and sericite from the alteration zones fall between compositions of these minerals from weakly altered Mine Granite and Ardlethan Granite. Tin analyses of biotite and muscovite indicate the same trend. The chemical compositions suggest that the hydrothermal alteration was caused probably by mixing components from the Ardlethan Granite and the Mine Granite, i.e., by fluid from the Ardlethan Granite reacting with the Mine Granite. This is supported by the fact that the Ardlethan Granite has a very high potentials to produce tin-rich fluids through fractionation.

Stable isotope studies of oxygen, sulphur and carbon indicate that a complex dynamic process was responsible for the cassiterite and sulphide mineralization within the breccia pipes. Tin-rich magmatic fluid from the deep parts of the Ardlethan Granite channelled into permeable zones, progressively reacted with the rock and left the system somewhere near the surface probably. As a consequence at any instant the fluid-rock oxygen isotope exchange was effectively rock-buffered although overall there was a significant increase in the $\delta^{18}\text{O}$ value of the altered rocks. This suggests that the fluid was sourced from the Ardlethan Granite which is enriched in ^{18}O relative to the Mine Granite.

An independent hydrothermal event led to cosalite, native bismuth and bismuthinite deposition with euhedral pyrite and chalcopyrite overprinting the cassiterite and sulphide mineralization in the Blackreef-

Godfrey area. Sulphides associated with this event contain much heavier sulphur, ($\delta^{34}\text{S}$ around 10 per mil), than the sulphides ($\delta^{34}\text{S}$ around 0 per mil) associated with cassiterite mineralization.

Fluid inclusions, stable isotopes and geothermometry indicate that cassiterite mineralization in the Ardlethan Tin Field occurred in the temperature range between 310 and 370°C, and sulphide mineralization between 220 and 270°C. The salinity of the fluid was between 12 and 17 wt% NaCl. Fluid inclusions suggest a hydrostatic pressure around 450 bars and a lithostatic pressure around 1200 bars during cassiterite and sulphide mineralization. A pH value of around 4.4 is estimated from fluid-mineral equilibria and salinity data from fluid inclusions. The estimated value of $\log f_{\text{O}_2}$ is about -31 at 350°C during cassiterite mineralization. Calculations of cassiterite solubilities indicate a reduction of total soluble tin from more than 14 ppm to less than 1 ppm mostly in response to declining temperature.

A dynamic model is proposed to interpret the process of brecciation and mineralization in the Ardlethan Tin Field. The process started with the intrusion of the Ardlethan Granite and its fractional crystallization, which produced large amounts of tin- and volatile-rich magmatic fluid. The accumulation of the tin- and volatile-rich fluid resulted in the brecciation to form the Mine Granite Breccia Pipe. Some fractionated magma, represented by the Mine Porphyry dykes, intruded the newly formed breccia pipe, forcing upward mass flow, stressing and milling of fragments. The continued fractional crystallization at depth in the Ardlethan Granite maintained a steady supply of fluid which was channelled into permeable zones in the breccia pipe. As the fluid flowed upwards, fluid-rock reactions progressed, energy and volatiles were released and physico-chemical gradients, especially a temperature gradient, established from depth to surface along the fluid path. Biotite alteration; cassiterite mineralization with tourmaline, milky quartz and sericite alteration; sulphide mineralization with tourmaline, sericite and clear quartz alteration; toothy quartz, fluorite and cookeite deposition and chlorite alteration occurred sequentially in zones from depth to surface in response to the physico-chemical gradients.

As this process proceeded, the permeability of the Mine Granite Breccia Pipe was steadily reduced by mineral deposition, causing a reduction of fluid flux and a slow retreat of the vertical zonation. As a result of the retreat, cassiterite mineralization in the upper levels of the Mine Granite breccia pipe was overprinted by sulphide mineralization and then chlorite alteration.

When the Mine Granite breccia pipe was completely sealed by mineral deposition, fluid accumulation started again at depth and resulted

in the brecciation of the Carpathia-Blackreef and the Stackpool-Godfrey Breccia Pipes and the dynamic processes were repeated. The White Crystal Breccia Pipe represents the final episode of the brecciation and mineralization process. The three brecciation and mineralization events resulted from the continued fractional crystallization in the Ardlethan Granite which is reflected by the increasing abundances of F-, W- and Li-rich minerals. The collapse of the White Crystal breccia pipe may suggest depletion of volatiles and completion of magma crystallization in the Ardlethan Granite.

Appendix 1

Mineral Chemistry and Whole Rock Chemistry Data

A1-1 Mineral Chemistry Data

A1-1.1 Plagioclase in the Mine Granite

Sample	SiO ₂	Al ₂ O ₃	FeO	MgO	CaO	Na ₂ O	K ₂ O	total	Si	Al	Fe	Mg	Ca	Na	K
RD62	64.6	22.83			1.11	8.04	1.5	100.1	2.83	1.18	0	0.13	0.06	0.69	0.07
RD62	64.22	22.36		0.22	0.21	9.69	2.9	99.6	2.84	1.16	0	0.01	0.01	0.84	0.14
RD114	64.27	22.83	0.13	0	1.56	7.99	3.09	99.87	2.84	1.19	0	0	0.09	0.69	0.15
RD114	64.65	22.93	0.2	0.31	1.83	9.27	1.17	100.4	2.84	1.19	0	0.02	0.1	0.8	0.06
RD114	67.23	21.23	0	0.14	0.18	11.04	1.2	101.0	2.92	1.09	0	0.01	0.01	0.94	0.06
RDW74	67.15	20.1	0	0.12	0.25	11.37	1.54	100.5	2.94	1.04	0	0.01	0.01	0.98	0.07

A1-1.2 Plagioclase in the Ardlethan Granite

TH03	67.2	19.57	0	0.18	0.58	11.27	0.92	99.72	2.96	1.02	0	0.01	0.03	0.98	0.04
TH03	68.25	19.83	0	0.3	0.27	11.37	0	100.0	2.98	1.02	0	0.02	0.02	0.97	0
TH03	67.17	20.1	0	0.16	0.58	10.68	0.61	99.3	2.96	1.04	0	0.01	0.03	0.92	0.03
TH03	67.6	19.73	0	0.14	0.2	11.37	0.14	99.18	2.98	1.03	0	0.01	0.01	0.98	0.01
TH07	68.44	19.81	0	0.14	0.12	11.48	0	99.99	2.98	1.02	0	0.01	0.01	0.98	0
RDB61	69.66	20.2	0	0.12	0.13	9.97	0	100.1	3.01	1.03	0	0.01	0.01	0.85	0

Sample	SiO2	Al2O3	FeO	MgO	CaO	Na2O	K2O	total	Si	Al	Fe	Mg	Ca	Na	K
RDB61	67.85	19.71	0	0.13	0.17	11.41	0	99.27	2.98	1.02	0	0.01	0.01	0.98	0
RDB61	68.21	19.59	0	0.14	0.1	11.52	0	99.56	2.99	1.01	0	0.01	0.01	0.99	0
RDB62	68.09	19.7	0.16	0.17	0	11.31	0	99.5	2.98	1.02	0.0	0.01	0	0.97	0
RDB64	67.67	19.5	0	0.19	0.25	11.4	0	99.01	2.98	1.01	0	0.01	0.01	0.99	0
RDB64	68.19	19.73	0	0.17	0.22	11.39	0.14	99.84	2.98	1.02	0	0.01	0.01	0.98	0.01
RDS70	69.13	20.01	0	0.1	0.13	11.58	0	100.95	2.99	1.02	0	0.01	0.01	0.98	0
RDS70	68.27	19.56	0	0.18	0	11.33	0	99.34	2.99	1.01	0	0.01	0	0.97	0
RDS70	68.12	19.72	0	0	0.06	11.51	0	99.41	2.99	1.02	0	0	0	0.99	0
RDS70	67.81	19.66	0	0.14	0	11.61	0.11	99.33	2.98	1.02	0	0.01	0	1	0.01

A1-1.3 K-feldspar in the Mine Granite

sample	SiO2	Al2O3	K2O	Na2O	CaO	total	α	Si	Al	K	Na	Ca
RD2	64.31	18.25	15.95	0.14	0	98.65	2.81	3.01	1.01	0.95	0.01	0
RD2	63.97	18.82	15.77	0	0.24	98.8	2.8	2.98	1.03	0.94	0	0.01
RD2	64.75	19.23	13.89	1.72	0	99.59	2.76	2.98	1.04	0.81	0.16	0
RD2	64.34	18.86	11.37	3.44	0.12	98.13	2.78	2.98	1.03	0.67	0.31	0.01
RD2	63.96	18.27	15.79	0.3	0.14	98.46	2.82	3	1.01	0.94	0.03	0.01
RD2	63.76	18.59	14.96	0.78	0	98.09	2.82	2.99	1.03	0.89	0.07	0
RD52	65.43	18.88	12.84	2.66	0.11	99.92	2.74	2.99	1.02	0.75	0.24	0.01
RD10	62.62	18.22	14.95	0.76	0	96.55	2.87	2.99	1.02	0.91	0.07	0
RD10	62.4	18.07	15.68	0.13	0	96.28	2.88	2.99	1.02	0.96	0.01	0
RD56	64.09	18.43	14.02	1.31	0	97.85	2.81	3	1.02	0.84	0.12	0
RD56	63.7	18.52	15.62	0.43	0	98.27	2.82	2.99	1.02	0.94	0.04	0
RD56	63.76	19.23	13.89	0	0	96.88	2.82	2.99	1.06	0.83	0	0
RD68	65.25	18.9	11.15	3.83	0.11	99.24	2.75	2.98	1.02	0.65	0.34	0.01
RD80	64.89	18.69	16.29	0.13	0	100	2.77	3	1.02	0.96	0.01	0
RDW74	64.89	18.7	11.79	0	0.3	95.68	2.82	3.04	1.03	0.71	0	0.02
RDW74	62.5	18.24	13.68	1.35	0	95.77	2.87	2.99	1.03	0.83	0.13	0
RDW74	62.02	18.02	14.98	0.41	0	95.43	2.9	2.99	1.02	0.92	0.04	0
RDW74	65.14	19.16	13.31	2.4	0	100.0	2.75	2.98	1.03	0.78	0.22	0
RDW74	67.06	19.66	11.23	3.77	0.21	101.9	2.67	2.98	1.03	0.64	0.33	0.01
RD58	65.27	18.19	16.24	0	0	99.7	2.78	3.02	0.99	0.96	0	0

A1-1.4 K-Feldspar in the Ardlethan Granite

sample	SiO2	Al2O3	K2O	Na2O	CaO	total	α	Si	Al	K	Na	Ca
TH02	64.83	18.1	16.09	0.16	0.14	99.32	2.79	3.01	0.99	0.95	0.01	0.01
TH03	66.27	17.27	15.02	1.08	0	99.64	2.77	3.05	0.94	0.88	0	0
RDB60	64.45	18.46	15.47	0.49	0	98.87	2.8	3	1.01	0.92	0	0
RDB61	64.95	18.38	16.04	0	0	99.37	2.79	3.01	1	0.95	0	0
RDB61	64.66	18.53	16.16	0	0	99.35	2.79	3	1.01	0.96	0	0
RDB61	64.56	18.31	16.01	0	0	98.88	2.8	3.01	1.01	0.95	0	0
RDB62	64.4	18.49	15.42	0	0	99.01	2.8	3	1.01	0.92	0	0
RDB64	65	18.43	16.12	0	0	99.55	2.78	3.01	1.01	0.95	0	0
RDS70	64.65	18.25	15.64	0.16	0	98.7	2.8	3.01	1	0.93	0	0
RDS70	63.97	18.45	15.93	0	0	99.1	2.81	2.99	1.02	0.95	0	0

A1-1.5 Primary Biotite in the Mine Granite

sample	SiO2	TiO2	Al2O3	FeO	MnO	MgO	K2O	total	α	Si(t)	Ti(o)	Al(t)	Al(o)	Fe(o)	Mn(o)	Mg(o)	K	total(o)	Mg/Mg+Fe
RD59	35.51	3.6	19.05	21.72	0	6.87	9.43	96.18	4.57	2.7	0.21	1.3	0.41	1.38	0	0.78	0.92	2.78	0.36
RD59	35.38	3.71	18.61	21.52	0.14	7.02	9.6	95.98	4.59	2.7	0.21	1.3	0.38	1.38	0.01	0.8	0.94	2.78	0.37
RD59	35.59	3.78	18.46	20.37	0	7.51	9.4	95.11	4.6	2.72	0.22	1.28	0.39	1.3	0	0.86	0.92	2.77	0.4
RD59	35.83	3.82	19.09	20.99	0	7.08	9.49	96.3	4.55	2.71	0.22	1.29	0.42	1.33	0	0.8	0.92	2.76	0.38
RD59	32.32	3.55	17.54	22.39	0.3	7.11	8.46	91.67	4.86	2.62	0.22	1.38	0.29	1.52	0.02	0.86	0.87	2.9	0.36
RD59	35.81	3.75	19.13	21.16	0	7.41	9.47	96.73	4.53	2.7	0.21	1.3	0.4	1.33	0	0.83	0.91	2.78	0.38
RD59	35.46	4.64	18.53	21.39	0	6.76	9.54	96.32	4.57	2.7	0.27	1.3	0.36	1.36	0	0.77	0.93	2.75	0.36
RD59	35.06	3.89	19.25	20.97	0	7.43	9.5	96.1	4.57	2.67	0.22	1.33	0.39	1.33	0	0.84	0.92	2.79	0.39
RD59	35.2	3.65	18.77	21.97	0.19	7.46	9.06	96.3	4.57	2.68	0.21	1.32	0.36	1.4	0.01	0.85	0.88	2.83	0.38
RD59	35.34	3.56	19.26	21.24	0	7.24	9.44	96.08	4.57	2.69	0.2	1.31	0.41	1.35	0	0.82	0.92	2.79	0.38
RD59	34.63	3.65	18.91	21.63	0	6.92	9.06	94.8	4.64	2.68	0.21	1.32	0.4	1.4	0	0.8	0.89	2.81	0.36
RD59	34.84	3.64	18.9	21.03	0	7.21	9.46	95.08	4.62	2.68	0.21	1.32	0.4	1.35	0	0.83	0.93	2.79	0.38
RD59	35.58	3.55	19.28	21.21	0.18	7.38	9.59	96.77	4.54	2.69	0.2	1.31	0.41	1.34	0.01	0.83	0.92	2.79	0.38
RD59	35.33	3.48	19.05	20.93	0.16	7.99	9.62	96.56	4.55	2.68	0.2	1.32	0.38	1.33	0.01	0.9	0.93	2.81	0.4
RD57	34.08	3.85	18.17	21.52	0	7.09	9.31	94.02	4.7	2.67	0.23	1.33	0.34	1.41	0	0.83	0.93	2.8	0.37
RD57	33.88	3.82	18.15	21.23	0	6.85	9.17	93.1	4.74	2.67	0.23	1.33	0.36	1.4	0	0.81	0.92	2.8	0.37

sample	SiO2	TiO2	Al2O3	FeO	MnO	MgO	K2O	total	α	Si(t)	Ti(o)	Al(t)	Al(o)	Fe(o)	Mn(o)	Mg(o)	K	total(o)	Mg/Mg+Fe
RD57	34.89	3.33	18.7	20.54	0.12	7.38	9.41	94.37	4.65	2.7	0.19	1.3	0.41	1.33	0.01	0.85	0.93	2.79	0.39
RD57	33.83	3.81	18.49	21.7	0	5.98	9.29	93.1	4.75	2.68	0.23	1.32	0.4	1.44	0	0.71	0.94	2.77	0.33
RD57	34.11	3.72	18.5	21.23	0	6.76	9.11	93.43	4.72	2.68	0.22	1.32	0.39	1.39	0	0.79	0.91	2.79	0.36
RD57	33.86	3.78	18.3	21.14	0.13	6.93	9.1	93.24	4.73	2.67	0.22	1.33	0.37	1.39	0.01	0.81	0.91	2.8	0.37
RD57	34.18	3.56	18.54	20.86	0.13	7.05	9.18	93.5	4.71	2.68	0.21	1.32	0.39	1.37	0.01	0.82	0.92	2.8	0.38
RD57	34.07	3.35	18.72	20.67	0.12	6.84	9.15	92.92	4.73	2.68	0.2	1.32	0.42	1.36	0.01	0.8	0.92	2.79	0.37
RD57	33.74	3.04	18.51	21.48	0	6.95	8.71	92.43	4.77	2.68	0.18	1.32	0.41	1.43	0	0.82	0.88	2.84	0.37
RD57	33.93	3.72	18.41	21.23	0.17	6.8	9.11	93.37	4.73	2.67	0.22	1.33	0.38	1.4	0.01	0.8	0.91	2.8	0.36
RD57	33.81	3.79	18.15	20.14	0	7.51	9.14	92.54	4.75	2.67	0.23	1.33	0.36	1.33	0	0.88	0.92	2.8	0.4
RD57	34.39	3.1	18.31	16.9	0	9.37	9.18	91.25	4.73	2.71	0.18	1.29	0.41	1.11	0	1.1	0.92	2.8	0.5
RD57	34.04	3.23	18.55	20.62	0	6.87	8.81	92.12	4.76	2.7	0.19	1.3	0.43	1.37	0	0.81	0.89	2.8	0.37
RD57	33.5	3.43	18.5	20.67	0.13	6.99	8.66	91.88	4.78	2.67	0.21	1.33	0.4	1.38	0.01	0.83	0.88	2.82	0.38
RD57	33.82	3.6	18	20.67	0	6.95	9.26	92.3	4.78	2.69	0.22	1.31	0.37	1.37	0	0.82	0.94	2.79	0.37
RD57	33.6	2.88	18.08	20.68	0	6.88	8.85	90.97	4.84	2.7	0.17	1.3	0.42	1.39	0	0.83	0.91	2.81	0.37
RD57	33.07	4.13	17.87	21.05	0.14	6.58	9.01	91.85	4.82	2.65	0.25	1.35	0.34	1.41	0.01	0.79	0.92	2.8	0.36
RD52	31.6	3.11	16.17	22.97	1.45	7.33	7.89	90.52	4.98	2.62	0.19	1.38	0.19	1.59	0.1	0.9	0.83	2.99	0.36
RD52	34.66	3.35	18.14	21.15	0	8	9.56	94.86	4.65	2.68	0.19	1.32	0.34	1.37	0	0.92	0.94	2.82	0.4
RD52	34.58	3.6	18.01	22.15	0	7.42	7.42	93.18	4.7	2.7	0.21	1.3	0.36	1.45	0	0.86	0.74	2.89	0.37
RD52	33.81	3.21	18.32	22.36	0	7.02	7.02	91.74	4.77	2.69	0.19	1.31	0.4	1.49	0	0.83	0.71	2.91	0.36
RD52	34.37	3.38	18.35	22.49	0	7.22	7.22	93.03	4.71	2.69	0.2	1.31	0.39	1.47	0	0.84	0.72	2.9	0.36
RD62	35.32	3.75	18.91	21.28	0	7.49	9.38	96.13	4.57	2.69	0.21	1.31	0.38	1.35	0	0.85	0.91	2.8	0.39
RD62	34.54	3.22	18.64	20.55	0	7.52	9.13	93.6	4.69	2.69	0.19	1.31	0.41	1.34	0	0.87	0.91	2.81	0.39
RD62	35.29	3.32	18.84	21.18	0.15	7.75	9.42	95.95	4.58	2.69	0.19	1.31	0.38	1.35	0.01	0.88	0.92	2.82	0.39
RD62	35.25	3.56	18.8	21.06	0.15	7.68	9.76	96.26	4.57	2.68	0.2	1.32	0.37	1.34	0.01	0.87	0.95	2.8	0.39
RD62	35.04	3.85	18.16	21.38	0.2	7.72	9.22	95.57	4.61	2.69	0.22	1.31	0.33	1.37	0.01	0.88	0.9	2.82	0.39
RD62	35.38	4.23	18.49	20.86	0.15	7.42	9.38	95.91	4.58	2.69	0.24	1.31	0.35	1.33	0.01	0.84	0.91	2.78	0.39
RD62	35.43	4.04	18.05	20.64	0	7.73	9.44	95.33	4.6	2.71	0.23	1.29	0.34	1.32	0	0.88	0.92	2.78	0.4
RD62	35.51	3.62	18.68	21	0.14	7.72	9.41	96.08	4.57	2.7	0.21	1.3	0.37	1.34	0.01	0.88	0.91	2.8	0.4
RD10	34.32	4.09	18.33	20.43	0	7.39	9.5	94.06	4.68	2.67	0.24	1.33	0.35	1.33	0	0.86	0.94	2.78	0.39
RD10	33.62	2.2	18.79	23.32	0	6.72	9.04	93.69	4.75	2.66	0.13	1.34	0.41	1.54	0	0.79	0.91	2.88	0.34
RD18	35.67	3.16	18.86	20.72	0	7.74	9.43	95.58	4.58	2.72	0.18	1.28	0.41	1.32	0	0.88	0.92	2.8	0.4
RD18	34.96	3.62	18.91	22.17	0	7.08	9.58	96.32	4.59	2.67	0.21	1.33	0.37	1.42	0	0.81	0.93	2.8	0.36
RD18	35.37	3.2	18.83	21.63	0	7.25	9.72	96	4.59	2.7	0.18	1.3	0.4	1.38	0	0.83	0.95	2.79	0.37
RD18	34.92	3.25	18.68	21.32	0	8.03	9.49	95.69	4.6	2.68	0.19	1.32	0.36	1.37	0	0.92	0.93	2.83	0.4
RD68	33.84	3.49	17.7	19.69	0	7.57	8.91	91.2	4.8	2.7	0.21	1.3	0.37	1.32	0	0.9	0.91	2.8	0.41

sample	SiO2	TiO2	Al2O3	FeO	MnO	MgO	K2O	total	α	Si(t)	Ti(o)	Al(t)	Al(o)	Fe(o)	Mn(o)	Mg(o)	K	total(o)	Mg/Mg+Fe
RD68	33.87	3.44	17.73	19.84	0	7.82	8.87	91.57	4.78	2.7	0.21	1.3	0.36	1.32	0	0.93	0.9	2.82	0.41
RD68	33.97	3.83	17.67	20.44	0	7.07	9.02	92	4.78	2.7	0.23	1.3	0.36	1.36	0	0.84	0.92	2.78	0.38
RD68	34.6	4.03	18.25	21.16	0	7.13	9.29	94.46	4.66	2.68	0.24	1.32	0.35	1.37	0	0.82	0.92	2.79	0.38
RD68	34.36	4.13	17.99	20.98	0	7.1	9.2	93.76	4.7	2.69	0.24	1.31	0.34	1.37	0	0.83	0.92	2.79	0.38
RD68	34.3	3.88	18.07	20.81	0	7.52	9.27	93.85	4.69	2.68	0.23	1.32	0.34	1.36	0	0.88	0.92	2.8	0.39
RD68	34.29	2.86	18.55	20.1	0	8.25	9.22	93.27	4.7	2.68	0.17	1.32	0.39	1.31	0	0.96	0.92	2.84	0.42
RD68	34.41	3.98	18.16	19.97	0	7.52	9.2	93.24	4.7	2.69	0.23	1.31	0.36	1.31	0	0.88	0.92	2.78	0.4
RD68	34.49	4.05	18.44	20.3	0	7.59	9.27	94.14	4.66	2.67	0.24	1.33	0.36	1.32	0	0.88	0.92	2.79	0.4
RD65	33.27	3.48	17.65	21	0.21	7.57	9.21	92.39	4.79	2.65	0.21	1.35	0.31	1.4	0.01	0.9	0.94	2.84	0.39
RD65	34.4	2.57	19.58	20.37	0	7.71	8.74	93.37	4.68	2.68	0.15	1.32	0.47	1.33	0	0.89	0.87	2.84	0.4
RD65	34.19	3.34	18	20.36	0.2	8.16	9.24	93.49	4.71	2.68	0.2	1.32	0.34	1.33	0.01	0.95	0.92	2.83	0.42
RD65	33.53	2.21	19.64	21	0	8.11	7.12	91.61	4.75	2.65	0.13	1.35	0.48	1.39	0	0.95	0.72	2.95	0.41
RD65	34.46	2.86	18.33	20.35	0	8.26	9.47	93.73	4.69	2.69	0.17	1.31	0.37	1.33	0	0.96	0.94	2.83	0.42
RD65	34.08	3.33	17.75	20.99	0	7.34	9.06	92.55	4.76	2.7	0.2	1.3	0.36	1.39	0	0.87	0.92	2.82	0.38
RD65	34.22	3.34	18.26	21.17	0	7.35	9.16	93.5	4.71	2.68	0.2	1.32	0.37	1.39	0	0.86	0.92	2.82	0.38
RD65	34.16	3.62	18.04	20.78	0.11	7.35	9.16	93.22	4.72	2.69	0.21	1.31	0.36	1.37	0.01	0.86	0.92	2.81	0.39
RD65	34.47	3	18.48	21.24	0	7.24	8.93	93.36	4.71	2.7	0.18	1.3	0.41	1.39	0	0.85	0.89	2.82	0.38
RD65	33.8	2.96	18.12	20.75	0.12	7.74	9.41	92.9	4.75	2.67	0.18	1.33	0.36	1.37	0.01	0.91	0.95	2.83	0.4
RD65	34.03	3.07	18.31	19.96	0.17	8.14	9.18	92.86	4.73	2.68	0.18	1.32	0.37	1.31	0.01	0.95	0.92	2.83	0.42
RD114	34.74	4.12	18.42	21.36	0	7.29	9.29	95.22	4.63	2.67	0.24	1.33	0.35	1.38	0	0.84	0.91	2.8	0.38
RD114	33.71	4.18	17.3	20.8	0	6.79	9.23	92.01	4.8	2.69	0.25	1.31	0.32	1.39	0	0.81	0.94	2.77	0.37
RD114	34.62	4.16	17.56	20.93	0	8.05	9.32	94.64	4.66	2.68	0.24	1.32	0.29	1.36	0	0.93	0.92	2.81	0.41
RD62	35.68	2.76	18.89	20.64	0.25	7.9	9.52	95.64	4.58	2.72	0.16	1.28	0.42	1.32	0.02	0.9	0.93	2.81	0.41
RD62	35.09	2.31	19.16	20.28	0.17	9.63	9.46	96.1	4.56	2.66	0.13	1.34	0.37	1.29	0.01	1.09	0.92	2.89	0.46
RD114	34.62	3.26	18.38	21.84	0	8.12	8.93	95.15	4.63	2.67	0.19	1.33	0.34	1.41	0	0.93	0.88	2.87	0.4
RDW74	34.68	3.29	18.42	20.87	0	7.15	8.44	92.85	4.71	2.72	0.19	1.28	0.42	1.37	0	0.84	0.84	2.82	0.38
RD67	34.28	3.81	17.42	20.39	0	7.13	8.59	91.62	4.78	2.73	0.23	1.27	0.36	1.36	0	0.85	0.87	2.79	0.38
RD27	33.8	3.09	17.5	20.65	0	6.79	9.67	91.5	4.83	2.72	0.19	1.28	0.38	1.39	0	0.81	0.99	2.77	0.37
RD27	36.56	3.18	19.5	20.67	0	8.36	9.37	97.64	4.46	2.72	0.18	1.28	0.42	1.28	0	0.93	0.89	2.81	0.42
RD27	36.93	2.96	19.4	21.7	0	8.8	9.14	98.93	4.42	2.71	0.16	1.29	0.39	1.33	0	0.96	0.86	2.86	0.42
RD27	35.65	3.89	17.68	20.03	0	7.47	9.28	94	4.65	2.76	0.23	1.24	0.37	1.3	0	0.86	0.92	2.75	0.4
RD27	33.27	3.56	17.79	21.87	0	7.43	9.08	93	4.77	2.64	0.21	1.36	0.31	1.45	0	0.88	0.92	2.85	0.38
RD27	33.76	3.51	17.75	21.91	0	7.05	8.99	92.97	4.76	2.68	0.21	1.32	0.34	1.45	0	0.83	0.91	2.83	0.36
RD27	34.36	2.67	18.8	20.55	0	7.37	9.24	92.99	4.72	2.7	0.16	1.3	0.44	1.35	0	0.86	0.93	2.81	0.39
RD31	31.98	4.73	18.04	24.47	0	4.53	8.06	91.81	4.88	2.6	0.29	1.4	0.33	1.66	0	0.55	0.84	2.83	0.25

A1-1.6 Secondary Biotite in the Mine Granite

sample	SiO2	TiO2	Al2O3	FeO	MnO	MgO	K2O	total	α	Si(t)	Ti(o)	Al(t)	Al(o)	Fe(o)	Mn(o)	Mg(o)	K	total(o)	Mg/Mg+Fe
RD59	32.37	1.01	19.62	26.60	0.16	7.22	7.51	94.49	4.76	2.56	0.06	1.44	0.40	1.76	0.01	0.85	0.76	3.08	0.33
RD10	32.61	1.16	18.95	24.01	0.00	6.50	9.05	92.28	4.86	2.64	0.07	1.36	0.44	1.62	0.00	0.78	0.93	2.92	0.33
RD10	32.71	0.51	18.96	24.18	0.00	6.92	8.54	91.82	4.87	2.65	0.03	1.35	0.46	1.64	0.00	0.84	0.88	2.97	0.34
RD10	32.24	1.63	19.33	23.10	0.00	6.60	8.82	91.72	4.86	2.61	0.10	1.39	0.45	1.56	0.00	0.80	0.91	2.91	0.34
RD10	33.87	0.51	17.87	23.18	0.00	7.18	8.83	91.44	4.87	2.74	0.03	1.26	0.45	1.57	0.00	0.87	0.91	2.92	0.36
RD10	32.21	0.59	18.04	25.52	0.00	6.56	8.57	91.49	4.94	2.65	0.04	1.35	0.40	1.75	0.00	0.80	0.90	2.99	0.31
RD10	33.73	0.63	17.94	23.73	0.00	7.21	8.87	92.11	4.85	2.72	0.04	1.28	0.43	1.60	0.00	0.87	0.91	2.93	0.35
RD10	33.95	1.01	18.12	23.60	0.00	7.21	8.92	92.81	4.80	2.71	0.06	1.29	0.42	1.58	0.00	0.86	0.91	2.92	0.35
RD10	33.08	0.91	17.62	24.84	0.00	7.23	7.71	91.39	4.89	2.69	0.06	1.31	0.38	1.69	0.00	0.88	0.80	3.01	0.34
RD10	34.20	0.88	18.56	23.03	0.00	6.94	9.41	93.02	4.79	2.72	0.05	1.28	0.47	1.53	0.00	0.82	0.96	2.88	0.35
RD10	33.54	1.47	17.49	24.35	0.00	6.96	8.14	91.95	4.86	2.71	0.09	1.29	0.38	1.65	0.00	0.84	0.84	2.95	0.34
RD10	33.43	1.16	17.14	24.64	0.00	6.68	8.94	91.99	4.89	2.72	0.07	1.28	0.36	1.68	0.00	0.81	0.93	2.92	0.33
RD10	33.95	1.10	17.98	23.92	0.00	6.79	9.15	92.89	4.81	2.72	0.07	1.28	0.42	1.60	0.00	0.81	0.94	2.90	0.34
RD10	33.76	0.83	18.89	23.62	0.00	6.91	9.08	93.09	4.79	2.69	0.05	1.31	0.47	1.57	0.00	0.82	0.92	2.91	0.34
RD10	33.81	0.70	18.86	21.74	0.00	6.85	9.06	91.02	4.85	2.73	0.04	1.27	0.53	1.47	0.00	0.82	0.93	2.86	0.36
RD10	34.17	1.00	18.15	23.65	0.00	6.99	9.05	93.01	4.79	2.73	0.06	1.27	0.43	1.58	0.00	0.83	0.92	2.90	0.35
RD10	33.46	1.91	18.77	22.60	0.00	6.61	9.23	92.58	4.80	2.67	0.11	1.33	0.44	1.51	0.00	0.79	0.94	2.86	0.34
RD10	33.32	0.59	19.69	22.52	0.00	7.09	9.13	92.34	4.81	2.66	0.04	1.34	0.52	1.51	0.00	0.85	0.93	2.91	0.36
RD10	32.99	0.39	18.92	24.46	0.00	7.01	8.68	92.45	4.84	2.66	0.02	1.34	0.46	1.65	0.00	0.84	0.89	2.97	0.34
RD10	33.42	0.75	18.73	24.46	0.00	7.02	8.61	92.99	4.81	2.67	0.05	1.33	0.44	1.64	0.00	0.84	0.88	2.96	0.34
RD10	32.45	0.44	20.84	23.40	0.00	6.87	9.43	93.43	4.78	2.58	0.03	1.42	0.54	1.56	0.00	0.82	0.96	2.94	0.34
RD10	32.79	1.38	18.22	23.58	0.00	6.58	8.14	90.69	4.91	2.68	0.08	1.32	0.44	1.61	0.00	0.80	0.85	2.93	0.33
RD10	33.02	0.63	17.81	25.75	0.00	7.22	7.79	92.22	4.87	2.68	0.04	1.32	0.38	1.75	0.00	0.87	0.81	3.03	0.33
RD10	33.14	1.17	17.64	25.00	0.00	7.21	8.11	92.27	4.86	2.68	0.07	1.32	0.36	1.69	0.00	0.87	0.84	2.99	0.34
RD12	35.32	0.73	19.08	24.40	0.00	5.42	9.36	94.31	4.72	2.78	0.04	1.22	0.54	1.60	0.00	0.64	0.94	2.83	0.28
RD12	34.93	0.90	18.65	24.50	0.00	5.11	9.30	93.39	4.78	2.78	0.05	1.22	0.53	1.63	0.00	0.61	0.94	2.82	0.27
RD12	33.70	1.05	18.67	24.89	0.00	5.69	8.37	92.37	4.84	2.71	0.06	1.29	0.49	1.68	0.00	0.68	0.86	2.91	0.29
RD12	35.52	0.80	19.12	24.31	0.00	5.50	9.02	94.27	4.71	2.78	0.05	1.22	0.55	1.59	0.00	0.64	0.90	2.84	0.29
RD12	32.02	0.80	17.73	27.71	0.00	6.62	7.02	91.90	4.93	2.63	0.05	1.37	0.34	1.90	0.00	0.81	0.73	3.10	0.30
RD12	33.03	1.01	18.03	27.95	0.00	5.66	8.11	93.79	4.84	2.66	0.06	1.34	0.38	1.88	0.00	0.68	0.83	3.00	0.27
RD12	33.75	0.62	17.95	24.66	0.00	5.36	8.83	91.17	4.92	2.76	0.04	1.24	0.49	1.69	0.00	0.65	0.92	2.87	0.28

sample	SiO2	TiO2	Al2O3	FeO	MnO	MgO	K2O	total	α	Si(t)	Ti(o)	Al(t)	Al(o)	Fe(o)	Mn(o)	Mg(o)	K	total(o)	Mg/Mg+Fe
RD12	33.57	0.91	17.46	26.44	0.00	6.27	8.48	93.13	4.85	2.71	0.06	1.29	0.37	1.79	0.00	0.75	0.87	2.97	0.30
RD12	32.59	0.97	17.55	28.30	0.00	6.57	7.25	93.23	4.87	2.64	0.06	1.36	0.32	1.92	0.00	0.79	0.75	3.09	0.29
RD12	33.75	0.62	17.95	24.66	0.00	5.36	8.83	91.17	4.92	2.76	0.04	1.24	0.49	1.69	0.00	0.65	0.92	2.87	0.28
RD12	33.57	0.91	17.46	26.44	0.00	6.27	8.48	93.13	4.85	2.71	0.06	1.29	0.37	1.79	0.00	0.75	0.87	2.97	0.30
RD12	32.59	0.97	17.55	28.30	0.00	6.57	7.25	93.23	4.87	2.64	0.06	1.36	0.32	1.92	0.00	0.79	0.75	3.09	0.29
RD12	35.10	1.14	19.20	24.37	0.00	4.92	9.36	94.09	4.74	2.77	0.07	1.23	0.55	1.61	0.00	0.58	0.94	2.80	0.26
RD12	35.51	0.99	18.72	23.92	0.00	5.41	9.31	93.86	4.73	2.80	0.06	1.20	0.54	1.58	0.00	0.64	0.94	2.81	0.29
RD80	34.28	3.11	18.23	24.58	0.00	5.34	9.51	95.05	4.72	2.69	0.18	1.31	0.38	1.61	0.00	0.63	0.95	2.80	0.28
RD80	32.74	2.48	17.23	24.48	0.00	5.16	8.77	90.86	4.95	2.70	0.15	1.30	0.37	1.69	0.00	0.63	0.92	2.85	0.27
RD80	33.12	2.30	17.90	27.47	0.00	4.92	8.12	93.83	4.83	2.66	0.14	1.34	0.36	1.85	0.00	0.59	0.83	2.93	0.24
RD80	34.95	3.41	17.93	23.26	0.00	6.76	9.41	95.72	4.65	2.70	0.20	1.30	0.34	1.50	0.00	0.78	0.93	2.82	0.34
RD80	35.90	0.00	20.18	23.54	0.00	5.91	9.65	95.18	4.65	2.78	0.00	1.22	0.62	1.52	0.00	0.68	0.95	2.83	0.31
RD80	33.63	2.04	18.42	23.26	0.00	5.62	9.14	92.11	4.84	2.71	0.12	1.29	0.46	1.57	0.00	0.67	0.94	2.82	0.30
RD80	34.53	2.54	18.16	24.21	0.00	5.62	9.46	94.52	4.73	2.72	0.15	1.28	0.41	1.60	0.00	0.66	0.95	2.81	0.29
RD80	35.25	1.05	19.84	23.23	0.00	5.53	9.48	94.38	4.69	2.75	0.06	1.25	0.58	1.52	0.00	0.64	0.94	2.80	0.30
RD80	34.16	3.69	17.50	23.26	0.00	6.59	9.15	94.35	4.72	2.69	0.22	1.31	0.31	1.53	0.00	0.77	0.92	2.83	0.34
RD16	35.21	1.43	19.46	25.30	0.00	4.19	7.35	92.94	4.75	2.79	0.09	1.21	0.60	1.67	0.00	0.49	0.74	2.85	0.23
RD16	33.69	1.42	19.10	26.09	0.00	4.00	8.52	92.82	4.84	2.72	0.09	1.28	0.53	1.76	0.00	0.48	0.88	2.85	0.21
RD16	34.74	3.97	18.11	25.21	0.00	4.97	9.31	96.31	4.66	2.69	0.23	1.31	0.35	1.63	0.00	0.57	0.92	2.79	0.26
RD16	33.62	2.48	18.26	24.81	0.00	4.19	8.84	92.20	4.86	2.72	0.15	1.28	0.46	1.68	0.00	0.51	0.91	2.80	0.23
RD16	33.62	2.77	18.07	25.98	0.00	4.39	9.10	93.93	4.81	2.69	0.17	1.31	0.40	1.74	0.00	0.52	0.93	2.83	0.23
RD16	34.23	3.51	18.00	23.67	0.00	5.09	9.01	93.51	4.77	2.72	0.21	1.28	0.40	1.57	0.00	0.60	0.91	2.78	0.28
RD16	34.86	2.00	20.31	25.31	0.00	4.06	8.44	94.98	4.68	2.72	0.12	1.28	0.58	1.65	0.00	0.47	0.84	2.82	0.22
RD16	32.27	1.60	19.03	29.09	0.00	4.14	7.75	93.88	4.86	2.61	0.10	1.39	0.42	1.97	0.00	0.50	0.80	2.99	0.20
RD16	32.91	1.32	18.63	28.67	0.00	4.39	8.20	94.12	4.84	2.65	0.08	1.35	0.42	1.93	0.00	0.53	0.84	2.96	0.21
RD16	34.08	1.36	18.17	27.57	0.00	4.36	9.00	94.54	4.80	2.72	0.08	1.28	0.44	1.84	0.00	0.52	0.92	2.88	0.22
RD16	32.92	0.87	19.90	27.54	0.00	4.48	7.93	93.64	4.82	2.64	0.05	1.36	0.52	1.85	0.00	0.54	0.81	2.96	0.22
RD16	33.06	1.51	18.26	24.96	0.00	4.79	8.41	90.99	4.93	2.71	0.09	1.29	0.48	1.71	0.00	0.59	0.88	2.87	0.25
RD16	33.85	1.97	17.94	27.62	0.00	4.24	8.48	94.10	4.82	2.71	0.12	1.29	0.41	1.85	0.00	0.51	0.87	2.89	0.21
RD50	33.90	1.94	18.09	23.32	0.00	5.72	9.16	92.13	4.84	2.73	0.12	1.27	0.45	1.57	0.00	0.69	0.94	2.82	0.30
RD50	33.38	2.34	18.18	22.79	0.00	5.43	9.07	91.19	4.88	2.71	0.14	1.29	0.45	1.55	0.00	0.66	0.94	2.80	0.30
RD50	31.47	1.84	19.12	24.62	0.00	5.43	8.60	91.08	4.94	2.59	0.11	1.41	0.44	1.69	0.00	0.67	0.90	2.92	0.28
RD50	33.23	2.74	17.96	22.51	0.00	6.04	9.02	91.50	4.86	2.69	0.17	1.31	0.40	1.52	0.00	0.73	0.93	2.82	0.32
RD50	32.83	2.14	18.38	24.57	0.00	5.91	9.09	92.92	4.84	2.65	0.13	1.35	0.39	1.66	0.00	0.71	0.93	2.89	0.30
RD50	33.99	2.69	18.29	23.67	0.00	6.14	9.29	94.07	4.75	2.69	0.16	1.31	0.39	1.56	0.00	0.72	0.94	2.84	0.32

sample	SiO2	TiO2	Al2O3	FeO	MnO	MgO	K2O	total	α	Si(t)	Ti(o)	Al(t)	Al(o)	Fe(o)	Mn(o)	Mg(o)	K	total(o)	Mg/Mg+Fe
RD50	32.91	2.88	18.40	24.80	0.00	6.21	8.63	93.83	4.78	2.62	0.17	1.38	0.35	1.65	0.00	0.74	0.88	2.91	0.31
RD50	33.28	2.47	18.35	24.48	0.00	6.18	8.77	93.53	4.79	2.65	0.15	1.35	0.38	1.63	0.00	0.73	0.89	2.89	0.31
RD50	32.50	2.46	18.65	25.01	0.00	6.26	8.45	93.33	4.81	2.60	0.15	1.40	0.37	1.68	0.00	0.75	0.86	2.94	0.31
RD50	33.63	2.70	18.58	23.46	0.00	6.18	9.26	93.81	4.76	2.66	0.16	1.34	0.40	1.55	0.00	0.73	0.94	2.84	0.32
RD50	32.77	1.75	18.07	25.76	0.00	5.57	8.33	92.25	4.89	2.66	0.11	1.34	0.40	1.75	0.00	0.68	0.86	2.93	0.28
RD10	32.10	2.02	17.55	25.59	0.00	6.66	8.23	92.15	4.90	2.62	0.12	1.38	0.31	1.75	0.00	0.81	0.86	2.99	0.32
RD10	32.42	0.65	18.07	26.31	0.00	7.27	7.83	92.55	4.87	2.63	0.04	1.37	0.36	1.79	0.00	0.88	0.81	3.06	0.33
RD10	32.34	1.00	17.14	26.06	0.00	7.59	7.27	91.40	4.92	2.65	0.06	1.35	0.31	1.79	0.00	0.93	0.76	3.08	0.34
RD10	32.76	0.77	18.20	25.93	0.00	6.91	8.08	92.65	4.86	2.65	0.05	1.35	0.39	1.75	0.00	0.83	0.83	3.02	0.32
RD10	32.55	0.00	18.97	25.11	0.00	7.31	7.69	91.63	4.88	2.64	0.00	1.36	0.46	1.71	0.00	0.89	0.80	3.05	0.34
RD10	32.53	0.70	20.04	22.91	0.00	6.93	8.94	92.05	4.83	2.62	0.04	1.38	0.52	1.54	0.00	0.83	0.92	2.93	0.35
RD10	32.91	1.18	18.40	24.06	0.00	7.65	7.77	91.97	4.84	2.65	0.07	1.35	0.40	1.62	0.00	0.92	0.80	3.01	0.36
RD10	31.58	0.89	17.25	26.65	0.00	8.10	6.01	90.48	4.96	2.61	0.06	1.39	0.29	1.84	0.00	1.00	0.63	3.18	0.35
RD19	32.48	1.46	17.21	28.21	0.00	4.21	8.41	91.98	4.98	2.69	0.09	1.31	0.37	1.95	0.00	0.52	0.89	2.94	0.21
RD19	33.31	0.69	18.99	26.73	0.00	4.42	8.87	93.01	4.87	2.70	0.04	1.30	0.51	1.81	0.00	0.53	0.92	2.90	0.23
RD19	32.69	1.43	16.74	28.21	0.00	5.30	7.90	92.27	4.95	2.69	0.09	1.31	0.31	1.94	0.00	0.65	0.83	3.00	0.25
RD19	32.76	1.12	18.03	27.75	0.00	4.48	8.80	92.94	4.91	2.68	0.07	1.32	0.42	1.90	0.00	0.55	0.92	2.93	0.22
RD19	38.34	0.48	17.54	23.88	0.00	4.61	8.36	93.21	4.70	3.00	0.03	1.00	0.62	1.56	0.00	0.54	0.83	2.75	0.26
RD19	33.12	0.91	18.55	27.48	0.00	4.62	8.99	93.67	4.86	2.68	0.06	1.32	0.45	1.86	0.00	0.56	0.93	2.92	0.23
RD19	34.51	0.86	17.96	24.95	0.00	5.09	9.30	92.67	4.84	2.78	0.05	1.22	0.49	1.68	0.00	0.61	0.96	2.84	0.27
RD19	34.34	1.10	17.35	25.89	0.00	5.34	9.30	93.32	4.84	2.77	0.07	1.23	0.41	1.74	0.00	0.64	0.96	2.87	0.27
RD19	33.16	0.55	18.76	27.26	0.00	4.99	8.87	93.59	4.85	2.68	0.03	1.32	0.46	1.84	0.00	0.60	0.91	2.94	0.25
RD19	31.09	0.55	17.07	21.08	0.00	4.07	8.57	82.43	5.40	2.80	0.04	1.20	0.60	1.59	0.00	0.55	0.98	2.77	0.26
RD19	32.55	1.67	17.88	28.39	0.00	3.96	8.84	93.29	4.91	2.66	0.10	1.34	0.39	1.94	0.00	0.48	0.92	2.91	0.20
RD19	33.20	1.17	18.41	27.11	0.00	4.81	9.37	94.07	4.84	2.68	0.07	1.32	0.42	1.83	0.00	0.58	0.96	2.90	0.24
RD19	32.39	1.31	17.38	27.98	0.00	4.53	8.61	92.20	4.97	2.68	0.08	1.32	0.37	1.93	0.00	0.56	0.91	2.94	0.22
RD19	34.14	1.82	18.91	25.37	0.00	3.95	8.96	93.15	4.82	2.74	0.11	1.26	0.52	1.70	0.00	0.47	0.92	2.80	0.22
RD19	32.51	1.61	16.74	28.58	0.00	4.14	8.96	92.54	4.98	2.69	0.10	1.31	0.33	1.98	0.00	0.51	0.95	2.92	0.21
RD19	32.32	1.96	17.09	28.07	0.00	4.21	8.55	92.20	4.97	2.67	0.12	1.33	0.34	1.94	0.00	0.52	0.90	2.92	0.21
RD19	32.83	2.00	17.79	27.21	0.00	4.32	8.68	92.83	4.90	2.68	0.12	1.32	0.39	1.86	0.00	0.53	0.90	2.89	0.22
RD19	32.00	1.45	18.67	27.01	0.00	4.46	7.00	90.59	4.97	2.65	0.09	1.35	0.47	1.87	0.00	0.55	0.74	2.98	0.23
RD19	32.06	1.66	17.70	27.98	0.00	4.55	7.60	91.55	4.97	2.65	0.10	1.35	0.38	1.94	0.00	0.56	0.80	2.98	0.22
RD21	35.29	3.07	19.00	23.90	0.00	5.81	9.61	96.68	4.60	2.70	0.18	1.30	0.42	1.53	0.00	0.66	0.94	2.79	0.30
RD21	35.10	3.15	18.60	24.71	0.00	5.40	9.54	96.50	4.63	2.71	0.18	1.29	0.40	1.59	0.00	0.62	0.94	2.80	0.28
RD21	33.86	1.53	19.82	27.13	0.00	4.30	8.77	95.41	4.73	2.67	0.09	1.33	0.50	1.79	0.00	0.50	0.88	2.89	0.22

sample	SiO2	TiO2	Al2O3	FeO	MnO	MgO	K2O	total	α	Si(t)	Ti(o)	Al(t)	Al(o)	Fe(o)	Mn(o)	Mg(o)	K	total(o)	Mg/Mg+Fe
RD21	33.68	1.11	18.75	27.74	0.00	4.88	8.94	95.10	4.78	2.68	0.07	1.32	0.44	1.84	0.00	0.58	0.91	2.92	0.24
RD21	33.13	1.48	17.73	27.60	0.00	4.18	9.17	93.29	4.90	2.70	0.09	1.30	0.40	1.88	0.00	0.51	0.95	2.88	0.21
RD21	35.12	3.44	17.61	23.51	0.00	6.07	9.24	94.99	4.68	2.74	0.20	1.26	0.35	1.53	0.00	0.71	0.92	2.79	0.32
RD114	31.36	1.93	18.85	23.52	0.00	7.97	7.30	90.93	4.89	2.55	0.12	1.45	0.36	1.60	0.00	0.97	0.76	3.05	0.38
RD114	33.99	1.70	18.58	21.12	0.00	8.93	8.57	92.89	4.73	2.67	0.10	1.33	0.40	1.39	0.00	1.05	0.86	2.93	0.43
RD114	34.01	3.39	17.80	21.15	0.00	8.24	8.63	93.22	4.72	2.67	0.20	1.33	0.32	1.39	0.00	0.96	0.86	2.87	0.41
RD81	32.38	1.52	16.80	27.53	0.00	3.29	8.69	90.21	5.08	2.74	0.10	1.26	0.41	1.95	0.00	0.41	0.94	2.86	0.18
RD81	34.76	1.56	17.33	27.49	0.00	3.67	9.04	93.85	4.83	2.80	0.09	1.20	0.44	1.85	0.00	0.44	0.93	2.82	0.19
RD81	35.94	1.22	18.99	26.18	0.00	3.44	8.49	94.26	4.73	2.83	0.07	1.17	0.59	1.72	0.00	0.40	0.85	2.79	0.19
RD81	35.09	1.53	17.80	27.72	0.00	3.61	9.57	95.32	4.77	2.78	0.09	1.22	0.45	1.84	0.00	0.43	0.97	2.81	0.19
RD81	35.34	1.39	18.33	28.23	0.00	3.86	9.72	96.87	4.70	2.76	0.08	1.24	0.45	1.85	0.00	0.45	0.97	2.83	0.20

A1-1.7 Biotite in the Ardlethan Granite

sample	SiO2	TiO2	Al2O3	FeO	MnO	MgO	K2O	total	α	Si(t)	Ti(o)	Al(t)	Al(o)	Fe(o)	Mn(o)	Mg(o)	K	total(o)	Mg/Mg+Fe
TH01	34.99	1.94	19.97	24.45	0.15	1.77	9.09	92.36	4.82	2.81	0.12	1.19	0.69	1.64	0.01	0.21	0.93	2.67	0.11
TH08	36.33	1.19	20.62	22.22	0.29	1.11	8.93	90.69	4.82	2.92	0.07	1.08	0.87	1.49	0.02	0.13	0.91	2.58	0.08
TH08	36.29	1	21.48	21.2	0.47	1.22	8.98	90.64	4.8	2.9	0.06	1.1	0.92	1.42	0.03	0.15	0.92	2.57	0.09
TH08	35.72	1.13	21.01	22.4	0.4	1.16	8.73	90.55	4.84	2.88	0.07	1.12	0.87	1.51	0.03	0.14	0.9	2.61	0.08
TH08	35.81	1.26	20.32	21.22	0.4	1.28	8.53	88.82	4.9	2.92	0.08	1.08	0.87	1.45	0.03	0.16	0.89	2.58	0.1
TH08	36.55	0.88	20.73	20.98	0.23	1.17	8.42	88.96	4.86	2.96	0.05	1.04	0.94	1.42	0.02	0.14	0.87	2.57	0.09
TH08	36.16	0.77	20.81	20.95	0.36	1.13	8.81	88.99	4.88	2.94	0.05	1.06	0.93	1.42	0.02	0.14	0.91	2.56	0.09
TH08	38.69	0.9	22.31	19.73	0.23	1.12	7.59	90.57	4.68	3.01	0.05	0.99	1.06	1.28	0.02	0.13	0.75	2.54	0.09
TH08	36.22	1.3	20.81	22.89	0.32	1.25	8.98	91.77	4.78	2.88	0.08	1.12	0.84	1.52	0.02	0.15	0.91	2.61	0.09
TH08	37.66	1.03	21.76	20.96	0.38	1.21	8.84	91.84	4.7	2.95	0.06	1.05	0.95	1.37	0.03	0.14	0.88	2.55	0.09
TH08	38.09	1.01	22.09	22.52	0.41	1.26	9.15	94.53	4.6	2.92	0.06	1.08	0.91	1.44	0.03	0.14	0.89	2.58	0.09
TH08	37.83	0.64	22.41	22.27	0.38	1.29	9.25	94.07	4.62	2.91	0.04	1.09	0.94	1.43	0.02	0.15	0.91	2.58	0.09
TH08	37.41	1.68	20.94	23.55	0.42	1.37	8.84	94.21	4.65	2.9	0.1	1.1	0.81	1.52	0.03	0.16	0.87	2.62	0.09
TH08	38.49	0.94	22.17	22.44	0.42	1.16	9.46	95.08	4.58	2.93	0.05	1.07	0.92	1.43	0.03	0.13	0.92	2.56	0.08
TH08	37.89	0.85	22	22.29	0.32	1.44	9.23	94.02	4.63	2.92	0.05	1.08	0.91	1.44	0.02	0.17	0.91	2.58	0.1
TH08	37.08	0.87	22	23.04	1.43	0	9.16	93.58	4.7	2.9	0.05	1.1	0.93	1.51	0.09	0	0.91	2.58	0
TH08	36.38	1.56	21.04	24.2	0.38	1.21	9.07	93.84	4.71	2.85	0.09	1.15	0.79	1.59	0.03	0.14	0.91	2.64	0.08

sample	SiO2	TiO2	Al2O3	FeO	MnO	MgO	K2O	total	α	Si(t)	Ti(o)	Al(t)	Al(o)	Fe(o)	Mn(o)	Mg(o)	K	total(o)	Mg/Mg+Fe
TH08	37.02	1.9	20.52	23.23	0.35	1.32	9.03	93.37	4.7	2.9	0.11	1.1	0.79	1.52	0.02	0.15	0.9	2.6	0.09
TH08	36.66	1.28	21.17	25.56	0.21	1.19	9.49	95.56	4.65	2.84	0.07	1.16	0.77	1.66	0.01	0.14	0.94	2.65	0.08
TH08	37.31	1.17	21.6	23.77	0.37	1.25	9.27	94.74	4.64	2.88	0.07	1.12	0.84	1.53	0.02	0.14	0.91	2.61	0.09
TH08	37.39	0.88	21.9	22.73	0.47	1.36	9.2	93.93	4.65	2.89	0.05	1.11	0.89	1.47	0.03	0.16	0.91	2.6	0.1
TH08	38.04	1.45	21.82	22.49	0.24	1.33	9.14	94.51	4.6	2.91	0.08	1.09	0.88	1.44	0.02	0.15	0.89	2.57	0.1
TH08	35.86	1.59	20.3	23.9	0.48	1.24	8.83	92.2	4.79	2.86	0.1	1.14	0.77	1.59	0.03	0.15	0.9	2.64	0.08
TH08	36	0.74	21.05	22.2	0.32	1.2	8.66	90.17	4.84	2.9	0.04	1.1	0.9	1.5	0.02	0.14	0.89	2.61	0.09
TH11	36.45	1.01	21.85	21.87	0.44	1.01	9.12	91.75	4.75	2.88	0.06	1.12	0.92	1.45	0.03	0.12	0.92	2.58	0.08
TH11	36.37	1.31	21.22	24.18	0.45	1.13	8.98	93.64	4.71	2.85	0.08	1.15	0.81	1.59	0.03	0.13	0.9	2.64	0.08
TH11	37.11	1.04	22.11	22.11	0.39	1.17	9.2	93.13	4.68	2.89	0.06	1.11	0.92	1.44	0.03	0.14	0.91	2.58	0.09
TH11	39.93	0.69	22.47	18.42	0.28	1.01	8.88	91.68	4.61	3.06	0.04	0.94	1.09	1.18	0.02	0.12	0.87	2.45	0.09
TH11	37.28	1.12	22.06	21.92	0.41	1.18	8.88	92.85	4.68	2.9	0.07	1.1	0.93	1.43	0.03	0.14	0.88	2.58	0.09

A1-1.8 Chlorite in the Ardlethan Granite

Sample	SiO2	TiO2	Al2O3	FeO	MnO	MgO	K2O	total	α	Si(t)	Al(t)	Ti(o)	Al(o)	Fe(o)	Mn(o)	Mg(o)	K	Mg/Mg+Fe
RDS70	22.9	0	21.12	41.28	0.99	2.27	0	88.56	6.90	2.63	1.37	0.00	1.49	3.97	0.10	0.39	0.00	0.09
RDS70	22.16	0	20.32	40.04	1.37	3.09	0	86.98	7.04	2.60	1.40	0.00	1.40	3.92	0.14	0.54	0.00	0.12
RDS70	22.16	0	21.63	41.37	1.56	1.9	0.15	88.77	6.93	2.56	1.44	0.00	1.50	3.99	0.15	0.33	0.02	0.08
RDS70	21.92	0	21.3	41.48	1.56	1.98	0.24	88.48	6.98	2.54	1.46	0.00	1.46	4.03	0.15	0.34	0.04	0.08
RDS70	23.02	0	21.21	41.63	1.2	2.63	0	89.69	6.82	2.61	1.39	0.00	1.45	3.95	0.12	0.45	0.00	0.10
RDS70	22.42	0	21.05	40.42	0.96	1.8	0.06	86.71	7.05	2.63	1.37	0.00	1.54	3.96	0.10	0.31	0.01	0.07
RDS70	21.88	0	22.14	42.55	1.48	0.95	0	89	6.94	2.53	1.47	0.00	1.54	4.11	0.14	0.16	0.00	0.04
RDS70	22.66	0	21.02	41.21	0.78	2.67	0	88.34	6.92	2.61	1.39	0.00	1.46	3.97	0.08	0.46	0.00	0.10
RDS70	21.53	0	21.53	42.24	0.88	1.7	0.07	87.95	7.02	2.52	1.48	0.00	1.48	4.13	0.09	0.30	0.01	0.07
RDS70	23.07	0	22.1	43.01	1.11	2.12	0.19	91.6	6.71	2.58	1.42	0.00	1.48	4.02	0.10	0.35	0.03	0.08

A1-1.9 Chlorite in the Mine Granite

Sample	SiO2	TiO2	Al2O3	FeO	MnO	MgO	K2O	total	α	Si(t)	Al(t)	Ti(o)	Al(o)	Fe(o)	Mn(o)	Mg(o)	K	Mg/Mg+Fe
RD59	25.48	0.17	20.94	30.42	0.44	11.57	0.57	89.59	6.39	2.71	1.29	0.01	1.33	2.71	0.04	1.83	0.08	0.40

Sample	SiO2	TiO2	Al2O3	FeO	MnO	MgO	K2O	total	α	Si(t)	Al(t)	Ti(o)	Al(o)	Fe(o)	Mn(o)	Mg(o)	K	Mg/Mg+Fe
RD23	27.41	0	21.02	29.1	0	8.74	0.28	86.55	6.50	2.96	1.04	0.00	1.64	2.63	0.00	1.41	0.04	0.35
RD23	24.79	0.17	19.36	33.21	0.2	9.4	0.13	87.26	6.67	2.75	1.25	0.01	1.29	3.08	0.02	1.56	0.02	0.34
RD23	25.18	0	20.04	32.58	0.14	9.43	0	87.37	6.61	2.77	1.23	0.00	1.37	3.00	0.01	1.55	0.00	0.34
RD23	26.08	0.31	18.95	31.93	0.24	8.87	0.97	87.35	6.63	2.88	1.12	0.03	1.34	2.95	0.02	1.46	0.14	0.33
RD57	23.11	0	20.51	30.13	0.39	10.42	0.16	84.72	6.80	2.62	1.38	0.00	1.35	2.85	0.04	1.76	0.02	0.38
RD57	23.92	0	19.91	30.19	0.34	10.91	0.12	85.39	6.74	2.68	1.32	0.00	1.31	2.83	0.03	1.82	0.02	0.39
RD57	26.24	0	21.15	27.13	0.29	9.56	0.99	85.36	6.59	2.88	1.12	0.00	1.61	2.49	0.03	1.56	0.14	0.39
RD2	23.61	0	19.79	32.53	0.53	9.34	0	85.8	6.80	2.67	1.33	0.00	1.31	3.08	0.05	1.57	0.00	0.34
RD2	24.13	0	20.49	33.83	0.57	9.32	0	88.34	6.62	2.66	1.34	0.00	1.32	3.12	0.05	1.53	0.00	0.33
RD2	24.14	0	20.43	33.31	0.73	9.28	0	87.89	6.64	2.67	1.33	0.00	1.33	3.08	0.07	1.53	0.00	0.33
RD2	24.1	0	20.2	33.24	0.57	9.52	0	87.63	6.66	2.67	1.33	0.00	1.31	3.08	0.05	1.57	0.00	0.34
RD2	24.14	0	20.43	33.31	0.73	9.28	0.08	87.97	6.64	2.67	1.33	0.00	1.33	3.08	0.07	1.53	0.01	0.33
RD52	24.87	0.25	19.87	33.1	0.28	10.07	0	88.44	6.56	2.72	1.28	0.02	1.27	3.02	0.03	1.64	0.00	0.35
RD52	24.74	0.11	19.72	32.46	0.2	10.05	0.19	87.47	6.63	2.73	1.27	0.01	1.29	2.99	0.02	1.65	0.03	0.36
RD52	25.56	0.12	18.93	31.34	0.27	11.45	0	87.67	6.56	2.79	1.21	0.01	1.23	2.86	0.02	1.86	0.00	0.39
RD52	24.65	0.2	19.75	32.9	0.26	9.9	0.07	87.73	6.62	2.72	1.28	0.02	1.28	3.03	0.02	1.63	0.01	0.35
RD52	25.54	0	19.42	31.66	0.24	10.59	0.39	87.84	6.57	2.79	1.21	0.00	1.29	2.89	0.02	1.73	0.05	0.37
RD52	24.42	0.96	19.59	32.71	0.17	10.14	0	87.99	6.60	2.68	1.32	0.08	1.22	3.00	0.02	1.66	0.00	0.36
RD52	24.58	0	19.96	32.91	0.35	9.72	0	87.52	6.64	2.71	1.29	0.00	1.31	3.04	0.03	1.60	0.00	0.34
RD52	24.86	0.22	19.7	32.14	0.26	10.61	0.09	87.88	6.58	2.72	1.28	0.02	1.27	2.94	0.02	1.73	0.01	0.37
RD52	25.32	0	19.23	31.89	0.34	10.88	0	87.66	6.58	2.77	1.23	0.00	1.26	2.92	0.03	1.78	0.00	0.38
RD52	24.51	0	19.59	32.38	0.18	10.28	0	86.94	6.67	2.72	1.28	0.00	1.28	3.00	0.02	1.70	0.00	0.36
RD52	24.52	2.98	18.58	31.26	0.22	10.27	0.08	87.91	6.57	2.68	1.32	0.25	1.08	2.86	0.02	1.67	0.01	0.37
RD52	24.21	0.22	19.37	31.67	0.12	9.7	0	85.29	6.78	2.73	1.27	0.02	1.31	2.99	0.01	1.63	0.00	0.35
RD52	25.19	0.58	19.31	31.88	0.14	9.97	0.1	87.17	6.62	2.77	1.23	0.05	1.28	2.94	0.01	1.64	0.01	0.36
RD10	24.04	0.11	19.22	31.57	0.19	10.13	0	85.26	6.79	2.72	1.28	0.01	1.28	2.98	0.02	1.71	0.00	0.36
RD62	26.11	0	19.37	30.15	0.37	12.92	0.05	88.97	6.41	2.78	1.22	0.00	1.22	2.69	0.03	2.05	0.01	0.43
RD62	26.24	0	20.09	29.53	0.45	12.98	0.13	89.42	6.35	2.77	1.23	0.00	1.27	2.61	0.04	2.04	0.02	0.44
RD62	25.35	0	19.77	28.03	0.45	12.82	0.13	86.55	6.54	2.76	1.24	0.00	1.29	2.55	0.04	2.08	0.02	0.45
RD62	25.75	0	20.35	28.72	0.39	13.18	0.34	88.73	6.39	2.74	1.26	0.00	1.29	2.55	0.04	2.09	0.05	0.45
RD10	23.97	0	19.31	31.61	0.22	10.13	0	85.24	6.80	2.71	1.29	0.00	1.28	2.99	0.02	1.71	0.00	0.36
RD56	26.93	0	23.36	27.55	0.39	8.24	0	86.47	6.43	2.88	1.12	0.00	1.83	2.47	0.04	1.31	0.00	0.35
RD56	27.14	0.32	22.08	25.87	0.3	10.54	0.69	86.94	6.38	2.88	1.12	0.03	1.65	2.30	0.03	1.67	0.09	0.42
RD56	23.95	0.15	21.14	31.76	0.61	9.22	0.06	86.89	6.66	2.65	1.35	0.01	1.41	2.94	0.06	1.52	0.01	0.34

Sample	SiO2	TiO2	Al2O3	FeO	MnO	MgO	K2O	total	α	Si(t)	Al(t)	Ti(o)	Al(o)	Fe(o)	Mn(o)	Mg(o)	K	Mg/Mg+Fe
RD56	23.89	0	20.48	30.58	0.6	9.93	0.09	85.57	6.73	2.68	1.32	0.00	1.38	2.87	0.06	1.66	0.01	0.37
RD68	26.98	0	17.01	25.1	0	16.35	0.07	85.51	6.50	2.92	1.08	0.00	1.09	2.27	0.00	2.64	0.01	0.54
RD68	27.56	0	17.97	25.12	0.12	15.78	0.71	87.26	6.37	2.92	1.08	0.00	1.17	2.23	0.01	2.50	0.10	0.53
DR34	25.03	0	21.01	27.4	0.19	9.75	0.48	83.86	6.72	2.80	1.20	0.00	1.57	2.56	0.02	1.63	0.07	0.39
RD65	24.46	0.11	19.9	29.26	0.4	12.06	0.07	86.26	6.62	2.69	1.31	0.01	1.28	2.70	0.04	1.98	0.01	0.42
RD65	24.31	0	20.33	29.13	0.35	12.31	0.06	86.49	6.59	2.67	1.33	0.00	1.30	2.67	0.03	2.01	0.01	0.43
RD65	24.11	0	21.96	27.33	0.26	11.84	0.84	86.34	6.56	2.63	1.37	0.00	1.46	2.49	0.02	1.93	0.12	0.44
RD10	24.6	0	18.72	33.4	0.24	9.86	0.08	86.9	6.72	2.75	1.25	0.00	1.22	3.12	0.02	1.64	0.01	0.34
RD10	24.69	0.19	18.38	32.82	0.21	9.71	0.2	86.2	6.76	2.78	1.22	0.02	1.22	3.09	0.02	1.63	0.03	0.35
RD4	24.56	0	18.88	31.33	0.55	9.63	0.28	85.23	6.80	2.78	1.22	0.00	1.30	2.97	0.05	1.62	0.04	0.35
RD4	25.7	0	19.79	33.37	0.43	10.63	0	89.92	6.45	2.76	1.24	0.00	1.26	2.99	0.04	1.70	0.00	0.36
RD4	26.37	0	20.16	33.15	0.59	10.19	0.13	90.59	6.38	2.80	1.20	0.00	1.32	2.94	0.05	1.61	0.02	0.35
RD4	25.57	0	20.06	33.94	0.71	10.44	0	90.72	6.41	2.73	1.27	0.00	1.25	3.03	0.06	1.66	0.00	0.35
RD4	25.13	0	19.21	31.52	0.59	9.78	0.26	86.49	6.69	2.80	1.20	0.00	1.32	2.93	0.06	1.62	0.04	0.36
RD114	25.47	0	18.68	28.7	0.19	13.11	0.09	86.24	6.59	2.79	1.21	0.00	1.21	2.63	0.02	2.14	0.01	0.45
RDW74	26.95	0	17.81	29.37	0.21	12.32	0.25	86.91	6.54	2.93	1.07	0.00	1.22	2.67	0.02	2.00	0.03	0.43
RDW74	25.93	0	19.59	30.88	0.26	11.61	0.11	88.38	6.48	2.79	1.21	0.00	1.28	2.78	0.02	1.87	0.02	0.40
RDW74	25.32	0	18.98	30.16	0.29	11.53	0.12	86.4	6.63	2.79	1.21	0.00	1.26	2.78	0.03	1.90	0.02	0.41
RDW74	26.59	0	20.75	32.24	0.19	11.92	0.09	91.78	6.24	2.76	1.24	0.00	1.30	2.80	0.02	1.85	0.01	0.40
RDW74	25.56	0	20.72	30.05	0.39	12.6	0.06	89.38	6.37	2.71	1.29	0.00	1.30	2.66	0.04	1.99	0.01	0.43
RDW74	26.62	0.16	19.99	28.5	0.29	13.36	0.44	89.36	6.32	2.80	1.20	0.01	1.28	2.51	0.03	2.09	0.06	0.46
RDW74	26.36	0.95	20.27	30.95	0.28	11.38	0.48	90.67	6.31	2.77	1.23	0.07	1.28	2.72	0.02	1.78	0.06	0.40
RD78	25.09	0	20.99	31.31	0.46	11.51	0	89.36	6.42	2.68	1.32	0.00	1.32	2.80	0.04	1.83	0.00	0.40
RD78	25.18	0	21.73	31.92	0.56	11.21	0	90.6	6.34	2.66	1.34	0.00	1.36	2.82	0.05	1.76	0.00	0.38
RD78	24.49	0	19.62	31.59	0.51	10.41	0	86.62	6.68	2.72	1.28	0.00	1.29	2.93	0.05	1.72	0.00	0.37
RD78	25.72	0	21.01	30.96	0.6	11.45	0.27	90.01	6.36	2.72	1.28	0.00	1.35	2.74	0.05	1.81	0.04	0.40
RD78	26.12	0.12	21.38	31.35	0.61	11.5	0.14	91.22	6.27	2.73	1.27	0.01	1.35	2.74	0.05	1.79	0.02	0.40
RD78	25.57	0	21.67	31.5	0.62	11.61	0.06	91.03	6.29	2.68	1.32	0.00	1.35	2.76	0.06	1.81	0.01	0.40
RD67	24.85	0	20.53	26.72	0.33	12.72	0.11	85.26	6.59	2.73	1.27	0.00	1.38	2.45	0.03	2.08	0.02	0.46
RD67	24.97	0	21.18	27.02	0.38	12.45	0.41	86.41	6.52	2.71	1.29	0.00	1.41	2.45	0.03	2.01	0.06	0.45
RD61	25.53	0	20.54	30.47	0.33	11.25	0.4	88.52	6.46	2.75	1.25	0.00	1.35	2.74	0.03	1.80	0.05	0.40
RD61	26.04	0	20.59	31.23	0.44	13.04	0	91.34	6.26	2.71	1.29	0.00	1.24	2.72	0.04	2.02	0.00	0.43
RD61	26.39	0	19.37	30.1	0.33	12.03	0.27	88.49	6.44	2.83	1.17	0.00	1.28	2.70	0.03	1.92	0.04	0.42

A1-1.10 Chlorite in Massive Chlorite Bands with Grey Interference Colour

Sample	SiO2	TiO2	Al2O3	FeO	MnO	MgO	K2O	total	α	Si(t)	Al(t)	Ti(o)	Al(o)	Fe(o)	Mn(o)	Mg(o)	K	Mg/Mg+Fe
RD194	24.34	0	23.63	35.58	0.26	6.76												
RD194	24.2	0	22.58	34.87	0.28	6.92												
RD194	23.67	0	23.3	35.46	0.3	5.86												
RD194	23.12	0.1	21.32	34.67	0.25	6.17												
RD194	23.17	0	22.73	35.7	0.3	6.03												
RD194	24.13	0	22.54	34.46	0.32	6.48												
RD194	23.01	0	24	36.8	0.22	4.79												
RD194	23.5	0	22.31	34.01	0.34	6.59												
RD194	23.11	0.19	22.05	35.61	0.29	5.8												
RD194	24.39	0.14	22.21	32.93	0.23	7.74												
RD194	23.13	0	22	35.04	0.39	5.46												
RD194	23.27	0.2	22.22	36.12	0.41	5.25												
RD194	23.19	0	21.8	35.56	0.24	5.67												
RD194	23.47	0.13	22.12	36.77	0.32	5.23												
RD194	23.51		22.22	36.54	0.35	5.78												
RD194	23.66	0	22.81	35.25	0.34	6.17												
RD194	23.45	0.1	21.75	34.13	0.33	6.38												
RD194	23.29	0.12	21.52	34.66	0.42	6.21												

A1-1.11 Chlorite in Massive Chlorite Bands with Purple Interference Colour

Sample	SiO2	TiO2	Al2O3	FeO	MnO	MgO	K2O	total	α	Si(t)	Al(t)	Ti(o)	Al(o)	Fe(o)	Mn(o)	Mg(o)	K	Mg/Mg+Fe
RD194	25.9		19.39	27.07	0.1	12.3												
RD194	25.69		22.22	30.2	0.23	9.8												
RD194	24.89		19.73	28.69	0.16	10.95												
RD194	25.46		20.63	31.12	0	10.63												
RD194	25.29		21.13	31.18	0.21	9.91												
RD194	24.05		22.56	31.8	0.35	7.66												
RD194	25.52		20.05	29.13	0.15	12.85												
RD194	25.91		20.13	28.66	0	13.05												

Sample	SiO2	TiO2	Al2O3	FeO	MnO	MgO	K2O	total	α	Si(t)	Al(t)	Ti(o)	Al(o)	Fe(o)	Mn(o)	Mg(o)	K	Mg/Mg+Fe
RD194	25.49		20.1	29.02	0.17	12.53												
RD194	26.27		20.14	29.32	0	12.4												
RD194	24.99		19.45	28.91	0.12	11.35												
RD194	25.6		20.46	29.62	0.16	12.05												
RD194	24.86		19.32	28.05	0	11.8												
RD194	25.17		20.44	29.88	0.19	10.44												
RD194	25.61		19.83	29.83	0.18	11.78												
RD194	25.39		19.13	28.06	0.2	11.88												

A1-1.12 Muscovite In the Ardlethan Granite

sample	SiO2	TiO2	Al2O3	FeO	MnO	MgO	K2O	total	α	Si(t)	Ti(o)	Al(t)	Al(o)	Fe(o)	Mn(o)	Mg(o)	K
TH01	49.34	0	32.26	2.11	0	0.78	10.44	94.93	4.03	3.31	0.00	0.69	1.86	0.12	0.00	0.08	0.89
TH01	45.06	0	31.94	5.18	0	0.86	10.23	93.27	4.20	3.15	0.00	0.85	1.78	0.30	0.00	0.09	0.91
TH01	50.06	0	30.4	2.42	0	0.99	9.63	93.5	4.08	3.40	0.00	0.60	1.83	0.14	0.00	0.10	0.83
TH01	50.24	0.25	27.1	3.66	0	1.94	9.62	92.81	4.14	3.46	0.01	0.54	1.67	0.21	0.00	0.20	0.85
TH01	50.24	0	28.56	3.22	0	1.35	9.65	93.02	4.12	3.44	0.00	0.56	1.75	0.18	0.00	0.14	0.84
TH01	49.75	0	26.8	4.62	0	1.67	10.3	93.14	4.17	3.45	0.00	0.55	1.65	0.27	0.00	0.17	0.91
TH02	47.03	0	29.11	5.2	0	0.71	10.55	92.6	4.23	3.31	0.00	0.69	1.72	0.31	0.00	0.07	0.95
TH02	45.17	0.22	31.02	4.72	0	0.76	10.48	92.37	4.24	3.18	0.01	0.82	1.76	0.28	0.00	0.08	0.94
TH02	45.68	0	28.31	6.11	0.15	0	10.47	90.72	4.35	3.30	0.00	0.70	1.72	0.37	0.01	0.00	0.97
TH03	46.37	0	31.06	6.55	0.17	0.59	10.18	94.92	4.15	3.20	0.00	0.80	1.73	0.38	0.01	0.06	0.90
TH03	47.89	0	30.42	6.39	0.18	0.4	10.13	95.41	4.11	3.28	0.00	0.72	1.73	0.37	0.01	0.04	0.88
TH03	46.3	0	30.3	5.76	0	0.2	9.32	91.88	4.24	3.26	0.00	0.74	1.78	0.34	0.00	0.02	0.84
TH03	48.1	0	29.41	5.52	0	0.32	10.28	93.63	4.17	3.34	0.00	0.66	1.74	0.32	0.00	0.03	0.91
TH03	46.46	0	30.62	6.5	0.13	0.61	10.35	94.67	4.16	3.22	0.00	0.78	1.72	0.38	0.01	0.06	0.91
TH03	47.68	0	29.92	5.99	0.38	0.12	10.73	94.82	4.15	3.29	0.00	0.71	1.73	0.35	0.02	0.01	0.95
TH04	46	0	27.65	6.65	0	0.22	10.24	90.76	4.35	3.33	0.00	0.67	1.68	0.40	0.00	0.02	0.94
TH04	46.37	0	28.99	6.19	0	0.73	9.12	91.4	4.27	3.29	0.00	0.71	1.72	0.37	0.00	0.08	0.83
TH04	46.69	0	29.49	5.71	0	0.21	10.42	92.52	4.24	3.29	0.00	0.71	1.74	0.34	0.00	0.02	0.94
TH04	47.84	0	33.28	3.11	0	0.35	10.79	95.37	4.05	3.22	0.00	0.78	1.87	0.18	0.00	0.04	0.93
TH04	47.9	0	29.4	6.59	0	0.29	10.66	94.84	4.15	3.31	0.00	0.69	1.70	0.38	0.00	0.03	0.94
TH04	47.03	0	29.58	6.5	0	0.1	10.7	93.91	4.20	3.28	0.00	0.72	1.72	0.38	0.00	0.01	0.95

sample	SiO2	TiO2	Al2O3	FeO	MnO	MgO	K2O	total	α	Si(t)	Ti(o)	Al(t)	Al(o)	Fe(o)	Mn(o)	Mg(o)	K
TH07	51.81	0	27.48	4.18	0	0.86	10.32	94.65	4.08	3.51	0.00	0.49	1.71	0.24	0.00	0.09	0.89
TH07	47.58	0.1	30.26	5	0	0.82	10.67	94.43	4.14	3.28	0.01	0.72	1.73	0.29	0.00	0.08	0.94
TH10	48.23	0	33.64	3.68	0	0.19	10.88	96.62	4.01	3.22	0.00	0.78	1.86	0.21	0.00	0.02	0.93
TH10	46.44	0.4	28.47	6.84	0	0.86	10.5	93.51	4.23	3.27	0.02	0.73	1.63	0.40	0.00	0.09	0.94
TH10	46.48	0.51	29.16	6.88	0	0.59	10.52	94.14	4.20	3.25	0.03	0.75	1.65	0.40	0.00	0.06	0.94
TH10	47.48	0	29.24	6.04	0	0.54	10.56	93.86	4.18	3.31	0.00	0.69	1.71	0.35	0.00	0.06	0.94
TH10	44.84	0	28.52	6.57	0	0.45	10.2	90.58	4.36	3.25	0.00	0.75	1.69	0.40	0.00	0.05	0.94
TH10	44.58	0.2	29.4	6.77	0	0.54	10.27	91.76	4.31	3.20	0.01	0.80	1.69	0.41	0.00	0.06	0.94
TH10	44.56	0	29.95	5.85	0	0.29	10.32	90.97	4.33	3.21	0.00	0.79	1.75	0.35	0.00	0.03	0.95
TH10	47.75	0	29.37	6.79	0	1	10.58	95.49	4.13	3.28	0.00	0.72	1.66	0.39	0.00	0.10	0.93
TH10	46.75	0	30.51	5.5	0	0	10.67	93.43	4.19	3.26	0.00	0.74	1.77	0.32	0.00	0.00	0.95
TH11	47.69	0	30.1	4.87	0	0.79	9.99	93.44	4.16	3.30	0.00	0.70	1.76	0.28	0.00	0.08	0.88
TH11	47.5	0	29.19	4.55	0	0.74	8.8	90.78	4.24	3.35	0.00	0.65	1.78	0.27	0.00	0.08	0.79
TH11	49.63	0	25.89	6.25	0	1.33	7.39	90.49	4.25	3.51	0.00	0.49	1.66	0.37	0.00	0.14	0.67
TH11	46.68	0	28.14	7.7	0	0.22	10.12	92.86	4.26	3.31	0.00	0.69	1.66	0.46	0.00	0.02	0.92
TH11	47.44	0.16	30.62	4.77	0	0.77	10.15	93.91	4.14	3.27	0.01	0.73	1.76	0.27	0.00	0.08	0.89
RDB61	48.42	0	29.4	3.18	0	0.86	9.25	91.11	4.20	3.38	0.00	0.62	1.81	0.19	0.00	0.09	0.82
RDB61	51.71	0.68	26.07	4.77	0	1.2	7.23	91.66	4.14	3.57	0.04	0.43	1.68	0.28	0.00	0.12	0.64
RDB61	49.05	0	30.5	4.55	0	0.39	10.46	94.95	4.09	3.34	0.00	0.66	1.78	0.26	0.00	0.04	0.91
RDB61	49.79	0	30.21	4.31	0	0.25	10.01	94.57	4.08	3.38	0.00	0.62	1.80	0.24	0.00	0.03	0.87
RDB61	48.28	0	33.08	2.78	0	0	10.58	94.72	4.06	3.26	0.00	0.74	1.90	0.16	0.00	0.00	0.91
RDB61	47.24	0	33.78	2.12	0	0.14	10.31	93.59	4.09	3.22	0.00	0.78	1.93	0.12	0.00	0.01	0.90
RDB61	47.75	0	31.23	4.75	0	0.22	10.52	94.47	4.12	3.27	0.00	0.73	1.80	0.27	0.00	0.02	0.92
RDB61	49.9	0	29.49	3.07	0	1.58	9.82	93.86	4.09	3.39	0.00	0.61	1.76	0.17	0.00	0.16	0.85
RDB61	50.79	0	30.63	2.03	0	1.64	9.44	94.53	4.02	3.40	0.00	0.60	1.81	0.11	0.00	0.16	0.81
RDB61	48.41	0	28.93	6.3	0	0.35	10.72	94.71	4.15	3.34	0.00	0.66	1.70	0.36	0.00	0.04	0.94
RDB62	45.6	0	30.91	5.87	0	0.27	10.48	93.13	4.22	3.20	0.00	0.80	1.76	0.34	0.00	0.03	0.94
RDB62	46.85	0	30.68	6.34	0	0	10.36	94.23	4.17	3.25	0.00	0.75	1.76	0.37	0.00	0.00	0.92
RDB62	49.18	0	28.87	4.89	0	0.32	10.56	93.82	4.15	3.39	0.00	0.61	1.74	0.28	0.00	0.03	0.93
RDB62	46.33	0	30.57	6.52	0	0	10.6	94.02	4.19	3.23	0.00	0.77	1.75	0.38	0.00	0.00	0.94
RDB62	45.41	0	31.77	6.11	0	0.14	10.42	93.85	4.19	3.17	0.00	0.83	1.78	0.36	0.00	0.01	0.93
RDB62	49.64	0	29.13	4.94	0	1.02	9.49	94.22	4.10	3.39	0.00	0.61	1.73	0.28	0.00	0.10	0.83
RDB62	50.02	0.18	28.13	3.19	0	1.72	9.68	92.92	4.13	3.44	0.01	0.56	1.71	0.18	0.00	0.18	0.85
RDB62	46.57	0	30.47	6.57	0	0	10.43	94.04	4.19	3.24	0.00	0.76	1.75	0.38	0.00	0.00	0.93
RDB64	50.98	0	29.12	3.92	0	1.21	9.52	94.75	4.05	3.44	0.00	0.56	1.75	0.22	0.00	0.12	0.82

sample	SiO2	TiO2	Al2O3	FeO	MnO	MgO	K2O	total	α	Si(t)	Ti(o)	Al(t)	Al(o)	Fe(o)	Mn(o)	Mg(o)	K
RDB64	46.51	0	31.95	5.16	0	0.22	10.57	94.41	4.14	3.20	0.00	0.80	1.80	0.30	0.00	0.02	0.93
RDB64	47.13	0	31.2	5.87	0	0	10.6	94.8	4.14	3.24	0.00	0.76	1.77	0.34	0.00	0.00	0.93
RDB64	50.6	0	28.87	4.6	0	0.92	10.16	95.15	4.07	3.42	0.00	0.58	1.73	0.26	0.00	0.09	0.88
RDB64	50.54	0	27.98	5	0	0.91	10.4	94.83	4.10	3.45	0.00	0.55	1.69	0.29	0.00	0.09	0.90
RDS70	47.16	0	31.33	4.69	0	0.58	10.6	94.36	4.13	3.24	0.00	0.76	1.78	0.27	0.00	0.06	0.93
RDS70	49.02	0	31.71	2.7	0	1.02	9.73	94.18	4.06	3.31	0.00	0.69	1.84	0.15	0.00	0.10	0.84

A1-1.13 Muscovite in the Mine Granite

sample	SiO2	TiO2	Al2O3	FeO	MgO	K2O	total	α	Si(t)	Ti(o)	Al(t)	Al(o)	Fe(o)	Mg(o)	K
RD59	47.84	0.00	36.14	1.05	0.90	10.87	96.80	3.92	3.12	0.00	0.88	1.90	0.06	0.09	0.90
RD59	47.33	0.00	36.50	0.95	0.67	11.03	96.48	3.93	3.10	0.00	0.90	1.92	0.05	0.07	0.92
RD59	47.28	0.00	36.83	0.74	0.62	11.10	96.57	3.93	3.09	0.00	0.91	1.93	0.04	0.06	0.93
RD59	46.53	0.41	36.37	1.28	0.84	10.57	96.00	3.96	3.06	0.02	0.94	1.89	0.07	0.08	0.89
RD59	47.32	0.00	36.75	0.95	0.75	10.77	96.54	3.93	3.09	0.00	0.91	1.92	0.05	0.07	0.90
RD59	46.93	0.41	36.79	0.99	0.65	10.79	96.56	3.93	3.07	0.02	0.93	1.91	0.05	0.06	0.90
RD59	47.44	0.10	36.28	0.91	0.50	10.86	96.09	3.94	3.11	0.00	0.89	1.92	0.05	0.05	0.91
RD59	47.35	0.00	36.39	0.98	0.90	10.77	96.39	3.93	3.10	0.00	0.90	1.91	0.05	0.09	0.90
RD59	46.97	0.00	36.78	0.89	0.92	11.02	96.58	3.93	3.07	0.00	0.93	1.91	0.05	0.09	0.92
RD23	45.17	0.21	34.33	1.93	1.25	10.44	93.33	4.09	3.08	0.01	0.92	1.83	0.11	0.13	0.91
RD57	45.30	0.00	35.40	0.98	0.73	10.12	92.53	4.09	3.08	0.00	0.92	1.93	0.06	0.07	0.88
RD57	44.49	0.00	34.77	1.08	0.73	10.24	91.31	4.16	3.08	0.00	0.92	1.91	0.06	0.08	0.90
RD57	44.05	0.00	34.56	1.59	0.93	9.78	90.91	4.18	3.06	0.00	0.94	1.90	0.09	0.10	0.87
RD57	44.73	0.00	35.61	0.82	0.72	10.24	92.12	4.11	3.06	0.00	0.94	1.94	0.05	0.07	0.89
RD2	45.76	0.00	35.71	0.83	0.71	10.66	93.67	4.05	3.08	0.00	0.92	1.92	0.05	0.07	0.92
RD2	45.45	0.00	34.77	1.66	1.22	10.48	93.58	4.07	3.08	0.00	0.92	1.86	0.09	0.12	0.91
RD39	45.89	0.00	35.45	1.45	0.69	10.41	93.89	4.05	3.09	0.00	0.91	1.91	0.08	0.07	0.89
RD39	46.47	0.00	35.97	0.88	0.82	10.74	94.88	4.00	3.09	0.00	0.91	1.91	0.05	0.08	0.91
RD39	46.52	0.00	36.00	0.89	0.73	10.45	94.59	4.00	3.10	0.00	0.90	1.92	0.05	0.07	0.89
RD39	46.24	0.00	35.63	0.86	0.65	10.71	94.09	4.03	3.10	0.00	0.90	1.92	0.05	0.07	0.92
RD66	45.88	0.43	36.01	0.82	0.43	10.52	94.09	4.03	3.08	0.02	0.92	1.92	0.05	0.04	0.90
RD66	45.08	0.42	35.42	0.73	0.43	10.13	92.21	4.10	3.08	0.02	0.92	1.93	0.04	0.04	0.88
RD66	47.12	0.14	36.22	0.63	0.63	10.54	95.28	3.97	3.11	0.01	0.89	1.93	0.03	0.06	0.89

sample	SiO2	TiO2	Al2O3	FeO	MgO	K2O	total	α	Si(t)	Ti(o)	Al(t)	Al(o)	Fe(o)	Mg(o)	K
RD62	46.32	0.00	36.63	0.87	0.65	10.65	95.12	3.98	3.07	0.00	0.93	1.94	0.05	0.06	0.90
RD62	47.11	0.00	36.46	0.95	0.74	10.72	95.98	3.95	3.10	0.00	0.90	1.92	0.05	0.07	0.90
RD116	46.61	0.11	35.65	0.97	0.69	10.35	94.38	4.01	3.11	0.01	0.89	1.91	0.05	0.07	0.88
RD116	46.33	0.00	35.65	1.02	0.98	10.64	94.62	4.01	3.09	0.00	0.91	1.90	0.06	0.10	0.91
RD6	46.58	0.00	36.06	0.74	0.55	10.74	94.67	4.00	3.10	0.00	0.90	1.93	0.04	0.05	0.91
RD6	47.84	0.00	32.82	1.92	1.09	10.91	94.58	4.03	3.21	0.00	0.79	1.81	0.11	0.11	0.93
RD10	45.12	0.71	34.09	1.19	0.85	10.62	92.58	4.12	3.09	0.04	0.91	1.84	0.07	0.09	0.93
RD10	45.68	0.00	35.26	0.96	0.82	10.16	92.88	4.08	3.10	0.00	0.90	1.92	0.05	0.08	0.88
RD10	45.33	0.00	35.65	0.87	0.67	10.51	93.03	4.08	3.08	0.00	0.92	1.93	0.05	0.07	0.91
RD10	45.11	0.00	35.38	1.32	0.83	10.45	93.09	4.09	3.07	0.00	0.93	1.90	0.08	0.08	0.91
RD10	44.78	0.22	35.14	0.91	0.64	10.11	91.80	4.13	3.08	0.01	0.92	1.92	0.05	0.07	0.89
RD10	45.74	0.00	35.72	0.75	0.75	10.44	93.40	4.05	3.09	0.00	0.91	1.93	0.04	0.08	0.90
RD10	45.85	0.00	35.13	1.03	0.72	10.18	92.91	4.07	3.11	0.00	0.89	1.92	0.06	0.07	0.88
RD10	45.21	0.00	35.14	1.13	0.68	10.56	92.72	4.10	3.08	0.00	0.92	1.91	0.06	0.07	0.92
RD10	44.93	0.00	36.14	0.95	0.26	10.41	92.69	4.09	3.06	0.00	0.94	1.96	0.05	0.03	0.90
RD10	46.00	0.00	35.76	0.86	0.62	10.37	93.61	4.04	3.10	0.00	0.90	1.93	0.05	0.06	0.89
RD56	45.43	0.24	35.36	0.86	0.73	10.22	92.84	4.08	3.08	0.01	0.92	1.91	0.05	0.07	0.89
RD56	45.09	0.00	35.54	0.87	0.59	10.05	92.14	4.11	3.08	0.00	0.92	1.94	0.05	0.06	0.88
RD56	45.97	0.00	35.97	0.71	0.77	10.62	94.04	4.03	3.08	0.00	0.92	1.93	0.04	0.08	0.91
RD18	46.59	0.00	37.13	0.67	0.57	10.36	95.32	3.96	3.07	0.00	0.93	1.96	0.04	0.06	0.87
RD68	45.42	0.00	35.91	1.04	0.80	10.36	93.53	4.06	3.07	0.00	0.93	1.92	0.06	0.08	0.89
RD68	45.31	0.00	35.19	0.82	0.73	10.24	92.29	4.10	3.09	0.00	0.91	1.93	0.05	0.07	0.89
RD80	45.77	0.00	35.87	1.15	0.65	10.53	93.97	4.04	3.08	0.00	0.92	1.92	0.06	0.07	0.90
DR34	44.44	0.00	35.00	0.88	0.77	10.14	91.23	4.15	3.07	0.00	0.93	1.93	0.05	0.08	0.89
DR34	45.72	0.00	34.16	1.36	1.15	10.70	93.09	4.09	3.11	0.00	0.89	1.86	0.08	0.12	0.93
DR34	45.10	0.00	35.08	0.99	0.85	10.22	92.24	4.11	3.08	0.00	0.92	1.91	0.06	0.09	0.89
DR34	45.60	0.00	33.42	0.97	1.05	10.10	91.14	4.15	3.15	0.00	0.85	1.88	0.06	0.11	0.89
DR34	43.82	0.00	34.87	0.85	0.67	10.14	90.35	4.20	3.06	0.00	0.94	1.93	0.05	0.07	0.90
DR34	43.90	0.00	34.56	0.90	0.66	9.98	90.00	4.21	3.08	0.00	0.92	1.93	0.05	0.07	0.89
RD13	44.33	0.00	35.04	1.02	0.61	10.26	91.26	4.16	3.07	0.00	0.93	1.93	0.06	0.06	0.91
RD50	46.27	0.00	33.92	1.28	1.04	10.81	93.32	4.08	3.14	0.00	0.86	1.86	0.07	0.11	0.94
RD50	45.10	0.00	35.87	0.75	0.45	10.20	92.37	4.10	3.07	0.00	0.93	1.96	0.04	0.05	0.89
RD65	45.58	0.00	35.17	0.94	0.77	10.35	92.81	4.08	3.10	0.00	0.90	1.91	0.05	0.08	0.90
RD10	45.88	0.00	35.35	0.98	0.71	10.46	93.38	4.06	3.10	0.00	0.90	1.92	0.06	0.07	0.90
RD10	43.80	0.00	32.86	2.29	1.03	10.51	90.49	4.24	3.09	0.00	0.91	1.83	0.14	0.11	0.95

sample	SiO2	TiO2	Al2O3	FeO	MgO	K2O	total	α	Si(t)	Ti(o)	Al(t)	Al(o)	Fe(o)	Mg(o)	K
RD10	45.43	0.00	35.69	1.01	0.59	10.64	93.36	4.07	3.08	0.00	0.92	1.92	0.06	0.06	0.92
RD10	45.09	0.00	35.96	0.93	0.66	10.26	92.90	4.08	3.06	0.00	0.94	1.94	0.05	0.07	0.89
RD10	45.71	0.00	35.40	0.94	0.72	10.44	93.21	4.07	3.09	0.00	0.91	1.92	0.05	0.07	0.90
RD4	47.84	0.00	36.52	1.06	0.62	10.72	96.76	3.91	3.12	0.00	0.88	1.92	0.06	0.06	0.89
RD4	44.58	0.00	35.43	0.91	0.42	10.46	91.80	4.14	3.07	0.00	0.93	1.94	0.05	0.04	0.92
RD4	45.40	0.00	35.54	0.71	0.60	10.32	92.57	4.09	3.09	0.00	0.91	1.94	0.04	0.06	0.90
RD4	45.49	0.00	35.70	0.82	0.74	10.33	93.08	4.07	3.08	0.00	0.92	1.93	0.05	0.07	0.89
RD21	46.88	0.14	36.71	0.80	0.56	10.81	95.90	3.95	3.08	0.01	0.92	1.93	0.04	0.05	0.91
RD21	46.91	0.00	36.78	0.87	0.73	10.82	96.11	3.95	3.08	0.00	0.92	1.93	0.05	0.07	0.91
RD21	47.18	0.00	36.25	1.11	0.75	10.74	96.03	3.95	3.10	0.00	0.90	1.91	0.06	0.07	0.90
RD21	47.65	0.00	35.98	0.92	0.77	10.65	95.97	3.94	3.13	0.00	0.87	1.91	0.05	0.08	0.89
RD114	46.47	0.00	36.11	0.84	0.79	10.97	95.18	3.99	3.09	0.00	0.91	1.91	0.05	0.08	0.93
RD114	47.36	0.00	35.61	1.48	0.92	10.89	96.26	3.95	3.12	0.00	0.88	1.88	0.08	0.09	0.91
RDW74	45.59	0.00	35.43	1.22	0.72	10.41	93.37	4.07	3.09	0.00	0.91	1.91	0.07	0.07	0.90
RDW74	44.74	0.10	34.24	0.81	0.66	10.00	90.55	4.18	3.11	0.01	0.89	1.92	0.05	0.07	0.89
RD67	45.89	0.00	34.81	0.85	0.65	10.18	92.38	4.09	3.13	0.00	0.87	1.92	0.05	0.07	0.88
RD61	47.22	0.29	36.18	0.84	0.49	10.53	95.55	3.96	3.11	0.01	0.89	1.92	0.05	0.05	0.89
RD61	47.41	0.00	36.28	1.31	0.74	10.95	96.69	3.93	3.10	0.00	0.90	1.90	0.07	0.07	0.91
RD31	45.50	0.00	32.66	2.85	1.06	10.20	92.27	4.15	3.14	0.00	0.86	1.80	0.16	0.11	0.90

A1-1.14 Nodular Tourmaline in the Ardlethan Granite

sample	SiO2	TiO2	Al2O3	FeO	MnO	MgO	K2O	Na2O	total	α	Si	Ti	Al	Fe	Mn	Mg	K	Na	Mg/Mg+Fe
TH01	34.81	0	31.44	17.68	0.17	0.96	0.15	2.62	87.83	10.20	5.91	0.00	6.30	2.51	0.02	0.24	0.03	0.87	0.09
TH01	35.45	0.58	32.92	15.72	0.15	1.25	0.09	2.43	88.59	9.98	5.89	0.07	6.44	2.18	0.02	0.31	0.02	0.79	0.12
TH01	35.24	0.67	30.94	16.81	0.13	1.65	0	2.67	88.11	10.12	5.94	0.08	6.14	2.37	0.02	0.41	0.00	0.88	0.15
TH01	35.4	0.16	32.16	16.47	0.16	1.43	0.07	2.38	88.23	10.06	5.93	0.02	6.35	2.31	0.02	0.36	0.01	0.78	0.13
TH01	35.15	0.2	33.91	14.84	0	1.47	0	2.24	87.81	9.99	5.84	0.03	6.65	2.06	0.00	0.36	0.00	0.73	0.15
TH01	35.05	0	34.18	14.69	0	1.46	0	2.2	87.58	10.01	5.84	0.00	6.71	2.05	0.00	0.36	0.00	0.72	0.15
TH01	35.05	0	33.28	15.39	0.17	1.18	0.06	2.33	87.46	10.08	5.88	0.00	6.58	2.16	0.02	0.30	0.01	0.77	0.12
TH01	35.1	0.32	32.76	15.49	0.13	1.58	0.08	2.47	87.93	10.05	5.87	0.04	6.46	2.17	0.02	0.39	0.02	0.81	0.15
TH01	35.06	0	33.85	14.91	0	1.61	0	2.25	87.68	10.01	5.84	0.00	6.65	2.08	0.00	0.40	0.00	0.74	0.16
TH01	35.6	0.14	34.53	14.49	0.17	1.31	0	2.05	88.29	9.90	5.87	0.02	6.71	2.00	0.02	0.32	0.00	0.66	0.14

sample	SiO2	TiO2	Al2O3	FeO	MnO	MgO	K2O	Na2O	total	α	Si	Ti	Al	Fe	Mn	Mg	K	Na	Mg/Mg+Fe
TH01	35.3	0	32.89	14.99	0.23	1.92	0	2.33	87.66	10.04	5.90	0.00	6.48	2.09	0.03	0.48	0.00	0.76	0.19
TH03	35.51	0.29	33.46	16.11	0.15	0.69	0	1.96	88.17	10.00	5.91	0.04	6.57	2.24	0.02	0.17	0.00	0.64	0.07
TH03	35.99	0	32.93	17.64	0.14	0.64	0	2.63	89.97	9.91	5.93	0.00	6.40	2.43	0.02	0.16	0.00	0.85	0.06
TH03	36.08	0.36	32.07	17.13	0	1.18	0.07	2.82	89.71	9.93	5.96	0.04	6.25	2.37	0.00	0.29	0.01	0.91	0.11
TH03	35.38	0.41	31.98	16.84	0	0.86	0	2.54	88.01	10.10	5.95	0.05	6.34	2.37	0.00	0.22	0.00	0.84	0.08
TH03	35.8	0.49	33.95	16.1	0	0.66	0.06	2.23	89.29	9.88	5.89	0.06	6.58	2.21	0.00	0.16	0.01	0.72	0.07
TH03	36.11	0.22	31.63	18.51	0	0.48	0.06	2.62	89.63	10.00	6.01	0.03	6.20	2.58	0.00	0.12	0.01	0.86	0.04
TH03	36.26	0.44	32.96	16.33	0	1.2	0	2.47	89.66	9.86	5.95	0.05	6.37	2.24	0.00	0.29	0.00	0.80	0.12
TH03	35.74	0	33.64	16.5	0	0.71	0	2.13	88.72	9.95	5.92	0.00	6.57	2.29	0.00	0.18	0.00	0.69	0.07
TH03	35.71	0	32.5	18.07	0	0.58	0	2.74	89.6	9.98	5.93	0.00	6.36	2.51	0.00	0.14	0.00	0.89	0.05
TH03	35.12	0	32.07	18.37	0	0.23	0	2.45	88.24	10.15	5.93	0.00	6.39	2.60	0.00	0.06	0.00	0.81	0.02
TH03	35.43	0	32.29	18.27	0	0.5	0.08	2.46	89.03	10.05	5.93	0.00	6.37	2.56	0.00	0.12	0.02	0.81	0.05
TH03	35.12	0	32.08	18.08	0	0.47	0	2.61	88.36	10.13	5.92	0.00	6.37	2.55	0.00	0.12	0.00	0.86	0.04
TH03	34.79	0	31.91	17.85	0.2	0.47	0	2.76	87.98	10.19	5.90	0.00	6.38	2.53	0.03	0.12	0.00	0.92	0.04
TH03	35.24	0	32.86	15.86	0.16	1.12	0	2.72	87.96	10.06	5.90	0.00	6.49	2.22	0.02	0.28	0.00	0.89	0.11
RDB61	34.55	0	32.43	16.58	0.14	0.5	0.17	2.69	87.06	10.23	5.88	0.00	6.51	2.36	0.02	0.13	0.04	0.90	0.05
RDB62	35.42	0	34.55	15.81	0.12	0.13	0.09	2.08	88.2	9.98	5.88	0.00	6.76	2.20	0.02	0.03	0.02	0.68	0.01

A1-1.15 Patchy Tourmaline in the Mine Granite

sample	SiO2	TiO2	Al2O3	FeO	MgO	CaO	Na2O	K2O	total	a	Si	Ti	Al	Fe	Mg	Ca	Na	K	Mg/Mg+Fe
RD116	35.33	0	31.29	8.11	7.13	0	1.67	1.62	85.15	10.03	5.9	0	6.16	1.13	1.77	0	0.55	0.29	0.61
RD116	35.88	0	32.48	7.66	6.13	0	1.76	0.85	84.76	9.99	5.97	0	6.37	1.07	1.52	0	0.57	0.15	0.59

A1-1.16 Granular Tourmaline in the Mine Granite

sample	SiO2	TiO2	Al2O3	FeO	MgO	CaO	Na2O	K	total	α	Si	Ti	Al	Fe	Mg	Ca	Na	K	Mg/Mg+Fe
RD52	35.84	0.28	33.27	9.12	5.85	0.06	2.22	0.55	87.19	9.81	5.85	0.03	6.4	1.25	1.42	0.01	0.71	0.1	0.53
RD52	35.51	1.04	31.6	9.48	6.24	0.07	2.14	0.74	86.82	9.91	5.85	0.13	6.14	1.31	1.53	0.01	0.69	0.13	0.54
RD52	35.7	0.43	34.66	8.59	5.41	0.06	2.1	0.25	87.2	9.75	5.8	0.05	6.63	1.17	1.31	0.01	0.67	0.04	0.53

sample	SiO2	TiO2	Al2O3	FeO	MgO	CaO	Na2O	K	total	α	Si	Ti	Al	Fe	Mg	Ca	Na	K	Mg/Mg+Fe
RD52	35.94	0.2	34.96	8.79	4.53	0	1.74	0.17	86.33	9.82	5.87	0.02	6.73	1.2	1.1	0	0.56	0.03	0.48
RD52	35.25	0.87	31.63	9.88	6.06	0.07	2.46	0.64	86.86	9.94	5.83	0.11	6.17	1.37	1.49	0.01	0.8	0.11	0.52
RD39	35.94	0.83	33.65	8.2	6.02	0.05	2.26	0.53	87.59	9.73	5.82	0.1	6.42	1.11	1.45	0.01	0.72	0.09	0.57
RD39	36.82	0.29	31.79	8.69	6.75	0	2.15	0.76	87.25	9.78	5.99	0.04	6.1	1.18	1.64	0	0.69	0.13	0.58
RD6	36.5	0.77	32.07	11	5.03	0	2.22	0.18	87.77	9.82	5.97	0.09	6.18	1.5	1.23	0	0.71	0.03	0.45
RD50	35.55	0.29	34.84	8.36	4.98	0	1.94	0.33	86.29	9.83	5.81	0.04	6.72	1.14	1.21	0	0.62	0.06	0.51
RD50	34.54	0.55	33.2	8.69	5.4	0	2.11	0.46	84.95	10.05	5.78	0.07	6.55	1.22	1.35	0	0.69	0.08	0.53
RD50	34.65	0.43	32.51	10.57	4.64	0	1.86	0.75	85.41	10.10	5.82	0.05	6.44	1.49	1.16	0	0.61	0.14	0.44
RD58	37.38	0.73	33.12	9.4	5.21	0	2.08	0.3	88.22	9.66	6.01	0.09	6.28	1.26	1.25	0	0.66	0.05	0.50
RD58	37.39	0.56	33.38	8.79	5.24	0	2.1	0.3	87.76	9.67	6.02	0.07	6.33	1.18	1.26	0	0.66	0.05	0.52
RD58	36.66	0	32.19	11.43	4.65	0	1.92	0.39	87.24	9.88	6.03	0	6.24	1.57	1.14	0	0.62	0.07	0.42
RD58	35.96	0.67	34.53	9.46	4.44	0	1.76	0.67	87.49	9.75	5.84	0.08	6.61	1.28	1.07	0	0.56	0.12	0.46
RD58	36.29	0.45	35.41	8.64	4.43	0	1.82	0.49	87.53	9.69	5.85	0.05	6.73	1.16	1.06	0	0.58	0.08	0.48
RD58	36.51	0.68	34.85	8.91	4.5	0	2.01	0.58	88.04	9.66	5.87	0.08	6.6	1.2	1.08	0	0.63	0.1	0.47
RD58	36.39	1.29	32.78	9.79	5.17	0.06	2.01	0.73	88.22	9.73	5.89	0.16	6.25	1.33	1.25	0.01	0.64	0.13	0.48
RD58	35.93	0.29	35.11	8.27	4.84	0	2	0.59	87.03	9.74	5.83	0.04	6.71	1.12	1.17	0	0.64	0.1	0.51

A1-1.17 Acute Tourmaline in the Mine Granite

sample	SiO2	TiO2	Al2O3	FeO	MgO	CaO	Na2O	K2O	total	α	Si	Ti	Al	Fe	Mg	Ca	Na	K	Mg/Mg+Fe
RD66	35.12	0.54	34.48	9.21	4.46	0.05	1.94	0.32	86.12	9.91	5.79	0.07	6.70	1.27	1.10	0.01	0.63	0.06	0.46
RD66	35.53	0.50	34.64	9.64	4.29	0.07	2.02	0.33	87.02	9.82	5.81	0.06	6.67	1.32	1.05	0.01	0.65	0.06	0.44
RD66	35.13	0.77	33.80	10.96	3.55	0.07	1.97	0.35	86.60	9.95	5.82	0.10	6.60	1.52	0.88	0.01	0.64	0.06	0.37
RD66	34.78	1.00	33.42	10.28	4.08	0.00	2.03	0.48	86.07	9.99	5.78	0.13	6.55	1.43	1.01	0.00	0.66	0.09	0.41
RD66	35.55	0.52	34.37	9.46	4.52	0.00	1.97	0.35	86.74	9.84	5.82	0.06	6.64	1.30	1.10	0.00	0.63	0.06	0.46
RD66	35.09	0.65	33.94	10.04	4.14	0.06	1.88	0.40	86.20	9.95	5.81	0.08	6.62	1.39	1.02	0.01	0.61	0.07	0.42
RD66	35.30	1.01	33.87	10.70	4.01	0.07	1.96	0.51	87.43	9.85	5.79	0.12	6.55	1.47	0.98	0.01	0.63	0.09	0.40
RD66	34.93	0.56	34.14	11.26	2.93	0.00	1.92	0.28	86.02	10.01	5.82	0.07	6.71	1.57	0.73	0.00	0.63	0.05	0.32
RD66	35.11	0.78	34.46	10.89	3.51	0.05	1.95	0.41	87.16	9.88	5.77	0.10	6.68	1.50	0.86	0.01	0.63	0.07	0.36
RD66	33.13	0.81	32.51	9.87	4.01	0.10	1.74	0.48	82.65	10.41	5.74	0.11	6.64	1.43	1.04	0.02	0.59	0.09	0.42
RD66	35.64	1.05	34.26	9.74	4.62	0.12	2.08	0.50	88.01	9.74	5.78	0.13	6.55	1.32	1.12	0.02	0.66	0.09	0.46
RD66	35.40	1.19	34.25	9.52	4.45	0.00	1.98	0.49	87.28	9.80	5.77	0.15	6.59	1.30	1.08	0.00	0.63	0.09	0.45
RD66	35.99	0.75	34.37	8.61	5.35	0.00	2.07	0.39	87.53	9.72	5.82	0.09	6.55	1.16	1.29	0.00	0.66	0.07	0.53

sample	SiO2	TiO2	Al2O3	FeO	MgO	CaO	Na2O	K2O	total	a	Si	Ti	Al	Fe	Mg	Ca	Na	K	Mg/Mg+Fe
RD66	35.40	1.33	34.00	9.67	4.62	0.00	2.04	0.50	87.56	9.79	5.77	0.16	6.53	1.32	1.12	0.00	0.65	0.09	0.46
RD6	36.50	0.77	32.07	11.00	5.03	0.00	2.22	0.18	87.77	9.82	5.97	0.09	6.18	1.50	1.23	0.00	0.71	0.03	0.45
RD6	34.10	0.31	30.62	12.62	3.97	0.07	2.60	0.23	84.52	10.36	5.88	0.04	6.22	1.82	1.02	0.02	0.88	0.04	0.36
RD6	36.50	0.23	34.24	10.16	4.52	0.00	2.14	0.19	87.98	9.72	5.91	0.03	6.53	1.37	1.09	0.00	0.68	0.03	0.44
RD6	35.95	0.50	32.69	10.93	4.61	0.25	2.18	0.29	87.40	9.88	5.91	0.06	6.33	1.50	1.13	0.05	0.70	0.05	0.43
RD12	35.17	1.55	31.65	13.32	3.02	0.00	2.00	0.11	86.82	10.06	5.89	0.20	6.25	1.87	0.75	0.00	0.66	0.02	0.29
RD12	35.50	0.51	32.25	13.01	3.68	0.00	2.46	0.13	87.54	9.97	5.89	0.06	6.31	1.80	0.91	0.00	0.80	0.02	0.34
RD80	36.00	0.00	33.45	12.11	2.78	0.24	2.08	0.07	86.73	9.97	5.97	0.00	6.54	1.68	0.69	0.05	0.68	0.01	0.29
RD13	34.88	0.17	33.51	12.09	3.14	0.00	1.87	0.31	85.97	10.07	5.84	0.02	6.62	1.69	0.78	0.00	0.62	0.06	0.32
RD13	34.67	0.28	31.61	12.62	3.51	0.00	2.28	0.20	85.17	10.23	5.90	0.04	6.34	1.80	0.89	0.00	0.76	0.04	0.33
RD50	35.55	0.29	34.84	8.36	4.98	0.00	1.94	0.33	86.29	9.83	5.81	0.04	6.72	1.14	1.21	0.00	0.62	0.06	0.51
RD50	34.54	0.55	33.20	8.69	5.40	0.00	2.11	0.46	84.95	10.05	5.78	0.07	6.55	1.22	1.35	0.00	0.69	0.08	0.53
RD50	34.65	0.43	32.51	10.57	4.64	0.00	1.86	0.75	85.41	10.10	5.82	0.05	6.44	1.49	1.16	0.00	0.61	0.14	0.44
RD19	34.59	0.40	33.30	10.93	3.93	0.07	2.10	0.20	85.52	10.09	5.81	0.05	6.59	1.53	0.98	0.01	0.69	0.04	0.39
RD19	34.66	0.48	33.12	12.27	2.76	0.08	2.03	0.26	85.66	10.13	5.84	0.06	6.58	1.73	0.69	0.02	0.67	0.05	0.29
RD19	35.09	0.16	34.01	10.99	3.55	0.00	1.90	0.21	85.91	10.01	5.84	0.02	6.68	1.53	0.88	0.00	0.62	0.04	0.37
RD19	35.00	0.59	31.37	11.64	4.47	0.08	2.41	0.39	85.95	10.11	5.89	0.07	6.22	1.64	1.12	0.02	0.80	0.07	0.41
RD19	35.06	0.00	32.29	13.23	2.63	0.00	2.01	0.00	85.22	10.21	5.96	0.00	6.47	1.88	0.67	0.00	0.67	0.00	0.26
RD21	36.58	0.00	34.46	11.77	3.71	0.00	1.98	0.00	88.50	9.72	5.92	0.00	6.57	1.59	0.90	0.00	0.63	0.00	0.36
DR42	34.52	0.00	32.68	11.86	4.24	0.06	1.99	0.15	85.50	10.14	5.82	0.00	6.50	1.67	1.07	0.01	0.66	0.03	0.39
DR42	35.83	0.18	32.40	12.25	3.92	0.00	2.28	0.00	86.86	9.98	5.95	0.02	6.34	1.70	0.97	0.00	0.74	0.00	0.36
DR42	35.19	0.00	34.09	9.75	4.81	0.00	2.03	0.31	86.18	9.93	5.81	0.00	6.64	1.35	1.18	0.00	0.66	0.05	0.47
DR42	34.88	0.00	33.66	11.54	3.56	0.00	2.05	0.32	86.01	10.04	5.83	0.00	6.63	1.61	0.89	0.00	0.67	0.06	0.36
DR42	35.19	0.00	34.09	9.75	4.81	0.00	2.03	0.31	86.18	9.93	5.81	0.00	6.64	1.35	1.18	0.00	0.66	0.05	0.47
DR42	36.09	0.00	32.59	13.20	3.78	0.00	2.50	0.07	88.23	9.88	5.93	0.00	6.32	1.82	0.93	0.00	0.81	0.01	0.34
DR42	36.37	0.00	33.20	11.64	4.25	0.13	2.86	0.00	88.45	9.79	5.93	0.00	6.38	1.59	1.03	0.03	0.91	0.00	0.39
DR42	36.52	0.18	33.58	11.15	4.34	0.07	2.88	0.41	89.13	9.70	5.90	0.02	6.39	1.51	1.04	0.01	0.91	0.07	0.41
DR42	35.96	0.21	32.43	13.84	3.67	0.06	2.39	0.12	88.68	9.87	5.91	0.03	6.28	1.90	0.90	0.01	0.77	0.02	0.32
DR42	36.46	0.00	33.23	12.23	4.29	0.05	2.06	0.00	88.32	9.79	5.94	0.00	6.38	1.67	1.04	0.01	0.66	0.00	0.38

A1-1.18 Radiating Tourmaline

WX07	33.45	0.06	32.27	10.95	3.34	0.05	1.62	0.23	81.97		5.85		6.65	1.6	0.87	0.01	0.55	0.04	0.35
WX07	33.29	0.1	32.69	10.49	3.37	0.05	1.64	0.27	81.9		5.81		6.72	1.56	0.88	0.01	0.56	0.05	0.36

A1-2 Whole Rock Chemistry Data

A1-2.1 Major Components of the Mine Granite (wt%)

sample	SiO ₂	TiO ₂	Al ₂ O ₃	Fe ₂ O ₃	FeO	MnO	MgO	CaO	Na ₂ O	K ₂ O	P ₂ O ₅	SO ₂	H ₂ O+	H ₂ O-	CO ₂
Ard045	70.76	0.41	14.47	0.41	2.41	0.06	1.00	0.93	2.47	4.87	0.18	0.02	1.47	0.17	0.31
Ard074	69.93	0.46	14.76	0.46	2.79	0.07	1.47	1.48	2.35	4.25	0.15	0.02	1.34	0.18	0.44
Ard084	70.92	0.42	16.43	0.37	2.41	0.05	1.11	1.28	2.04	4.74	0.21	0.06	1.36	0.15	0.34
Ard085	69.39	0.46	15.09	0.59	2.46	0.05	1.26	1.57	2.24	4.78	0.21	0.01	1.39	0.10	0.35
Ard086	69.87	0.45	14.28	0.54	2.50	0.05	1.26	1.38	2.05	4.61	0.18	0.01	1.45	0.20	0.34
Ard087	69.20	0.53	14.58	0.63	3.10	0.06	1.66	1.70	2.03	4.03	0.17	0.16	1.63	0.18	0.12
Ard088	70.49	0.44	14.71	0.54	2.30	0.04	1.19	1.54	2.23	4.76	0.21	0.01	1.12	0.15	0.17
Ard001	71.20	0.42	14.64	0.62	2.24	0.05	1.15	1.38	2.49	4.47	0.21	0.00	1.23	0.22	0.09

A1-2.2 Major components of the Ardlethan Granite (wt%)

sample	SiO ₂	TiO ₂	Al ₂ O ₃	Fe ₂ O ₃	FeO	MnO	MgO	CaO	Na ₂ O	K ₂ O	P ₂ O ₅	SO ₂	H ₂ O+	H ₂ O-	CO ₂
Ard011	75.55	0.12	12.69	0.51	0.94	0.04	0.05	0.52	2.99	4.70	0.16	0.00	0.67	0.23	0.35
Ard012	76.89	0.08	12.60	0.45	0.83	0.03	0.04	0.37	3.06	4.76	0.10	0.00	0.49	0.12	0.44
Ard013	75.48	0.09	13.08	0.49	0.51	0.03	0.12	0.50	3.77	3.66	0.17	0.00	0.74	0.27	0.24
Ard018	74.75	0.05	13.90	0.35	0.93	0.03	0.05	0.19	3.28	4.69	0.14	0.00	0.63	0.30	0.51
Ard019	75.63	0.09	13.28	0.42	0.82	0.03	0.13	0.31	3.02	4.80	0.24	0.00	0.56	0.21	0.37
Ard020	75.72	0.05	12.96	0.46	0.74	0.03	0.06	0.29	3.35	4.62	0.26	0.00	0.56	0.24	0.32
Ard021	75.40	0.15	13.05	0.55	0.95	0.04	0.16	0.83	3.52	4.66	0.03	0.00	0.46	0.10	0.13
Ard022	75.26	0.14	12.90	0.77	0.65	0.03	0.18	0.69	3.46	4.59	0.02	0.00	0.67	0.27	0.22
Ard024	75.99	0.09	13.36	0.20	0.98	0.04	0.10	0.50	3.21	4.70	0.16	0.03	0.61	0.03	0.27
Ard027	75.80	0.08	13.05	0.57	0.92	0.04	0.03	0.44	2.82	4.54	0.17	0.00	0.77	0.22	0.28

sample	SiO ₂	TiO ₂	Al ₂ O ₃	Fe ₂ O ₃	FeO	MnO	MgO	CaO	Na ₂ O	K ₂ O	P ₂ O ₅	SO ₂	H ₂ O+	H ₂ O-	CO ₂
Ard113	76.30	0.11	12.60	0.06	1.15	0.02	0.16	0.40	2.86	5.00	0.14	0.00	0.76	0.10	0.20
Ard115	75.10	0.06	12.60	0.20	2.08	0.06	0.08	0.50	2.92	5.10	0.10	0.06	0.93	0.06	0.28
Ard119	77.10	0.06	12.30	0.15	0.74	0.01	0.13	0.06	3.27	5.10	0.06	0.00	0.62	0.07	0.08
Ard122	75.00	0.04	13.50	0.18	0.79	0.03	0.04	0.28	3.44	4.70	0.26	0.01	0.57	0.08	0.10
Ard123	76.70	0.10	12.50	0.11	1.15	0.03	0.12	0.25	2.75	5.00	0.14	0.00	0.71	0.07	0.10
Ard110	73.50	0.27	13.30	0.60	1.72	0.02	0.37	0.75	2.45	5.00	0.15	0.00	1.34	0.15	0.13
Ard117	76.70	0.18	12.40	0.27	1.15	0.03	0.19	0.39	2.86	5.00	0.08	0.01	0.62	0.05	0.12
Ard120	76.50	0.09	12.40	0.03	1.40	0.03	0.13	0.17	2.99	4.50	0.17	0.00	0.85	0.17	0.07
Ard101	76.20	0.07	12.30	0.15	0.40	0.03	0.06	0.55	3.24	5.70	0.03	0.02	0.57	0.09	0.18
Ard102	76.10	0.08	12.30	0.28	0.59	0.01	0.06	0.85	2.93	5.65	0.02	0.02	0.80	0.08	0.08

A1-2.3 Major Components of the GQFP (wt%)

sample	SiO ₂	TiO ₂	Al ₂ O ₃	Fe ₂ O ₃	FeO	MnO	MgO	CaO	Na ₂ O	K ₂ O	P ₂ O ₅	SO ₂	H ₂ O+	H ₂ O-	CO ₂
Ard002	72.74	0.34	13.47	0.74	1.63	0.06	0.43	1.44	2.91	5.01	0.14	0.00	0.87	0.22	0.01
Ard003	72.92	0.34	13.06	0.93	1.40	0.05	0.42	1.39	2.68	4.92	0.15	0.00	0.95	0.28	0.01
Ard026	74.34	0.27	12.82	1.01	1.02	0.03	0.23	1.13	2.41	5.02	0.15	0.00	0.79	0.22	0.21
Ard034	72.50	0.43	13.47	0.58	2.11	0.03	0.53	1.75	2.65	4.73	0.18	0.00	0.93	0.16	0.16
Ard014	74.42	0.28	12.94	0.69	1.29	0.02	0.47	1.19	2.62	4.91	0.16	0.00	0.85	0.19	0.01
Ard017	69.44	0.53	14.39	1.74	2.60	0.07	0.78	2.32	2.70	4.25	0.20	0.00	0.79	0.26	0.15
Ard009	71.00	0.48	13.70	0.83	2.18	0.05	0.61	1.86	2.65	4.57	0.18	0.00	1.04	0.24	0.27

A1-2.4 Major Components of the Microgranite (wt%)

Ard056	76.46	0.07	13.11	0.28	0.58	0.03	0.14	0.61	4.04	3.24	0.13	0.10	0.69	0.08	0.71
Ard107	74.50	0.06	13.50	0.05	0.86	0.03	0.20	0.60	3.61	4.95	0.14	0.05	0.62	0.05	0.23
Ard112	75.20	0.06	13.70	0.62	0.62	0.02	0.20	0.30	3.23	4.25	0.23	0.04	0.75	0.75	0.28
Ard114	76.70	0.07	12.30	0.17	1.00	0.02	0.20	0.45	2.70	4.50	0.13	0.01	0.63	0.08	0.57

A1-2.5 Major Components of the Mine Porphyry (wt%)

sample	SiO ₂	TiO ₂	Al ₂ O ₃	Fe ₂ O ₃	FeO	MnO	MgO	CaO	Na ₂ O	K ₂ O	P ₂ O ₅	SO ₂	H ₂ O ⁺	H ₂ O ⁻	CO ₂
Ard079	76.24	0.05	12.05	0.36	0.83	0.02	0.26	0.72	2.01	4.93	0.12	0.16	1.15	0.53	0.58
Ard080	76.03	0.05	12.17	0.36	1.50	0.02	0.13	0.63	3.12	4.29	0.12	0.16	0.84	0.09	0.22
Ard090	76.08	0.05	12.12	0.56	1.22	0.01	0.23	0.14	0.17	6.80	0.01	0.01	1.13	0.13	0.98
Ard098	76.86	0.11	12.27	0.35	1.13	0.04	0.07	0.58	3.38	4.20	0.01	0.01	0.43	0.23	0.15

A1-2.6 Trace Components of the Mine Granite (ppm)

sample	Ba	Rb	Sr	Pb	Th	U	Zr	Nb	Y	La	Ce	Nd	Sc	V	Cr	Co	Ni	Cu	Zn	Ga	Li	B	Mo	Sn	F	As	Sb	Ta	W	Bi
Ard045	335	333	105	34	15.5	6.2	114	13	20	31	63	23	10	41	27	6	12	11	131	17	40	15	0	56	600	9	5	0	12	3
Ard074	355	261	111	40	13.0	5.6	126	12	19	20	45	15	10	47	35	9	14	7	61	17	90	70	0	15	700	28	2	4	4	3
Ard084	360	310	120	34	20.0	8.0	130	18	22	45	75	15	4	44	26	6	8	60	50	20	45	20	0	22	90	2	3	5	25	4
Ard085	320	290	130	38	20.0	10.0	130	24	18	50	80	15	5	54	26	6	7	15	65	15	60	30	0	18	110	4	3	5	15	4
Ard086	360	300	130	36	16.0	8.0	140	20	26	40	85	15	5	56	28	8	9	20	85	20	45	30	0	26	120	4	3	5	25	5
Ard087	350	320	210	22	26.0	6.0	160	24	24	30	60	15	4	66	40	4	12	10	45	25	60	200	0	44	120	34	3	5	20	5
Ard088	320	350	140	36	18.0	6.0	130	24	20	20	80	15	4	46	14	3	5	15	50	20	25	70	0	44	110	4	4	5	15	4
Ard001	330	295	103	38	17.0	5.0	136	15	22	26	60	22	9	38	25	8	11	12	64	18	90	15	0	8	1000	0	1	0	4	1

A1-2.7 Trace components of the Ardlethan Granite

sample	Ba	Rb	Sr	Pb	Th	U	Zr	Nb	Y	La	Ce	Nd	Sc	V	Cr	Co	Ni	Cu	Zn	Ga	Li	B	Mo	Sn	F	As	Sb	Ta	W	Bi
Ard011	65	610	19	22	17.5	44.2	78	17	26	11	26	9	3	4	4	2	2	2	53	21	230	250	2	23	3300	7	1	0	8	1
Ard012	10	780	6	18	22.5	28.0	61	24	29	27	20	7	4	0	3	1	4	5	48	22	220	15	2	65	5100	40	1	6	20	3
Ard014	45	453	20	19	8.5	17.8	50	15	19	7	16	5	4	2	4	0	0	9	122	19	220	150	1	91	3400	3	1	4	10	3
Ard018	25	1050	33	15	23.0	24.4	37	28	24	7	16	6	4	0	4	0	3	0	24	27	340	25	2	17	7300	3	2	6	30	53
Ard019	30	880	31	17	15.5	34.0	57	26	20	9	18	6	4	3	3	0	3	0	44	24	320	85	2	38	5700	26	1	6	28	3
Ard020	5	915	5	15	10.0	44.8	43	23	12	4	7	2	3	1	2	0	3	0	46	25	350	60	4	36	4500	13	1	12	20	3
Ard021	165	401	51	26	35.0	9.6	134	34	56	32	72	24	5	5	4	3	2	0	20	18	120	15	0	23	1200	0	1	4	6	1
Ard022	165	417	47	24	37.0	13.6	130	34	65	34	76	28	4	5	4	2	0	0	22	18	110	15	2	14	1600	0	1	8	6	1
Ard024	35	495	16	22	8.5	16.8	53	13	18	8	13	4	3	3	4	0	1	2	41	19	140	140	0	22	2000	2	2	2	10	4
Ard027	10	555	7	19	10.5	14.8	50	18	20	5	13	5	3	2	3	0	1	24	76	22	200	10	3	26	3400	0	2	0	10	4
Ard101	150	540	36	20	70.0	28.0	230	130	190	5	30	16	3	2	5	1	2	10	40	30	30	1	2	24	3300	2	4	18	50	20
Ard102	220	580	38	18	79.0	26.0	220	130	210	10	50	0	3	6	2	1	2	15	42	30	60	1	2	55	6600	1	4	10	75	10
Ard113	80	630	30	24	20.0	20.0	80	20	60	15	20	0	0	2	3	0	0	20	43	20	90	120	0	40	2700	0	0	10	20	0
Ard115	80	800	20	24	35.0	25.0	85	35	45	20	40	0	0	2	3	17	9	116	32	25	28	70	0	40	2700	0	0	9	85	0
Ard119	150	560	30	22	30.0	15.0	35	20	200	40	90	0	0	4	2	12	9	4	7	25	68	210	0	25	800	0	0	3	3	0
Ard122	55	840	60	17	40.0	40.0	30	25	45	7	15	0	0	2	8	16	13	8	26	30	91	170	0	35	5400	0	0	7	25	0
Ard123	65	680	45	16	20.0	65.0	70	20	30	15	20	0	0	4	3	5	6	9	28	20	138	60	0	40	2600	0	0	3	15	0
Ard110	370	340	85	25	25.0	7.0	200	15	35	40	65	0	0	15	5	6	5	13	25	20	31	90	0	20	500	0	0	3	3	0
Ard117	230	640	40	38	35.0	15.0	140	25	150	150	110	0	0	6	2	17	10	6	24	25	165	60	0	40	1700	0	0	3	9	0
Ard120	170	880	110	21	20.0	50.0	65	30	50	50	50	0	0	5	10	16	12	13	30	25	150	130	0	35	4200	0	0	8	10	0

A1-2.7 Trace Components of the GQFP

sample	Ba	Rb	Sr	Pb	Th	U	Zr	Nb	Y	La	Ce	Nd	Sc	V	Cr	Co	Ni	Cu	Zn	Ga	Li	B	Mo	Sn	F	As	Sb	Ta	W	Bi
Ard002	580	246	133	43	21.5	4.8	214	19	32	39	92	35	6	17	6	4	2	2	64	19	50	30	0	7	800	0	1	0	4	1
Ard003	530	239	111	39	22.5	4.6	210	18	29	38	90	36	5	15	5	3	4	4	57	18	65	30	0	8	800	0	1	2	2	1
Ard009	810	223	149	35	25.5	4.6	263	18	34	46	111	41	7	27	9	6	6	0	88	19	60	15	1	9	1100	14	1	0	6	4
Ard014	515	261	92	36	22.0	6.2	185	18	21	38	91	36	4	9	3	3	3	6	63	19	55	15	2	6	1000	0	1	2	6	1
Ard017	960	200	178	34	29.5	4.8	451	23	48	66	154	58	11	28	10	5	6	9	100	21	50	35	3	5	800	3	1	2	6	3
Ard026	600	267	96	37	21.5	5.8	191	19	21	39	92	35	3	7	3	2	0	3	75	19	55	15	2	8	900	2	1	4	4	1
Ard034	765	223	137	35	24.0	4.8	234	18	31	42	101	36	6	21	7	5	3	6	63	18	70	45	2	7	1000	0	2	0	2	2

A1-2.9 Trace Components of the Microgranite

sample	Ba	Rb	Sr	Pb	Th	U	Zr	Nb	Y	La	Ce	Nd	Sc	V	Cr	Co	Ni	Cu	Zn	Ga	Li	B	Mo	Sn	F	As	Sb	Ta	W	Bi
Ard056	75	260	22	38	4.0	20.4	27	8	9	2	7	3	2	0	4	0	0	14	77	15	15	60	0	34	500	26	1	4	4	3
Ard112	190	670	55	10	2.0	15.0	10	35	6	7	7	0	0	2	2	6	3	8	43	25	8	1350	0	45	800	0	0	10	15	0
Ard114	80	360	30	29	2.0	15.0	20	10	10	4	7	0	0	2	11	14	14	13	21	15	8	620	0	45	300	0	0	3	3	0
Ard107	25	430	25	41	2.0	15.0	30	15	10	7	7	0	0	2	3	11	10	22	18	15	13	150	0	25	100	0	0	10	15	0

A1-2.10 Trace Components of the Mine Porphyry

sample	Ba	Rb	Sr	Pb	Th	U	Zr	Nb	Y	La	Ce	Nd	Sc	V	Cr	Co	Ni	Cu	Zn	Ga	Li	B	Mo	Sn	F	As	Sb	Ta	W	Bi
Ard079	120	520	44	30	50.0	22.0	210	140	95	40	70	15	7	7	15	4	7	75	55	30	10	10	0	80	5100	15	3	5	40	4
Ard080	100	450	40	13	55.0	18.0	220	140	85	50	110	15	7	30	2	4	7	40	25	25	10	10	0	44	3900	5	3	5	25	10
Ard090	480	760	40	18	60.0	22.0	210	130	110	50	65	15	7	3	20	4	7	15	20	20	20	10	0	85	180	7	3	5	65	5
Ard098	30	740	15	38	85.0	34.0	200	90	85	75	110	15	7	3	6	3	2	15	45	30	85	10	0	28	360	3	3	5	32	5

Appendix 2: Catalog of Key Samples

A2-1 Handspecimens

Sample	Description	Location
PV1	Pyroclastic volcanics	Volcanics around the GQFP stock (Fig. 2-2)
PV2	Pyroclastic volcanics	
PV3	Pyroclastic volcanics	
G1	GQFP	Sampled from the GQFP stock (Fig. 2-2)
G2	GQFP	
G3	GQFP	
TH01	Coarse A. G.*	This group of samples were from outcrops in Taylor' Hill area southwest to the Ardlethan Tin Mine. Figs. 2-1 and 2-2 show the location of Taylor's Hill
TH02	Porphyritic A. G.	
TH03	Porphyritic + nonporphyritic A. G.	
TH04	Strongly altered A. G.	
TH05	Porphyritic A. G.	
TH06	Porphyritic A. G.	
TH07	Coarse A.G.	
TH08	Coarse A.G.	
TH10	Porphyritic A.G.	
TH11	Porphyritic A.G.	
TH12	Porphyritic A.G.	
TH13	Porphyritic A.G.	
TH14	Porphyrotic A.G.	
TH15	Porphyritic A.G.	
TH18	Porphyritic A.G.	
TH21	Porphyritic A.G.	
WX01	White Crystal ore	White Crystal
WX02	White Crystal ore	White Crystal
WX03	White Crystal ore	White Crystal
WX04	Mineralized breccia	White Crystal
WX05	White Crystal ore	White Crystal
WX06	Vugy breccia	White Crystal
WX07	White Crysatl ore	White Crystal
WX08	White Crysatl ore	White Crystal
WX09	Vugy breccia	White Crystal
WX10	Altered M.G.**	White Crystal
WX11	White Crysatl ore	White Crystal
WX12	Altered M.G.	White Crystal
WX13	Altered M.G.	White Crystal
WX14	Sulphide rich ore	White Crystal
WX15	Sulphide rich ore	White Crysatl
WX16	Altered M.G.	White Crystal
WX17	Massive sulphides	White Crystal
WX18	Sulphide rich breccia	White Crystal

WX19	Sulphide rich ore	White Crystal
WX20	Vugy breccia	White Crystal
WX21	White Crystal ore	White Crystal
WX22	Vugy breccia	White Crystal
WX23	Vugy breccia	White Crystal
WX24	Vugy breccia	White Crystal
WX25	White Crystal ore	White Crystal
WX26	White Crystal ore	White Crystal
WX27	White Crystat ore	White Crystat
WX28	Vug infilling fluorite+siderite	White Crystal
WX29	White Crystal ore	White Crystal
WX30	White Crystal ore	White Crystal
WY01	Contact of Mine Porphyry and breccia	Ardwest
WY02	Deeply altered rock flour rich breccia	Wildcherry South
WY03	Mine porphyry and breccia	Wildcherry
WY04	Wildcherry South ore	Wildcherry South
WY05	Wildcherry South ore	Wildcherry South
WY06	Mine porphyry	Ardwest
WY07	Mine porphyry	Ardwest
WY08	Rock flour supported breccia	Ardwest
WY09	Mine porphyry	Wildcherry South
WY10	Mine porphyry and breccia	Wildcherry South
WY11	Wildcherry South ore	Wildcherry South
WY12	Mine porphyry	Wildcherry South
WY13	Ardwest ore	Ardwest
WY14	Ardwest ore	Ardwest
WY15	Wildcherry South ore	Wildcherry South
WY16	Wildcherry ore	Wildcherry
WY17	Cassiterite rich ore	Wildcherry
WY18	Wildcherry South ore	Wildcherry South
WY19	Wildcherry ore	Wildcherry
WY20	Altered M.G.	Ardwest
WY21	Ardwest ore	Ardwest
WY22	Wildcherry ore	Wildcherry
WY23	Wildcherry ore	Wildcherry

RB1	Blackreef ore	Blackreef
RB2	Blackreef ore	Blackreef
RB3	Tourmaline rich ore	Blackreef
RB4	Sulphide rich breccia	Blackreef
RB5	Zoned fragments	Blackreef
RB6	Fluorite bearing ore	Blackreef
RB7	Sulphide rich ore	Blackreef
RB8	Zoned fragment	Blackreef
RB9	Fragment+vug infilling minerals	Blackreef
RB10	Sulphide rich ore	Blackreef
RB11	Blackreef ore	Blackreef
RB12	Milky+clear quartz	Blackreef
RB13	Fine sulphides	Blackreef
RB14	Breccia with vug infilling minerals	Blackreef
RB15	Layered vug infilling minerals	Blackreef
RB16	Tourmaline rich ore	Blackreef
RB20	PbS rich Blackreef ore	Blackreef

RB21	Zoned fragments	Blackreef
RB22	Tourmaline bands	Blackreef
RB23	Sericite-tourmaline altered breccia	Blackreef
RB25	Siderite rich sample	Blackreef
RB26	Sulphide rich ore	Blackreef
RB27	Sulphide rich ore	Blackreef
RB28	Sericite altered M.G.	Blackreef
RB29	Sericite-tourmaline altered M.G.	Blackreef
RB30	Vug infilling sulphides and siderite	Blackreef
RB31	Arsenopyrite rich ore	Blackreef
RB32	Fragment supported breccia	Blackreef

A2-2 Drill Core Samples (Drill hole paths are shown in Fig. A2-1. Down Hole depth in metres)

Sample	Description	Drill hole/Depth
RD1	Weakly altered M.G.	B1110/148.7
RD2	Chlorite altered M.G.	B1110/151.7
RD3	Sericite-Chlorite altered M.G.	B1110/181.2
RD4	M.G.	B1110/202
RD5	Chlorite altered breccia	B1110/289.1
RD6	Strongly altered breccia	B1110/312
RD7	Chlorite altered breccia	B1110/313
RD8	Strongly chlorite altered breccia	B1110/321.5
RD9	Altered breccia	B1110/339.5
RD10	Altered breccia	B1110/351.45
RD11	Mineralized breccia	B1110/369.8
RD12	Perseverance ore	B1110/376.8
RD13	Breccia	B1110/414
RD14	Breccia	B1110/423
RD15	Altered M.G.	B1110/467.4
RD16	Altered M.G.	B1110/495
RD17	Altered breccia	B1110/510
RD18	Altered breccia	B1110/521.7
RD19	Altered breccia	B1110/535.2
RD20	Altered breccia	B1110/541.15
RD21	Alterde M.G.	B1110/560.5
RD22	Altered M.G.	B1110/585.85
RD23	Alterde breccia	B1110/637
RD24	Altered breccia	B1110/657
RD25	Alterde breccia	B1110/692.3
RD26	Mine Porphyry	B1110/726.6
RD27	Alterde breccia	B1110/789.46
RD28	Altered breccia	B1110/803.1
RD29	Mineralized breccia	B1110/821.1
RD30	Mineralized breccia	B1110/826.5
RD31	Altered Mine porphyry	B1110/838.9
RD32	Altered Mine porphyry	B1110/879.9
RD33	Altered rock	B1110/893.7
RD34	Breccia	B1110/894.5
RD35	Mineralized Mine porphyry	B1110/912.3

RD36	Mineralized Mine porphyry	B1110/914.5
RD37	Quartz vein in altered M.G.	B1110/923.6
RD38	Dolerite dyke	B1110/936.6
RD39	Mine porphyry	B1110/944.8
RD40	Altered rock	B1110/947.4
RD41	Mine porphyry	B1110/981
RD42	Mine porphyry	B1110/982
RD43	Mine porphyry with granite inclusion	B1110/986
RD44	Breccia	B1110/992
RD45	Massive fluorite in vugs	B1110/992.8
RD46	Altered porphyry	B1110/1003.2
RD47	Microgranite	B1110/1004.8
RD48	Dolerite dyke	B1110/1008.1
RD49	Altered breccia	B1110/1011.8
RD50	Breccia	B1110/1018.5
RD51	Altered breccia	B1110/1021.9
RD52	Altered M.G.	B1110/1022.35
RD53	Biotiter rich altered M.G.	B1110/1034.15
RD54	Altered M.G.	B1199/401.2
RD55	Altered M.G.	B1199/413.3
RD56	Altered M.G.	B1199/446.6
RD57	Weakly altered M.G.	B1199/494.35
RD58	Breccia	B1199/501.3
RD59	Reatively fresh M.G.	B1199/506.9
RD60	Weakly altered M.G.	B1199/526.4
RD61	Relatively fresh M.G.	B1199/549.1
RD62	Relatively fresh M.G.	B1199/587.7
RD63	Massive tourmaline	B1199/627
RD64	Altered M.G.	B1199/628.3
RD65	Altered breccia	B1199/662.6
RD66	Quartz-tourmaline altered breccia	B1199/671.3
RD67	Relatively fresh M.G.	B1199/680
RD68	Relatively fresh M.G.	B1199/701.6
RD69	Fresh A.G. and GQFP	B1120/180.3
RD70	Microgranite	B1120/204.3
RD71	Contact of A.G. and microgranite	B1120/215
RD72	Contact of A.G. and microgranite	B1120/220.5
RD73	Porphyritic and nonporphyritic A.G.	B1120/239.36
RD74	A.G.	B1120/249.7
RD75	Altered rock	B1122/207.05
RD76	Altered sediments	B1122/369.2
RD77	Altered rock	B1122/416.6
RD78	Contact of sediments and granite	B1122/441.8
RD79	Microgranite	B1122/472.1
RD80	Fresh M.G.	B1195/481.6
RD81	Altered M.G.	B1195/502.8
RD82	Sulphide rich breccia	B1195/508.15
RD83	Sulphide rich breccia	B1195/520
RD84	Sulphide rich breccia	B1195/523
RD85	Altered porphyry	B1195/570.8
RD86	Breccia	B1195/592.7
RD87	Tourmaline rich rock	B1195/593
RD88	Altered M.G.	B1196/404.4

RD89	Altered M.G.	B1196/458.0
RD90	Altered M.G.	B1196/523.1
RD91	Altered M.G.	B1197/506
RD92	Altered M.G.	B1197/532
RD93	Relatively fresh M.G.	B1198/405.4
RD94	Quartz-tourmaline rich breccia	B1198/427.5
RD94A	Microgranite dyke	B1198/429.5
RD95	Relatively fresh M.G.	B1198/454.6
RD96	Microgranite	B1198/554.5
RD97	Relatively fresh M.G.	B1198/583.4
RD98	Microgranite	B1198/619.1
RD99	Altered rock	B1198/649.4
RD100	Altered M.G.	B1198/721.0
RD101	Microgranite	B1198/624.8
RD102	Coarse microgranite	B1198/625.4
RD103	Coarse microgranit	B1198/628.3
RD104	Microgranite	B1198/631.3
RD104A	Altered microgranite	B1185/343.1
RD105	Pegmatite	B1185/344
RD106	Pegmatite	B1185/350
RD107	Microgranite with Q-T nodules	B1185/355.4
RD108	Massive sulphides	B1185/612.6
RD109	Mineralized breccia	B1185/613.4
RD110	Cassiterite rich breccia	B1185/614
RD111	Chlorite vein	B1188/320
RD112	Chlorite vein	B1188/375
RD113	Sulphide bearing rock	B1188/407.8
RD114	Mineralized breccia	B1188/469.1
RD115	Dolerite dyke	B1188/592.5
RD116	M.G. with patchy tourmaline	B1188/570
RD117	Altered breccia	B1115/201
RD118	Altered Breccia	B1115/230
RD119	Sericite-siderite altered M.G.	B1115/240
RD121	Altered M.G.	B1197/440
RD122	Breccia	B1190/410
RD123	Strongly altered breccia	B1190/510
RD124	Strongly altered breccia	B1190/511
RD125	Mineralized vein	B1138/180
RD126	Mineralized vein	B1138/250
RD127	Mineralized vein	B1138/260
RD128	Microgranite and Mine porphyry	B1173/305
RD129	Godfrey South ore	B1173/435
RD131	Fluorite rich breccia	B1177/549
RD132	Godfrey South ore	B1177/616.4
RD133	Wolframite rich ore, Godfrey South	B1177/568.5
RD134	Fluorite and clay, Godfrey South	B1177/592.5
RD135	Secondary biotite in fractures	B1183/683.1
RD136	Fresh Mine porphyry	B1183/714.2
RD137	Sericite-siderite altered Mine porphyry	B1183/691.2
RD138	Altered breccia	B1136/233.5
RD138A	Foot contact of Microgranite	B1196/209.2
RD139	Quartz-cassiterite vein, Perseverance	B1130/315
RD140	Altered breccia	B1130/344

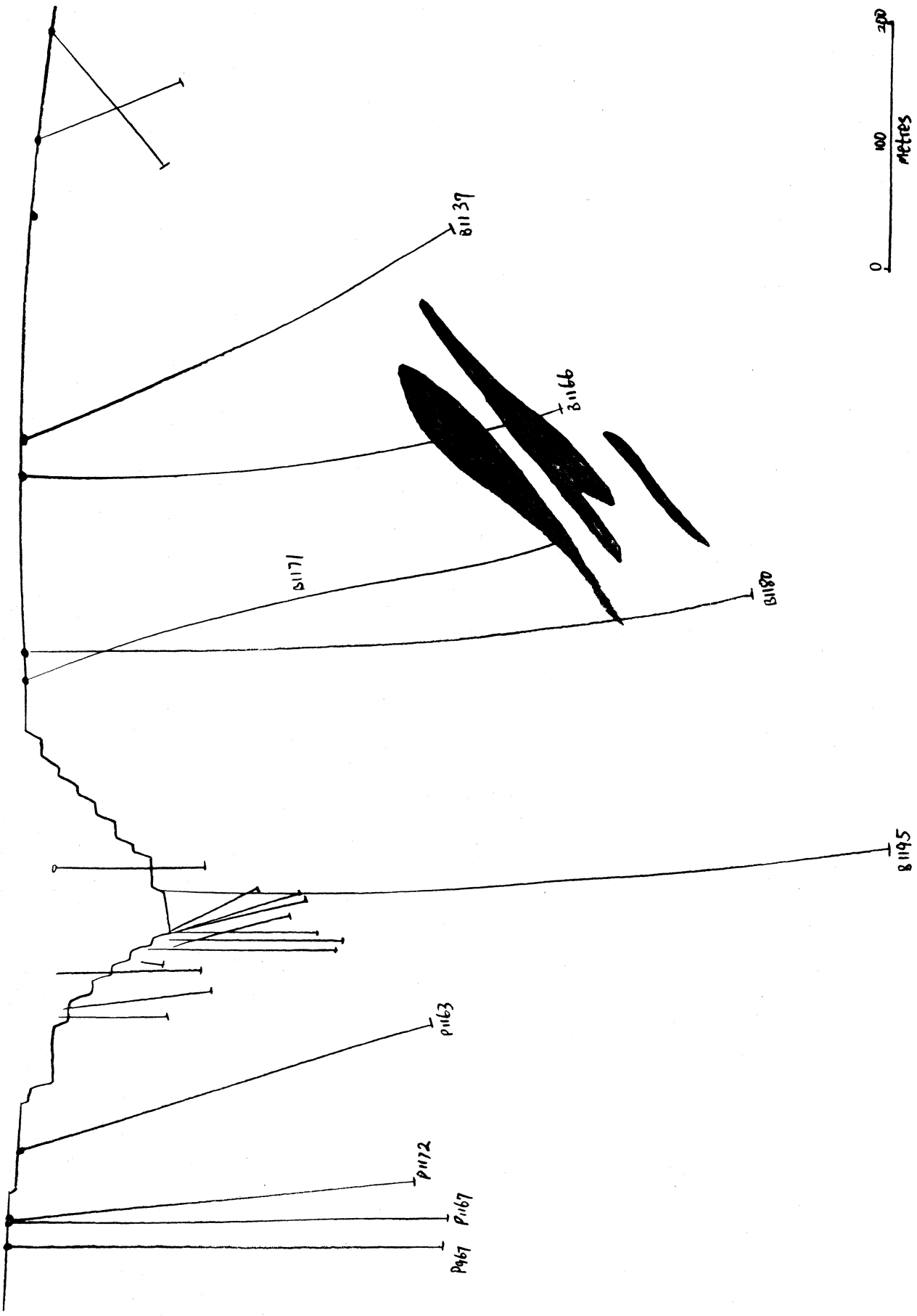
RD141	Strongly chlorite altered breccia	B1198/515
RD142	Chlorite altered breccia	B1198/680
RD143	Altered breccia	B1198/700
RD144	Biotite altered breccia	B1170/525.5
RD145	Godfrey ore	B1185/635
RD146	Godfrey ore	B1185/637
RD147	Godfrey ore	B1185/639
RD148	Godfrey ore	B1176/509
RD149	Godfrey ore	B1176/546
RD150	Altered M.G.	B1103/129
RD153	Godfrey ore	B1168/515
RD154	Perseverance sulphide poor ore	B1103/235
RD155	Altered sediment breccia	B1174/309.8
RD156	Fluorite rich breccia	B1174/464.3
RD157	Cassiterite rich Godfrey ore	B1174/466.4
RD158	Mineralized breccia, near Godfrey	B1166/356.8
RD159	Godfrey ore	B1166/387.5
RD161	Mineralized breccia	B1176/400
RD170	Strongly sericite altered breccia	B1176/546.5
RD180	Breccia	B1110/897.5
RD190	Massive chlorite	B1176/504
RD191	Massive chlorite	B1176/503.5
RD192	Strongly altered breccia	B1176/507.5
RD193	Massive chlorite	B1176/506.4
RD194	Massive chlorite	B1176/507.1
RD195	Vug infilling pyrite and siderite	B1177/627
RD196	Rock flour rich breccia	B1110/904.5
RD197	Rock flour rich breccia	B1110/902
RD198	Dolerite dyke	B1110/940
RD199	Breccia	B1110/897.3
RD201	Sediment breccia	B1176/687
RD202	Chlorite altered breccia	B1110/726
DR4	Godfrey ore	B1185/677.2
DR5	Godfrey ore	B1185/663
DR6	Godfrey ore	B1185/653
DR7	Godfrey ore	B1185/613
DR8	Godfrey ore	B1185/611.6
DR9	Godfrey ore	B1185/608
DR50	A.G.	B1120/168
DR51	A.G.	B1120/196
DR52	Microgranite	B1120/212
DR53	A.G.	B1120/243
RDB60	A.G.	B1109/201
RDB61	A.G.	B1108/162
RDB62	A.G.	B1108/184
RDB63	A.G.	B1108/190
RDB64	A.G.	B1108/201
RDS65	A.G.	B1120/190.8
RDS66	A.G.	B1120/171.7
RDS67	A.G.	B1120/199.8
RDS68	A.G.	B1120/216.6
RDS69	A.G.	B1120/228.0
RDS70	A.G.	B1120/246.1

RDS71	A.G.	B1120/249.7
RDW74	Altered M.G.	B1110/151.3
RDW77	Altered Breccia	B1110/228.9
RDW82	Mineralized breccia	B1110/377.2
RDW84	Biotite altered breccia	B1110/445.8
RDW85	Biotite altered breccia	B1110/513.1

A2-3 S. S. Sun's Samples

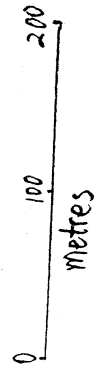
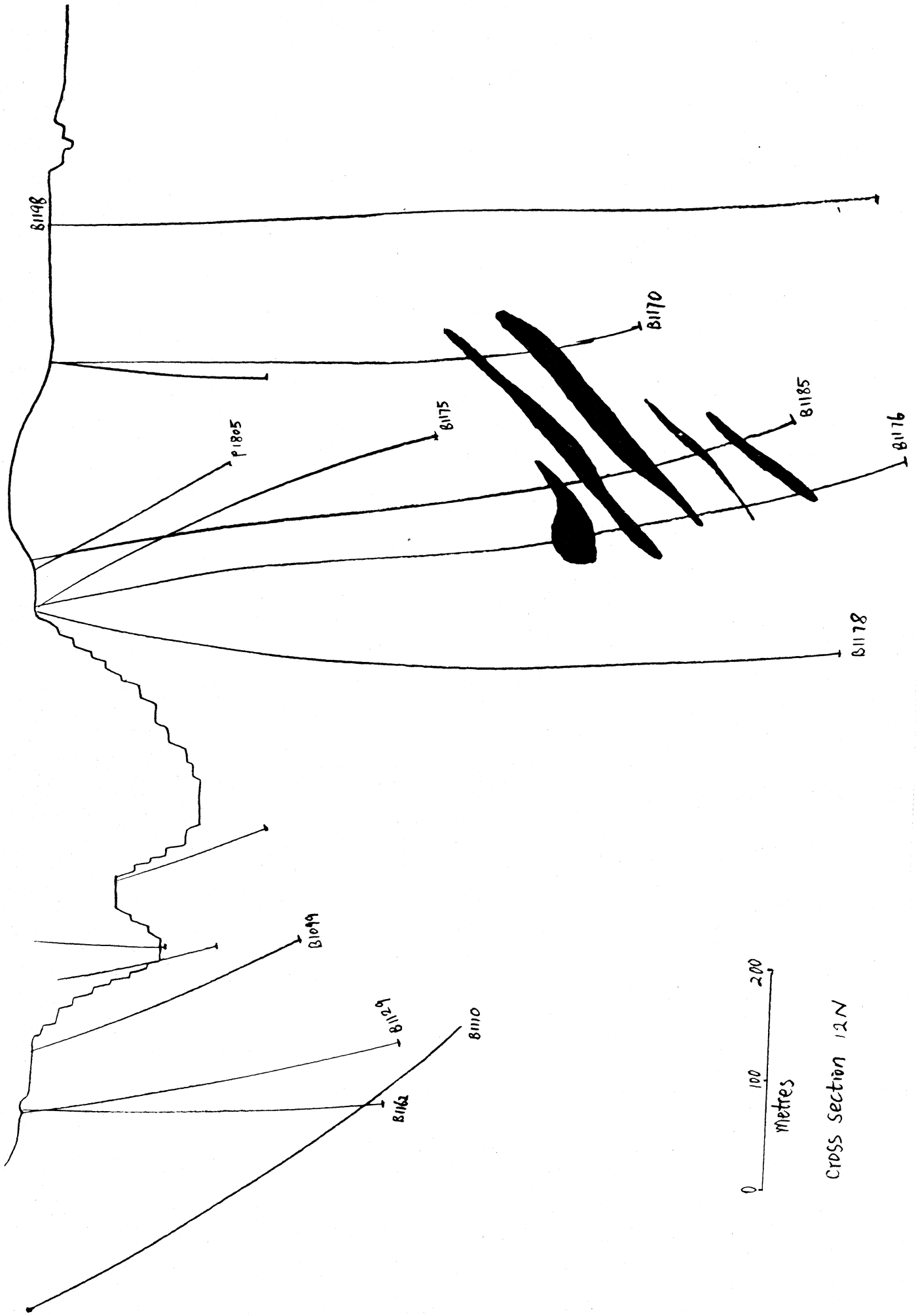
67872	White Crystal ore	White Crystal
67968	White Crystals ore	White Crystal
8382	Wildcherry ore	Wildcherry
8417	Wildcherry ore	Wildcherry
8449	Wildcherry South ore	Wildcherry South
75A2	White Crystal ore	White Crystal
75A7	White Crystal ore	White Crystal
75A11	White Crystal ore	White Crystal

Fig. A2-1 Key drill hole paths and major remaining ore-grade intersections showing on Cross Sections of 16N, 12N, 8N, 2N, 2S, 4S, 8S, 14S and 24S (see Fig. 4-1 for reference)

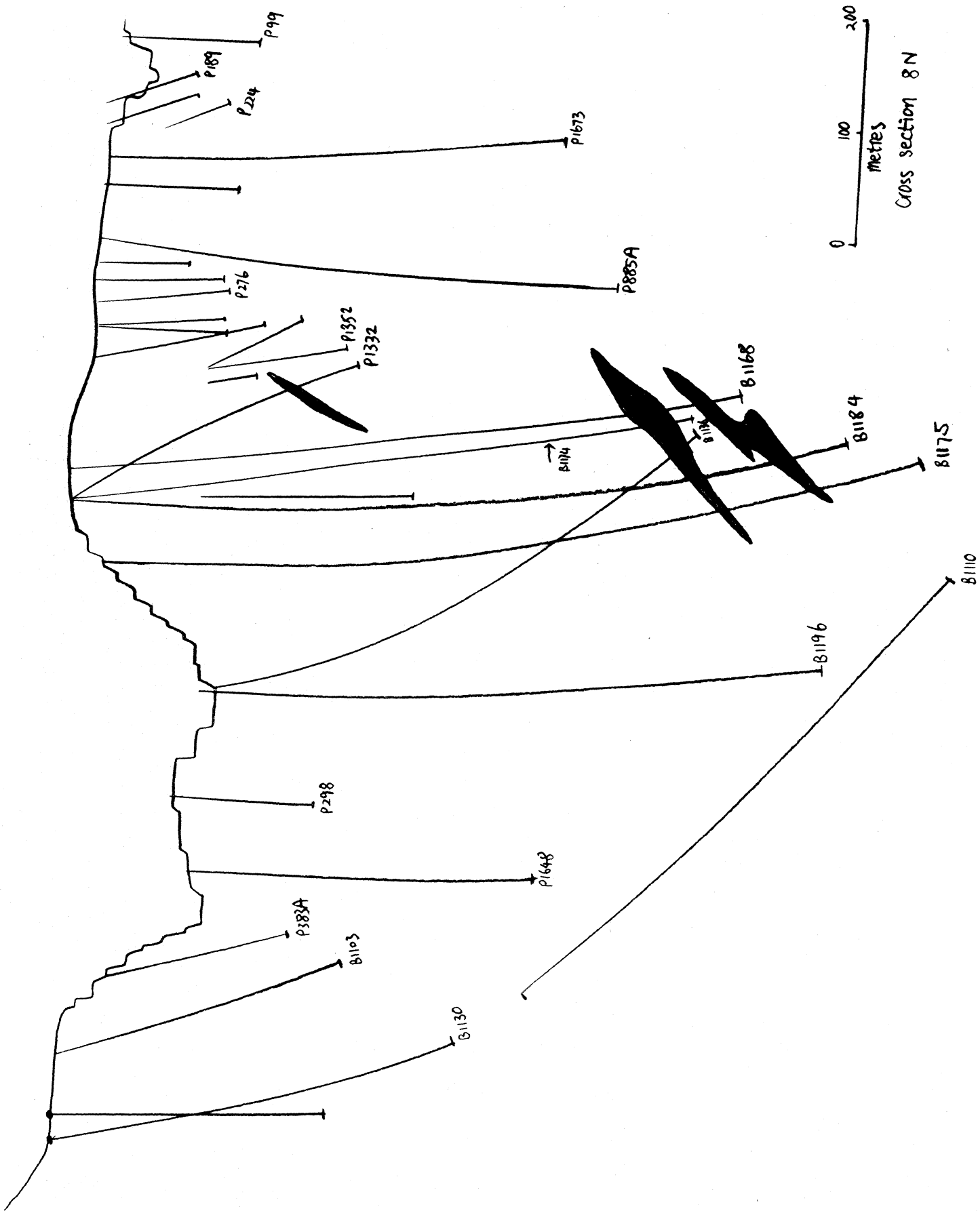


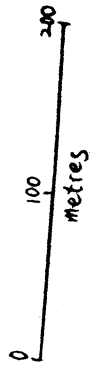
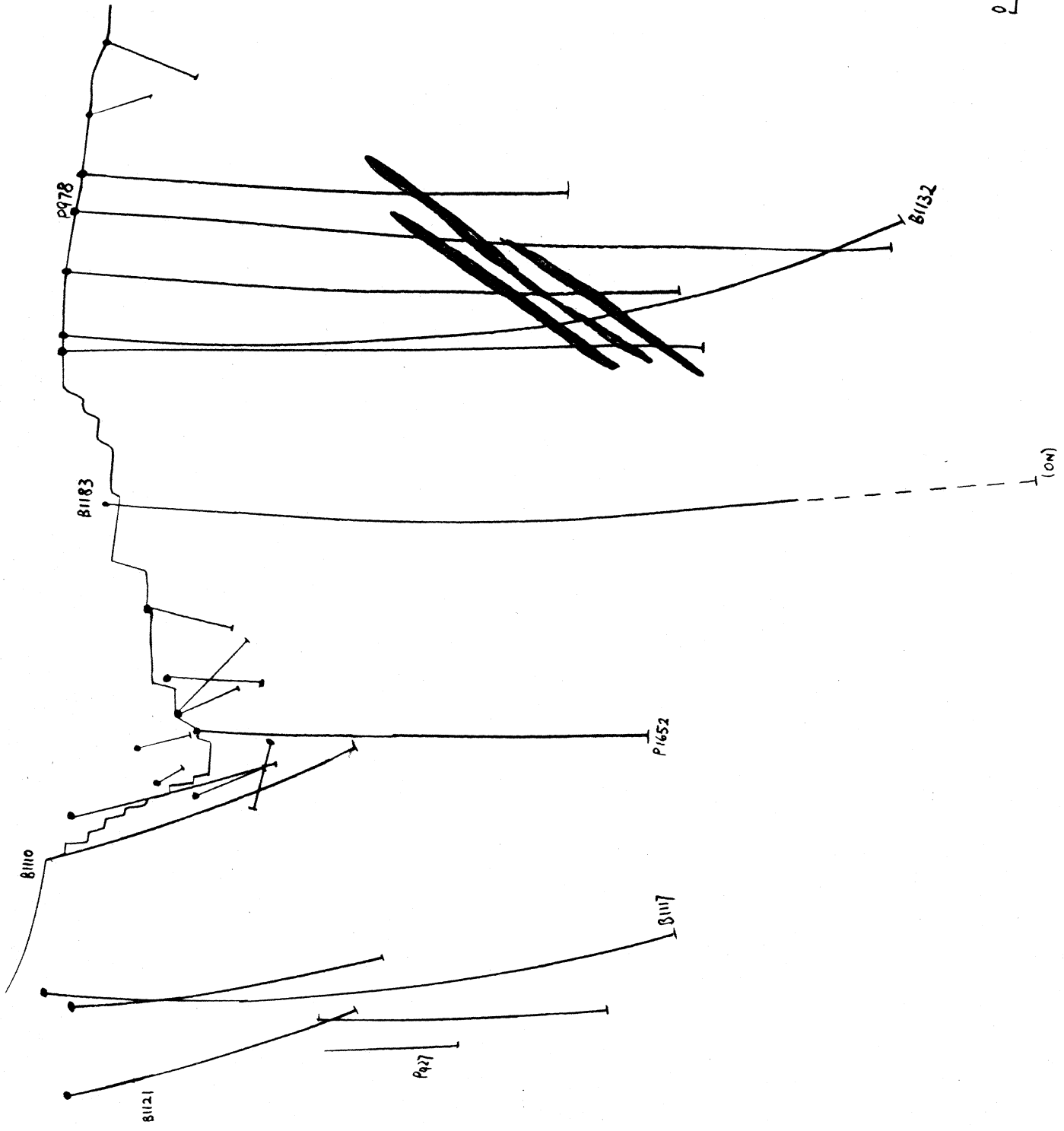
0 100 200
metres

Cross section 16N

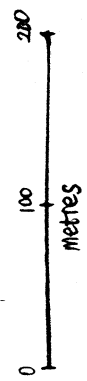
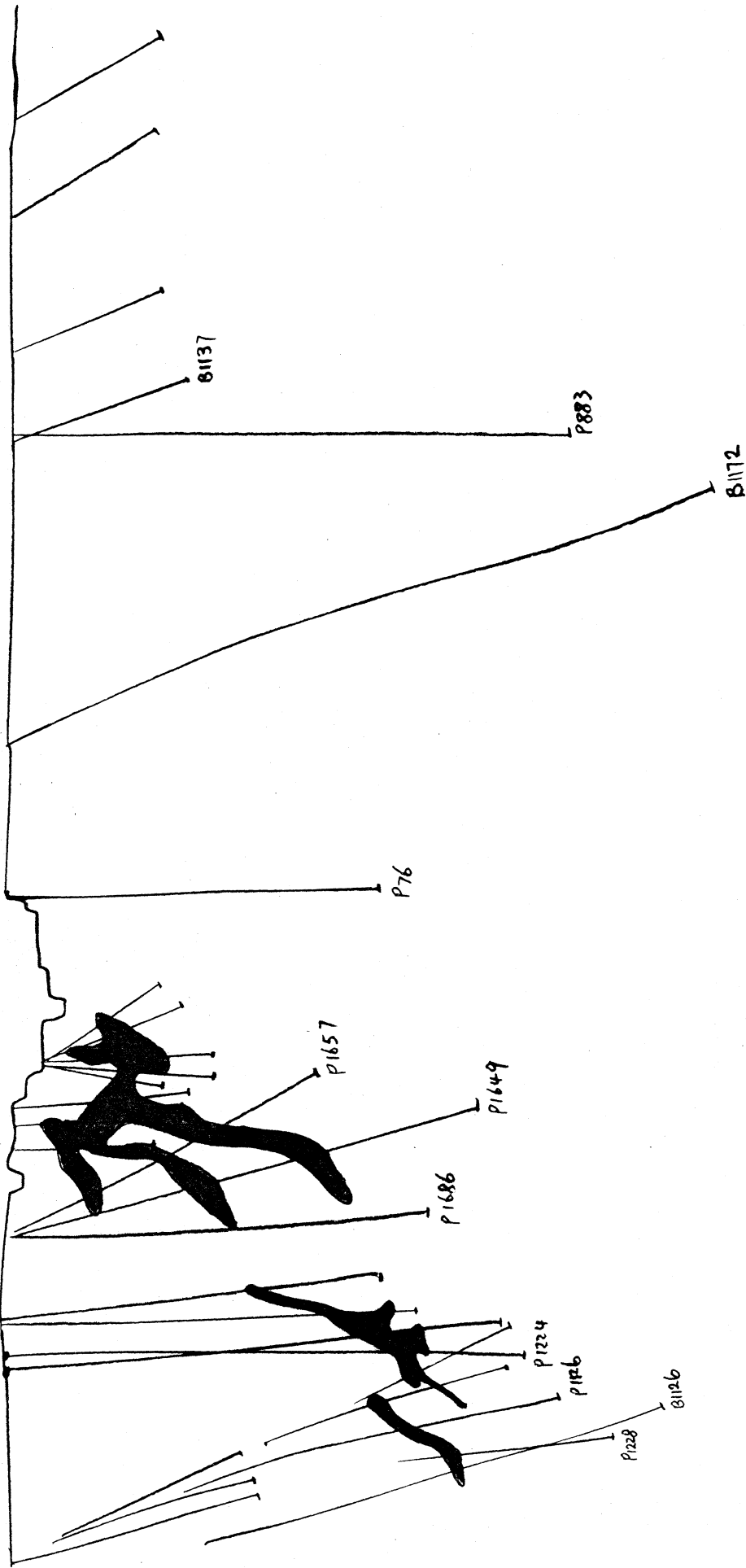


Cross section 12N

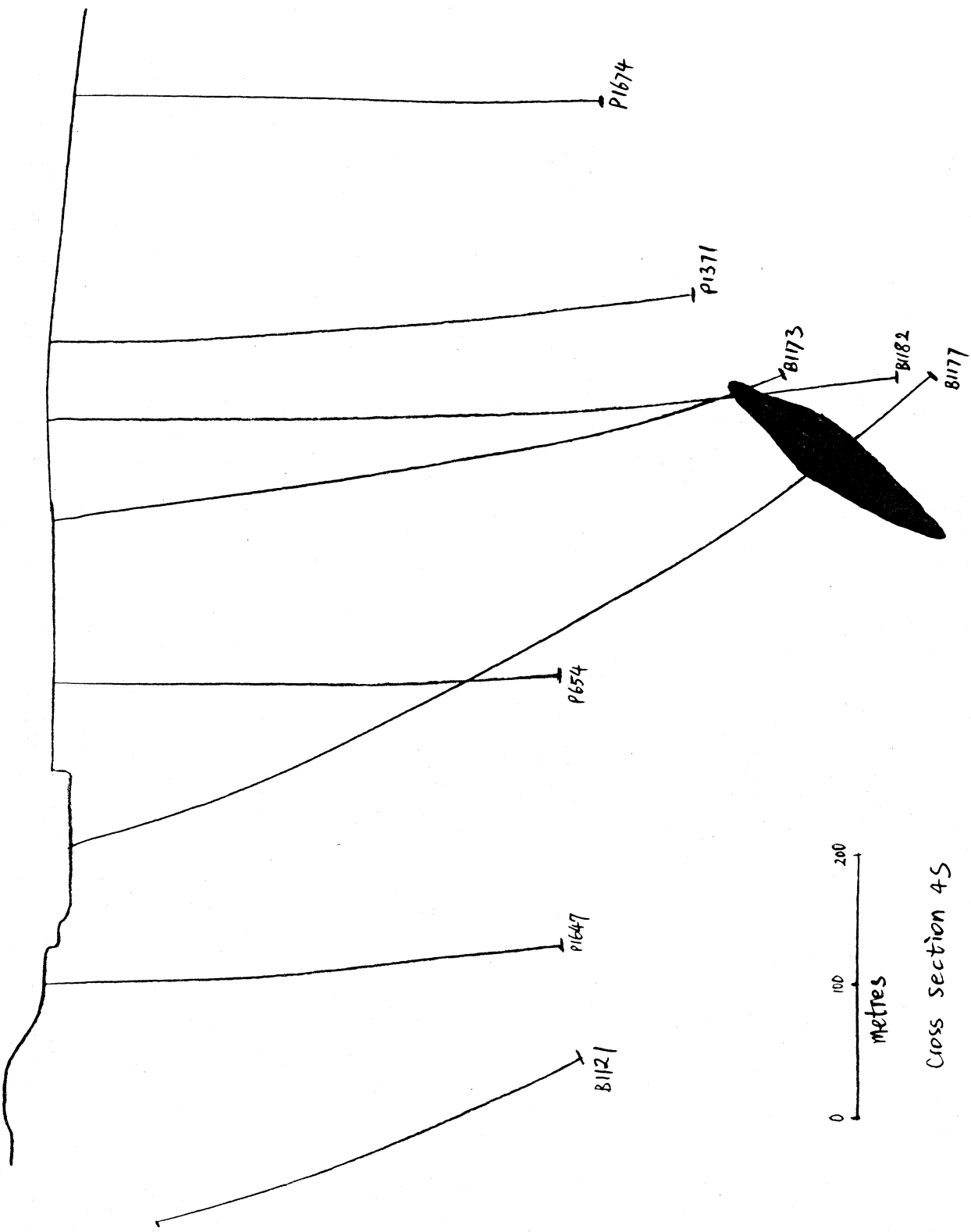




Cross section 2N

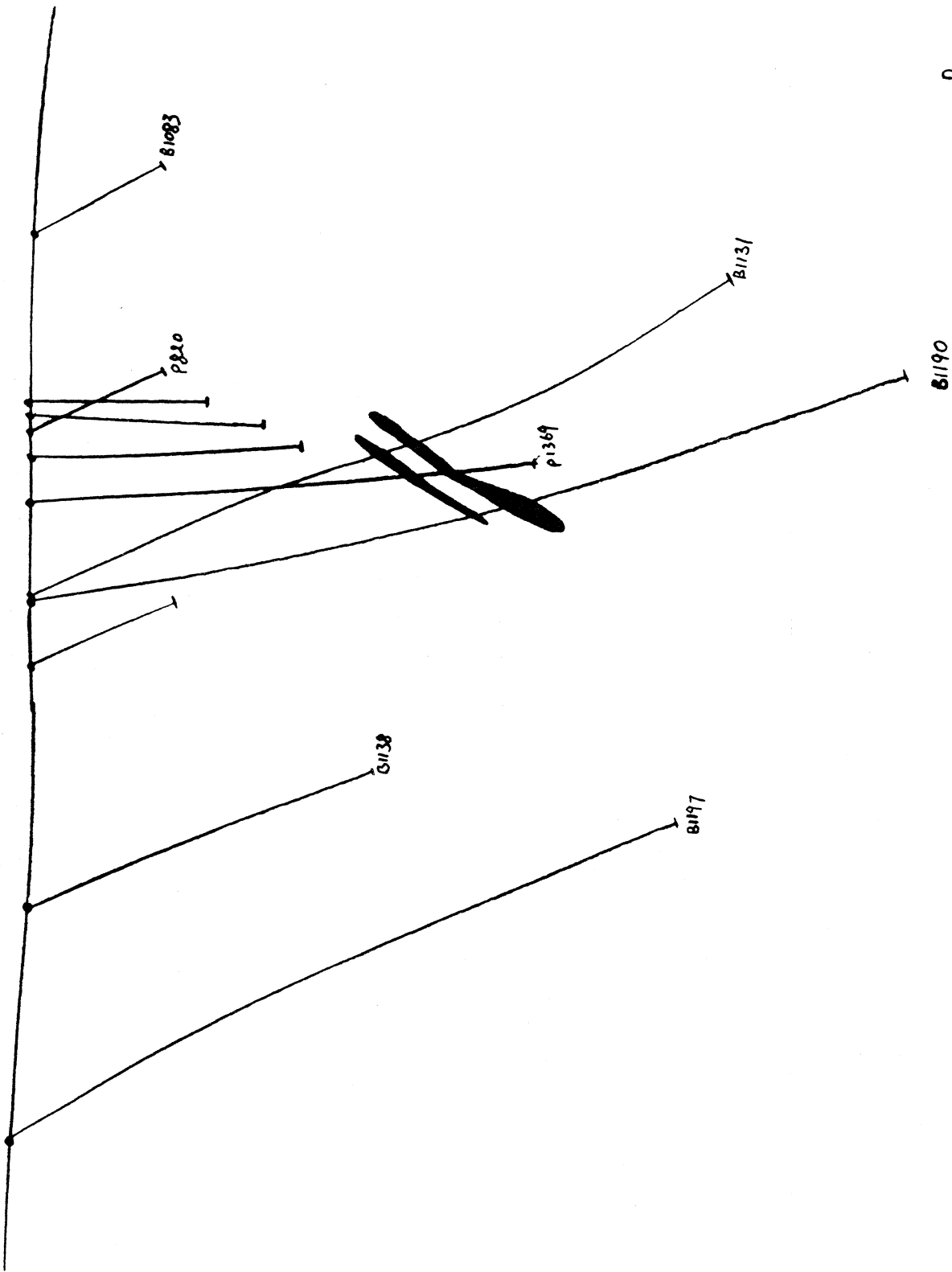


Cross section 2S

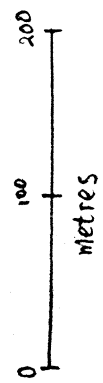
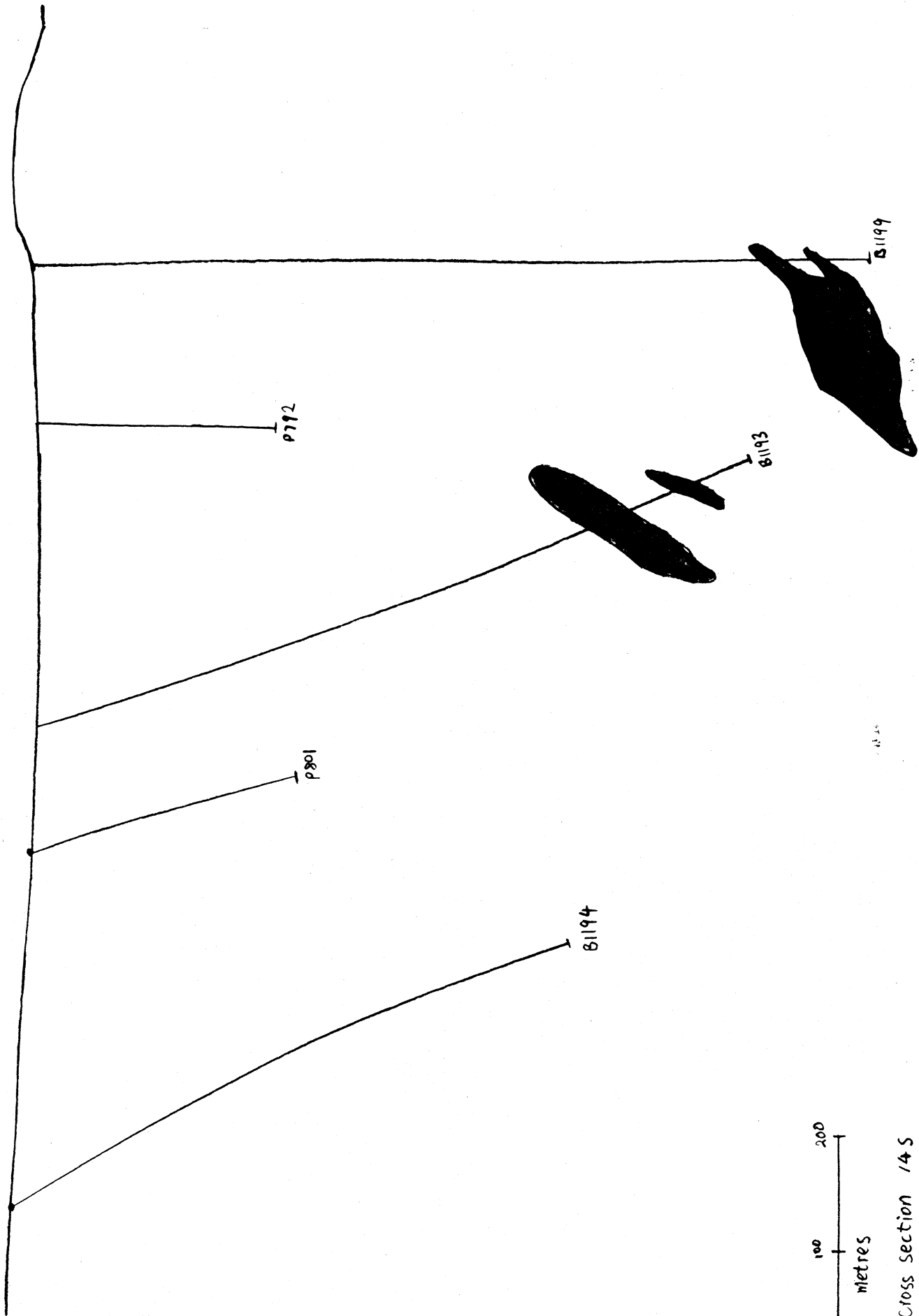


0 100 200
metres

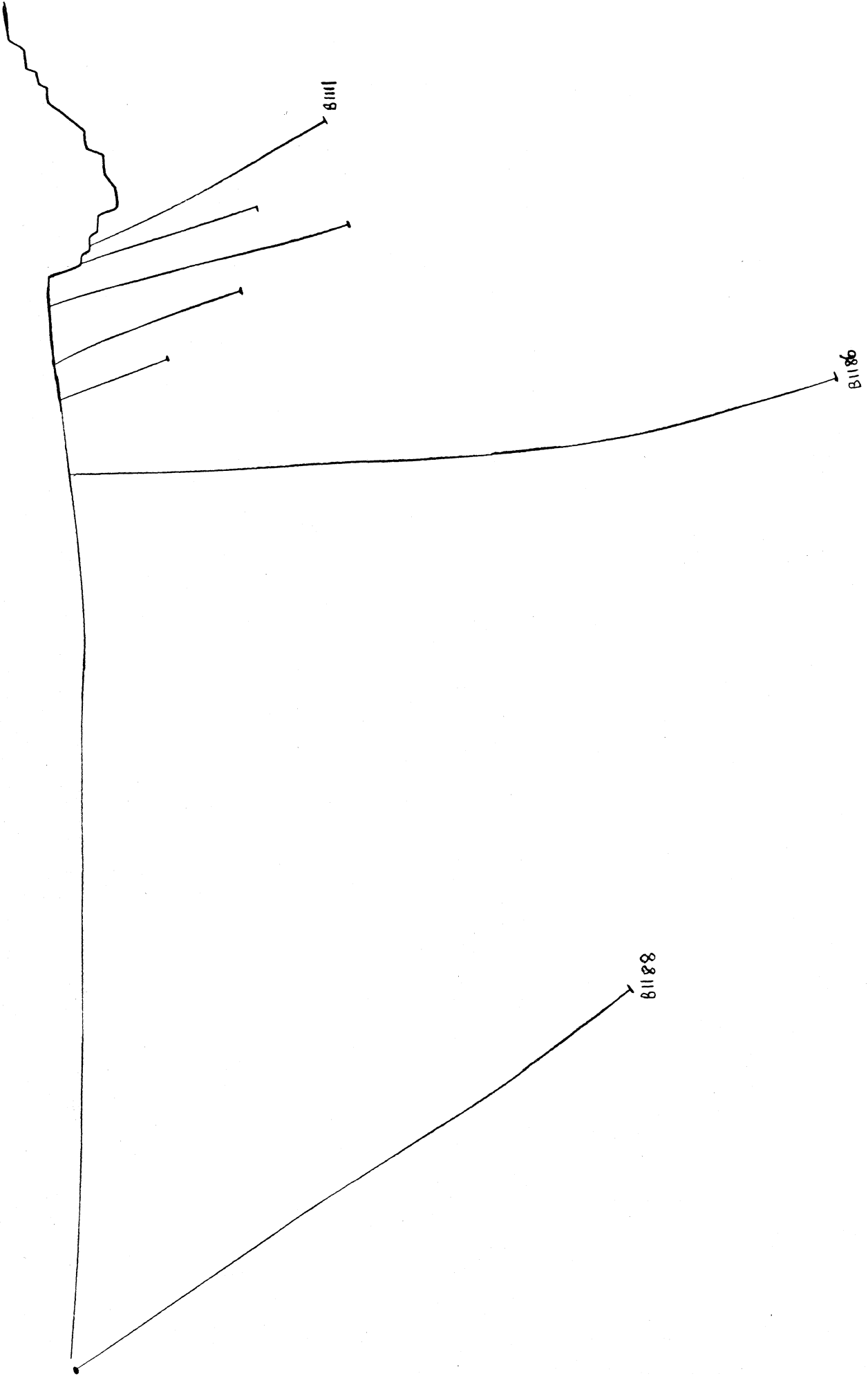
Cross section 45



0 100 200
metres
Cross section 85



Cross section 14 S



0 100 200
Metres
Cross section 245

Appendix 3 Tin Enrichment During Granitoid Differentiation and Implications

A3-1 Introduction

Although most of the world's tin production is obtained from secondary residual, elluvial, and alluvial deposits, primary tin resources, especially lode tin mineralization and low-grade disseminated ore bodies are becoming increasingly important tin producers (Taylor, 1979). Primary tin mineralization is almost always associated with granitic intrusive rocks and this spatial relationship has been recognized as reflecting a genetic relationship (Stanton, 1972). Because not all granitoids are associated with tin mineralization, to distinguish whether a granite is tin bearing or tin barren by some simple methods has become the "holy" goal of many geoscientists. The geochemical research in the last three decades by Rattigan (1960), Hesp and Rigby (1972), Flinter (1971), Sheraton and Black (1973), Olade (1980), and many others, has concluded that most of the geochemical characteristics of tin bearing and tin barren granitoids are not distinctive from regional deviations although tin bearing granites commonly have higher SiO_2 and K_2O contents (Taylor, 1979). White and Chappell (1974) classified granites into S- and I-types. Although granitoids which are associated with tin mineralization are mostly S-type, tin mineralization could occur in association with I-type granitoids (J. Walshe, *pers. comm.*, 1989). Furthermore, not all S-type granitoids are associated with tin deposits either. This suggests that geochemical characteristics alone are not sufficient to identify whether a granite is tin bearing or tin barren, and studies beyond geochemistry are necessary for further understanding.

Tin, with a crustal Clarke value of only about 2-3ppm (Hamaguchi & Kuroda, 1970), is not an abundant element in most of the geochemical environments in Earth's crust. Tin is concentrated in granitoids but the average content is only 3.5 - 3.6 ppm (Hamaguchi & Kuroda, 1970). Economic grades for hard rock tin mining varies from time to time and from country to country depending on marketing prices and labor costs. However, a grade of 0.3 to 0.6 wt% Sn is essential for large tonnage hard rock operations (Taylor, 1979). Processes to enrich tin to several hundred times its Clarke value or more are necessary for the formation of a tin deposit. Although granitoids associated with tin mineralization may be of higher tin than average, this is not enough to

change the order of the tin enrichment factor.

Tin can be enriched via both magmatic and hydrothermal processes. Taylor (1979) listed several possible tin enrichment processes: 1. fusion and incorporation of tin rich source material into silicate melt; 2. differentiation and/or diffusion in melt phase; 3. selective partitioning into immiscible fluids derived from the melt, and 4. leaching of rocks by hydrothermal fluids (Table A3-1).

Table A3-1: Possible tin enrichment processes

Processes	Comments
1) Enrichment of tin within the melt phase	
(a) Via fusion and incorporation of tin rich source material.	Via original melting or partial melting or by subsequent assimilation. Tin may be enriched homogeneously or locally enriched in magma.
(b) Via differentiation process.	Tin, etc. progressively enriched in late stage differentiates.
(c) Via diffusion.	Selective enrichment, particularly in upper regions by diffusion partitioning in melt phase.
2) Concentration of tin within fluid phases.	
a) Via selective partitioning into immiscible fluids derived from the melt, i.e. hydrothermal systems, immiscible B- rich phases etc.	Fluid release via pressure change, and/or resurgent boiling. Selective partitioning may influence the amount of tin entering to crystalline phases.
b) Via leaching of rocks (enriched in tin) by magmatically derived (or associated) fluids.	Normally associated with significant alteration of pre-existing rocks.

From Taylor (1979).

It is unlikely that a single process, either magmatic or hydrothermal, could enrich tin by several hundreds of even thousands of times. Tin deposits were probably formed by combinations of different processes one following the other. The importance of the hydrothermal process is apparent as primary tin deposits are generally all hydrothermal. The importance of the magmatic process is discussed in the following

sections.

First of all, a large amount of tin is needed to form a deposit. For example, a deposit of 10,000,000 tons of 0.5 wt% Sn ore contains 50,000 tons of tin metal. Ore bodies are usually enclosed by much larger volumes of rocks with a high tin anomaly. The large volumes of these zones mean that they also contain large amounts of tin, perhaps even more than that in the ore bodies. If a process can mobilize 0.5 ppm Sn from a source rock, a volume of close to one hundred cubic kilometers of source rock would be required to derive the necessary amount of tin. Processes which can operate on such a volume, roughly equivalent to the volume of a small pluton, are likely magmatic.

Secondly, the alteration halos around tin deposits usually contain higher than background tin. Apart from their suggestion of the importance of hydrothermal processes to the formation of tin deposits, these high tin anomalies may also indicate that instead of extracting tin from these zones, the fluid responsible for the alteration added tin to them. Therefore, the fluid must have derived its tin from elsewhere, its parental magma, for example.

Fusion and diffusion (Taylor, 1979) can enrich tin significantly. Magma formed by partial melting of tin rich materials would certainly have a tin concentration higher than magma formed by partial melting tin barren materials. But migration and convection in magma chambers would tend to homogenize all the magma before it started to consolidate. This process may produce a high tin granitoid if other processes were not involved and possibly account for the variations of tin contents in granitoids. Diffusion happens when a homogeneous melt separates into two immiscible phases and tin preferentially partitions into one phase. The order of this enrichment depends on the partitioning property of tin, and the volume ratio of the two phases.

Of all the magmatic processes, differentiation is probably the mostly important, as it has the ability to enrich tin in the melt by several orders of magnitudes.

A3-2 Dynamics of Tin Enrichment During Granite Differentiation

A3-2.1 Differentiation

A differentiation process occurs when a multicomponent, monophasic system becomes multiple phases by variation of external or internal intensive variables, such as temperature, pressure, and volatile

contents. During this process, the components that partition unevenly among the phases will be enriched in some phases and diluted in the others. Consolidation of a magma chamber may result in differentiation. As crystallization proceeds, some components are enriched in the crystallized phases and others in melt phase. Because exchange rate between solid and melt is very slow, such enrichment in melt phase can be cumulative. Late stage differentiates can be very different from the parental magma and the early consolidated rocks (Bowen and Tuttle, 1949).

Through a differentiatonal consolidation of a granitic magma chamber, the major components, like SiO_2 , Al_2O_3 , probably vary only in the order of several percent because the compositions of the major components of granitoid are usually not too far away from their eutatic compositions. But trace components, such as Sn, W, Mo, Zn, Cu, B, Pb, Th, U, H_2S , CO_2 , H_2O and HCl, can be greatly enriched in late-stage differentiates (Burnham, 1979 and Taylor, 1979).

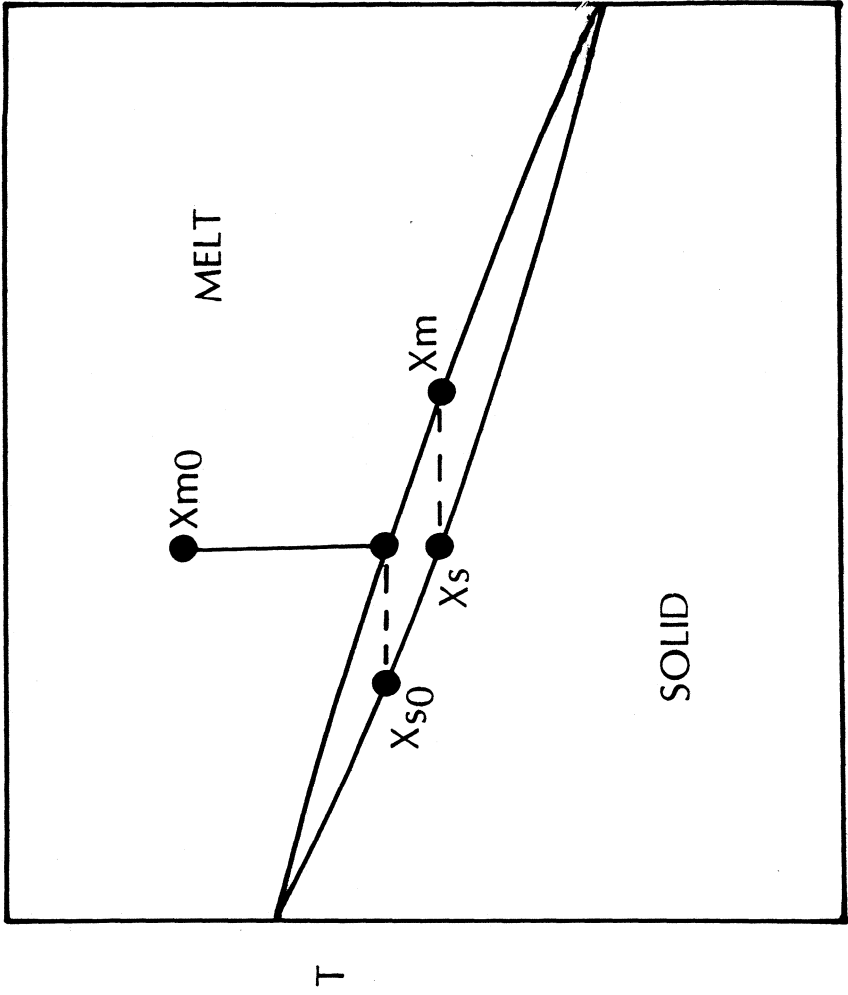
Mathematically, the order of differentiation of a component can be described by its differentiation factor: the ratio of its concentrations in solid phase and in melt phase (Allegre and Minster, 1978):

$$D_{s-m} = C^s/C^m \quad (\text{A3.1})$$

where D_{s-m} is the differentiation factor, c^s is the concentration of a component in the solid phase and c^m the concentration in the melt phase. The differentiation factor is a quantitative description of the partitioning properties of the component between the two phases. If it is unity, no differentiation occurs; if it is less than unity, the component will be enriched in the melt phase; if it greater than unity, the component will be enriched in the solid phase. The greater the difference of the differentiation factor from unity, the more significant the differentiation is likely to be. Although differentiation during consolidation in a magma chamber is very complex, the principles can be illustrated on a simple two component phase diagram (Fig. A3-1). By cooling a melt system with the composition X_m^i , at the temperature T_s , a solid phase is formed but with a composition of X_s^i which is less than X_m^i . Consequently, the formation of the solid phase results in a change in composition of the melt phase which in turn lead to a change in composition of the solid phase to form. Although complex, the melt-solid relations can be considered in terms of two extreme situations: complete solid-melt re-equilibration or no solid-melt re-equilibration. These situations can be described mathematically assuming that A: the melt phase remains homogeneous all times and B: the differentiation factors remain constant.

Firstly, consider a system which cools very slowly and re-equilibrate completely. At the temperature $T_i - dT$, the solid materials

Fig. A3-1 A diagram showing the principles of differentiation during a cooling process of a two component system. X_m^0 : composition of the initial melt; X_m : composition of the melt phase; X_s^0 : composition of the solid phase at the start of crystallization; X_s : composition of solid phase.



X

T

crystallized at temperature T_i with a composition X_i becomes unstable and react with the melt phase to form a larger mass of solid materials with a composition of X_i+dX_s in equilibrium with the melt phase of composition X_i+dX_m . Such process keeps going until the stable solid composition is identical to X_i , the original composition of the melt and by then the whole system has consolidated completely. Mathematically, at any temperature lower than T_i and higher than T_f , coexisting solid and melt phases have their compositions constrained by

$$F_m X_m + (1-F_m) X_s = X_i \quad (\text{A3.2})$$

$$D_{s-m} = X_s / X_m \quad (\text{A3.3})$$

where F_m stands for the fraction of melt phase, D_{s-m} the differentiation factor, X_s the compositions of solid phase, X_m the compositions of the melt phase, and X_i the initial compositions of the system.

At temperatures higher than the upper solvus, the system is a monomelt phase with compositions of X_m^0 . At T lower than the lower solvus, the system is a solid phase with an average composition of X_m^0 too. It is apparent that no matter what the value of the differentiation factor is, no differentiation results in such a process because of the continuous re-equilibration.

Crystallization without any re-equilibration between crystallized solid phase and remaining melt phase lead to Rayleigh fractionation (Rayleigh, 1896; Neuman *et al.*, 1954). Since there is no solid-melt exchange throughout consolidation, the initial compositions of the solid materials formed are preserved. Continued crystallization of the system results in a continual change of the compositions of the solid phase and the melt phase (Fig. A3-1). The variation in the composition of the melt phase is constrained by its original compositions, the value of the differentiation factor, and degree of crystallization

$$X_m = X_0 F_m^{D-1} \quad (\text{A3.4})$$

Equation A3.4 indicates that if D is greater than unit, X_m will be always less than X_0 and therefore the highest concentration of component X , $D_{s-m} X_0$, will be in very first solid materials consolidated. As most of the economically interesting metals in granitoids occur in very low concentrations, this enrichment process is not of significance. On the other hand, if D_{s-m} is less than unity, X_m will always be greater than X_0 . With decreasing of F_m , X_m increases very rapidly and therefore component X could be greatly enriched in the last bit of the melt phase. It

is apparent that no matter how the absolute of D_{s-m} varies, and also no matter how the initial concentration varies, the concentration of X in the final melt can become very high through a Rayleigh fractionation.

A geological process is apparently more complex than either of the two situations described. Because of the limited rate of migration the melt phase cannot be homogeneous all times. Chemical gradients commonly occur in melt phase especially in places close to the crystallization front. Differentiation factors vary if there are changes in physico-chemical conditions through the crystallization process. Nevertheless, the migration rate in solid phase is generally much slower than in melt phase. If the differentiation factors do not vary significantly, Rayleigh fractionation model can be used to describe the process.

Other differentiation models have been proposed by Holland (1972) to account for simultaneous escape of a fluid phase and by Jackson (1961), Shaw (1965), and Bartlett (1969) to account for convection in magma chamber. Comprehensive reviews of these models is given by Allegre and Minster (1978). Differentiation with a simultaneous escape of a fluid phase is clearly important at late stages when the remaining melt of a magma chamber is saturated with volatiles.

A3-2.2 Differentiation of Tin

Tin is an amphoteric element as indicated by its position in the Periodical Table. Its chemical and physical properties make it difficult to be incorporated into most of the silicate minerals in granitoids. Consequently it tends to be enriched in the melt phase in a consolidating granitoid (Bergerhoff 1970). Factors which may significantly affect the fractionation of tin are complex but generally include redox conditions, volatile (Cl, F, B, H₂O, CO₂) contents, pH (Hesp, 1973; Hesp & Rigby, 1972; Jackson & Helgeson, 1985a), and chemical composition of the melt (Taylor, 1979).

Tin can occur as Sn²⁺ or Sn⁴⁺ in magmatic conditions. Sn²⁺ is more easily enriched in volatile rich magma phase than Sn⁴⁺ because it is more difficult for Sn²⁺ to enter the rock-forming minerals than Sn⁴⁺ (Jackson and Helgeson, 1985a). At high oxidation condition, Sn⁴⁺ is the dominant state and it can be locked into silicate minerals or crystallize as trace cassiterite in granite (Taylor, 1979). This consequently reduces the amount of tin that can be enriched into the late-stage melt phase. Like all the other cations, the solubility of tin increases with acidity if other conditions are the same. High contents Cl, F, B, CO₂, and H₂O can also increase the solubility of tin as they either form complex with Sn²⁺ or provide suitable physico-chemical conditions to increase its solubility in

melt phase (Jackson & Helgeson, 1985a; Heinrich & Eadington, 1986).

Granitoids are multiple component systems. Solid phases formed during crystallization may include quartz, plagioclase, K-feldspar, biotite and muscovite and accessory minerals. The melt contains all the components and volatiles. The bulk partition factor is the statistic mean of the differentiation factors of all the minerals occurring in the solid phase

$$D_{s-m} = D_{KF}X_{KF} + D_qX_q + D_{bi}X_{bi} + \dots \quad (A3.5)$$

where D the differentiation factor for the footnoted phase and X its fraction in crystallized phase.

As discussed above, for an effective tin enrichment process to occur, the statistic mean partition factor must be less than unity. The smaller the value of the statistic mean partition factor, the more effective tin enrichment will be. The bulk partition factor varies with the tin partition factors of all the minerals in the system and the proportions of the minerals. The value of the bulk partition factor is minimized if firstly, all individual tin partition factors are at their minimum, or/and secondly, the system contains small proportions of minerals that have great values of tin partition factors. Although it is well known that the values of partition factors of minerals are functions of T, P, pH, volatile contents, and other thermodynamic parameters, their exact relationships are not well understood. However, equation A3.5 indicates that variation in mineralogy can also affect the tin enrichment process and this will be discussed in the following.

The partition factors of tin for minerals in granitoids vary widely. The main tin carrying minerals in granitoids are sphene, biotite, muscovite, and hornblende (Table A3-2). Very approximately, the partition factors for micas are in the range from 2 to 100, sphene 40 to 500, hornblende 5 to 20, albite 0.2 to 0.5, K-feldspar 0.1 to 0.3, and quartz 0 to 0.1. Other minerals in granitoids do not contain appreciable amounts of tin (Groves & McCathy, 1978; Hesp & Rigby, 1972; Durosava & Barukov, 1973; Imeokparia, 1982).

Table A3-2 lists Sn distribution in several types of igneous rocks. Column 1 (from left to right) lists the minerals; column 2 the abundance of the corresponding mineral; column 3 the concentration of Sn in that mineral; column 4 is the amount of Sn hosted in the corresponding mineral in every gram of rock; column 5 the proportion of Sn hosted in the corresponding mineral and column 6 the partition factor of Sn. It is common to see that a small amount of sphene (less than 1%) can contain more than 50% of the total Sn in the rock.

Table A3-2: Tin contents of minerals of Dzbida granitic rocks

Mineral	2 fraction (wt%)	3 Sn (ppm)	4 mineral ug/g rock	5 Proportion of Sn	6 C(min.)/ C(rock)
Quartz-diorite (Sn content 5.4ppm)					
K-feldspar	21.3	1.0	0.21	3.9	0.18
Plagioclase	49.5	2.0	0.90	18.3	0.37
Quartz	1.4	0.5	0.007	0.13	0.09
Biotite	7.6	6.0	0.46	8.5	1.1
Hornblende	13.7	7.0	0.96	17.8	1.3
Sphene	1.9	120	2.28	42.3	22.2
Others	4.6				
Total	100.0	4.97	92.1		
Granodiorite (Sn content 5.4ppm)					
K-feldspar	16.1	1.4	0.22	4.08	0.26
Plagioclase	43.8	2.3	1.00	18.5	0.42
Quartz	17.1	1.0	0.01	0.20	0.18
Biotite	9.2	5.5	0.50	9.25	1.0
Hornblende	13.1	10.0	1.31	24.30	1.8
Sphene	0.5	400	2.00	37.00	74.0
Others	0.2				
Total	100.0	5.04	93.33		
Quartz-syenite (Sn content 4.0 ppm)					
K-feldspar	29.3	1.0	0.29	7.25	0.25
Plagioclase	48.2	1.7	0.82	20.50	0.42
Quartz	13.4	0.5	0.07	1.75	0.12
Biotite	2.4	4.0	0.0	2.25	1.0
Hornblende	4.2	6.8	0.29	7.25	1.7
Sphene	0.7	310	2.17	54.30	77.5
Others	1.8				
Total	100.0	3.73	93.30		
Porphyritic Granite (Sn content 3.8ppm)					
K-feldspar	32.0	1.3	0.42	11.06	0.3
Plagioclase	35.7	1.9	0.68	17.9	0.5
Quartz	20.6	0.5	0.10	2.63	0.13
Biotite	6.7	5.0	0.34	8.95	1.3
Hornblende	3.2	10.3	0.33	8.70	2.7
Sphene	0.4	440	1.76	46.31	116
Others	1.4				
Total	100.0	3.63	95.55		
Leucocratic Granite(Sn content 3.8ppm)					
K-feldspar	34.3	1.1	0.38	9.70	0.3
Plagioclase	29.6	1.5	0.44	11.30	0.4
Quartz	32.7	0.7	0.23	6.00	0.18
Biotite	1.7	10.0	0.17	4.30	2.5
Sphene	0.5	475	2.38	61.0	122
Others	1.2				
Total	100.0	3.60	92.30		

From Bergerhoff (1970)

Table A3-3 lists data to illustrate Sn distribution in porphyritic rocks. As the groundmass in porphyritic rocks represents the quenched melt of a partially crystallized system, partition factors equal tin concentrations in crystalline phases divided by tin concentration in the melt phase, the groundmass.

Although theoretically tin can be enriched in a late-stage melt phase of a granite magma chamber as long as the bulk tin partition factor is less than 1, the complexity of geological process and the difference of real geological conditions from the ideal assumptions probably require the bulk partition factor to be significantly less than 1 for an effective tin enrichment process to occur. If we assume 0.9 is the maximum value of the D_{s-m} we can then examine the limits of mineral assemblages that may permit tin enrichment through fractionation.

Table A3-3: Tin distribution in high tin ongonite

Sample	Material	mol%	Sn ppm	proportion of tin	Partition factor
Stockwork dyke					
Okh841/14	Groundmass	53.0	90	86.7	
	pheno. albite	21.1	11.2	4.3	0.124
	KFs	16.2	7.2	2.1	0.08
	rock		50		

Amazonite dyke					
Okh 855	Groundmass	66.5	45.7	81.7	
	pheno. albite	21.4	19.0	10.9	0.416
	KFs	9.5	8.0	2.0	0.175
	Micas	0.9	966	23.4	21.14
	rock		37.2		

Okh1951	Groundmass	63.4	79	73.4	
	pheno. Albite	16.6	14	2.9	0.177
	KFs	7.1	2.7	0.2	0.034
	micas	0.3	630	2.4	7.97
	rock		79		

Okh 856	Groundmass	51.6	51	72.3	
	pheno. albite	23.6	8.9	6.2	0.175
	KFs	15.1	12.9	6.9	0.253
	micas	0.9	725	19.2	14.2
	rock		34		

From Antipin (1981)					

Tables A3-2 & A3-3 suggests that the content of sphene, although very minor in granitoids, is an important parameter controlling tin enrichment via fractionation. For example, if a granite contain 0.5% sphene, timed by a partition factor of 100 yields a contribution to the statistic mean differentiation factor of 0.5. As contributions of the major minerals of biotite, muscovite, K-feldspar, and plagioclase to the statistic mean differentiation factor are inevitable, it would easily exceed 0.9 for granitoid containing more than 0.5% sphene. In granitoids which do not contain sphene, biotite and muscovite are the minerals with highest values of tin partition factors. If we assume the minimum tin partition factor for biotite and muscovite are between 3 and 5, 15% total mica will be the upper limit for tin enrichment process to take place in a granitoid.

Feldspars are the next important minerals controlling the bulk tin partition factor. Although the proportions of total feldspars in granitoids vary, the range of such variations are relatively small. As the value of the tin partition factor of plagioclase is almost always twice as great as that of K-feldspar, tin is more effectively enriched into late stage melt in K-rich granitoids than Ca-rich granitoids. This is particularly important because the total feldspar contents in granitoids do not vary very much, and therefore Ca-poor granitoids have higher potential to enrich tin into late-stage melts than Ca-rich granitoids. Similarly, as the value of partition factor between quartz and melt is the smallest, the bulk tin partition factors is less for quartz rich granitoids and tin is enriched easily during fraction of granitoids which are high in quartz.

In summary, although we cannot draw precise conclusions whether tin could be enriched or not through fractionation consolidation of a particular granitoid of given mineralogy, it is clear that granitoids which are sphene free, low in total mica and plagioclase, high in quartz and K-feldspar, have high potential to enrich tin into its late stage differentiates.

According to Hesp (1972 & 1973), Netzel (1970), and Stempork and Skvor (1974), tin partition factors vary with tin concentration in the melt phase. Antipin (1981) suggests that tin partition factors decrease with increasing tin concentration in the melt.

These conclusions can be used to interpret the geochemical characteristics of tin bearing and tin barren granitoids. Stempork (1963, 1965) and Taylor (1979) summarized that tin bearing granitoids are higher in total SiO₂ and K₂O and lower in FeO, MgO, MnO, and CaO, which reflect the high quartz and K-feldspar, low mica and plagioclase mineralogy. Geological observations of many tin bearing granitoids also suggest that most of them are low in mica (Olade, 1980; Eadington, 1982), high in SiO₂ and peralkaline (Taylor, 1979).

A3-3 Kinetic Factors

In a cooling magma chamber, crystallization results from changes of physico-chemical conditions. Heat loss resulting in temperature depression is probably the most important control over crystallization. Heat loss occurs in a number of ways, such as conduction, volatile loss, convection and incorporation of cold materials from country rocks. Heat conduction is likely the most important mechanism of heat loss at the beginning of crystallization. If we assume that heat is only lost through conduction, the temperatures of the magma chamber and its surrounding are constrained by the following equations:

$$\partial T/\partial t = k(\partial^2 T/\partial X^2 + \partial^2 T/\partial Y^2 + \partial^2 T/\partial Z^2) + Q(t)/Cp(\text{countryrock}) \quad (\text{A3.6})$$

$$\partial T/\partial t = k(\partial^2 T/\partial X^2 + \partial^2 T/\partial Y^2 + \partial^2 T/\partial Z^2) + L/Cp \partial \Phi/\partial t + Q(t)/Cp(\text{magma}) \quad (\text{A3.7})$$

where C_p is the isobaric heat capacity and L the latent heat per unit mass (the amount of heat produced by complete crystallization of magma of unit mass), K the thermal diffusivity, $Q(t)$ the amount of heat generated by radioactive decay in unit mass, Φ the crystal content per unit volume with values from 0 to 1. It is constrained by the equation

$$\partial \rho/\partial t = 4\pi[1-\rho]Y(t) \int_0^1 I(v) \left[\int_v^1 Y(u) du \right] dv \quad (\text{A3.8})$$

where Y and I are the growth and nucleating rate functions respectively (Kirkpatrick, 1976; Brandeis et al. (1984); Brandeis and Jaupart, 1987).

Brandeis and Jaupart (1987) solved these equations in one dimension at simplified conditions. Their solution suggests that the crystallization process is controlled by the degree of under-cooling, the rate of nucleation, the rate of crystal growth, and other physical and chemical properties of the magma. Crystallization of minerals take place in a region of finite thickness called the crystallization interval, which occurs between the melt and solid phases and moves into the melt phase gradually during cooling. Crystal contents in the crystallization interval increase from 0 to 100%. The thickness of the crystallization interval is proportional to $K^{1/2} Y_m^{-3/8} I_m^{-1/8}$, of which Y and I are defined in equation A3.8. They are functions of thermal diffusivity, rate of crystal growth, rate of nucleation. Because the rates of crystal growth and nucleation all depend strongly on the degree of under-cooling, the thickness of the crystallization interval is indirectly controlled by the temperature gradient. The higher the temperature gradient, the higher the degree of under cooling and the thinner the crystallization interval.

When a magma chamber starts to crystallize, the uneven partition of

tin results in different concentrations in crystallized phases and the melt. If tin is to be enriched in a late-stage melt phase, the crystallized part must contain less tin than the magma. Therefore, the melt in the crystallization interval will contain a higher concentration of tin than the rest of the melt in the chamber. Consequently, tin starts to migrate to the rest of the melt in response to this gradient.

Because minerals growth in the crystallization interval are in equilibrium with a melt with a tin concentration higher than that of the total melt. As a result more tin will be incorporate into the crystallized phases and consequently the amount of tin that can be enriched in later stage melts is reduced. The degree of such reduction depends on the ratio of tin migration rate and crystal growth rate. The rate of tin migration is controlled by a number of factors, such as temperature, viscosity, and concentration gradient and takes a constant value at given conditions in a cooling magma chamber. Therefore, the rate ratio depends almost completely on the rate of crystal growth. If the minerals grow very slowly, tin will migrate out of the crystallization interval to be enriched in late-stage differentiates. Otherwise, tin will be incorporated into the crystallized if the mineral grow very fast, taking an extreme case when a magma is quenched, tin cannot migrate out of the crystallization interval, and it will be incorporated into consolidating phases.

K-feldspar, plagioclase, quartz and micas in granitoids do not nucleate at exactly the same temperature and the actual crystallization interval includes several crystallization fronts partially or completely overlapping one another. The speed of tin migration is probably much slower in the crystallization interval due to the partial crystallization. Tin accumulated at the final crystallization front has a much smaller chance to migrate out than that at the initial crystallization front. As a consequence, the amount of tin that can be enriched into late-stage differentiates may not include the amount expelled out by at the final crystallization front. In such cases, the effective kinetic partition factor is a statistic mean of the minerals crystallized in region close to the initial crystallization fronts. If these are the minerals with small values of tin partition factors, such as quartz and K-feldspar, tin will be better enriched in late-stage melts due to the small value of the effective partition factor. Otherwise, if biotite or muscovite nucleates at the initial crystallization front, tin will be depleted initially. Although the crystallization of feldspars and quartz inside the crystallization interval may accumulate tin but as it cannot migrate out of the crystallization interval, tin cannot be enriched into late-stage melts.

The thickness of the crystallization interval also affects tin enrichment. This is apparent as it is much easier for tin to migrate out a thin crystallization interval than a thick one. As mentioned previously the thickness of the crystallization interval depends mainly on temperature

gradient. It is thin under a high temperature gradient. Otherwise it is thick, in an extreme case if there is no temperature gradient the crystallization interval will extend throughout the whole magma chamber. When this occurs the amount of tin expelled out by crystallization cannot be effectively accumulated into a late-stage phase. The important factors in establishing a high temperature gradient include high radioactive element in the magma chamber, high thermal conductivity of country rocks and high level of emplacement. This is supported by the observations that most of the tin granitoids are with radioactive anomaly (Taylor, 1979).

A3-4 Conclusions

Tin deposits are products of consequential geological processes involving magmatic and hydrothermal events to enrich tin from background levels to economic concentrations.

Tin enrichment during granitoids crystallization are affected by many physico-chemical factors. The above discussion indicates that granitoids of the following characteristics:

1. high in quartz and K-feldspar, low in plagioclase, biotite and muscovite, and free of sphene;
 2. high in volatiles and radioactive elements;
 3. emplacement at a high level of emplacement in the crust;
 4. consolidated slowly under a high temperature gradient;
- and
5. early crystallization of quartz and K-feldspar rather than plagioclase and micas, have better chances of being associated with tin mineralization.

Appendix 4

A Geothermometer and a Geobarometer based on a Eight-Component Biotite Solid Solution Model

A4-1 Introduction

Biotite is a nonstoichiometric mineral with a wide range in chemical compositions (Baily, 1984). Ideally, the chemical formula of biotite is expressed as $KX_3Y_4O_{10}(OH)_2$: where X represents the octahedral cations, Y the tetrahedral cations, and K the interlayer potassium cation. The octahedral sites are filled by Fe^{2+} , Mg^{2+} , Mn^{2+} , Ti^{4+} , Fe^{3+} , Li^+ , Al^{3+} , and other similar ions. The tetrahedral sites are mainly occupied by aluminum and silica but ferric iron may also occur in significant proportions. The interlayer potassium can be partially substituted for by sodium and calcium. Cl^- and F^- commonly substitute into the hydroxyl site (Table A4-1). As a result of these complex substitutions, the octahedral occupancy and interlayer occupancy of natural biotite are commonly slightly less than unity. Therefore, the number of total cations in biotite is also a variable. Similarly, because the hydroxyl can be substituted for by oxygen to a certain degree at high $\log f_{O_2}$ conditions (Hewitt & Wones, 1984), the total charges of biotite also vary.

The nonstoichiometry of biotite reflects the physical and chemical conditions of its formation. If the relationship between its composition and the conditions of formation is understood, the varying composition of biotite may potentially tell us important information and thus contribute to the study of many complex hydrothermal systems.

There have been many studies on the relationships between biotite composition and conditions of formation. The experimental study by Bowen and Tuttle (1949) on talc stability and by Yoder and Eugster (1954, 1955) and Eugster and Yoder (1954a, b) on the stability of paragonite, muscovite and phlogopite were the early approaches to the problem. Eugster and Wones (1962) studied the stability of FeO rich biotite and constructed a T-P- f_{O_2} diagram. This was followed by the study of the stability of Fe-Mg mixed biotite (Wones & Eugster 1965). Rutherford (1973) studied the properties of Tschermak's substitution of peraluminous biotite. The substitution of interlayer K by Na was studied

by Garman₁ (1974). Reports about Ti substitutions in biotite are controversial (Dymek, 1983; Labotka, 1983).

Most of these studies are based on an individual substitution reaction in biotite, which limits their applications since natural biotites are of complex compositions due to combined substitutions.

Table A4-1: Important substitutions in biotite

Substitutions*	Brief Expression
Octahedral Site	
Fe = Mg	FeMg ₋₁
Al = Mg	AlMg ₋₁
Ti = Mg	TiMg ₋₁
Mn = Mg	MnMg ₋₁
Fe(3+) = Mg	Fe(3+)Mg ₋₁
Li = Mg	LiMg ₋₁
Tetrahedral Site	
Al = Si	AlSi ₋₁
Fe(3+) = Si	Fe(3+)Si ₋₁
Ge = Si	GeSi ₋₁
Hydroxyl Site	
Cl = OH	Cl(OH) ₋₁
F = OH	F(OH) ₋₁
O = OH	O(OH) ₋₁
Interlayer Site	
Na = K	NaK ₋₁
Ca = K	CaK ₋₁
Vac = K	VacK ₋₁

*Charge balance is not considered in these expressions

Leaving aside the halogens, minor elements and titanium, the nonstoichiometry of biotite can be described by a eight component system of K₂O-Na₂O-FeO-MgO-Fe₂O₃-Al₂O₃-SiO₂-H₂O. Biotite with different composition can be represented by eight thermodynamic components (Table A4-2) which define the extremes in composition. Then equilibrium within biotite among the eight components and with other minerals can be analyzed to study the thermodynamic conditions of formation of biotite. As this model considers most of the major substitution reactions, its application is not limited by any single substitution reaction and therefore it has a wide applicability. This approach to the problem is similar to the

study of chlorite (Walshe & Solomon, 1981; Walshe, 1986), which has been used to improve our understanding to many complex systems (Walshe *et al.*, 1987).

There are a total of 10 variables (eight compositional variables plus temperature and pressure) in this eight-component system but only nine of them can vary independently according to the Gibbs-Duhem equation

$$\sum n_j du_j = 0 \quad (\text{A4.1})$$

where n and u stand for the moles and chemical potential of the denoted phase in the system. If the eight components are fully described compositionally and thermodynamically, one extra chemical or physical constraint, for example, an extra solid mineral phase in equilibrium with biotite plus the Gibbs-Duhem equation, is sufficient to describe the system uniquely. However, full chemical analyses are not always available because it can only be derived from wet chemical methods, which are not only difficult but also impractical because multiple generations of biotite may occur together.

Electron microprobe methods are commonly used to determine the chemical composition of biotite, but these data are short of ferric iron and water analyses. As the result, three other phases in equilibrium with biotite are required to define the system uniquely. As commonly pressure is not important or can be estimated independently, two other phases are sufficient to describe the system together with the Gibbs-Duhem equation..

Alternatively, three additional phases in equilibrium with biotite, say K-feldspar, quartz and water with an estimated pressure also allows the condition of its formation to be solved without using the Gibbs-Duhem equation. This method is used in the following approach.

A4-2 Choice of End Members

As mentioned above, the compositional variations in the eight component system can be described by eight end members, which can be oxides or sheet silicates as long as they are not linearly correlated. Eight sheet silicate end members are used in this study (Table A4-2).

C1 is phlogopite. Phlogopite occurs in the nature. It has been studied experimentally through decomposing and synthesizing reactions by Yoder and Eugster (1954b), Crowley and Roy (1964), Luth (1967) and Wones (1967). Phlogopite is stable under a wide range of physico-chemical conditions.

Table A4-2: Eight sheet silicate end members

Component	Name	formula
C1	Phlogopite	$\text{KMg}_3\text{Si}_3\text{AlO}_{10}(\text{OH})_2$
C2	Annite	$\text{KFe}_3\text{Si}_3\text{AlO}_{10}(\text{OH})_2$
C3	Al-Eastonite	$\text{KAlMg}_2\text{Si}_2\text{Al}_2\text{O}_{10}(\text{OH})_2$
C4	Fe-Eastonite	$\text{KFe}(3+)\text{Mg}_2\text{Si}_2\text{Fe}(3+)\text{AlO}_{10}(\text{OH})_2$
C5	Muscovite	$\text{KAl}_2\text{Si}_3\text{AlO}_{10}(\text{OH})_2$
C6	KD-phlogopite	$\text{Mg}_3\text{Si}_4\text{O}_{10}(\text{OH})_2$
C7	Oxyannite	$\text{KFe}(3+)_2\text{FeSi}_3\text{AlO}_{12}$
C8	Paragonite	$\text{NaAl}_2\text{Si}_3\text{AlO}_{10}(\text{OH})_2$

C2 is annite. Annite was firstly experimentally studied by Eugster and Wones (1962) under solid-oxygen buffers. Rutherford (1969) redetermined the data and this was followed by Hewitt (1977) and Hewitt and Wones (1981). On the basis of the experimental studies and analytical results of natural biotite it has been concluded that pure annite is not stable. This was interpreted by Hazen and Wones (1972) as a structural constraint because the pure Fe(2+) octahedral sheet is too large to be bonded by the tetrahedral sheets. They predicted that the most reduced annite would still contain about 12% ferric octahedral iron which is a structural requirement. This had been confirmed by recent experimental studies (Partin *et al.*, 1983; Partin, 1984) which have found 11% ferric iron in annite formed at a f_{H_2} of 25 bars. Experimental data suggest that the smaller octahedral and larger tetrahedral sheets in siderophyllite do not require ferric iron to be present to fit the structure. Biotite with 10% Tschermak's component or 24% phlogopite component do not require the presence of ferric iron to fit structure either. Therefore their Fe^{3+} contents depend on oxidation state of formation (Hewitt & Wones, 1984).

C3 is Al-eastonite. It is an idealized extrapolation of the product of the Mg-Tschermak's substitution, $\text{Al}_2\text{Mg}_{-1}\text{Si}_{-1}$, of phlogopite. Hewitt and Wones (1984) found that the maximum of Al substitution along the boundary of phlogopite and aluminous eastonite occurred at the tetrahedral composition of $\text{Si}_{2.25}\text{Al}_{1.75}$ and octahedral composition of $(\text{Mg,Fe})_{2.25}\text{Al}_{0.75}$. This is significantly lower than the reported values by Crowley and Roy (1964). The limit of this Mg-Tschermak's substitution is controlled by the following reasons:

- 1: the Mg-Tschermak's substitution which causes α -rotation of tetrahedral sheet and

2: the large size of the interlayer K^+ limits the degree of such rotation and consequently limits the substitution.

The successful synthesis of a pure sodium aluminous eastonite (Hewitt & Wones, 1984) supported this argument.

C4 is an idealized extrapolation of the product of ferric iron substitution for Al, $Fe^{3+}Al_{-1}$, in octahedral and tetrahedral sheets of Al-eastonite. This is a hypothetical end member introduced in this study.

C5 is muscovite. Although muscovite is quite well studied, the mixing properties of biotite and muscovite have not been fully understood. Toraya *et al.* (1976) reported micas having octahedral occupancies close to 2.5 indicating the possible existence of micas with compositions between muscovite and biotite. This suggests that biotite-muscovite mixing, though probably not ideal, occurs in a wide range. A review of published natural biotite analyses in this study indicates that the octahedral site occupancy of biotite is always less than unity. A muscovite end member is necessary to describe such vacancies.

C6 is introduced to represent the substitutions which produce vacancies in the interlayer site. As with the octahedral site occupancy, interlayer site occupancy of natural biotite is also less than unity (Bailey, 1984).

C7 is a hypothetical endmember to represent the substitution $Fe^{3+}Fe^{2+}_{-1}H^{+}_{-1}$ or $Fe^{3+}O^{2-}Fe^{2+}_{-1}OH^{-}_{-1}$. This substitution increases the total charges of biotite. Levillain (1980) reviewed all published biotite compositions and found that the average of total numbers of hydroxyl, Cl and are always less than 4 in a structural unit, indicating common presences of C7.

C8 is paragonite. It represents the substitution NaK_{-1} . The properties of paragonite have been studied experimentally by Eugster and Yoder (1954a, b), Sand *et al.* (1957), Chatterjee (1970), Holland (1979) and others. Paragonite is usually a small component in biotite as the sodium content of biotite is generally low.

A4-3 Standard States and Activity-Composition Relationship

The conventional standard states for rock forming minerals are used for all the end members, i.e., a pure end member has unit activity at any temperature and pressure. The chemical potentials of each end member is;

$$u_{i,T,P} = u_{i,T,P}^0 + RT \ln a_i \quad (\text{A4.2})$$

where u is the chemical potential of the i 'th component at footnoted temperature (T) and pressure (P), a is the activity of footnoted component; u^0 its chemical potential at standard state and R the gas constant. The activity of each end member is a function of composition only and independent of temperature and pressure.

$$[d a_i / d T]_{x_i} = [d a_i / d P]_{x_i} = 0 \quad (\text{A4.3})$$

The random site mixing activity is used in this study for all the biotite end members. It assumes that cations in the equal energetic sites are randomly mixed (Price, 1985; Walshe, 1986). The activity of each end member in relation to composition are expressed in Table A4-3.

A4-4 Calculation of Ferric Iron and Water Contents and Temperature of Formation

The structural formula, temperature and oxygen fugacity of formation can be calculated utilizing probe analysis data of biotite formed in equilibria with K-feldspar, quartz, and fluid.

The eight chemical and structural constraints are:

$$X_K^{II} = \alpha W_{K_2O} / M_{K_2O} \quad (\text{A4.4})$$

$$X_{Na}^{II} = \alpha W_{Na_2O} / M_{Na_2O} \quad (\text{A4.5})$$

$$3X_{Fe(2+)}^O + 2X_{Fe(3+)}^T + 3X_{Fe(3+)}^O = \alpha W_{FeO} / M_{FeO} \quad (\text{A4.6})$$

$$3X_{Mg}^O = \alpha W_{MgO} / M_{MgO} \quad (\text{A4.7})$$

$$2X_{Al}^T + 3X_{Al}^O = \alpha W_{Al_2O_3} / M_{Al_2O_3} \quad (\text{A4.8})$$

$$2X_{Si}^{T+2} = \alpha W_{SiO_2} / M_{SiO_2} \quad (\text{A4.9})$$

$$X_{Si}^T + X_{Al}^T + X_{Fe(3+)}^T = 1.0 \quad (\text{A4.10})$$

$$\alpha = \frac{24 - X_{OH}}{\sum X_i W_i / M_i + 3X_{Fe(3+)}^O + 2X_{Fe(3+)}^T} \quad (\text{A4.11})$$

where W the weight percent of the footnoted component from microprobe analyses, M the mole weight of the footnoted species, X the site (supernote) fraction of footnoted species, and χ the charge number of footnoted cation.

Table A4.3: Composition-activity* relationship used in this study

C1	$a_1 = \alpha_1 X_K^{IL} [X_{Mg}^O]^3 X_{Al}^T X_{Si}^T [X_{OH}^H]^2$
C2	$a_2 = \alpha_2 X_K^{IL} [X_{Fe}^O]^3 X_{Al}^T X_{Si}^T [X_{OH}^H]^2$
C3	$a_3 = \alpha_3 X_K^{IL} [X_{Mg}^O]^2 X_{Al}^O [X_{Al}^T]^2 [X_{OH}^H]^2$
C4	$a_4 = \alpha_4 X_K^{IL} [X_{Mg}^O]^2 X_{Fe(3+)}^O X_{Fe(3+)}^T X_{Al}^T [X_{OH}^H]^2$
C5	$a_5 = \alpha_5 X_K^{IL} [X_{Al}^O]^2 X_{Vac}^O X_{Si}^T X_{Al}^T [X_{OH}^H]^2$
C6	$a_6 = \alpha_6 X_{Vac}^{IL} [X_{Mg}^O]^3 [X_{Si}^T]^2 [X_{OH}^H]^2$
C7	$a_7 = \alpha_7 X_K^{IL} [X_{Fe(3+)}^O]^2 X_{Fe}^O X_{Al}^T X_{Si}^T [2 - X_{OH}^H]^2$
C8	$a_8 = \alpha_8 X_{Na}^{IL} [X_{Al}^O]^2 X_{Vac}^O X_{Al}^T X_{Si}^T [X_{OH}^H]^2$

X stands for the site fraction; IL stands for interlayer; O for Octahedral; T for tetrahedral and H for hydroxyl sites. α_1 to α_8 are stoichiometric constants and

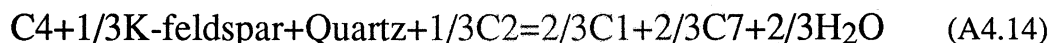
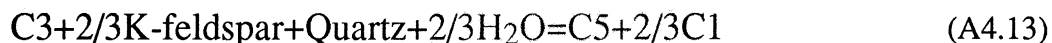
$$\alpha_1 = \alpha_2 = 4$$

$$\alpha_3 = \alpha_4 = 27/4$$

$$\alpha_5 = \alpha_7 = \alpha_8 = 27$$

$$\alpha_6 = 1$$

For the biotite formed in equilibrium with quartz, K-feldspar and water there are three thermodynamic equilibria:



These equilibria provide three thermodynamic constraints as follows:

$$\log K_{A4.12} = \log a_6 - \log a_1 \quad (\text{A4.15})$$

$$\log K_{A4.13} = \log a_5 - 2/3 \log a_1 - \log a_3 \quad (\text{A4.16})$$

$$\log K_{A4.14} = 2/3 \log a_1 + 2/3 \log a_7 - 1/3 \log a_2 - \log a_4 \quad (\text{A4.17})$$

Where a_i represents the activity and K the thermodynamic equilibrium constant. The values of K are functions of temperature and pressure. Equations A4.4 to A4.11 and A4.15 to A4.17 provide eleven constraints for the eleven variables, $X_{K^{IL}}$, $X_{Na^{IL}}$, $X_{Fe(2+)^O}$, X_{Mg^O} , $X_{Fe(3+)^O}$, $X_{Fe(3+)^T}$, X_{Al^O} , X_{Al^T} , X_{Si^T} , X_{OH^H} and T can be resolved if pressure is assumed or known. Then the water and ferric iron contents can be converted from site fractions to weight percent using

$$W_{H_2O} = \frac{M_{H_2O} * X_{OH^H}}{M_{total}} \quad (A4.18)$$

and

$$W_{Fe_2O_3} = \frac{M_{Fe_2O_3} * (2X_{Fe(3+)^T} + 3X_{Fe(3+)^O})}{M_{total}} \quad (A4.19)$$

where W stands for the weight percent, M the mole weight and M_{total} the mole weight of biotite with the calculated formula.

A4-5 Calculating $\log f_{O_2}$ and Cation/Proton Activity Ratios

Oxidation conditions of biotite formation can be calculated through the following equilibrium,



which gives

$$\log K_{20} = -1/2 \log f_{O_2} + \log a_7 - \log a_2 \quad (A4.21)$$

in which $\log K_{20}$, a_7 and a_2 are all known and therefore $\log f_{O_2}$ is defined.

Given T , $\log f_{O_2}$, and the calculated activities of each endmember, cation/proton activity ratios in the fluid can be calculated from hydrolysis reactions for each of the endmembers. A Fortran-77 program has been written to perform all the calculations.

A4-6 Source of Thermodynamic Data and Estimations

Thermodynamic properties for K-feldspar, quartz, water, phlogopite, annite, muscovite, and paragonite are taken from Helgeson *et*

al. (1978) and Helgeson (1978). The thermodynamic properties for C7 are estimated by assuming ideal mixing between annite and the oxyannite of Beane (1974). The estimations of the thermodynamic properties of reaction A4.12, endmember C3 and C4 are documented in the following.

A4-6.1 Thermodynamic Equilibria in the Salton Sea Geothermal Biotite and the Thermodynamic Properties of Reaction A4.12

McDowell and Elders (1980) investigated the mineralogy and mineral chemistry variations in the Salton Sea geothermal system, particularly the compositions of the hydrothermal sheet silicates. Their study revealed several regular compositional variations with temperature of formation.

According to their report, the biotite samples analyzed contained varying small proportions of vermiculite, with a composition of $\text{Ca}_{0.25}[\text{Mg}_{1.80}\text{Fe}^{3+}_{0.88}\text{Fe}_{0.14}][\text{Si}_{2.97}\text{Al}_{1.03}\text{O}_{10}](\text{OH})_2$. This was used to calculate pure biotite composition from their analyses by projecting their analysis data to the Ca free environment. The re-calculated formula (Table A4-4) are used to calculate $\log K_{12}$ using

$$\log K_{12} = \log [\alpha_6 * X_{\text{Si}}^{\text{T}} * X_{\text{vac}}^{\text{IL}}] / [\alpha_1 * X_{\text{Al}}^{\text{T}} * X_{\text{K}}^{\text{IL}}] \quad (\text{A4.22})$$

where α stands for the stoichiometric constants (Table A4-3).

The plot of the calculated values of $\log K_{\text{A4.12}}$ against $10000/T$ (Fig. A4-1) indicates a linear correlation for samples 1, 2, 3, 5 and 8. They yield an regression equation of

$$\log K_{\text{A4.12}} = 7099/T - 12.56 \quad (\text{A4.23})$$

Sample 4 and 6 are above the correlation line which due probably to quartz contamination as they are from single analyses of fine grained samples and sample 7 falls below the line probably due to changed assemblage (McDowell and Elders, 1980). The slope and intersection of the regression line of sample 1, 2, 3, 5 and 8 are related to ΔH_r and ΔS_r of reaction A4.12 through equation

$$\Delta G_r = \Delta H_r - T\Delta S_r \quad (\text{A4.24})$$

Equation A4.23 is used to calculate $\log K_{\text{A4.12}}$ at given temperature.

Table A4-4: Corrected structural formula of the Salton Sea geothermal biotite and calculated values of $\log K_{A4.12}$

Sample	1	2	3	4	5	6	7	8
T(°C)	330	335	338	348	353	357	361	360
Si	3.25	3.154	3.129	3.126	2.984	3.067	2.934	2.926
Al(T)	0.75	0.846	0.871	0.874	1.016	0.933	1.066	1.074
Al	0.03	0.015	0.002	0.069	0.045	0.054	0.020	0.093
Ti	0.01	0.004	0.007	0.008	0.015	0.032	0.019	0.019
Fe(t)	0.56	0.562	0.778	0.634	0.891	0.826	1.090	1.371
Zn	0.0	0.0	0.0	0.0	0.005	0.0	0.005	0.005
Mn	0.02	0.006	0.008	0.000	0.003	0.000	0.006	0.006
Mg	2.38	2.407	2.204	2.287	2.040	2.088	1.860	1.542
K	0.72	0.73	0.75	0.74	0.79	0.77	0.83	0.87
Na	0.00	0.022	0.016	0.034	0.013	0.008	0.004	0.015
$\log K_{12}$	-0.790	-0.870	-0.967	-0.946	-1.191	-1.069	-1.491	-1.348

* For original data see McDowell and Elders (1980)

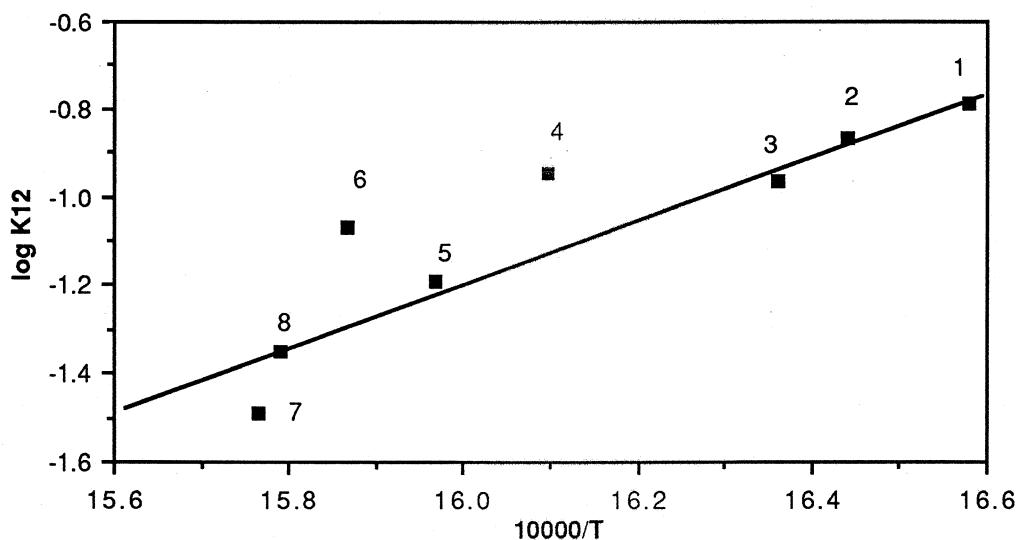


Fig. A4-1 Plot of $\log K_{12}$ vs $10000/T$ of the Salton Sea geothermal biotite. The numbers correspond to sample in Table A4-4

A4-6.2 Thermodynamic Properties of Mg-Tschermak's Substitutions and Estimations of the Thermodynamic Properties of C3

C3 is related to C1 through a Mg-Tschermak's substitution reaction. To estimate its thermodynamic properties, a study of the thermodynamic properties of a number of Mg-Tschermak's substitution reactions between minerals whose thermodynamic properties are known has been carried out. Table A4-5 is a list of thermodynamic properties of several Mg-Tschermak's substitution reactions between ring-, band-, chain- and sheet-structured silicates.

Table A4-5: A list of Mg-Tschermak's Substitution Reactions

$\text{MgSi} + \text{Al}_2\text{O}_3 = \text{MgO} + \text{SiO}_2 + \text{Al}^{\text{OAl}}\text{T}$	(A4.25)*
$\text{MgSiO}_3 + \text{Al}_2\text{O}_3 = \text{MgO} + \text{SiO}_2 + \text{Al}_2\text{O}_3$	(A4.26)
$\text{Mg}_2\text{SiO}_4 + \text{Al}_2\text{O}_3 = \text{MgO} + \text{SiO}_2 + \text{MgAl}_2\text{O}_4$	(A4.27)
$\text{CaMgSiO}_4 + \text{Al}_2\text{O}_3 = \text{MgO} + \text{SiO}_2 + \text{Ca}[\text{AlO}_2]_2$	(A4.28)
$\text{CaMgSi}_2\text{O}_3 + \text{Al}_2\text{O}_3 = \text{MgO} + \text{SiO}_2 + \text{CaAl}_2\text{SiO}_6$	(A4.29)
$\text{Ca}_2\text{MgSi}_2\text{O}_7 + \text{Al}_2\text{O}_3 = \text{MgO} + \text{SiO}_2 + \text{Ca}_2\text{Al}_2\text{SiO}_7$	(A4.30)
$\text{Mg}_6\text{Si}_4\text{O}_{10}(\text{OH})_8 + \text{Al}_2\text{O}_3 = \text{Mg}_5\text{Al}_2\text{Si}_3\text{O}_{10}(\text{OH})_8 + \text{MgO} + \text{SiO}_2$	(A4.31)

*Reaction A4.25 is an extrapolation of Mg-Tschermak's substitution in metals, standard state ΔH° and ΔG° values for MgSi and $\text{Al}^{\text{OAl}}\text{T}$ are assumed to be zero. Substitution 26, 27 and 28 strictly are not Mg-Tschermak's substitutions as the reactant and product silicates are of different structures.

In general, Mg-Tschermak's substitution can be expressed by



in which S_r and S_p stand for reactant and product silicates (see Table A4-5 for examples). Strictly speaking, S_p and S_r must have same structure. The substitution involves two Al cations to substitute one tetrahedrally coordinated Si and one octahedrally coordinated Mg.

The ΔG_r and ΔH_r of the Mg-Tschermak's substitution reactions (Table A4-6) listed in Table A4-5 vary with the structure of the silicates. To describe these variations quantitatively, a term excess structural oxygen is introduced.

Excess Structural Oxygen (ESO) is defined as the equivalent number of oxygens not bonded with tetrahedrally coordinated Si or its substitute. It is equivalent in value to the number of oxygens bonded with

nontetrahedrally coordinated metal atoms in silicates. Mathematically, the number of ESO in a aluminosilicate can be calculated using

$$N_{\text{ESO}} = N_{\text{O}} - 2N_{\text{Si}^{\text{T}}} - 1.5N_{\text{Al}^{\text{T}}} - 0.5N_{\text{OH}} \quad (\text{A4.33})$$

in which N is the number of footnoted species, supernote T stands for tetrahedral sites. Table A4.6 lists the thermodynamic properties of the Mg-Tschermak's substitution reactions listed in Table A4-5 and the ESO values of their products.

Table A4-6: Thermodynamic properties of Mg-Tschermak's substitution reactions listed in Table A4-5

Reaction	product	ESO	ΔG_r°	ΔH_r°	$\Delta C_{p,r}^\circ$	ΔS_r
25	$\text{Al}^{\text{O}}\text{Al}^{\text{T}}$	-1.5	142.71	149.44		
26	Corundum	3	34.30	34.55	3.16	0.5
27	Spinel	4	36.19	37.11	1.08	2.76
28	Ca-allu.*	1	82.91	89.19	0.73	20.87
29	Pyroxene	2.5	66.13	72.39	11.25	20.67
30	Gehlenite	3.5	43.12	45.98	-3.33	9.24
31	Clinoclore	6.5	-13.86	-27.11	4.28	-44.72

* Ca-Aluminate

Plots of ΔG_r and ΔH_r vs ESO of substitution products (Figs. 2 & 3) clearly show that the ΔH_r and ΔG_r of Mg-Tschermak's substitution reactions are strongly correlated to the ESO values of the substitution product.

The two regression lines yielded empirical equations of

$$\Delta G_r = -19.10 \text{ ESO} + 110.46 \text{ (KJ)} \quad (\text{A4.34})$$

and

$$\Delta H_r = -21.09 \text{ ESO} + 117.40 \text{ (KJ)} \quad (\text{A4.35})$$

for Mg-Tschermak's substitution reactions at standard state. The combination of Equations A4.34 & A4.35 indicated that

$$\Delta S_r = -2.45 \text{ ESO} + 18.73 \text{ (J/k)} \quad (\text{A4.36})$$

at standard state for Mg-Tschermak's substitution reactions.

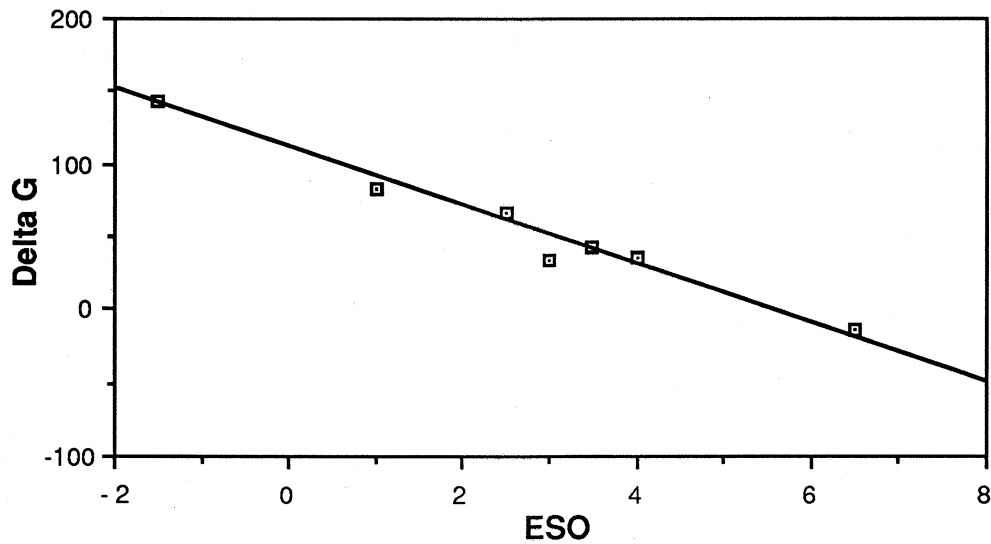


Fig. A4-2 Plot of ΔG_r (in KJ) for Mg-Tschermak's substitution reaction listed in table A4.5 vs ESO values of the substitution products

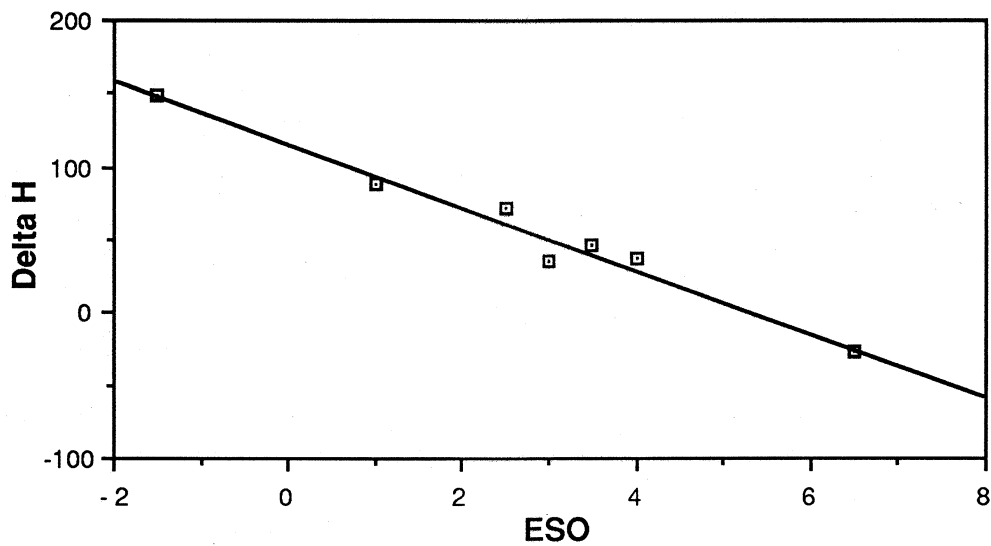


Fig. A4-3 Plot of ΔH_r (in KJ) for Mg-Tschermak's substitution reactions listed in table A4.5 vs ESO values of the substitution products

The thermodynamic properties of Al-eastonite can be estimated using those empirical relations through the following substitution reaction



The ESO value for C3 is 4, which was substituted into Equations A4.34, A4.35 and A4.36 to calculate the ΔH , ΔG , and ΔS of substitution reaction 37. As the thermodynamic properties of C1, Al_2O_3 , SiO_2 and

MgO are known (Helgeson, 1978), the thermodynamic properties of C3 can be calculated.

Table A4-6 also indicates that the ΔC_p of Mg-Tschermak's substitution reactions are all very close to zero. Therefore the heat capacity of C3 can also be calculated from heat capacities of C1, SiO₂, Al₂O₃ and MgO with an assumption that the ΔC_p for reaction A4.37 is zero. The estimated thermodynamic properties for C3 are listed in Table A4-7.

Table A4-7: Estimated Thermodynamic Data of C3, C4 and C7

Component	ΔH° (J)	ΔS° (J/K)	$C_p = a + b \times 10^{-3} T + c \times 10^5 / T^2$		
			a	b	c (J/K)
C3	-6315979	308.8	444.4	90.21	-107.1
C4	-5485029	345.2	427.7	156.0	-86.96
C7	-4959158	336.8	391.2	178.2	-105.0

A4-6.3 Estimating the Thermodynamic Properties of C4

The procedure used to estimate the thermodynamic properties of C4 is very approximate. It assumes that the ΔH_r , ΔS_r and ΔC_p of reaction



all equal to zero in value. Then the standard enthalpy, entropy and heat capacity of C4 were calculated from those of C3, Fe₂O₃ and Al₂O₃. Table A4-7 lists the estimated thermodynamic properties for C6, C3 and C4.

A4-7 Summary

A eight-component biotite solid solution model is proposed to describe the nonstoichiometry caused by a wide ranges of substitutions. This model can be used to calculate temperatures, oxidation conditions and cation/proton activity ratios of formation from biotite compositional data derived from microprobe analysis.

Appendix 5

Solubility of Cassiterite in Saline Fluid

A5-1 Introduction

The solubility of cassiterite in saline hydrothermal fluid is a complex function of temperature, oxidation state, pH and salinity.

Table A5-1 is a list of equilibria between tin bearing species and cassiterite. For a quantitative calculation of the solubility it is essential to know the thermodynamic properties of these equilibria. Table A5-2 lists the corresponding logK values recalculated from the estimated data of Jackson and Helgeson (1985a). Thermodynamic properties of tin bearing complexes have also been estimated by Patterson *et al.* (1981) and Eadington (1982). The results of a recent high temperature experimental study do not differ significantly from these estimated data.

The activity coefficient for Cl^- is calculated from Debye-Huckel equation

$$-\log \gamma_i = \frac{AZ_i^2 I^{1/2}}{1 + aB I^{1/2} + bI} \quad (\text{A5.1})$$

where a is the ionic radius, Z the charge number, I and ionic strength, b a constant, values of A and B at various temperatures are listed by Henley *et al.* (1984). The activity-concentration relationships for tin bearing complexes are very poorly understood and in the following their activity coefficients are assumed to be 1 in values. Apparently this assumption is rough, however, it is probably good enough for the first order estimation.

The value of pH, governed by various buffers in different systems, affects the solubility of cassiterite. An artificial range between 3 and 9 was taken in the following discussions.

Table A5-1: Thermodynamic equilibria between cassiterite and aqueous tin species

Equilibrium	Reactions
1	$\text{SnO}_2 + 2\text{H}^+ = \text{Sn}^{2+} + \text{H}_2\text{O} + 1/2\text{O}_2$
2	$\text{SnO}_2 + 4\text{H}^+ = \text{Sn}^{4+} + 2\text{H}_2\text{O}$
3	$\text{SnO}_2 + \text{H}^+ = \text{SnOH}^+ + 1/2\text{O}_2$
4	$\text{SnO}_2 + \text{H}_2\text{O} = \text{SnOH}_2 + 1/2\text{O}_2$
5	$\text{SnO}_2 + 2\text{H}_2\text{O} = \text{SnOH}_3^- + \text{H}^+ + 1/2\text{O}_2$
6	$\text{SnO}_2 + 2\text{H}_2\text{O} = \text{SnOH}_4$
7	$\text{SnO}_2 + \text{H}^+ + \text{H}_2\text{O} = \text{SnOH}_3^+$
8	$\text{SnO}_2 + 2\text{H}^+ = \text{SnOH}_2^{2+}$
9	$\text{SnO}_2 + 3\text{H}^+ = \text{SnOH}^{3+} + \text{H}_2\text{O}$
10	$\text{SnO}_2 + \text{Cl}^- + 2\text{H}^+ = \text{SnCl}^+ + 1/2\text{O}_2 + \text{H}_2\text{O}$
11	$\text{SnO}_2 + 2\text{Cl}^- + 2\text{H}^+ = \text{SnCl}_2 + 1/2\text{O}_2 + \text{H}_2\text{O}$
12	$\text{SnO}_2 + 3\text{Cl}^- + 2\text{H}^+ = \text{SnCl}_3^- + 1/2\text{O}_2 + \text{H}_2\text{O}$
13	$\text{SnO}_2 + \text{F}^- + 2\text{H}^+ = \text{SnF}^+ + 1/2\text{O}_2 + \text{H}_2\text{O}$
14	$\text{SnO}_2 + 2\text{F}^- + 2\text{H}^+ = \text{SnF}_2 + 1/2\text{O}_2 + \text{H}_2\text{O}$
15	$\text{SnO}_2 + 3\text{F}^- + 2\text{H}^+ = \text{SnF}_3^- + 1/2\text{O}_2 + \text{H}_2\text{O}$

Table A5-2: $\log K_T^*$ values of equilibria in Table A5-1

T(°C)	25	100	125	150	175	200	225	250	275	300	325	350
1#	-44.8	-34.5	-31.9	-29.5	-27.4	-25.5	-23.8	-22.3	-20.8	-19.6	-18.7	-18.0
2	-8.42	-6.85	-6.38	-5.96	-5.57	-5.02	-4.83	-4.84	-4.64	-4.74	-5.19	-6.42
3	-48.7	-37.8	-35.0	-32.5	-30.2	-28.1	-26.0	-24.0	-21.9	-20.1	-19.0	-18.3
4	-52.7	-40.4	-38.1	-35.4	-32.8	-30.6	-28.4	-26.3	-24.1	-22.2	-21.0	-20.3
5	-62.2	-48.7	-45.3	-42.2	-39.7	-37.3	-35.0	-32.9	-30.8	-29.9	-29.0	-28.1
6	-7.55	-6.59	-6.26	-6.74	-6.09	-5.50	-5.31	-5.30	-5.46	-5.88	-5.17	-7.06
7	-7.89	-6.76	-6.39	-6.00	-5.21	-4.58	-4.59	-4.71	-4.43	-4.82	-4.15	-5.00
8	-8.60	-7.22	-6.79	-6.34	-5.63	-4.96	-4.77	-4.82	-4.60	-4.86	-4.23	-5.04
9	-7.81	-6.46	-6.06	-5.62	-4.95	-4.34	-4.05	-4.13	-3.97	-4.20	-2.81	-4.38
10	-43.7	-33.0	-30.2	-27.6	-25.3	-23.1	-21.2	-19.4	-17.5	-15.8	-14.0	-12.2
11	-43.1	-32.2	-29.3	-26.6	-24.2	-21.9	-19.8	-17.8	-15.7	-13.8	-11.6	-9.00
12	-43.1	-31.8	-28.8	-26.1	-23.5	-21.2	-19.0	-18.0	-14.8	-12.8	-11.6	-7.97
13	-40.7	-30.4	-27.8	-25.4	-23.3	-21.3	-19.4	-17.8	-16.0	-14.5	-13.1	-11.5
14	-38.1	-27.7	-25.0	-22.7	-20.3	-18.2	-16.2	-14.4	-12.5	-10.7	-8.84	-6.46
15	-35.3	-24.9	-22.2	-19.8	-17.6	-15.5	-13.4	-11.7	-9.67	-7.93	-6.06	-3.68

*Recalculated from Jackson and Helgeson (1985a)

#Numbers correspond to reaction numbers in Table A5-1.

The values of $\log f_{\text{O}_2}$ is another intensive parameter affecting the solubility of cassiterite and the distribution of tin in aqueous phases. As the fluid phase is dominated by water, the reaction



gives an estimate of the minimum $\log f_{O_2}$, which is calculated through

$$\log f_{O_2} = \log K_{A5.2} - 2 \log f_{H_2} + 2 \log f_{H_2O} \quad (A5.3)$$

assuming f_{H_2} equals to f_{H_2O} . The buffer



is used as the maximum limit of $\log f_{O_2}$ as hematite is very rarely seen in tin deposits. The maximum $\log f_{O_2}$ is estimated through

$$\log f_{O_2} = -2 \log K_{A5.4} \quad (A5.5)$$

in which $\log K$ can be calculated from tabulated thermodynamic properties of hematite, magnetite, and oxygen gas (Helgeson, 1978).

Fig. A5-1 shows the range of the most probable T- $\log f_{O_2}$ space for primary cassiterite mineralization.

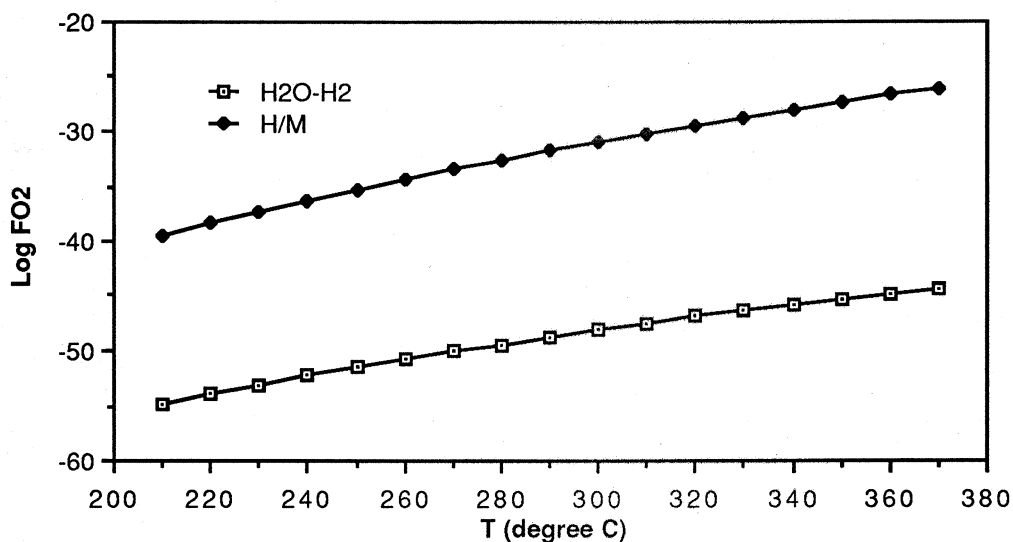


Fig. A5-1 T- $\log f_{O_2}$ space bounded by hematite/magnetite buffer and H₂O/H₂ buffer.

A5-2 Sn²⁺, Sn⁴⁺, and Sn-OH Complexes

The activity of Sn²⁺ is controlled by equilibrium 1 in Table A5-1

$$\log a_{Sn^{2+}} = \log K_1 - 2pH - 1/2 \log f_{O_2}$$

As $\log K_1$ decreases quickly from -18 at 350°C to -44 at 25°C (Table A5-2), the activity of Sn^{2+} in fluid saturated with cassiterite declines with temperature. Using the activity-concentration relationship assumed above, at the minimum $\log f_{\text{O}_2}$ calculated from equilibrium A5.2 and minimum pH assumed, the maximum concentration of Sn^{2+} is approximately equivalent to 10^{-4} ppm Sn at 350°C and 10^{-6} ppm Sn at 25°C.

Temperature and pH control the $a_{\text{Sn}^{4+}}$ as equilibrium between Sn^{4+} and cassiterite is not related to oxygen fugacity (Table A5-1).

$$\log a_{\text{Sn}^{4+}} = \log K_2 - 4\text{pH} \quad (\text{A5.7})$$

As the values of $\log K_2$ are between -4.64 and -8.4, at pH of 3 the maximum concentration of Sn^{4+} is only about 10^{-12} ppm Sn.

Both Sn^{2+} and Sn^{4+} forms complexes with the hydroxyl ion. These complexes are SnOH^+ , SnOH_2 , SnOH_3^+ , SnOH_3^- , SnOH_2^{2+} , SnOH_3^+ , and SnOH_4 . The concentrations of SnOH_2 and SnOH_4 are not related to pH values of the fluid (Equation A5.8 and A5.9) as they are neutral species.

$$\log C_{\text{SnOH}_2} = \log K_4 - 1/2 \log f_{\text{O}_2} \quad (\text{A5.8})$$

$$\log C_{\text{SnOH}_4} = \log K_6 \quad (\text{A5.9})$$

Along the $\text{H}_2/\text{H}_2\text{O}$ buffer the maximum concentration of SnOH_2 is about 6 ppm Sn at 350°C. The maximum concentration of SnOH_4 is only about 0.5 ppm Sn at 250°C.

The activity of SnOH^+ is a function of f_{O_2} and pH (Equation A5.10).

$$\log a_{\text{SnOH}^+} = \log K_3 - 1/2 \log f_{\text{O}_2} - \text{pH} \quad (\text{A5.10})$$

Taking the maximum value of $\log K_3$ of -18.3 at 350°C (Table A5-2), at minimum pH (3) and $\log f_{\text{O}_2}$ (along $\text{H}_2\text{O}/\text{H}_2$ buffer) the maximum concentration of SnOH^+ is about 0.2 ppm Sn.

On the other hand, the activity of SnOH_3^- increases with pH, i.e.,

$$\log C_{\text{SnOH}_3^-} = \log K_5 - 1/2 \log f_{\text{O}_2} + \text{pH} \quad (\text{A5.11})$$

The calculated concentrations of SnOH_3^- along the $\text{H}_2\text{O}/\text{H}_2$ buffer at 350°C is about 20 ppm Sn at pH=9, however, it decreases to less than 0.01 ppm Sn at neutral pH.

The concentrations of SnOH^{3+} , SnOH_2^{2+} and SnOH_3^+ are only affected by temperature and pH of fluid as their equilibria with cassiterite are independent of oxygen.

$$\log a_{\text{SnOH}_3^+} = \log K_7 - \text{pH} \quad (\text{A5.12})$$

$$\log a_{\text{SnOH}_2^{2+}} = \log K_8 - 2\text{pH} \quad (\text{A5.13})$$

$$\log a_{\text{SnOH}^{3+}} = \log K_9 - 3\text{pH} \quad (\text{A5.14})$$

The maximum values of $\log K_7$, $\log K_8$ and $\log K_9$ are -4.43, -4.6 and -2.81 respectively at 350°C. They correspond to the maximum concentrations of SnOH_3^+ , SnOH_2^{2+} and SnOH^{3+} of 10^{-3} , 10^{-7} , and 10^{-8} ppm Sn respectively at pH=3.

In summary, neither the concentration of free Sn^{2+} nor Sn^{4+} is significant under most hydrothermal conditions. For the Sn-OH complexes only SnOH_2 could yield concentration of several ppm Sn at weakly acidic and very reduced conditions. However, the concentration of SnOH_3^- increases with pH and become significant in fluids of high pH (>8).

A5-3 Sn-Cl Complexes

Sn^{2+} forms several complexes with Cl^- (Patterson *et al.* 1981; Eadington, 1982; Jackson & Helgeson, 1985) which are SnCl^+ , SnCl_2 , and SnCl_3^- . The concentrations of these complexes at cassiterite saturation are functions of temperature, a_{Cl^-} , pH and $\log f_{\text{O}_2}$ (Tables A5-1 & A5-2). Equations

$$\log a_{\text{SnCl}^+} = \log K_{10} + \log a_{\text{Cl}^-} - 1/2 \log f_{\text{O}_2} - 2\text{pH} \quad (\text{A5.15})$$

$$\log a_{\text{SnCl}_2} = \log K_{11} + 2 \log a_{\text{Cl}^-} - 1/2 \log f_{\text{O}_2} - 2\text{pH} \quad (\text{A5.16})$$

$$\log a_{\text{SnCl}_3^-} = \log K_{12} + 3 \log a_{\text{Cl}^-} - 1/2 \log f_{\text{O}_2} - 2\text{pH} \quad (\text{A5.17})$$

describe these relationships. The values of $\log K_{10}$, $\log K_{11}$, and $\log K_{12}$ vary from -12.23 to -43.7, -9.00 to -43.06, and -7.97 to -43.8 respectively from 350°C to 25°C.

The supply of Cl^- for the formation of Sn-Cl complexes is adequate as NaCl is usually the main solute in hydrothermal fluid responsible for tin mineralization. However, at high temperatures NaCl does not dissociate as much as at low temperatures and therefore the dissociation equilibrium must be considered in calculating the activities of Cl^- . Table

A5-3 lists activities of Cl^- at varying temperatures and salinity using the dissociation constant calculated from the thermodynamic data of Helgeson (1978) and the activity coefficient calculated from Debye-Huckel equation.

Table 5-3: Values of a_{Cl^-} at various temperatures and salinities

T (°C)	molal of NaCl		
	1	2	3
25	0.530	0.907	1.223
50	0.527	0.908	1.233
75	0.513	0.883	1.197
100	0.493	0.840	1.133
125	0.467	0.784	1.046
150	0.435	0.715	0.942
175	0.397	0.636	0.825
200	0.354	0.550	0.701
225	0.306	0.460	0.577
250	0.255	0.371	0.457
275	0.204	0.288	0.348
300	0.153	0.209	0.249
325	0.104	0.138	0.162
350	0.058	0.074	0.085

The concentration-pH variation curves of these Sn-Cl complexes can be examined at fixed temperature under assumed salinity and f_{O_2} buffer. Fig. A5-2A to Fig. A5-2D show the concentrations of SnCl_3^- , SnCl_2 and SnCl^+ at 275, 300, 325 and 300°C in fluid of 3m NaCl.

SnCl_2 and SnCl_3^- are important tin bearing species at weak acidic conditions at high temperatures. Temperature is apparently a very important factor as it is apparent from Fig. A5-2A to A5-2D that a cooling from 350 to 300°C can cause more than 3 orders of change in concentrations of Sn-Cl complexes.

A5-4 Sn-F Complexes

Like Sn-Cl complexes in saline fluids, Sn^{2+} also forms three species of complexes with F^- if there is adequate supply of F^- in the fluid.

It is difficult to estimate the maximum activity of F^- in hydrothermal fluid. However, for the fluids in equilibrium with granitic rocks, the reaction

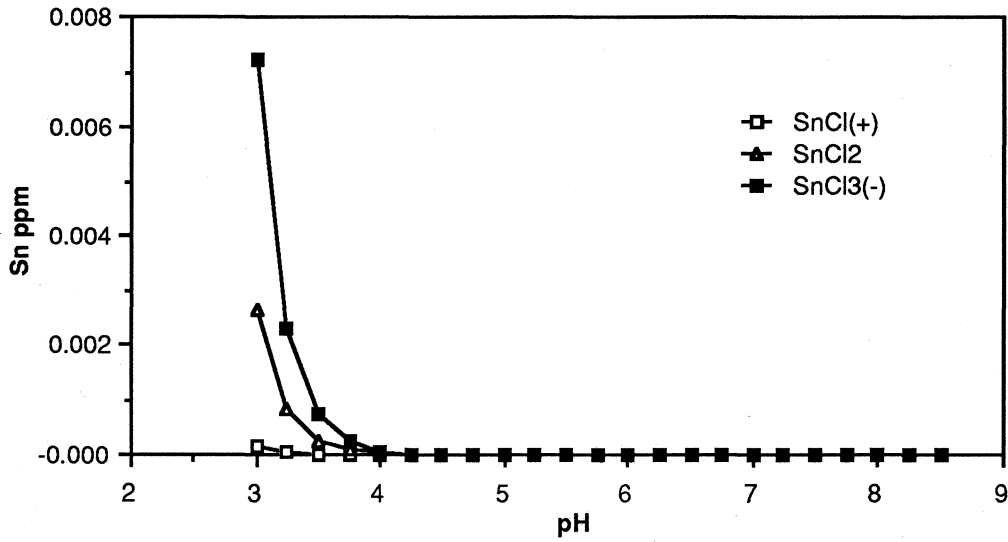


Fig. A5-2A Concentrations of Sn-Cl complexes in cassiterite saturated fluid of 3m NaCl. T=275°C , logfO2 =-30

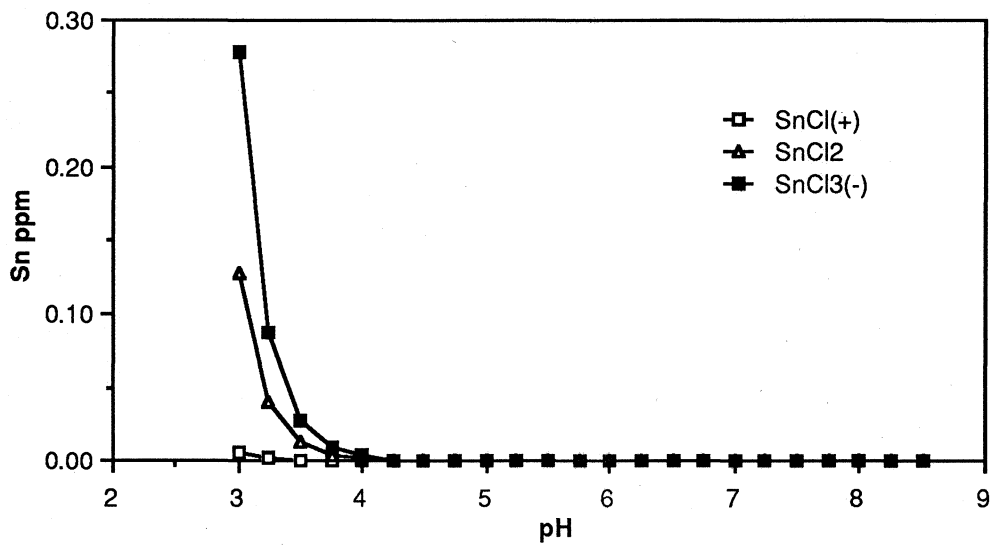


Fig. A5-2B Concentrations of Sn-Cl complexes in cassiterite saturated fluid of 3m NaCl. T=300°C , logfO2 =-30

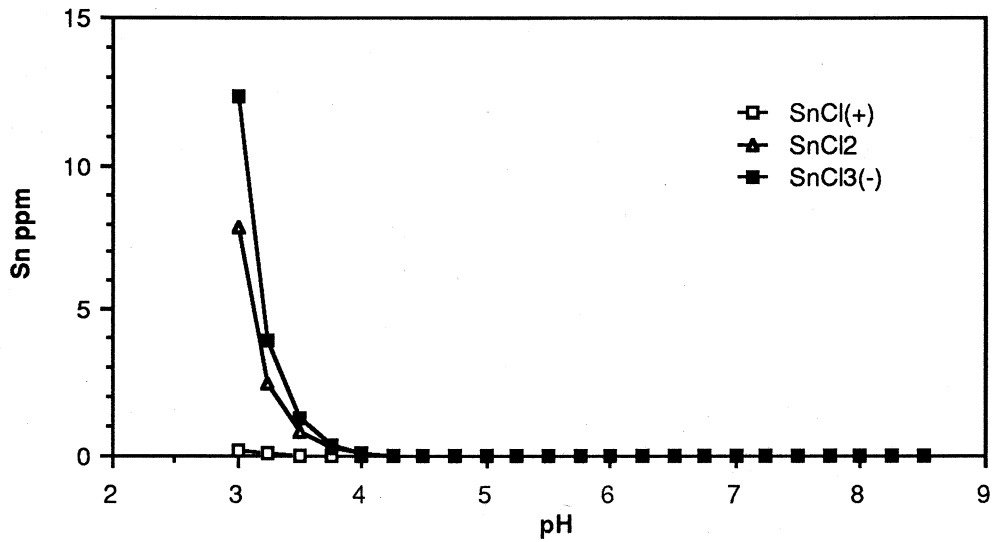


Fig. A5-2C Concentrations of Sn-Cl complexes in cassiterite saturated fluid of 3m NaCl. T=325°C , logfO₂ =-30

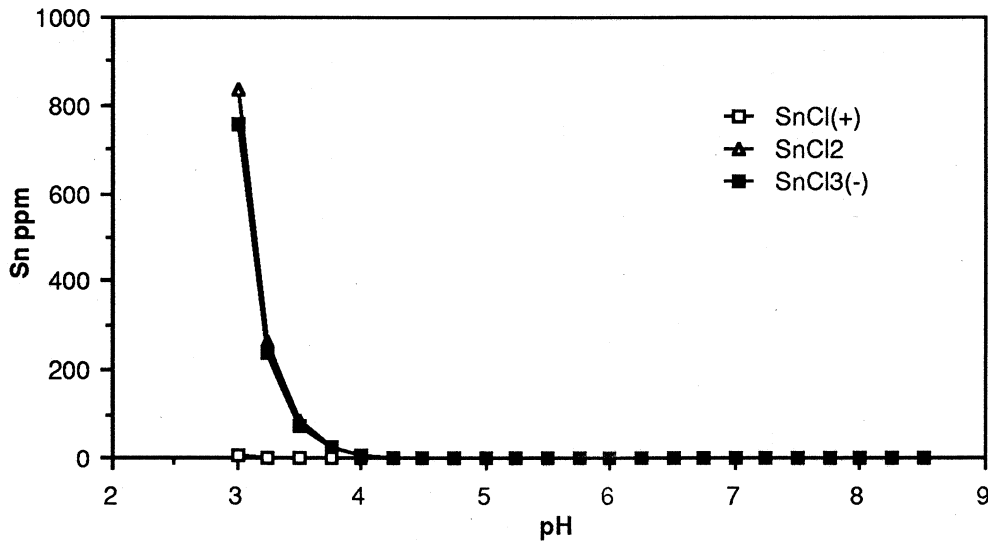
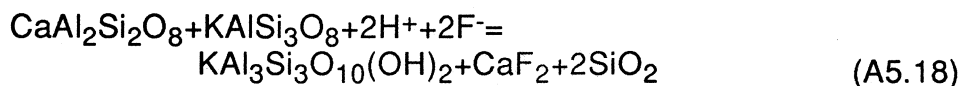


Fig.A5-2D Concentrations of Sn-Cl complexes in cassiterite saturated fluid of 3m NaCl. T=350°C , logfO₂ =-30



can probably provide a rough estimate. If we assume the activities of plagioclase, K-feldspar, muscovite and quartz are all unity, a maximum activity of unity for fluorite corresponds to a maximum activity of F^- , which is

$$\log a_{\text{F}^-} = -1/2 \log K_{\text{A5.18}} + \text{pH} \quad (\text{A5.19})$$

The calculated values of $\log K_{\text{A5.18}}$ for the above reaction along the vapor/liquid curve of H_2O using the thermodynamic data tabulated by Helgeson (1978) decrease from 33.27 to 20.82 with temperature increase from 25 to 280°C and then increase slowly to 26.64 at 370°C. The maximum activity of F^- is estimated to be around $10^{-10.4}$ at 280°C.

The equilibrium 13, 14 and 15 (Table A5-1) give constraints to the maximum concentrations of Sn-F complexes in hydrothermal conditions.

$$\log C_{\text{SnF}^+} = \log K_{13} + \log a_{\text{F}^-} - 1/2 \log f_{\text{O}_2} - 2\text{pH} \quad (\text{A5.20})$$

$$\log C_{\text{SnCl}_2} = \log K_{14} + 2 \log a_{\text{F}^-} - 1/2 \log f_{\text{O}_2} - 2\text{pH} \quad (\text{A5.21})$$

$$\log C_{\text{SnF}_3^-} = \log K_{14} + 3 \log a_{\text{F}^-} - 1/2 \log f_{\text{O}_2} - 2\text{pH} \quad (\text{A5.22})$$

The maximum values of $\log K_{13}$, $\log K_{14}$ and $\log K_{15}$ at temperatures between 25 and 350°C are -11.5, -6.46 and -3.68 (Table A5-2). The corresponding maximum concentrations of SnF^+ , SnF_2 and SnF_3^- in fluid in equilibrium with granitoids are 10^{-11} , 10^{-16} , and 10^{-24} ppm Sn along $\text{H}_2\text{O}/\text{H}_2$ buffer at acid conditions ($\text{pH}=3$). Clearly, Sn-F complexes are not important tin bearing species.

A5-5 Solubility of Cassiterite

It is apparent from the above discussion that although there may be many tin bearing species in hydrothermal fluid, only Sn-Cl complexes and $\text{Sn}(\text{OH})_2$ and SnOH_3^- are important in computing cassiterite solubility.

The relative stability of SnCl_2 , SnCl_3^- , SnOH_2 and SnOH_3^- has been discussed by Jackson and Helgeson (1985a). Chloride complexes of tin predominate in concentrated solutions of NaCl at $\text{pH}<3$ at 250°C, which increases to $\text{pH}<4.5$ at 350°C. With increasing temperature, SnCl_2 forms

to an increasing degree at the expense of SnCl_3^- . The minimum pH of the $\text{Sn}(\text{OH})_3^-$ field decreases from 250°C, but increases again from 300 to 350°C as a consequence of the formation of $\text{Sn}(\text{OH})_2$ at the expense of $\text{Sn}(\text{OH})_4$ with increasing temperature. At 250°C, $\text{Sn}(\text{OH})_4$ is the predominant tin complex at intermediate pH, but at temperatures higher than 300°C $\text{Sn}(\text{OH})_2$ predominates in this pH range (Jackson and Helgeson, 1985).

The solubility of cassiterite can be calculated in respect to pH, $\log f_{\text{O}_2}$, temperature, and salinity by adding the concentrations of all the tin bearing species. However, as only Sn-Cl complexes, $\text{Sn}(\text{OH})_2$, and $\text{Sn}(\text{OH})_4$ are important in our considered temperature, pH, $\log f_{\text{O}_2}$ and salinity ranges, this is simplified to

$$T_{\text{Sn}} = C_{\text{SnCl}^+} + C_{\text{SnCl}_2} + C_{\text{SnOH}_3^-} + C_{\text{SnOH}_2} + C_{\text{SnOH}_4} \quad (\text{A5.23})$$

in which T_{Sn} represents the total Sn in fluid, C the concentration of footnoted complex.

The plots (Figs. A5-3A to A5-3D) of total Sn concentrations against pH at assumed temperatures and $\log f_{\text{O}_2}$ suggest that the minimum Sn solubilities occur in moderate pH. It increases with decreasing pH and increasing pH. Solubility of Sn also increases greatly with temperature if oxygen fugacity, pH and salinity are not changed. It is clear that fluid at temperatures below 275°C have very little capacity to transport tin by Sn-Cl or Sn-OH complexes unless it is extremely acidic.

From these diagrams (Figs. A5-3A to A5-3D) and above discussion, it is clear that at temperatures between 300 and 350°C, oxygen fugacity between $\text{H}_2\text{O}/\text{H}_2$ buffer and hematite/magnetite buffer, salinities around 3 molal NaCl, in a slightly acidic fluid any minor changes of pH, oxygen fugacity, temperature or salinity can lead to significant changes of solubility of cassiterite to cause cassiterite deposition. As solubility of cassiterite is very low at temperatures below 275°C it implies that the probability of tin mineralization at temperatures below 275°C is very low. This is consistent with many other studies of temperatures of tin mineralization (Sillitoe et al. 1975; Patterson et al., 1981; Jackson et al., 1982; Heinrich and Eadington, 1986; Ren and Walshe, 1986; Sun and Eadington, 1988 and many others).

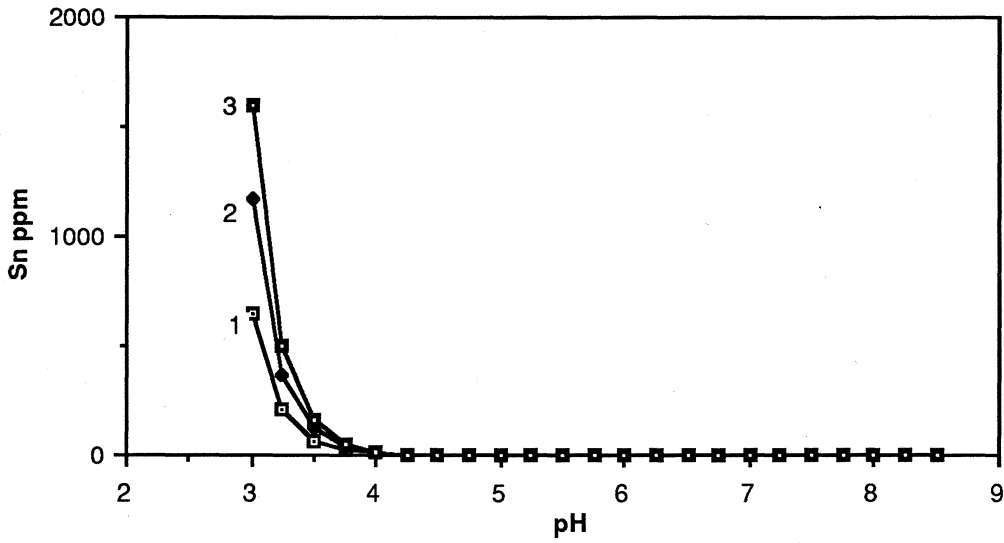


Fig. A5-3A Calculated cassiterite solubility (Sn ppm) in 1, 2 and 3m NaCl fluid; T=350°C; logfO₂=-30

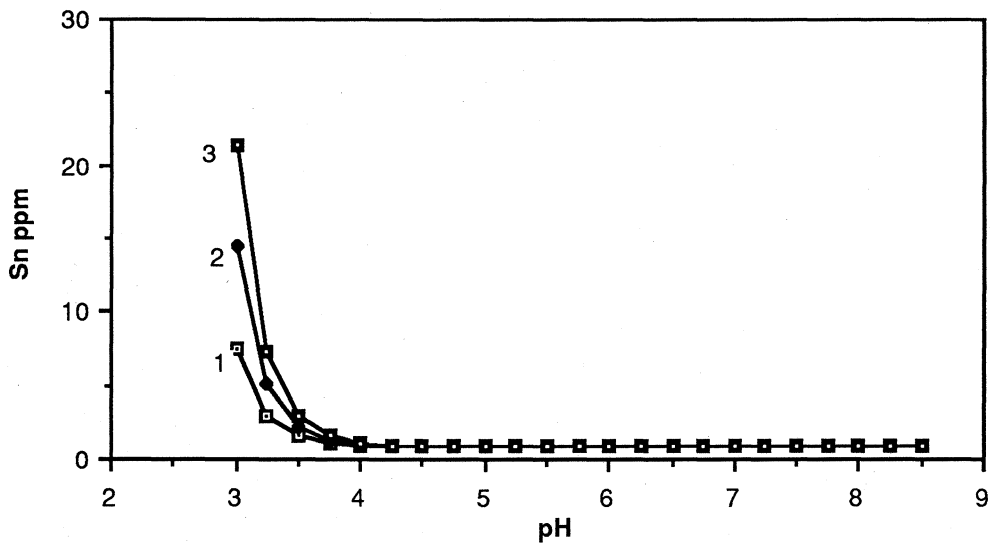


Fig. A5-3B Calculated cassiterite solubility (Sn ppm) in 1, 2 and 3m NaCl fluid; T=325°C; logfO₂=-30

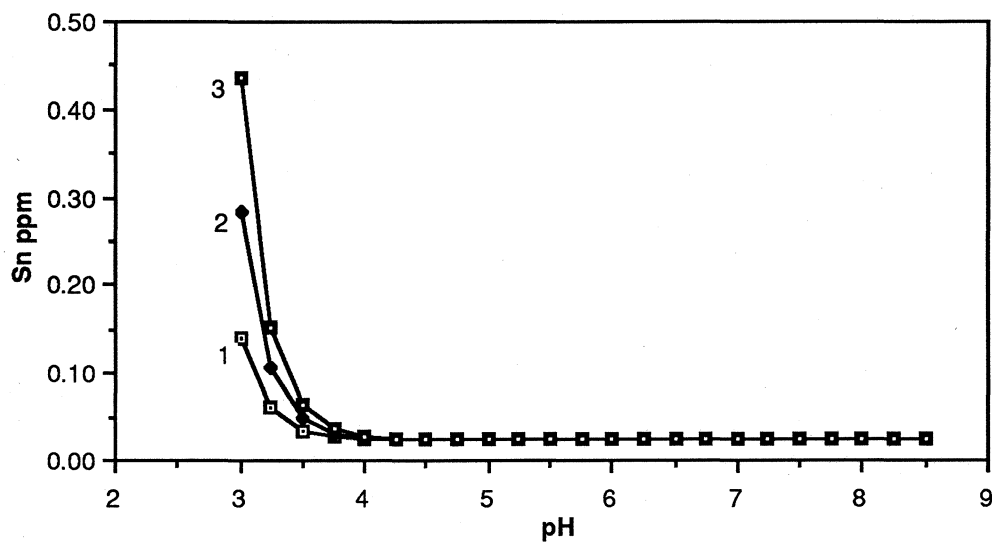


Fig. A5-3C Calculated cassiterite solubility (Sn ppm) in 1, 2 and 3m NaCl fluid; T=300°C; logf_{O2}=-30

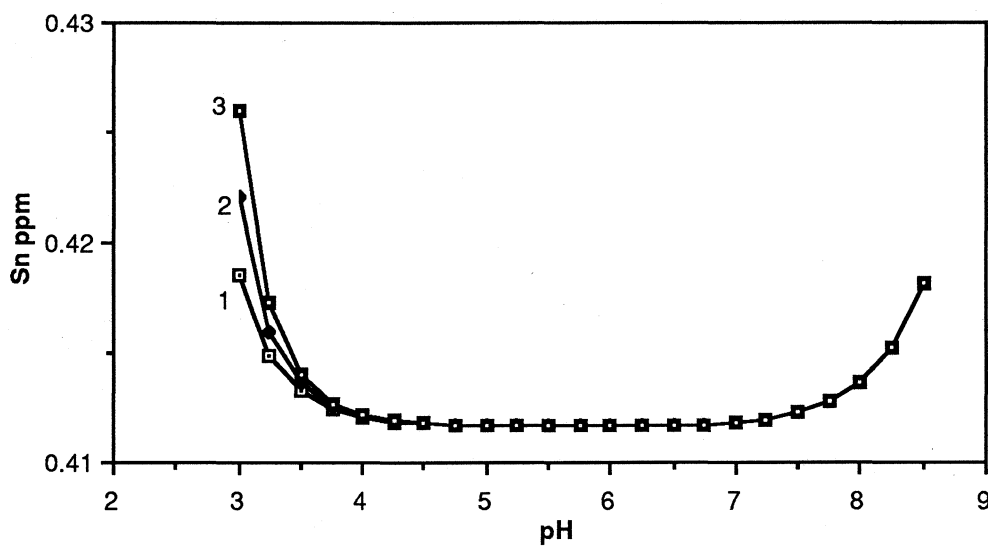


Fig. A5-3D Calculated cassiterite solubility (Sn ppm) in 1, 2 and 3m NaCl fluid; T=275°C; logf_{O2}=-30

References

- Ashmad, S. N. & Rose A. W. 1982. Fluid inclusions in porphyry and skarn ore at Santa Rita, New Mexico. *Econ. Geol.* v.77, p229-250
- Allegre, C. J. and Minster, J. F. 1978. Quantative models of trace element behaviour in magmatic process. *Earth Plannett. Sci. Lett.* v.38, p1-25.
- Antipin, V. S. 1981. Distribution coefficient for tin and tungsten in ore-forming acid-igneous rocks. *Geochem. Inter.* No.1, v.18.
- Arai, Y., Kaminish, G. & Saito, S. 1971. The experimental determination of the P-V-T-X relations for the carbon dioxide-nitrogen and carbon dioxide-methane systems. *Jour. of Eng. Japan.* v.4, p113-122.
- Ault, W. V. & Jensen, M. L. 1963. Summary of sulfur isotope standards: in "Biogeochemistry of sulfur isotopes" M. L. Jensen (eds), *Natl. Sci. Found. Symposium Proc.* Yale University
- Baily, S. W. 1984, *Micas: Reviews in mineralogy.* v.13, Mineralogical Society of America.
- Bartlett, R. W. 1969. Magma convection, temperature distribution and differentiation. *Am. Jour. Sci.* v.267, p1067.
- Beane, R. E. 1974. Biotite stability in the porphyry copper environment. *Econ. Geol.* v.69, p241-256.
- Becker, R. & Clayton, R. N. 1976. Oxygen isotope study of a pre-cambrian banded iron-formation, Hamersley range, Western Australia. *Geochim. Cosmochim. Acta*, v.40, p1153-1165.
- Bergerhoff, G. 1970. Tin: in' *Handbook of Geochemistry*", 50-A. Springer-Verlag, Berlin, Heidelberg.
- Borshchevskiy, Y. A. 1979. Oxygen isotope features of cassiterite from tin-ore deposits of central Asia: *Internat. Geol. Rev.* v.21, p937-944.
- Borshchevskiy, Y. A., Borisova, S. L., Zakharova, O. Y., Lugov, S. F., Makeyev, B. V., Podol'skiy, A. M. & Politov, V. K. 1983. Oxygen isotope systematics of tin deposits of the northest USSR: *Internat. Geol. Rev.* v.25,

p102-116.

Bowen, N. L. & Tuttle, O. F. 1949. The system MgO-SiO₂-H₂O. Bull. Geol. Soc. Am. v.60, p439-460.

Brammall, A., Leech, J. G. C. & Bannister, F. A. 1937. The paragenesis of cookeite and hydromuscovite associated with gold at Ogofau, Carmarthenshire. Mineral. Mag. v.24, p507-520.

Brandeis, G. & Jaupart, C. 1987. The kinetics of nucleation and crystal growth and scaling for magmatic crystallization. Contrib. Mineral. Petrol. v.96, p24-34.

Brandeis, G., Jaupart, C., & Allegre, C. J. 1984, Nucleation, crystal growth, and the thermal regime of cooling magmas. Jour. Geophys. Res. v.89, p10161-10177.

Bryant, D. G. 1968. Intrusive breccia associated with ore, Warren (bisbee) mining district, Arizona. Econ. geol. v.63, p1-12.

Bulter, B. S. 1913. Geology and ore deposits of the San Francisco region, Utah. U. S. geol. Survey, Prof. Paper 80, p172-178.

Burnham, C. W. 1979. Magmas and Hydrothermal fluids. in Barnes H. L. (eds) " geochemistry of hydrothermal ore deposits", p71-136.

Burnham, C. W. 1985. Energy release in subvolcanic environments: Implications for breccia formation. Econ. geol. v.80, p1515-1522.

Burruss, R. C. 1981. Analysis of the phase equilibria in C-O-H-S fluid inclusions. In "short course in fluid inclusions: applications to petrology" L. S. Hollister and M. L. Crawford (eds), Mineral. Assoc. Canada.

Cerny, P. 1970. Compositional variation in cookeite. Can. Mineral. 10., p636-647

Chappell, B. W. & White A. J. R. 1974. Two contrasting granites types. Pacific Geology, v.8, p173-174.

Chatterjee, N. D. 1970. Synthesis and upper stability of paragonite. Contrib. Mineral. Petrol. v.27, p244-257.

Chen, Y., Huang, M., Xu, J., Ai, Y., Li, X., Tang, S. & Meng, L. 1985. Geological features and metallgenetic series of the Dachang cassiterite-sulfide polymetallic belt. Acta Geol. Sinica, v.3, p228-240 (Chinese with english abstract).

Clarke, G. W. 1979. Brecciation, alteration and mineralization associated with disseminated tin deposits of the Ardlethan district, south central NSW. Unpub thesis, James Cook University of north Queensland.

Clarke, G. W., Paterson, R. G. & Taylor, R. G. 1984. Major brecciation styles at the Ardlethan tin mine, NSW. Fractures and veins and accretionary prisms-state of the art symposium. *geol. Soc. Aust.* extended abstract, p22.

Collins, P. F. 1979. Gas hydrates in CO₂-bearing fluid inclusions and the use of freezing data for estimation of salinity. *Econ. geol.* v.74 p1435.

Collins, P. F. 1981. Geology and Genesis of the Cleveland tin deposits, West Tasmania, fluid inclusion and isotopic studies. *Econ. geol.* v.76, p365-392.

Craig, H. 1957. Isotopic standards for carbon and oxygen and correction factors for mass-spectrometric analysis of carbon dioxide. *Geochim. Cosmochim. Acta*, v.12, p133-149.

Crowley, M. S. & Roy, R. 1964. Crystalline solubility in muscovite and phlogopite groups. *Am. Mineralogist.* v.49, p348-363.

Durasova, N. A. & Barsukov, V. L. 1973. The behaviour of tin in liguidating boron bearing silicate melts. *Geochem. Inter.* No.10, p920-922.

Dymek, R. F., 1983. Titanium, aluminum and interlayer cation substitutions in biotite from high-grade gneisses, west greenland, and the occurrence of a barian-chromian muscovite. *Raap. Cronlands Geol. Anders.* v.112, p71-82. Cited by Guidotti (1984).

Eadington, P. J. 1977, A study of fluid inclusions and their significance in minerals from hydrothermal ore deposits, New England, New South Wales. (unpub) Ph.D thesis, University of Newcastle.

Eadington, P. J. & Giblin, A. 1980. Alteration minerals and precipitation of tin in granite rocks. *Tech. Comm.* 68, CSIRO Div. Miner. Res. (unpub)

Eadington, P. J. 1982. Calculated solubility of cassiterite in high temperature hydrothermal brines, and some applications to mineralization in granitic rocks and skarns. *Internat. Symposium Hydrothermal Reactions*, 1st Japan, March 22-26, Proc, p335-345

Eadington, P. J. & Paterson R. G. 1984. Microdeformation and fluid inclusion and their significance in mineralized breccia columns in the Ardlethan tin mine, NSW: in "Geoscience in the development of natural

- resources", the 7th Australian Geological convention, Sydney, p154-155
- Eadington, P. J., 1985a. Fluid inclusions, brecciation and cassiterite mineralization at the Ardlethan Tin Mine, N.S.W. CSIRO Review, p62-63
- Eadington, P. J., 1985b. Alteration, microfractures and brecciation at the Ardlethan Tin Mine, N.S.W. CSIRO Reviews, p61-62
- Eugster, H. P & Wones, D. R. 1962. Stability relations of ferruginous biotite, annite. *Jour. of Petrol.* v.3, p82-125.
- Eugster, H. P. & Yoder, H. S. 1954a. Stability and occurrence of paragonite. *Bull. Geol. Soc. Am.* v.65, p1248-1249.
- Eugster, H. P. & Yoder H. S. 1954b. Annual report of the director of the geophysical laboratory. *Garnegie institute Wash Year Book.* v.53, p95-145.
- Flinter, B. H., 1971. Tin in acid granitoids, the search for geochemical scheme of mineral exploration. *Cand. Inst. Min. Metall.* V.2, p323-330
- Garman, J. H. 1974. Synthetic sodium and its two hydrates: stabilities, properties, and mineralogical implications. *Am. Mineral.* v59, p261-273
- Godfrey, J. R. 1915. Report on the Ardlethan Tin Field. NSW Geol. Survey No. 20
- Greedwood, H. J. & Barnes, 1966. Binary mixtures of volatile compounds, In "Handbook of physical constants". ed. S. P. Clark, *Jour. Geol. Am. Mem.* v.97, revised edition, p385-400.
- Groves, D. I. & Mccathy, T. S. 1978. Fractionation crystallization and origin of Sn deposits in granitoids. *Mineral Deposits* v.13, p11-26.
- Guidotti, C. V. 1984. Micas in metamorphic rocks. in "Micas: Reviews in mineralogy V.13", Baily S. W. (eds), Mineralogical Society of America.
- Halley, S. W. 1987. Genesis of the Mount Bischoff tin deposits, Ph.D thesis (unpub), Australian National University.
- Hamaguchi, H. & Kuroda, R. 1970. Tin: in "Handbook of Geochemistry" 50-B to 50-M. Springer-Verlag Berlin Heidelberg.
- Hazen, R. M. & Wones, D. R. 1972. The effect of cation substitutions on the physical properties of trioctahedral micas. *Am. Mineralogist* v.57, p103-129.
- Hedenquist, J. W. & Henley, R. W. 1985a. Hydrothermal eruptions in the Waiotapu geothermal system, New Zealand: their origin, associated

breccias, and relation to precious metal mineralization. *Econ. Geol.* v.80, p1640-1668

Hedenquist, J. W. & Henley, R. W. 1985b. The importance of CO₂ on freezing point measurements of fluid inclusions: evidence from active geothermal systems and implications for epithermal ore deposition. *Econ. Geol.* v.80, p1379-1406

Hedges, M. M. & Walshe, J. L. 1986. Progress in the development of a seven-component solid solution model for muscovite. Final AMIRA report (unpub.). Project 81/P147

Heinrich, C. A. & Eadington, P. J. 1986. Thermodynamic predictions of the hydrothermal chemistry of Arsenic, and their significance for the paragenetic sequence of some cassiterite-arsenopyrite-base metal sulfide deposits. *Econ. Geol.* v.81, p511-529.

Helgeson, H. C., Delany, J. M., Nesbitt, H. W. & Bird, D. K. 1978. Summary and critique of the thermodynamic properties of rock-forming minerals. *Am. Jour. Sci.* v.278A, p1-229.

Helgeson, H. C. 1978. "Supcrt" program and its data base. unpublished

Henley, R. W., Truesdell, A. H. & Barton, P. B. Jr. 1984. Fluid mineral equilibria in hydrothermal systems: Society of economic geologists, *Reviews in economic geology* v.1, 267p

Hesp, W. R. 1973. Transport of tin in acid igneous rocks. *Vestnik ostrednoho ustavu geologikeho*, v.48, p197-205 (cited in Taylor, 1979).

Hesp, W. R. & Rigby, D. 1972. The transport of tin in acid igneous rocks. *Pacific Geology*, v.4, p135-152.

Hewitt, D. A. 1977. Hydrogen fugacity in shaw bomb experiments. *Contrib. Mineral. Petrol.* v.65, p165-169.

Hewitt, D. A. & Wones, D. R., 1984. Experimental phase relations of micas. in "Micas, *Reviews in Mineralogy* v.13", Baily S. W. (eds), Mineral. Soc. Am.

Higgins, N. C. 1985. Wolframite deposition in a hydrothermal vein system: the Grey River tungsten prospect, New Foundland, Canada. *Econ. Geol.* v.80, p1297-1327.

Higgins, N. C. 1989. Comment on "orogin of alkali feldspar granite: an example from the Poimena granite, northeastern Tasmania". *Geochim.*

Cosmochim. Acta, in press.

Higgins, N. C., Solomon, M. & Varne, R., 1985. The genesis of the Blue Tier Batholith, northeastern Tasmania, Australia. *Lithos*. v.18, p129-149.

Higgins, N. C., Turner, N. J. and Black, L. P. 1986. The petrogenesis of an I-type volcanic-plutonic suite: The St. Marys porphyrite, Tasmania. *Contrib. Mineral Petrol*. v92, p248-259.

Holland, H. D. 1972. Granite, solutions and base metal deposits. *Econ. Geol.* v.67, p281-301

Holland, T. J. B. 1979. Experimental determination of the reaction $\text{paragonite} = \text{jadeite} + \text{kyanite} + \text{H}_2\text{O}$ and internally consistent thermodynamic data for part of the system $\text{Na}_2\text{O}-\text{Al}_2\text{O}_3-\text{SiO}_2-\text{H}_2\text{O}$ with applications to eclogite and blueschists. *Contrib. mineral. Petrol.* v.68, p293-301.

Hollister, L. S. & Burruss, R. C. 1976. Phase equilibria in fluid inclusions from the Khtada lake metamorphic complex. *Geochim. Cosmochim. Acta* v.40, p163-175.

Hollister, L. S., Roedder, E., Burruss, R. C., Spooner, E. T. C. & Touret, J. 1981. Practical aspects of microthermometry. In L. S. Hollister & M. L. Crawford eds., *Fluid inclusions: Applications to Petrology*. Mineral. Assoc. Canada. Short course handbook v.6, p278-304.

Hunt, R. 1887. *British mining*, 2nd ed. London, Crosby, Lockwood, 944p.

Imeokparia, E. G. 1982. Tin content of biotite from Afu Younger granite complex, central Nigeria. *Econ. geol.* v.77, p1710-

Jackson, E. D. 1961. Primary textures and mineral associations in the ultramafic zone of the stillwater complex, Montana. U. S. Geol. Survey, Prof. Paper 358.

Jackson, K. J. & Helgeson, H. C. 1985a. Chemical and thermodynamical conditions on the hydrothermal transport and deposition of tin, I: calculation of the solubility of cassiterite at high pressure and temperature. *Geochim, Cosmochim. Acta*, v.49, p1-22.

Jackson, K. J. & Helgeson, H. C. 1985b. Chemical and thermodynamical conditions on the hydrothermal transport and deposition of tin, II: Interpretation of the phase relations in the south east Asian tin belt. *Econ. geol.* v.80, p1365-1378.

Javory, M. L., Pineau, F. & Iyama, I. 1978. Experimental determination of

the isotopic fractionation between gases CO₂ and carbon dissolved in theoleiitic magma. *Contrib. Mineral. Petrol.*, v.67, p35-69.

Kelly, W. C. & Rye, R. O. 1979. Geologic, fluid inclusion, and stable isotope studies of the tin-tungsten deposits of Panasqueira, Portugal. *Econ. Geol.* v.74, p1721-1822.

Kendall, C., Chou, I-M. & Coplen, T. P. 1983. Salt effect on oxygen isotopes equilibria (abs). *EOS. Trans. Amer. Geophys. Union* v.64, p334-335.

Khaibullin, I. Kh., Novokov, B. Ye., Copeliovich, A. M. & Besedin, A. M. 1980. Phase diagrams for steam solutions and calorific properties of two- and three-component systems: H₂O-NaCl, H₂O-Na₂SO₄, and H₂O-NaCl-Na₂SO₄. In J. Straub and K. Scheffler eds. *Water and Steam*. Pergamon Press, New York NY. p641-647.

Kirkpatrick, R. J. 1976. Toward a kinetic model for the crystallization of magma bodies. *Jour. Geophys. Res.* v.81, p2565-2571.

Konnerup-Masden, J. 1977. Composition and microthermometry of fluid inclusions in the Kleivan granite, south Norway. *Am. Jour. Sci.* v.277, p673-696.

Kyser, T. K., 1987. Equilibrium fractionation factors for stable isotopes. in "Stable Isotopes"; Review in Mineralogy. Mineral. Soc. Am.

Labotka, T. C. 1983. Analysis of the compositional variations of biotite in pelitic hornfels from northeastern minnesota. *Am. Mineral.* v.68, p900-914.

Levillain, C. 1980. Etude statistique des variations de la teneur en OH et F dans les micas. *Tscher. Mineral. Petrol. Mitt.* v.27, p209-223.

Lister, J. S. 1966. The crystal structure of two chlorite. Ph.D thesis (unpub), University of Wisconsin.

Luth, W. C. 1967. Studies in the system KAlSi₃O₈-Mg₂SiO₄-SiO₂-H₂: I, inferred phase relations and petrologic applications. *Jour. Petrol.* v.8, p372-416.

Mackenzie, D. E., Black, L. P. & Sun, S. S. 1988. Origin of alkali-feldspar granites: An example from the Poimena granite, northeastern Tasmania, Australia. *Geochim. Cosmochim. Acta*, v.52, p2507-2524.

Markham N. L. & Basden H. 1974, Wagga Anticlinorial Zone: Mineral

deposits. in "The mineral deposit of NSW", Geol. Survey of NSW, dept. of Mines. p135-141.

Markham, N. L. 1980. CARGELLIGO-NARANDERRA 1:250,000 metallogenic map: Geol. Survey of New South Wales, Dept. of Mineral Resource and Development.

Matthews, A., Goldsmith, J. R. & Clayton, R. T. 1983. On the mechanisms and Kinetics of oxygen isotope exchange in quartz and feldspar at elevated temperatures and pressures. Geol. Soc. Amer. Bull. v.94, p396-412.

McCallum, M. E. 1985. Experimental evidence for fluidation processes in breccia pipe formation. Econ. Geol. v.80, p1523.

McDowell, S. D. & Elders, W. A. 1980. Authigenic layer silicate minerals in Borehole Elmore 1, Salton Sea geothermal field, California, USA. Contrib. Mineral. Petrol. v.74, p293-310.

Miser, H. D. & Milton, C. 1964. Quartz, Rectorite, and cookeite from the Jeffrey Quarry, Near North Little Rock, Pulaski County, Arkansas. Bull. ArKansas Geol. Comm. v.21, p29.

Mitcham, T. W. 1974, Origin of breccia pipe. Econ. Geol. v.69, p412-

Netzel, R. K. 1970. Trace tin distribution in the Ardlethan granite, New South Wales. B.Sc (Hons) thesis (unpub), University of Adelaide.

Neuman, H., Mead, J. & Vitaliano, C. J. 1954. Trace element variation during fractional crystallization as calculated from distribution law. Geochim. Cosmochim. Acta, v.6, p90-

Norman, D. I. & Sawkins F. J., 1985, The tribag breccia pipes, precambrian Cu-Mo deposits, Batchwana Bay, Ontario. Econ. Geol. v.80, p1593-

Norton, D. L. & Cathles, L. M. 1973. Breccia pipes-Products of exsolved vapor from magmas. Econ. geol. v.68, p540-546.

Ohle, E. L. 1985. Breccias in Mississippi Valley-type deposits. Econ. Geol. v.80, p1736-

Ohmoto, H. & Rye, R. O. 1979. Isotopes of sulfur and carbon: in "Geochemistry of hydrothermal ore deposits" 2nd ed. Barnes H. L. (eds) New York/Chichester/Brisbane/Toronto, 798p.

Olade, M. A. 1980. Geochemistry characteristics of tin-bearing and tin-

barren granite. *Econ. geol.* v.75, p71-82.

O'neil, J. R. & Chappell, B. W. 1977. Oxygen and hydrogen isotope relations in Berridale Batholith. *Geol. Soc. London.* v133, p559-571

Packham, G. H. 1960. Sedimentary history of part of the Tasman geosyncline in southeastern Australia. 21st inter. Geol. Cong. Copenhagen, rept 12, p84-93

Partin, E. 1984. Ferric/ferrous determinations in synthetic biotite. M. S. thesis, Virginia Polytechnic institute and state university, Blacksburge.

Partin, E., Hewitt, D. A. & Wones, D. R. 1983. Quantification of ferric iron in biotite. *Geol. Soc. Am. Abstr.* with Program 15, p659.

Paterson, D. J., Ohmoto, H. & Solomon, M. 1981. Geological setting and genesis of the cassiterite-sulfide mineralization at Renison Bell, Western Tasmania. *Econ. Geol.* v.76, p393-438.

Paterson, R. G. 1976. Ardlethan tin mine. 25th Inter. Geol. Cong. Sydney, p36-43.

Price, J. G. 1985. Ideal site mixing in solid solutions, with an application to two-feldspar geothermometry. *Am. Mineralogist* v.70, p696-701
Raggatt H. G. 1938, Carpathia mine, Ardlethan tin field. in "Ann. Rept. Dept. Mines NSW" p103-107.

Reggatt, H. G. 1938. Carpathia Mine, Ardlethan Tin Field. Ann. Rept. Dept. Mines NSW p103-107

Rattigan, J. H. 1960. Residual characteristics of crystallates genetically associated with ore deposits. *Econ. Geol.* v55. p1272-1284

Rayleigh, J. W. S. 1896. Theoretical considerations respecting the separation of gases by diffusion and similar processes. *Philos. Mag.* v.42, p493 (cited in Allegre and Minster, 1978).

Reed, S. J. B. & Ware, N. G. 1975. Quantitative electron microprobe analysis of silicate using energy-dispersive X-ray spectrometry method. *Jour. Petrol.* v.16, p499-519.

Ren, S. K. and Walshe, J. L. 1986. Geology, brecciation and paragenesis of the Ardlethan tin field. in "Genesis of tin-tungsten deposits & their associated granitoids" IGCP project 220. Proceedings of Conference 30th June-2nd July, 1986, Canberra, Australia.

Ren, S. K., Eggleton, R. A. & Walshe, J. L. 1988. The formation of cookeite in breccia pipes in the Ardlethan tin field, New South Wales, Australia. *Cand. Mineral.* v.26, p407-412.

Reynolds, D. L. 1954. Fluidation as a geological process and its bearing on the problem of intrusive granites. *Am. J. Sci.* v.252, p577-613.

Richards, J. R., Compston, W. & Paterson, R. G., 1982. Isotopic information on the Ardlethan tin field, NSW. The Aust. Inst. Min. Metall. No. 284 p11-16.

Robie, R. A., Hemingway, B. S. & Fisher, J. R. 1978. Thermodynamic properties of minerals and related substances at 298.15K and 1 bar (100,000 pascals) pressure and higher temperatures. U. S. Geol. Survey Bull. v.1452, 456p.

Roedder, E. 1981. Origin of fluid inclusions and changes that occur after trapping. in "Short Course in Fluid Inclusions: application to petrology". Hollister L. S. & Crawford M. L. (eds), Mineralogical Association of Canada.

Roedder, E. 1984. Fluid Inclusions: in "Reviews in mineralogy" v.12, Mineralogical Society of America.

Roedder, E. & Bodnar, R. J. 1980. Geological pressure determinations from fluid inclusion studies. Ann. Rev. Earth Planet Sci. v.8, p263-301.

Rutherford, M. J. 1969. An experimental determination of iron biotite-alkali feldspar equilibria. Jour. of Petrol. v.10, p381-408.

Rutherford, M. J. 1973. The phase relations of aluminous iron biotite in the system $AlSi_3O_8$ - $KAlSi_3O_8$ - SiO_2 - Fe - O - H . Jour. of Petrol. v.14, p159-180.

Rye, R. O. & Sawkins, F. J. 1974. Fluid inclusion and stable isotope studies on Casapalca Ag-Pb-Zn-Cu deposits, central Andes, Peru. Econ. Geol. v.69, p181-205.

Sand, L. B., Roy, R. & Osborn, E. F. 1957. Stability relations of some minerals in the $NaCl$ - Al_2O_3 - SiO_2 - H_2O system. Econ. Geol. v.52, p169-179.

Sawkins, F. J. 1969. Chemical brecciation: an unrecognized mechanism for breccia formation. Econ. Geol. v.64, p613-617.

Scheibner, E. 1975. Definition and review of structural elements. in "Miner. Dept. of NSW" Markham N. L. & Basden H. (eds), p108-113.

Scott, K. M. 1980. Mineralogical and Geochemical variations at Ardlethan and their implications for exploration investigation. (unpub) Internal report, 1143R, CSIRO division of mineralogy, North Ryde NSW.

Sharp, J. E. 1979. Cave Peak, a molybdenum-mineralized breccia pipe

complex in Culberson County, Texas. *Econ. Geol.* v.74, p517-534.

Shaw, H. R. 1965. Comments on viscosity, crystal settling and convection in granite magmas. *Am. Jour. Sci.*, v.263, p120 .

Shelnutt, J. P. & Noble, D. C. 1985. Premineralization radial dikes of tourmalinized fluidation breccia, Tulcani district, Peru.. *Econ. Geol.* v.80, p1622.

Sheraton, J. W. & Back, L. P. 1973. Geochemistry of mineralized granitic rocks of northeast Queensland. *Jour. Geochem. Explor.* v.2, p331-348.

Sillitoe, R. H. 1985. Ore-related breccias in volcanicpluton arcs. *Econ. Geol.* v.80, p1467-1514.

Sillitoe, R. H., Halls, C. & Grant, J. N. 1975. Porphyry tin deposits in Bolivia; *Econ. Geol.* v.70, p913-927.

Sillitoe, R. H. & Sawkin,s F. J. 1971. Geology, mineralogy and fluid inclusion study relating to the origin of Cu-bearing tourmaline breccia pipes, Chile. *Econ. Geol.* v.66, p1028-1041.

Speer, J. A. 1981. Petrology of cordierite- and almandine-bearing granitoid plutons of the southern Appdachian Piedmont, USA. *Cand. Mineral.* v.19, p35-46.

Stanton, R. L. 1972,. *Ore Petrology*. New York, McGriaw-Hill, 713p.

Stempork, M. 1963. Distribution of Sn-W-Mo formation deposits around granites. in "Problem of post magmatic ore deposition", Stempork M. (eds) v.1, Geological survey of Czechoslovakia, Prague, P69-72.

Stempork, M. 1965. Genetic features of the deposits of tin, tungsten, and molybdenum formation. in "Problem of post magmatic ore deposition", Stempork M. (eds), v.2, Geological survey of Czechoslovakia, prague, p472-481.

Stempork, M. & Skvor, P. 1974. Composition of tin bearing granites from the Krusne-hory metallic province of Czechoslovakia. *Sbornik Geologickych ved (Jour. of geological Science) Loziskova geologie (economic geology)* v.16, p7-87 (in English).

Stone C. G. 1969. *Geology of the Ardlethan area*. M.Sc. preliminary thesis report. Sydney University
Sun, S. S. & Eadington, P. J. 1987. Oxygen isotope evidence for the mixing of magmatic and meteoric waters during tin mineralization in the Mole granite, New South Wales, Australia. *Econ. geol.* v.82, p43-52.

- Taknouchi, S. & Kennedy, G. 1964. The binary system H₂O-CO₂ at high temperature and pressures *Am. Jour. Sci.* v.262, p1055-1071.
- Taylor, B. E. & Bucher-Nurminen 1986. Oxygen and carbon isotope and cation geochemistry of metasomatic carbonates and fluids, Bergel aureda, Northern Italy. *Geochim. Cosmochim. Acta*, v.50, p1267-1279.
- Taylor, B. E. 1987., Stable isotope geochemistry of ore-forming fluids: in "Stable Isotopes", *Reviews in mineralogy*, Mineral. Soc. Am.
- Taylor, H. P. Jr. 1974. The application of oxygen and hydrogen isotope studies to problems of hydrothermal alteration and ore deposition. *Econ. geol.* v.69, p843-
- Taylor, H. P. Jr. 1974. Oxygen and hydrogen isotope studies of plutonic granitic rocks. *Earth Plantt. Sci. Lett.* v.38, p177-210.
- Taylor, R. G. 1972. The relationship between structure and orebody types in Ardlethan tin field, NSW. *Econ. Geol.* v.67, p116-117
- Taylor, R. G. 1979, *Geology of tin deposits*. Elsevier Scientific publishing company, Amsterdam-Oxford-New York.
- Toraya, H., Iwai, S., Marumu, F., Daimon, M. & Kondo, R. 1976. The crystal structure of tetrasilicic potassium fluor mica KMg_{2.5}Si₄O₁₀F₂. *Kristallogr* v.144, p42-52.
- Truesdell, A. H. 1974. Oxygen isotopic activity and concentrations in aqueous salt solution at elevated temperatures: consequence for isotopic geothermometry. *Earth Plant. Sci. Lett.* v.23, p387-396.
- Turner, N. J., Black, L. P. and Higgins, N. C. 1986. The St. Marys porphyrite-a Devonian ash-flow tuff and its feeder. *Australian Jour. of Earth Sciences*, v.33, p201-218.
- Walker, R. T. 1928. Mineralized volcanic explosion pipes. *Eng. Min. Jour.* v.126, p895-898, p939-942, p976-984.
- Walsh, J. F., Kesler, S. E., Duff, D. & Cloke, A. P. L., 1988. Fluid inclusion geochemistry of high-grade, vein-hosted gold ore at Pamour Mine, Porcupine Camp, Ontario. *Econ. Geol.*, v.83, p1347-1367.
- Walshe, J. L. 1986. A six-component chlorite solid solution model and the conditions of chlorite formation in hydrothermal and geothermal systems. *Econ. geol.* v.81, p681-703.

Walshe, J. L., Heithersay P. S. & Ren S. K., 1987. Alteration study of Nash's Hill: Application of GRADMAP. Confidential report to Peko Wallsend Exploration Ltd.

Walshe, J. L. & Solomon, M. 1981. An investigation into the environment of formation of the volcanic hosted Mt. Lyell copper deposits using geology, mineralogy, stable isotopes, and a six-component chlorite solid solution model. *Econ. Geol.* v.76, p246-284.

Walters, A. C. & Campbell, C. D. 1935. Mylonites from San Andreas fault zone. *Am. J. Sci.* v.229, p473-503.

Walters, A. C. & Krauskopf, K. B. 1941. Protoclastic border of Colvill batholith. *Geol. Soc. Am. Bull.* v.52, p1355-1418.

Ware, N. G. 1981. Computer programs and calibration with the Pibs technique for quantitative electron probe analysis using lithium-drifted silicon detector. *Computers and Geoscience* v.7, p167-184.

Warnaars, F. W. et al, 1985. Porphyry copper and tourmaline breccias at Los Bronces Blanco, Chile. *Econ. geol.* v.80, p1544.

White, A. J. R. & Chappell, B. W. 1977. Ultrametamorphism and granitoid genesis. *Tectonophysics*, v.43, p7-23.

White, A. J. R. & Chappell, B. W. 1983. Granitoid types and their distributions in Lachlan fold belt, southeastern Australia. *Geol. Soc. Am. Memori.* p21-34.

Wilson, C. J. N. 1980. The role of fluidization in the emplacement of pyroclastic flows: An experimental approach. *Jour. Volcanology geotherm. Research.* v.8, p231-249.

Wones, D. R. 1967. A low pressure investigation of the stability of phlogopite. *Geochim. Cosmochim. Acta* v.31, p2248-2253.

Wones, D. R. & Eugster, H. P. 1965. Stability of biotite, experiment, theory, and application. *Am. Mineralogists* v.50, p1228-1272.

Yoder, H. S. & Eugster, H. P. 1954. Phlogopite synthesis and stability range. *Geochim. Cosmochim. Acta*, v.6, p157-185.

Yoder, H. S. & Eugster, H. P. 1955. Synthetic and natural muscovite. *Geochim. Cosmochim. Acta*, v.8, p225-280.

